UNIVERSITY OF TECHNOLOGY SYDNEY

Electrode Materials for Lithium-ion Batteries and Supercapacitors

This thesis is submitted in fulfilment of the requirements for the degree of

Doctor of Philosophy

from

University of Technology, Sydney

by

Anjon Kumar Mondal

B. Sc. (Hons) & M. Sc.

Centre for Clean Energy Technology

Faculty of Science

2015

CERTIFICATE OF ORIGINAL AUTHORSHIP

I, Anjon Kumar Mondal certify that the work presented in this thesis has not previously been submitted for a degree nor has been submitted as part of requirements for a degree except as fully acknowledged within the text.

I also certify that the thesis has been written by me. Any help that I have received in my research work and the preparation of the thesis itself has been acknowledged. In addition, I certify that all information sources and literature used are indicated in the thesis.

Anjon Kumar Mondal

Sydney, Australia

May, 2015

DEDICATION

This thesis is dedicated to my family. Thank you for all of your love and support.

ACKNOWLEDGEMENTS

I would like to express my deepest gratitude to my supervisor, Professor Guoxiu Wang for his invaluable advice and supervision throughout this research work. His inventive research ideas and motivation enlightened and encouraged me during my PhD study.

I am grateful to my co-supervisor Assoc. Professor Alison Ung for her constant suggestion, contribution to reviewing my thesis and the fruitful discussion. I also acknowledge Assoc. Professor Andrew McDonagh for his kind help and suggestion.

Special thanks are given to my colleagues, Dr. Hao Liu, Dr. Zhimin Ao, Dr. Xiaodan Huang, Dr. Ali Reza Ranjbartoreh, Dr. Bei Wang, Dr. Bing Sun, Dr. Ying Wang, Dr. Dawei Su, Mr. Shuangqiang Chen, Mr. Kefei Li, Mr. Yiying Wei, Mr. Xiuqiang Xie, Mr. Jinqiang Zhang, Miss Yufei Zhao, Miss Katja Kretschmer, Miss Jing Xu, and Mr. Linfeng Zheng for their innovative ideas, kind co-operation and assistance during the period of this research. It is my pleasure to have worked with all of you and I really appreciate everyone's efforts in creating an intimate atmosphere for the research work.

I would like to acknowledge Dr. Jane Yao for her kind help and support in many ways throughout this study period.

I appreciate the administrative and technical support I received from Dr. Ronald Shimmon, Dr. Linda Xiao, Mrs. Rochelle Seneviratne, Mrs. Era Koirala, Ms. Sarah King, and Ms. Emaly Black.

Finally, I would like to express my sincere gratitude to my wife, my son, my daughter my parents, my family members and relatives. Without their support and encouragement, it would have been impossible for me to complete the research. Their

love is the mental strength that supported me to study abroad and it will hold a special

place in my heart forever.

RESEARCH PUBLICATIONS

1   **A. K. Mondal,** D. Su, S. Chen, A. Ung, H. S. Kim, G. X. Wang, Mesoporous $MnCo_2O_4$ with a flake-like structure as advanced electrode materials for lithium ion batteries and supercapacitors, ***Chemistry–A European Journal***, 2015, 21, 1526-1532. **IF: 5.696**

2   **A. K. Mondal,** D. Su, S. Chen, K. Kretschmer, X. Xie, H. J. Ahn, G. X. Wang, A microwave synthesis of mesoporous $NiCo_2O_4$ nanosheets as electrode materials for lithium ion batteries and supercapacitors, ***ChemPhysChem***, 2015, 16, 169-175. **IF: 3.36**

3   **A. K. Mondal,** D. Su, S. Chen, X. Xie, G. X. Wang, Highly porous $NiCo_2O_4$ nanoflakes and nanobelts as anode materials for lithium ion batteries with excellent rate capability, ***ACS Applied Materials & Interfaces,*** 2014, 6, 14827-14835. **IF: 5.9**

4   **A. K. Mondal,** D. Su, S. Chen, J. Zhang, A. Ung, G. X. Wang, Microwave-assisted synthesis of spherical β-$Ni(OH)_2$ superstructures for electrochemical capacitors with excellent cycling stability, ***Chemical Physics Letters,*** 2014, 610-611, 115–120. **IF: 1.991**

5   **A. K. Mondal,** D. Su, S. Chen, B. Sun, K. Li, G. X. Wang, A simple approach to prepare nickel hydroxide nanosheets for enhanced pseudocapacitive performance**, *RSC Advances,*** 2014, 4, 19476-19481. **IF: 3.708**

6   **A. K. Mondal,** B. Wang, D. Su, Y. Wang, S. Chen, X. Zhang, G. X. Wang, Graphene/MnO_2 hybrid nanosheets as high performance electrode materials for supercapacitors, ***Materials Chemistry and Physics,*** 2014, 143, 740-746. **IF: 2.129**

7   **A. K. Mondal,** D. Su, Y. Wang, S. Chen, Q. Liu, G. X. Wang, Microwave hydrothermal synthesis of urchin-like NiO nanospheres as electrode materials for lithium-ion batteries and supercapacitors with enhanced electrochemical performances, ***Journal of Alloys and Compounds,*** 2014, 582, 522-527. **IF: 2.726**

8   **A. K. Mondal,** S. Chen, D. Su, H. Liu, G. X. Wang, Fabrication and enhanced electrochemical performances of MoO_3/graphene composite as anode material for lithium-ion batteries, ***International Journal of Smart Grid and Clean Energy,*** 2014, 3, 142-148.

9   **A. K. Mondal,** D. Su, Y. Wang, S. Chen, G. X. Wang, Hydrothermal synthesis of nickel oxide nanosheets for lithium-ion batteries and supercapacitors with excellent performance, ***Chemistry - An Asian Journal,*** 2013, 8, 2828-2832. **IF: 3.935**

10 **A. K. Mondal,** B. Wang, D. Su, Y. Wang, X. Zhang, G. X. Wang, Preparation and enhanced electrochemical performance of MnO_2 nanosheets for supercapacitors, ***Journal of the Chinese Chemical Society,*** 2012, 59, 1275-1279. **IF: 0.856**

TABLE OF CONTENTS

LIST OF TABLES

LIST OF FIGURES

xviii

ABSTRACT

With the increasing demand for energy and growing concern about environmental pollution caused by the enormous consumption of fossil fuels, it is an urgent need of renewable energy and clean energy sources. Development of suitable mobile electronics or energy storage technologies that can be used in electric vehicles would help to address problem. As energy storage devices, lithium-ion batteries have attracted attention due to their high energy density and storage capacity. Supercapacitors have attracted enormous attention due to high power density and long cycle life. The exploration of new electrode materials for lithium-ion batteries and supercapacitors is the focus of research to satisfy the ever-rising demands for better performance including longer cycle life and improved safety. Nanostructured materials exhibit excellent electrochemical performances, and they are regarded as promising materials for high-performance lithium-ion batteries and supercapacitors. In this doctoral study, various nanostructured materials such as, nanosheets, nanospheres, nanobelts, nanoflakes, hybrid nanostructures and mesoporous structures have been successfully synthesized and characterised, using different methods. Their electrochemical properties have also been evaluated by cyclic voltammetry, galvanostatic charge-discharge, and electrochemical impedance spectra.

Nickel oxide (NiO) nanosheets have been synthesized, using a simple ethylene glycol mediated hydrothermal method. When evaluated as anode materials for lithium ion batteries, NiO nanosheets exhibited high reversible capacities of 1193 mA h g^{-1} at the current density of 500 mA g^{-1} with enhanced rate capability and good cycling stability. While as electrode materials for supercapacitors, NiO nanosheets also demonstrated a

superior specific capacitance of 999 F g^{-1} at the current density of 20 A g^{-1} with excellent cycling performance.

The spherical β-Ni(OH)$_2$ superstructures was successfully synthesised in a single-step microwave-assisted process, without using any templates. Due to its unique morphology, the prepared β-Ni(OH)$_2$ electrode displayed a high and specific capacitance of 2147 F g^{-1} at a discharge current of 1 A g^{-1} with excellent cycling stability (99.5 % capacitance retained after 2000 cycles).

A straight forward microwave reaction was employed to successfully prepare α-Fe$_2$O$_3$ nanoparticles with two different sizes. When used as anode materials for lithium ion batteries of both the materials showed good electrochemical performances. Remarkably, the electrode made of larger particles (200-300 nm) exhibited higher reversible capacity of 1012 mA h g^{-1} with better rate capability and excellent cycling stability (88 % retention after 80 cycles) than those of the smaller particles (20-30 nm) (49 % retention after 80 cycles). The better lithium storage properties of the large particles can be attributed to their structural integrity during cycling, which offers adequate spaces to accommodate volume expansion during Li$^+$ insertion/extraction and shortens the diffusion paths of lithium ions.

Highly porous NiCo$_2$O$_4$ nanoflakes and nanobelts were prepared in two steps; the NiCo$_2$O$_4$ intermediates were first formed by a hydrothermal method and the intermediates were simply thermal treated to the final product. Owing to their unique porous structural features, the NiCo$_2$O$_4$ nanoflakes and nanobelts exhibited high specific capacities of 1033 mA h g^{-1} and 1056 mA h g^{-1}, respectively, good cycling stability and rate capability. These exceptional electrochemical performances could be attributed to the unique structure of high surface area and void spaces within the surface of

nanoflakes and nanobelts, which provides large contact areas between electrolyte and active materials for electrolyte diffusion and cushions the volume change during charge-discharge cycling.

Graphene/MnO_2 hybrid nanosheets were prepared by the incorporating graphene and MnO_2 nanosheets in ethylene glycol. As electrode materials for supercapacitors, graphene/MnO_2 hybrid nanosheets of different ratios were investigated. The graphene/MnO_2 hybrid nanosheets with a weight ratio of 1:4 (graphene: MnO_2) delivered the highest specific capacitance of 320 F g^{-1}, and exhibited good capacitance retention on 2000 cycles.

Mesoporous $NiCo_2O_4$ nanosheets were synthesized by microwave method and applied as electrode materials for lithium ion batteries and supercapacitors. Due to its porous nanosheet structure, the $NiCo_2O_4$ electrodes exhibited a high reversible capacity of 891 mA h g^{-1} at the current density of 100 mA g^{-1} with good rate capability and stable cycling performance. When used as electrode materials for supercapacitors, $NiCo_2O_4$ nanosheets demonstrated a specific capacitance of 400 F g^{-1} at the current density of 20 A g^{-1} and superior cycling stability over 5000 cycles. The excellent electrochemical performance could be ascribed to the thin porous nanosheet structure, which provided high specific surface area to increase electrode-electrolyte contact area and facilitate rapid ion transport.

Mesoporous flake-like Manganese-cobalt composite oxide ($MnCo_2O_4$) was successfully synthesized, using the hydrothermal method. The flake-like $MnCo_2O_4$ was evaluated as anode materials for lithium ion batteries. It exhibited superior rate capability and good cycling stability with a high reversible capacity of 1066 mA h g^{-1}. As electrode materials for supercapacitors, $MnCo_2O_4$ also demonstrated a high super capacitance of

1487 F g^{-1} at the current density of 1 A g^{-1} and superior cycling stability over 2000 charge-discharge cycles.

INTRODUCTION

Background

One of the current intractable issues that dominate the world politics, economics and climate change is energy. Major sources of energy for human activity are fossil and mineral fuels and nuclear sources. All of these are very destructive to the environment and causes global warming, reduction of the ozone layer, damage of biosphere and geosphere and ecological devastation. 90% of the world's energy consumption is fossil fuel, and it is expected to peak around the year 2050. Massive consumption of this fossil fuel has led to the increase of environmental pollution. Moreover, the availability of fossil fuel is limited and eventual it will be exhausted. World scientific communities are now urgently seeking renewable, clean and alternative energy sources to that of fossil fuel. Sustainable technologies that could provide clean and affordable energy to our society needs have been the biggest challenges and concerns not only of the scientific communities but also the governments, the business sectors, and wider communities. For instance, the issues of carbon footprint and carbon tax, in the context of pollution caused by fossil fuels are vigorously debated and truly controversial. Inspire this controversial issue, the fact remains that there is an urgent need for alternative sources of clean energy and new technology is required to store this energy.

Among different renewable energy sources, solar, wind, geothermal and tidal energy have been developed. However, the mentioned sources of energy are intermittently available. High-performance energy storage systems are urgently needed to capture and store the energy generated form these renewable sources. Furthermore, the storage systems would be able to stabilize the electricity grid at the high capturing of enegy. Electrochemical energy storage systems are promising to serve as such supporting

facilities, and by compare is the most convenient form of energy storage is portable chemical energy, which is the reason for our interest. It provides the portability of stored chemical energy and delivers this energy as electrical energy with high conversion efficiency. Lithium ion batteries and supercapacitors are typical energy storage devices, both of which store renewable energy in the electrochemical process. In the past twenty years, lithium-ion batteries proved themselves as one of the most important electrochemical power sources for portable electronic devices. However, they cannot meet the rigorous requirement for high power electric vehicles (EVs) and hybrid electric vehicles (HEVs). In recent years, supercapacitors have attracted significant attention due to their high power density and long cycle life. Supercapacitors play a vital role in accompanying batteries or fuel cells in their energy storage function by providing back-up power supplies to protect against power interruptions. Many research groups and industries are continuing intensive research to develop new materials for high-performance lithium-ion batteries and supercapacitors.

Importance of this work

Owing to the high demand for portable electronics and electric vehicles, the safer energy storage systems are indispensable with high rate charge-discharge capability and long cycle life. The performance of lithium-ion batteries and supercapacitors are intimately related to the electrode materials. The development of new electrode materials that are low-cost and environmentally friendly have been progressing rapidly with the advancement of materials design strategies, synthesis techniques, and characterization methodologies. Nanostructured materials with different morphologies have attracted extensive attention due to their intriguing mechanical, optical and electronic properties compared to their bulk counterparts. The aim of this work is to develop nanostructured electrode materials with various morphologies and to find out

possible way to improve electrochemical performances, which provides potential opportunities for further research. The development of electrode materials for lithium-ion batteries and supercapacitors should focus on:

1) Higher specific capacity/capacitance, high energy density and power density.

2) High charge-discharge rates and long cycle life.

3) Low cost and safety for large scale applications.

4) Structural integrity, higher reactivity and reversibility during cycling.

5) Environmental benignity and simple preparation process.

Outline of study

In this PhD work, nanostructured electrode materials with different morphologies have been successfully synthesized by using hydrothermal methods, microwave methods and precipitation methods,. The morphologies, crystal structures and electrochemical properties of the materials were systematically evaluated for lithium-ion batteries and supercapacitors. The results and significant outcomes are briefly presented as follows:

1. Chapter 1 explores a literature review of lithium-ion batteries and supercapacitors. In this Chapter, fundamental concepts and principles of lithium-ion batteries and supercapacitors are presented. Contemporary developments in anode materials, cathode materials and electrolyte for lithium-ion batteries and electrode materials and electrolytes for supercapacitors are also systematically reviewed.

2. The overall experimental parts are introduced in Chapter 2. The materials preparation methods are firstly presented, followed by physical and structural characterizations, using X-ray diffraction, Field Emission Scanning Electron Microscopy, Transmission Electron Microscopy, Nitrogen adsorption-desorption isotherm, Atomic Force Microscopy, Raman Spectroscopy, Thermogravimetric Analysis and Fourier Transform

Infrared (FT-IR) Spectroscopy. Electrode preparation, cell assembly and electrochemical testing techniques are also demonstrated in this Chapter.

3. Chapter 3 reports a simple ethylene glycol mediated hydrothermal technique to prepare NiO nanosheets. The electrochemical properties of the NiO nanosheets are systematically investigated for lithium-ion batteries and supercapacitors. Chapter 4 focuses on spherical $Ni(OH)_2$, which are prepared by a simple microwave method without using any template. Structure characterizations show that the spherical β-$Ni(OH)_2$ composed of twisted nanosheets. The electrochemical properties of the as-prepared materials are evaluated by cyclic voltammetry and chronopotentiometry technology in 2 M KOH solution.

4. Chapter 5 demonstrates Fe_2O_3 nanoparticles with two different sizes via a microwave method. As anode materials for lithium-ion batteries, the electrochemical properties of these two materials are investigated and compared on the basis of electrochemical performances. Chapter 6 deals with the preparation of highly porous $NiCo_2O_4$ nanoflakes and nanobelts by a simple template-free hydrothermal method. The porous structure is beneficial for the enhancement of electrochemical properties, which are discussed in this chapter. Based on the specific capacity, rate capability and cycling stability, $NiCo_2O_4$ nanoflakes and nanobelts are also compared for lithium-ion battery applications.

5. Chapter 7 presents the preparation of MnO_2 nanosheets and graphene nanosheets separately without any surfactant and fabrication of graphene/MnO_2 hybrid nanosheets using ethylene glycol as dispersing agent. In this hybrid material, the effect of graphene nanosheets and MnO_2 nanosheets on electrochemical performances such as specific capacitance and cycling stability are discussed for supercapacitors. The specific

capacitance and cycling stability of bare MnO_2 nanosheets are also described in this chapter.

6. In chapter 8, a microwave synthesis of mesoporous $NiCo_2O_4$ nanosheets as electrode materials for lithium-ion batteries and supercapacitors are introduced. The effect of high surface area and mesoporous structure on electrochemical performances of lithium-ion batteries and supercapacitors are also discussed. Chapter 9 reports the synthesis of mesoporous flake-like $MnCo_2O_4$ by using a hydrothermal method. The electrochemical properties of the flake-like $MnCo_2O_4$ are evaluated for lithium-ion batteries and supercapacitors.

7. Finally, a general conclusion is given in chapter 10, which contains the main achievement, challenges and an outlook on future development in this area.

Chapter 1 Literature Review

1.1 Lithium-ion Batteries

1.1.1 History and Development

Rechargeable batteries can store electrical energy in the form of chemical energy. Among rechargeable batteries, lithium-ion batteries have become popular with many advantages such as, high energy density, low maintenance, long cycle life, no memory effect and low self-discharge. In the past two decades since the first commercial products manufactured by SONY, lithium-ion batteries (LIBs) have been widely applied for portable electronic devices. These include notebook computers, cell phones, digital cameras, etc. Its energy density is 2-3 times and power density 5-6 times higher than traditional nickel-metal hybrid, nickel-cadmium and lead-acid batteries. The worldwide market of lithium-ion batteries is valued at 10 billion US dollars per annum. Lithium-ion batteries are now being intensively pursued upcoming large-scale transportation applications including hybrid electric vehicles (HEV), plug in hybrid electric vehicles (PHEV) and electric vehicles (EV) [1-5]. They are also seriously considered for the efficient storage and utilization of intermittent renewable energies such as, solar and wind.

Around 1970, Geballe et al. discovered that a range of electron-donating molecules and ions could be intercalated into the layered dichalcogenides [6]. Among the various dichalcogenides, titanium disulphide was the most promising electrode for energy storage [7, 8]. It is lightest semi-metal and highly conductive. It can also form a single phase with lithium over the entire composition range of Li_xTiS_2 ($0 \leq x \leq 1$), which enable to remove all the lithium reversibly [9, 10]. However, the high production cost and low potential limit its practical application [11]. In early 1970s, the first lithium

batteries were used for selective military applications. Lithium metal was used as anode material, owing to its light weight, high voltage, superior conductivity and high energy density. However, their applications were constrained due to the safety concerns [12]. After that, researchers tried to investigate the lithium intercalation behaviour of metal oxides, particularly, vanadium pentoxide (V_2O_5). The relatively complex structural behaviour during lithium intercalation and reduced cycling performance makes this material inappropriate for commercialization [13, 14]. In the 1980s, Goodenough and co-workers reported that $LiCoO_2$ had a similar layered structures to the dichalcogenides, where the extracted lithium could be inserted reversibly, therefore making it a potential positive electrode material [15]. In 1982, Yazami and Touzain demonstrated the world's first successful experiment on the electrochemical insertion and extraction of lithium in graphite using solid organic electrolyte [16, 17]. For the carbon anode, the lithium insertion product is LiC_6, which reduces dendrite formation and avoiding short-circuiting compared to the pure lithium metal. After further improvement, the lithium-ion battery combining $LiCoO2$ as the cathode materials and graphite as the anode materials was commercialized by SONY in 1991 and Ashai Kasei and Toshiba in 1992 [18].

1.1.2 Basic Concepts and Energy Storage Mechanism

The rechargeable lithium battery is a lithium-ion devices and it does not contain lithium metal. Lithium intercalation compounds are used as positive and negative electrode materials in lithium-ion batteries. In a typical lithium-ion cell, graphite and lithium metal oxide ($LiCoO_2$) are used as a negative electrode (anode) and a positive electrode (cathode), respectively. A non-aqueous Li^+ conducting medium is used as electrolyte. The positive and negative electrodes are separated by an electrolyte-filled porous polymer membrane that allows lithium ion transfer but prevents electrolyte from direct

contact. The lithium ions are shuttled between two host electrodes (anode and cathode) during the charge-discharge process. When the battery is discharging, Li^+ ions de-intercalate from the anode, pass through the electrolyte and intercalate into the cathode. Meanwhile, the electrons pass through the external circuit from the negative electrode to the positive electrode. On charging, the process is reversed when an external voltage is applied to the battery. During charge-discharge process, Li ions move between the negative and positive electrode, empowering the conversion of chemical energy into electrical energy and storage of electrochemical energy within the battery [19].

Figure 1.1 illustrates the basic lithium-ion battery system that leads the current battery market. The cell reactions are reversible lithium-ion intercalation and de-intercalation cycles between two layered structures. The redox reactions involved in $LiCoO_2$/graphite cell are presented as follows:

Cathode:

$$LiCoO_2 \leftrightarrow Li_{1-x}CoO_2 + xLi^+ + xe^- \ (1<x<0) \tag{1.1}$$

Anode:

$$6C + xLi^+ + xe^- \leftrightarrow Li_xC_6 \ (1<x<0) \tag{1.2}$$
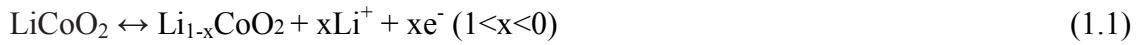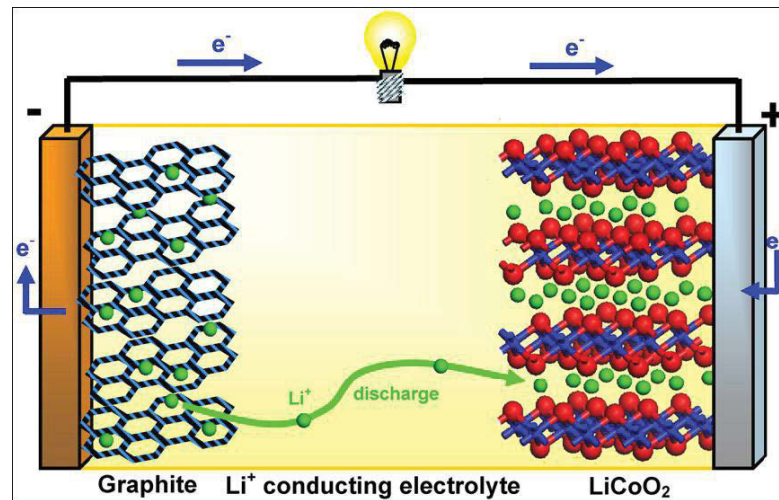
Figure 1.1 Schematic illustration of the charge/discharge process involved in a lithium-ion cell [20].

3

1.1.3 Advantages and Disadvantages of Lithium-ion Batteries

Advantages:

➢ Can operate a wide range of temperature. Most of the lithium-ion batteries perform over a temperature range from about 70 to -40 ^{o}C.

➢ High specific energy and power density: the energy output of a lithium-ion battery is 2 to 4 times better than that of conventional zinc anode batteries.

➢ Long cycle life

➢ High Coulombic and energy efficiency

➢ High voltage: Lithium-ion batteries have voltages up to 4 V, depending on the active materials used.

➢ Superior shelf life: Lithium-ion batteries can be stored for long periods, even at elevated temperatures, with no memory effect.

Disadvantages

➢ Capacity loss when overcharged

➢ Degrade at high temperature

➢ Moderate initial cost and extra cost for recycling

➢ Possible thermal runaway and venting when crushed.

The following terms are frequently used throughout this study for evaluating the performances of lithium-ion batteries:

Electrode (Anode and Cathode): The anode and cathode are the negative and positive electrode in an electrochemical cell, associated with the oxidation and reduction, respectively. Electrodes are the composite of active materials, conductive materials and binder, which adhering to the current collector/substrate (copper foil for anode and aluminium foil for cathode). The conductive materials (e.g. carbon black) are used to increase the electronic conductivity of the electrode and the binder (a long-chain

polymer, e. g. polyvinylidene fluoride (PVDF)), which hold all the electrode materials together on the substrate.

Active materials: The material that generate electrical currents by means of a chemical reaction within the battery [21]. For lithium-ion batteries, material with a potential higher than 2 V is defined as a cathode material and potential lower than 2 V is defined as an anode material. The theoretical potential of an electrochemical cell depends on the nature of active materials used in the cell. The potentials and specific capacities of various electrode materials are summarized in Fig. 1.2.
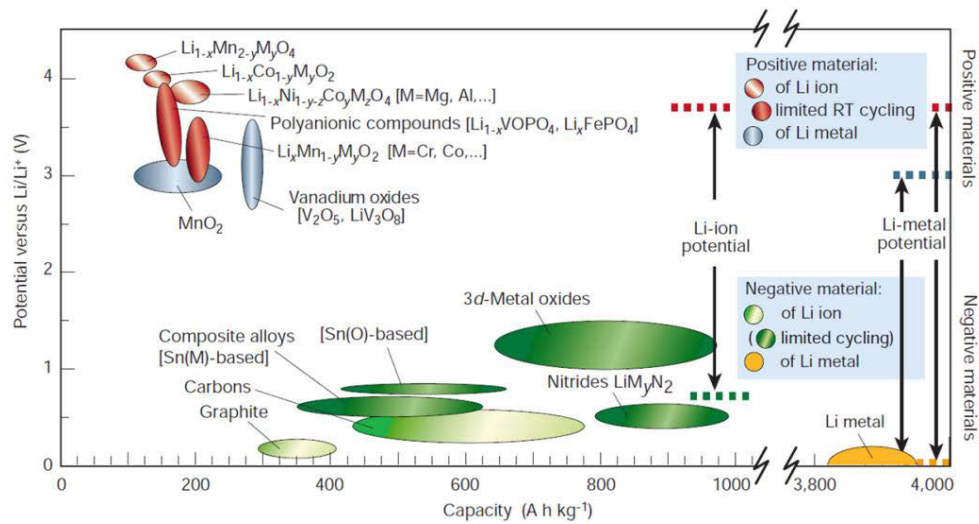
Figure 1.2 Voltage versus capacity for electrode materials for the next generation of rechargeable Li-based cells [5].

Electrolyte: The electrolyte is a material that provides pure ionic conductivity between the positive and negative electrodes of a cell [21]. The electrolyte must satisfy the following requirements [1, 22]:

1) Low electronic conductivity of $\sigma_e < 10^{-10}$ S cm^{-1} and high lithium ion conductivity of $\sigma_e > 10^{-10}$ S cm^{-1} over the temperature range of battery operation.

2) Chemical stability over ambient temperature ranges.

3) Safe materials, i.e., preferably non-flammable and non-explosive materials if short-circuited

4) Chemical stability with respect to the electrodes, including the ability to rapidly form a passivating solid electrolyte interface (SEI) layer.

5) Low cost and low toxicity.

6) Excellent retention of the electrode/electrolyte interface during cycling when the electrode particles are changing their volume.

7) A transference number $\sigma_{Li+}/\sigma_{total} \approx 1$, where σ_{total} includes conductivities by other ions in the electrolyte as well as σ_{Li+} and σ_e.

It is challenging to meet all these requirements. The choice of electrolyte solutions is a vital issue related to the operation of lithium-ion batteries. Around twenty years ago, alkyl carbonates were found to be the best and most suitable solvents for lithium-ion batteries [23]. A major innovation was the selection of binary solvent mixtures such as, ethylene carbonate (EC) and either dimethyl carbonate (DMC), ethyl methyl carbonate (EMC) or diethyl carbonate (DEC) and the lithium salt, lithium hexa-fluorophosphate (LiPF$_6$), as the basic standard electrolyte solutions for lithium-ion batteries [24]. The electrolyte for lithium-ion batteries consists of a lithium salt and solvents. The lithium salts provide the lithium source in the electrolyte for the insertion/extraction between the electrodes, and the solvents provide a medium for lithium ion diffusion. Table 1.1 shows a series of electrolytes with different compositions.

Separator: A separator is a porous membrane and act as a physical barrier between the positive and negative electrodes. Their primary function is to keep the positive and negative electrodes apart to prevent electrical short circuits. At the same time allows rapid transport of ionic charge carriers that are needed to complete the circuit during the passage of current in an electrochemical cell. Separators must be permeable to the ions and inert in the battery environment. Microporous membranes using polyolefins have been developed and used extensively for lithium-ion batteries. At presence, the

polyolefin membranes are made of polyethylene (PE), polypropylene (PP) or laminates of polyethylene and polypropylene.

Table 1.1 Nonaqueous electrolytes for lithium ion batteries [1].

Electrolytes	Example of classical electrolytes	Ionic conductivity (10^{-3} s/cm) at room temperature	Electrochemical window (V) vs Li^+/Li^0		Remark
			Reduction	Oxidation	
Liquid organic	1M $LiPF_6$ in EC:DEC(1:1)	7	1.3	4.5	Flammable
	1M $LiPF_6$ in EC:DEC(1:1)	10	1.3	>5.0	
Ionic liquids	1M LiTFSI in EMI-TFSI	2.0	1.0	5.3	Non-flammable
	1M $LiBF_4$ in EMI-BF_4	8.0	0.9	4.7	
Polymer	LiTFSI-P(EO/MEEGE)	0.1	<0.0	4.7	Flammable
	$LiClO_4$-PEO_8 + 10 % TiO_2	0.02	<0.0	5.0	
Inorganic solid	$Li_{4-x}Ge_{1-x}P_xS_4$ (x = 0.75)	2.2	<0.0	>5.0	Non-flammable
	$0.05Li_4SiO_4 + 0.57Li_2S + 0.38SiS_2$	1.0	<0.0	>8.0	
Inorganic liquid	$LiAlClO_4 + SO_2$	70	-	4.4	Non-flammable
Liquid organic + polymer	$0.04LiPF_6$ + 0.2 EC + 0.62DMC + 0.14PAN	4.2	-	4.4	Flammable
	$LiClO_4$ + EC + PC + PVDF	3.0	-	5.0	
Ionic liquid + Polymer	1MLiTFSI + P_{13}TFSI + PVDF-HFP	0.18	<0.0	5.8	Less flammable
Ionic liquid + Polymer + Liquid organic	56 wt % LiTFSI-Py_{24}TFSI + 30 wt % PVdF-HFP + 14 wt % EC/PC	0.81	1.5	4.2	Less flammable
Polymer + Inorganic solid	2 vol % $LiClO_4$-TEC-19 + 98 vol % $95(0.6Li_2S + 0.4Li_2S)$ + 14 wt % EC/PC	0.03	<0.0	>4.5	Non-flammable

These can provide adequate cost, chemical stability and excellent mechanical properties [21, 25].

Specific capacity: The specific capacity is defined as the amount of electric charge the battery can store per unit mass. The theoretical specific capacity (Q_{TSC}, mA h g^{-1}) can be calculated from the following equation:

$$Q_{TSC} = n \times F/M \tag{1.3}$$

Where n is the number of electrons transferred during the electrochemical reactions, F is the

Faraday constant (96,485.33 C mol^{-1}) and M is the molecular weight of the active material (g mol^{-1}).

The specific charge capacity (Q_c, mA h g^{-1}) or specific discharge capacity (Q_d, mA h g^{-1}) can be calculated from the following equation:

$$Q_c \text{ (or } Q_d) = I \times t/m \tag{1.4}$$

Where I is the charge or discharge current (mA), t is the charge or discharge time (s), m is the mass of the active materials (g).

Cell potential: The potential difference between the cathode and anode materials.

Coulombic efficiency: The coulombic efficiency (η) is a term to represent the ratio of the charge capacity (Qc) to the discharge capacity (Qd). It indicates the reversibility of a particular battery and can be defined by the following equation:

$$\eta = Q_c/Q_d \times 100 \text{ %} \tag{1.5}$$

Specific energy: defined as the energy per unit mass.

Energy density: a term used for the amount of energy stored per unit volume in a given system. The specific energy (*SE*, Wh kg^{-1}) and energy density (*ED*, Wh L^{-1}) can be calculated from the following equations:

$$SE = (E \times Q)/1000 \tag{1.6}$$

$$ED = (E \times Q \times m) / (100 \times V) \tag{1.7}$$

Specific power: the ability of the battery to deliver power per unit mass.

Power density: a term used for the ability of the battery to deliver power per unit volume.

The specific power (SP, Wh kg^{-1}) and power density (PD, Wh L^{-1}) can be calculated from the following equations:

$$SP = SE/t \tag{1.8}$$

$$PD = ED/t \tag{1.9}$$

Where t is the discharge time (h).

Irreversible capacity (QI): used to define the capacity loss after each cycle.

For cathode materials:

$$Q_I = Q_d - Q_c \tag{1.10}$$

For anode materials:

$$Q_I = Q_c - Q_d \tag{1.11}$$

1.1.4 Nanostructured Electrode Materials

The performance of rechargeable lithium-ion batteries mainly depends on active electrode materials. The electrode materials should have some basic requirements such as, high reversible capacity, fast Li-ion diffusion, environmental friendliness, structural flexibility and stability, long cycle life, low cost and improved safety [26]. Micro-sized electrode materials are used in commercial lithium-ion batteries. The intrinsic diffusivity of lithium ion in the solid state is less that 10^{-8} cm^2 s^{-1}, which considerably limits the rate of insertion/extraction, and hence charge-discharge rate performance. In order to meet the future demands of EVs and HEVs, the increased charge-discharge rates are required for lithium-ion batteries. Nanostructured materials have a significant impact on the performance of lithium-ion batteries. The employment of nanostructured materials instead of existing micro-sized materials are considered to be most promising

strategy to overcome present limitations. Their reduced dimensions can significantly shorten the lithium-ion diffusion path and enable far higher intercalation/de-intercalation rates and therefore high power [27]. The benefits and drawbacks of nanostructured electrode materials are presented as follows [28]:

Benefits

➢ The reduced dimensions increase the rate of lithium insertion/extraction significantly, because of the short distances for lithium ion transport within the particles. The characteristic time for diffusion is given by $t = L_{ion}^2/D_{Li}$, where L_{ion} is the lithium diffusion length and D_{Li} is the lithium-ion diffusion co-efficient [27].

➢ Nano-sized electrode active material can also shorten the path length for electronic transport, and thus alleviate the limitation of electronic conductivity [29].

➢ Nanostructured material with high specific surface area permits a high contact area between electrode and electrolyte, which create more active sites for lithium-ion diffusion across the interface.

➢ The nanometre-sized electrode materials can accommodate large volume expansion/contraction during cycling, preserving the integrity of the electrode and leading to stable cycling performance [30, 31].

➢ Recent studies show that nano active electrode materials can lead to new Li-storage mechanisms, affording high capacities, general applicability and rechargeability. Nanomaterials increase the surface and interface storage [32-34]. Lithium ion can also be stored in nanopores [35, 36].

➢ The chemical potentials for lithium ions and electrons may be modified by nano-size materials, resulting in a change of electrode potential [37, 38].

➢ It has been observed that nano active electrode materials become active for lithium ion insertion, an episode unable to take place in bulk form [27, 39]

Drawbacks

➢ The synthesis routes for nanomaterials are more complex and difficult to control their dimensions.

➢ High surface area and high surface energy of nanomaterials also increase undesirable side reactions between electrode and electrolyte, which results in a high irreversibility and reduced cycle life.

➢ The packing density of nanomaterial-based electrodes is lower than that of micromaterial-based electrodes thus reducing the volumetric energy density.

➢ Nanomaterials tend to aggregate during electrode fabrication and difficult to make a homogeneous mixture with conductive agent and binder.

➢ Nanometer-sized electrode materials have noticeable electrochemical agglomeration during charge-discharge cycling.

1.1.4.1 Anode Materials

In a lithium-ion battery, anode materials are associated with the oxidation reaction. An ideal anode material for lithium-ion batteries should have the following properties:

➢ It must contain compounds or elements with low formula weights and low density.

➢ The materials should accommodate relatively large amounts of Li per formula unit.

➢ It must possess good electronic conductivity for electron transportation and high ionic conductivity for lithium ion transportation.

➢ It must react with lithium ion reversibly.

➢ The materials should be cheap and environmentally friendly.

- ➤ The materials must show a potential as close to that of lithium metal.

- ➤ It should be stable and safe over the entire operation environment.

- ➤ The material should react with lithium at a low operating voltage.

- ➤ It must not be soluble in the solvents of the electrolyte and must not chemically react with the salt or solvents of the electrolyte.

Nano carbons

Micrometer-sized graphite is the most used commercial anode material for lithium-ion batteries because of its low and flat working potential, low cost and long cycle life. It has been used as negative electrodes for rechargeable lithium-ion batteries for many years [40, 41]. However, the most lithium enriched intercalation compound of graphite has a stoichiometry of LiC_6, which results in a less than expected theoretical capacity (372 mA h g^{-1}) and a small practical energy density [42, 43]. Besides, the lithium ion transport rates of graphite anode are always less than 10^{-6} cm^2 s^{-1}, causing in a low power density since the chemical diffusion coefficient of lithium ions is related to power density of the battery [44]. To further increase the rate of lithium insertion/extraction and thus the power of the battery, nano-sized graphite has been investigated as a replacement. When lithium ions are inserted into the graphite layers at a potential of less than 1 V versus Li/Li+, the electrolyte begins to reduce accompanied by the formation of a passivating (solid electrolyte interface, SEI) layer on the graphite surface [45-47]. The formation of such a layer protects graphite electrode from exfoliation. The severity of layer formation on nano-sized high-surface area graphite, results in the consumption of excessive charge, which is irreversible and causes energy loss from the cell. A concomitant safety concerns has also been raised due to the deposition of highly reactive lithium on the surface of graphite because of the SEI layer [20]. To increase the energy and power densities of lithium ion batteries nanostructured

carbon anode materials including one-dimensional (1D), two-dimensional (2D) and porous carbons have been developed for lithium storage.

Carbon nanotubes

Owing to their high surface-to-volume ratios and exceptional surface activities 1D nano-sized carbon materials have been widely investigated as anode materials for lithium ion batteries. After the discovery of carbon nanotubes (CNTs), researchers studied the interactions of Li vapour with CNTs and measured the corresponding electrochemical properties [48, 49]. It was observed that Li can intercalate between pseudo-graphitic layers and also inside the central tubes. The small diameters of CNTs can impose strain on the planner bonds of the hexagon. The strain causes de-localization of electrons and makes the structure more electronegative than regular graphitic sheets, which increases the rate of Li intercalation. Different CNTs including bamboo-shaped CNTs and CNTs with a quadrangular cross section (q-CNTs) have been used as anode materials for rechargeable LIBs [50, 51]. However, the Coulombic efficiency of CNTs was found to be low compared with that of graphite due to the high voltage hysteresis and large structure defects [52, 53].

Carbon nanofibers

Different methods were employed to synthesize Carbon nanofibers (CNFs) and their electrochemical properties have also been evaluated as anode materials for LIBs [54, 55]. Unlike CNTs, which require a long diffusion time for Li for intercalation/deintercalation, carbon nanofibers are expected to stimulate fast Li intercalation/deintercalation due to their huge amount of lattice and surface defects throughout the fiber length [56, 57]. A simple and low cost electro-spinning method and consequent carbonization process was developed to prepare CNF-based anodes by Endo et al. As an anode material, electrospun CNF delivered a reversible of around

450 mA h g^{-1} at 30 mA g^{-1} [58]. Ji et al. prepared porous CNFs via the electrospinning/carbonization process combined with chemical treatments. The porous structure possessed higher specific surface area than non-porous CNF anodes, which improved Li ion diffusion at the electrolyte/electrode interface and effectively accommodate volume variation during charge-discharge cycling, leading to enhanced electrochemical properties [59].

Porous carbon

Owing to their high specific surface area and open pore structure porous carbons with different sizes are promising anode materials for LIBs. These unique structures can provide large amount of electroactive sites for lithium storage and minimize the mechanical stress for volume change during Li insertion and extraction. Porous carbons show conspicuously increased electrochemical properties in comparison with the traditional graphitic carbons [60, 61]. Porous carbons can be categorized as microporous (pore size < 2 nm), mesoporous (2-50 nm) and macroporous (pore size > 50 nm) carbons. Among them, mesoporous carbons have been widely studied as anode materials for LIBs and demonstrated [62]. Ichihara and co-workers reported ordered mesoporous carbon materials with uniform pore size, large pore volumes and high surface areas by using silica SBA-15 as a template. The materials showed high reversible and irreversible capacity of 1100 and 2000 mA h g^{-1}, respectively, at the first cycle. It was to remain unchanged after the first cycle, which could be attributed to the ordered mesoporous structure [63].

Graphene

Graphene, a one atom thick two dimensional (2D) SP^2 bonded honeycomb carbon lattice, and is a basic building block for graphitic materials of all other dimensionalities discovered by Geim et al. in 2004 (Fig. 1.3). Because of its unique structure and

intriguing mechanical, thermal and electrical properties, graphene has emerged as the material of great interest worldwide [64, 65].
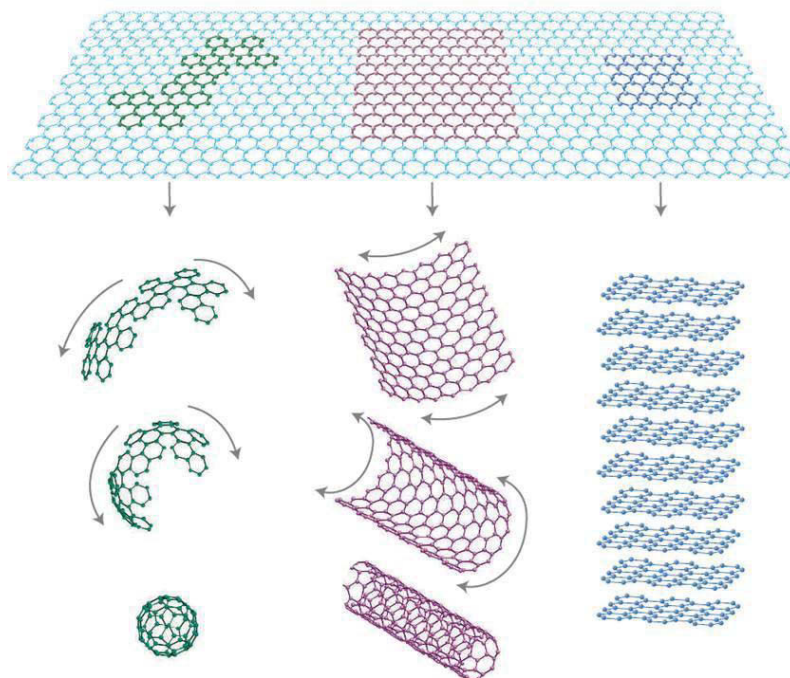
Figure 1.3 Mother of all graphitic forms. Graphene is a 2D building material for carbon materials of all other dimensionalities. It can be wrapped up into 0D buckyballs, rolled into 1D nanotubes or stacked into 3D graphite [60].

Graphene has increasingly attracted attention in recent years in the field of microelectronic and optoelectronic devices [66, 67], polymer composites [68] and electrocatalysts [69, 70]. It has large specific surface area (2630 m^2 g^{-1}), light weight, low cost materials having the strongest chemical bond in nature. These unique properties are favourable for energy storage applications and other energy-related systems [71-74]. The chemical synthesis of graphene comprises the oxidation of graphite to graphene oxide and the chemical reduction of graphene oxide [75]. Graphene has a significant Li-storage ability, since Li can be bound not only on both side of graphene, but also on the edges, disorders, defects and covalent sites of graphene. A free-standing graphene sheet can supply two surfaces for hosting Li ions

(via adsorption rather than intercalation; Fig. 1.4). Therefore, the theoretical capacity of single layer graphene should be 744 mAh g^{-1}, corresponding to the chemical composition of LiC_3.

In recent years, Li storage properties of graphene have been explored by several groups. For instance, Chen et al. synthesized graphene nanosheets (GNSs) from artificial graphite by oxidation, rapid expansion and ultrasonic treatment. The reversible capacity of GNSs was almost double (672 mA h g^{-1}) than that of the artificial graphite, due to the storage of Li ion on both sides of GNSs [76].
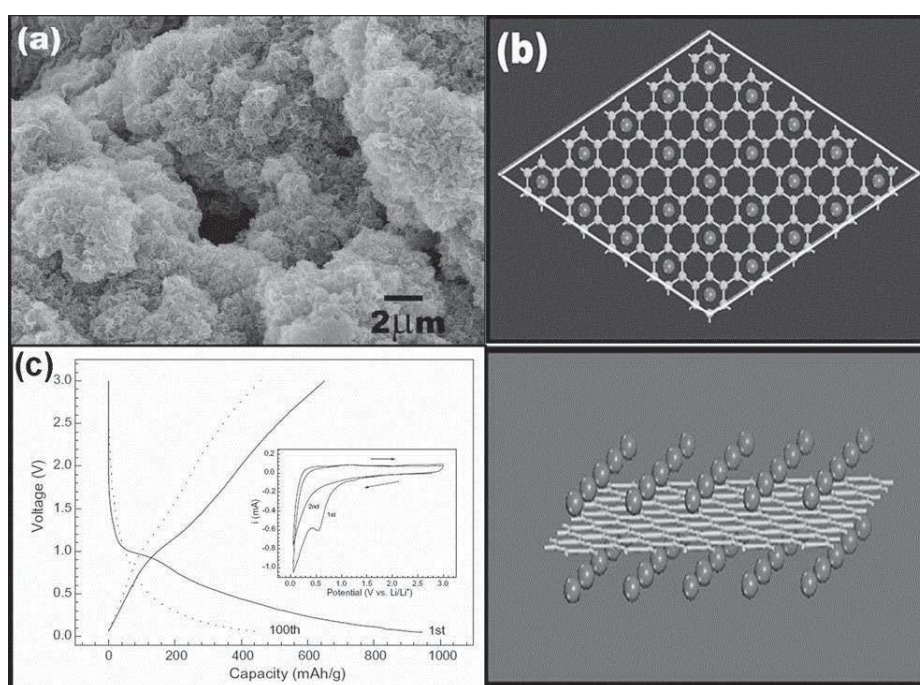
Figure 1.4 (a) Low magnification FESEM image of loose graphene nanosheets powder. (b) Atomic model of LiC_3 graphene. Top: top view; bottom: side view. (c) Charge and discharge curves of graphene nanosheets as anode in lithium-ion cells [72, 82].

Wang et al. reported that graphene nanosheets obtained from a soft-chemistry approach had a high discharge capacity of 945 mA h g^{-1} in the first cycle and 460 mA h g^{-1} after 100 cycles [72]. Although the specific capacity of graphene anodes are higher than that of graphite there are several problems such as high irreversible capacities in the first

cycle and poor rate performances. In addition, the electrolyte intercalation into the graphene layers is high due to the large surface-to-volume ratio, which also contributes to the increased irreversible capacities [77]. This confined the practical application of graphene as anode.

Generally GNS aggregated during the chemical reduction. The aggregation of GNS reduced its surface area which prevents GNS from maximum loading of lithium. To overcome this issue many groups developed graphene-based nanocomposite materials to improve the capacity [78-80]. The excellent properties of graphene including superior electrical conductivity, high surface to volume ratio, ultrathin flexible nature and chemical stability make it an ideal candidate for construction of composites with metal and metal oxide nanoparticles. The materials would be suitable for energy storage applications. Wang et al. demonstrated that their nanocomposite material composed of GNS and tin (Sn) nanoparticle was shown to have superior storage capacity up to 994 mA h g^{-1}, 2.67 time higher than that of graphite counterpart [81]. Graphene/Si composite was reported by Chou and co-workers. This material showed a capacity of 1168 and an average coulombic efficiency of 93 % up to 30 cycles [82]. Graphene-metal oxide composites as alternative anode materials also intensively investigated for application in lithium-ion batteries due to their high specific capacities. Recent studies show that the addition of graphene to metal oxides enhances the specific capacity of the electrodes at high discharge rate and improve the electrochemical stability for longer cycles. Paek and co-workers demonstrated an enhanced cyclic performance and lithium storage capacity of SnO_2/graphene nanoporous electrodes with three-dimensionally delaminated flexible structure. They fabricated SnO_2/graphene nanoporous electrode materials with delaminated structure with the reassembly of graphene nanosheets (GNS) in the presence of SnO_2 nanoparticles. It was demonstrated that the obtained SnO_2/GNS

electrode exhibited an enhanced reversible capacity of 810 mA h g^{-1} and after 30 cycles the charge capacity of SnO$_2$/GNS still maintained at 570 mA h g^{-1} as well as superior cycling performance in comparison with that of the bare SnO$_2$ electrode [83].

Graphene anchored with other transition metal oxides and hydroxides have widely been studied as anode materials for lithium-ion batteries [84-88]. The improved electrochemical performance of these nanocomposites can be attributed to the following factors, (i) graphene and both metal/metal oxide nanoparticles have higher lithium storage properties, (ii) due to its high electronic conductivity graphene ensures good electrical contact between adjacent active particles, (iii) metal or metal oxide nanoparticles can take place in between graphene nanosheets, which mitigates the restacking of graphene sheets, and consequently keeps their high active surface areas for lithium storage and (iv) the conductive and flexible graphene nanosheets can accommodate large volume change of the electrodes during Li intercalation/deintercalation, alleviating the aggregation and pulverization problems connected with metal/metal oxides. Owing to these synergistic effects of graphene and metal or metal oxide nanoparticles, the graphene/metal and graphene/metal oxide nanocomposites demonstrate high lithium storage properties, good rate capability and improved cycling performance.

Alloy-based anode materials

Lithium can be electrochemically alloyed with other metals at room temperature in organic electrolyte [89]. Owing to their ability to store large amount of lihium, lithium metal alloys, Li$_x$M$_y$, are of great interest as high capacity anode materials for lithium-ion batteries [90]. These alloying materials provide larger specific capacities than graphite (372 mA h g^{-1}). The main challenge for the application of these anode materials is large volume variation during lithium alloying/dealloying processes. The large

volume change causes severe cracking and crumbling of the electrode and subsequent loss of electrical contact between individual particles, which in turn results in large irreversible capacity and severe capacity fading.

Considerable research effort has been devoted to overcome the large volume change and preserve the structural integrity. One of the earliest approaches involved replacing bulk material with nanostructured alloys. The unique nanostructure can alleviate the mechanical strain generated due to volume change as the lithium ion intercalated to and de-intercalated from the host electrode materials. Nanostructured materials also reduce the electronic and ionic transport pathways and provide additional lithium storage sites [91, 92]. The second approach is to introduce a second component to form nanocomposites; for instance, metal nanoparticles can be coated with carbon or dispersed in a carbon matrix. Moreover, carbon phase has also the benefits of low volume expansion, excellent tolerance to mechanical stress and good ionic conductivity carbon matrix act as a buffer for the volume change and improves the electric conductivity of the electrode. The presence of carbon can also suppress SEI film and provide additional capacity as because carbon is an electrochemical active material and has significant capability to store lithium [92, 35,]. Owing to the high capacity Li-rich binary alloys, group IV elements such as silicon (Si) and tin (Sn) have been the main focus as Li-alloying metals. The crystal structures of group IV elements are presented in Fig. 1.5 (a) and their volumetric and gravimetric capacities are shown in Fig. 1.5 (b). The electrochemical properties of these two elements as anode in Li-ion batteries are reviewed in the following section.

Silicon (Si)

Among the group IV elements, Si is probably the most investigated anode material since it demonstrates a low discharge potential of 0.06 V *vs.* Li/Li$^+$ and has the highest

theoretical specific capacity of 4200 mA h g^{-1} [93-95]. It is also abundant, cheap and environmentally benign. Electrochemical reactions of lithium with silicon at elevated temperature have demonstrated that silicon can alloy with lithium up to $Li_{22}Si_4$, corresponding to a capacity of 4212 mAh g^{-1} [96].
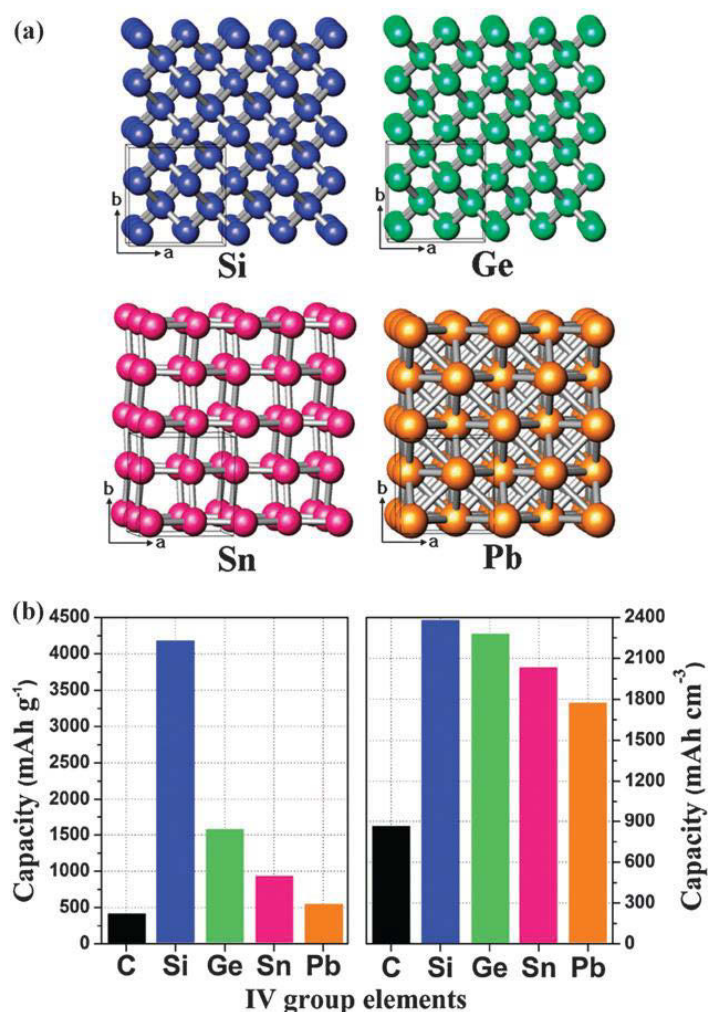
Figure 1.5 Crystal structures and capacities of Group IV elements. (a) Crystal structures of cubic Si (blue), cubic Ge (green), tetragonal Sn (red), and cubic Pb (orange). (b) Gravimetric and volumetric capacities of C (LiC_6), Si ($Li_{4.4}Si$), Ge ($Li_{4.25}Ge$), Sn ($Li_{4.25}Sn$), and Pb ($Li_{4.25}Pb$) [90].

The structure changes during lithium reacting with Si have been studied by ex-situ and in situ X-ray powder diffraction (XRD) [97, 98]. From the ex situ and in situ XRD results, the reaction mechanism was explained as follows:

During discharge:

$$Si \text{ (crystalline)} + xLi^+ + xe^- \rightarrow Li_xSi \text{ (amorphous)} \qquad (1.12)$$

$$Li_xSi \text{ (amorphous)} + (3.75 - x)Li^+ + (3.75 - x)e^- \rightarrow Li_{15}Si_4 \text{ (crystalline)} \qquad (1.13)$$

During charge:

$$Li_{15}Si_4 \text{ (crystalline)} \rightarrow Si \text{ (amorphous)} + yLi^+ + ye^- + Li_{15}Si_4 \text{ (residual)} \qquad (1.14)$$
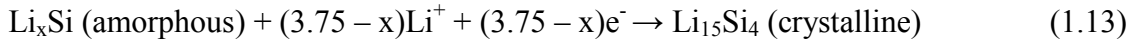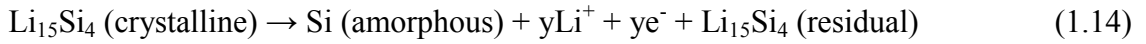
Crystalline silicon becomes an amorphous during lithium intercalation. The amorphous phase suddenly crystallizes as a $Li_{15}Si_4$ phase around 50 mV to form another phase during the delithiation process. Delithiation of the $Li_{15}Si_4$ phase results in the formation of amorphous silicon [99]. However, it showed rapid capacity fading due to mechanical failure of the active material caused by the large volume variation up to 400 % during the discharge/charge reactions. In order to overcome this problem various nanostructured Si [100], Si-metal alloys [101] and Si/carbon nanocomposites [102, 103] have been prepared by several groups to improve cycling stability of Si-based anodes by enhancing the structural integrity of Si.

Li et al. reported that nano-sized silicon anode (78 nm) showed better capacity retention than silicon powder due to the smaller volume variation by the distribution of nanoparticles [104]. The nano-silicon showed a high reversible capacity, over 1700 mA h g^{-1}, at the tenth cycle. SiAg anode materials by using a mechanical alloying process were investigated by Hwang et al. Silicon was uniformly distributed in a ductile silver (Ag) matrix. The electrode prepared by 50 h milling presented a reversible capacity of 280 mA h g^{-1} after 50 cycles with good capacity retention [105]. Yoshio et al. prepared carbon-coated silicon by thermal vapor deposition (TVD) using benzene, which showed a first reversible capacity of 737 mA h g^{-1}, a Coulombic efficiency of 92.1 %, and a little capacity loss up to 50 cycles. The carbon coating not only inhibited the electrolyte decomposition on the Si-based electrode but also provided essential and continuous

electrical contact networks around the Si particles [106]. To improve the first Coulombic efficiency and cycle performance several electrode architectures have also been suggested. For instance, Shin et al. fabricated porous silicon electrodes with one-dimensional (1D) channels using an electrochemical etching process [107]. The channel structure of the porous silicon electrode showed excellent cycling stability and remained the same even after 35 cycles. Ma et al. prepared nest-like hollow Si nanospheres and achieved enhanced rate capability and cycling performance, which is attributed to the inhibition of Si aggregation by the nest-like Si nanospheres [108]. Recently vertically-aligned Si nanowire arrays on a current collector have been reported by Cui group [102]. This architecture could provide better accommodation of large volume variation, exclusion of extra weight for binders and conducting agents, and efficient 1D electrical pathway for charge transport. A high reversible capacity of over 3000 mA h g^{-1} was achieved and was maintained up to ten cycles with a slight capacity fading.

Tin (Sn)

Tin is also an important group IV element that has attracted much attention as promising anode materials. Although Sn has a lower gravimetric capacity than Si and metallic lithium, Sn is an attractive anode material due to its volumetric capacity of about 2000 mA h cm^{-3}, which is higher than metallic lithium and is comparable to Si [109]. It can alloy with lithium up to a chemical composition of $Li_{17}Sn_4$ with a theoretical specific capacity of 959.5 mA h g^{-1} [110] Unfortunately, like other alloying materials, its commercial use is limited by its poor cycling performance due to mechanical degradation including cracking and pulverization because of the huge volume changes that occur in the coexisting Li-Sn intermetallic phase region during cycling.

In the past, many attempts have been carried out to prepare composite materials formed from Sn nanoparticles, embedded in a carbon matrix. Carbon matrix can provide

sufficient strength to cushion volume changes and effectively prevent aggregation of Sn nanoparticles. Kim et al. synthesized Sn/C composites by infiltrating tetraethyltin into mechanically milled polystyrene resin powder with subsequent annealing in Ar at 600 ^{o}C, which results in crystalline Sn and amorphous carbon [111]. The resultant composite exhibited a capacity of 480 mA h g^{-1} with good capacity retention. The embedment of nanocrystalline tin within carbon appears to be the main reason for the good cycling stability. Scrosati's group also reported Sn-C composite. The electrode maintained a constant capacity as high as 500 mA h g^{-1} for 200 cycles at 0.8 C and 200 mA h g^{-1} at 5 C [112].

Tin oxides (SnO$_2$)

Tin-based materials have also been attracted much interest as promising anode materials for lithium ion batteries in both scientific communities and industries [113, 114]. At the first lithiation, Sn-O bonding is irreversibly dissociated by the introduction of lithium ions and electrons, forming Li$_2$O and Sn, and the later continues to form an alloy with lithium with an upper limit of Li$_{4.4}$Sn. Tin oxide offers a high theoretical lithium storage capacity of ~783 mA h g^{-1}, which is more than twice that of graphite anode. In addition, SnO$_2$-based anodes work at a relatively low potential comparable to that of graphite. Therefore, they can match well with most available cathode materials. The basic reaction mechanisms Sn-based oxides have been reported as follows [115, 116].

$$SnO_2 + 4Li^+ + 4e^- \rightarrow Sn + 2Li_2O + 4.4Li^+ + 4.4e^- \leftrightarrow Li_{4.4}Sn + 2Li_2O \qquad (1.15)$$
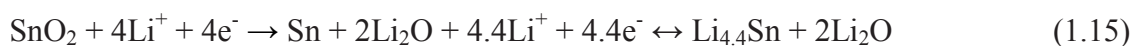
Two reasons are identified in Sn-based anode materials that are unsuitable for the practical application. Firstly, their Coulombic efficiency typically low, which caused by the reduction of SnO$_2$ to Sn and the formation of a solid-electrolyte interface (SEI) layer [117]. Another problem is rapid capacity fading due to terrific volume change of up to 200 % upon full lithiation of metallic tin, forming the Li$_{4.4}$Sn alloy [118].

Several strategies have been suggested to improve the capacity retention of tin oxide anode material as shown in Fig. 1.6. One of the effective protocol is to prepare materials with void spaces such as, hollow and mesoporous particles, which can accommodate the volume variation [120, 121]. Nanosheets demonstrate two-dimensional structures that can sustain large lithium ion intercalation strain [122].
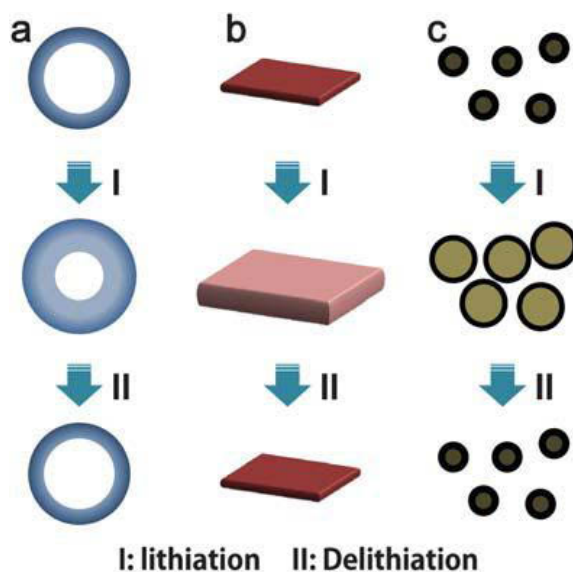
Figure 1.6 Schematic illustration of three basic nanostructures to alleviate the pulverization problem in SnO_2 anode materials: (a) hollow structures, (b) 2D nanosheets, and (c) amorphous carbon coating [119].

The enhanced capacity retention has been found since these two approaches take place in nanoscale dimension. Another approach is to introduce carbonaceous materials, which improve the electrical conductivity, effectively mitigate the aggregation of nanoparticles and can also help to buffer the mechanical strain during charge discharge process due to their elastic nature. For instance, Archer et al. reported SnO_2/carbon nanocomposite material with hollow spherical structure. This approach involves two main steps: synthesis of porous hollow spheres of SnO_2 and deposition of carbon onto both the interior and exterior surfaces of the shell as well as in the pores. The carbon acts as both physical buffering cushion for the volume change and electronic conductive

24

path, which results in the improved capacity retention of the composite electrode [123]. Aksay et al. demonstrated SnO_2/graphene nanaocomposites using both molecular and extended nanoscale building blocks. SnO_2/graphene nanaocomposites displayed superior cycling stability compared to bare SnO_2 and graphene [124].

Transition metal oxides

Another extensively investigated category of anode materials for lithium ion batteries is transition metal oxides. In 2000, Poizot et al. reported for the first time that lithium can be stored reversibly in transition metal oxides through a conversion reaction. The reaction mechanism involves the formation and decomposition of Li_2O, along with the reduction and oxidation of metal nanoparticles. The electrochemical reactions could be summarized as follows [125]:

$$MO + 2\,Li + 2e^- \leftrightarrow Li_2O + M \; (M = Co, Ni, Fe, Mn, Cu\; etc.) \tag{1.16}$$

Most of these metal oxides exhibit diverse chemical and physical properties and can deliver high reversible capacities (500-1000 mA h g^{-1}) and energy densities because the oxidation state is utilized fully and more than one electron is involved in the conversion reaction (Fig. 1.7) [126]. In nanoscale, the conversion reaction is more facile and reversible. There full reduction leads to nanometallic particles (2-8 nm) dispersed in an amorphous Li_2O matrix. Owing to the nanometric nature of these materials the reactions were shown to be highly reversible, providing exceptional capacities to store lithium. However, transition metal oxides often show low Coulombic efficiency at the first cycle, large potential hysteresis, unstable solid electrolyte interface (SEI) layer formation and poor cycling stability [127].

These limitations of transition metal oxides could be possibly overcome by making nanostructured porous transition metal oxide materials and transition metal oxide/carbon composites with capabilities to sustain structural disintegration and

promote lithium storage reactions. In the following section, the most widely investigated conversion reaction based nanostructured transition metal oxide anodes will be discussed.
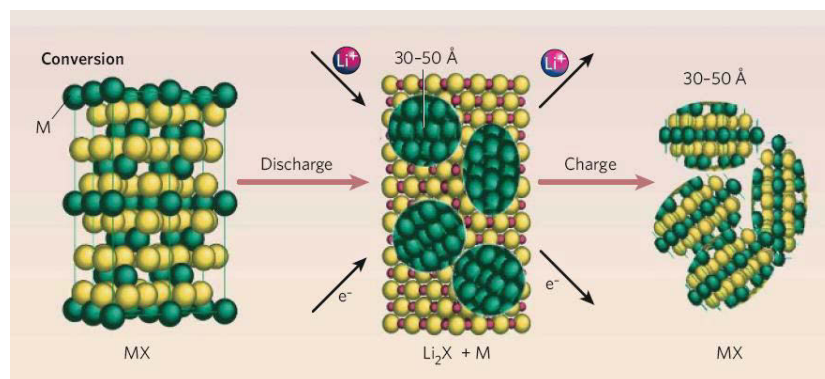
Figure 1.7 Schematic representation of conversion reaction mechanism. The insertion reaction demonstrates a maximum of 1 electron transfer per transition metal (here designated M), whereas the conversion reaction can transfer 2 to 6 electrons [2, 128].

Nickel oxides

Different groups have studied nanostructured nickel oxide, and their composites with good electrochemical performances. Ni et al. reported NiO nanoflakes with a thickness of 20 nm by a simple two-step method. At a current density of 100 mA g^{-1}, the NiO nanoflakes showed a stable cycling performance and the reversible capacity of 1015 mA h g^{-1} was retained even after 50 charge-discharge cycles [129]. Nickel oxide nanocone arrays were fabricated by He's group (Fig. 1.8). The NiO nanocone electrode delivered a capacity up to 1058 mA h g^{-1} after 100 cycles at the current rate of 0.4 C and a capacity higher than 436 mA h g^{-1} even at a high rate of 20 C [130].

Zhong et al. prepared self-assembled sandwich-like NiO film which is constructed by regular triangular prisms with side length of 500 nm. The NiO film electrode exhibited a high discharge capacity and excellent cycling performance over 50 cycles [131]. Hosono et al. studied mesoporous Ni/NiO structures and observed a capacity of 695 mA

h g^{-1} at a high current density of 10 A g^{-1} [132]. Xu group prepared NiO/multiwalled carbon nanotubes in large scale by using a direct thermal decomposition method. The lithium storage capacity maintained at similar to 800 mA h g^{-1} after 50 cycles [133]. Zou et al. demonstrated a hydrothermal preparation of NiO/graphene sheet-on-sheet and nanoparticle-on-sheet nanostructures. The sheet-on-sheet nanocomposite showed highly reversible capacities of 1056 mA h g^{-1} at the current rate of 0.1 C and good rate capabilities.
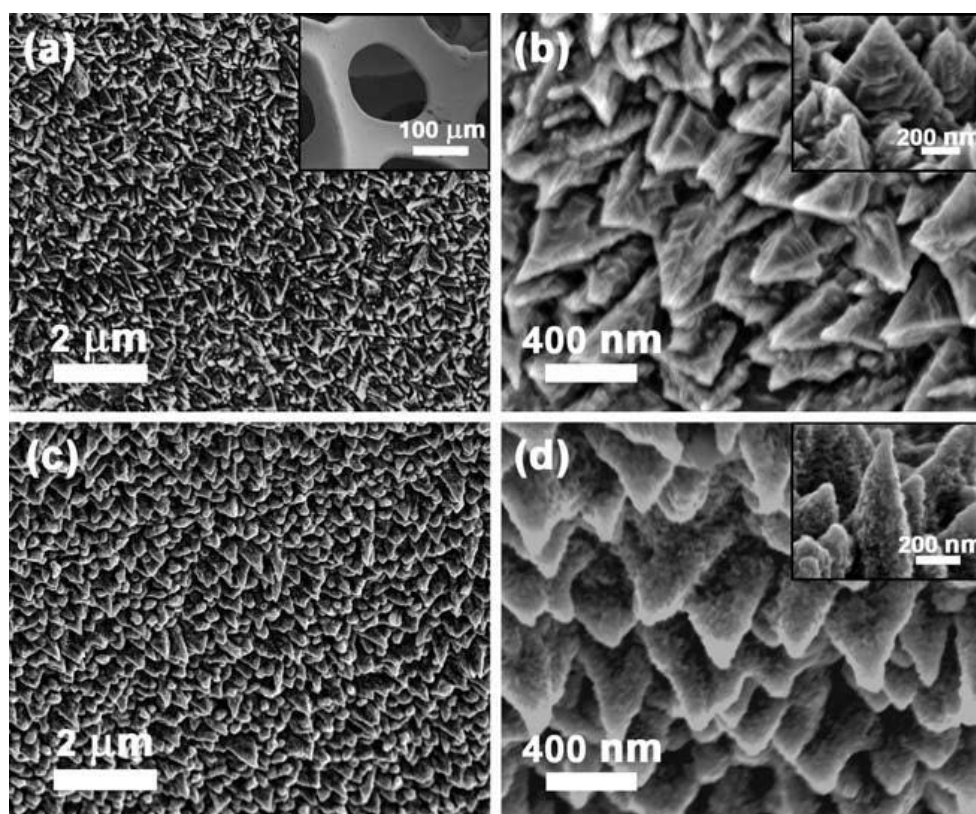
Figure 1.8 SEM images of the nickel oxide nanocone arrays (Ni NCAs) before and after oxidation. (a, b) SEM images of Ni NCAs deposited on Ni foam; the inset in (a) shows the SEM image of Ni foam. (c, d) SEM images of NiO NCAs by thermal oxidation at 400 °C for 1 h in air [130].

The discharge capacity decreased to 1031 mA h g^{-1} after 40 cycles, which is only 2.4 % of the initial discharge capacities [134]. We also prepared NiO nanosheets by using hydrothermal method, which will be discussed in Chapter 3.

Iron oxides

Iron oxides such as hematite (α-Fe$_2$O$_3$) and magnetite (Fe$_3$O$_4$) are attractive conversion-based anode materials for lithium ion batteries because of their low cost and non-toxicity. One-step template-engaged precipitation method has been employed to prepare α-Fe$_2$O$_3$ nanotubes with thin walls by Lou et al. Owing to its unique structural features (Fig. 1.9) α-Fe$_2$O$_3$ nanotubes exhibited superior lithium storage properties and excellent capacity retention. A comparative study has also been made between α-Fe$_2$O$_3$ nanotubes and α-Fe$_2$O$_3$ particles [135]. This group also demonstrated a quasiemulsion-templated method to synthesize α-Fe$_2$O$_3$ hollow spheres. When this material was used as anode materials for lithium ion batteries, it showed excellent reversible capacities with very good cycling performance and a reversible capacity of 710 mA h g^{-1} at the end of 100 charge-discharge cycles [136]. Liu et al. synthesized α-Fe$_2$O$_3$ nanorods with diameters of 60-80 nm and lengths extending from 300 to 500 nm. The α-Fe$_2$O$_3$ nanorod anodes exhibited a stable specific capacity of 800 mA h g^{-1}, a significantly improved electrochemical performances compared to that of commercial microcrystalline α-Fe$_2$O$_3$ powders [137]. Zhang et al. fabricated fiber-like Fe$_2$O$_3$ macroporous nanomaterials by the in situ synthesis in generated cellulose fibers followed by the removal of the cellulose matrix via the calcination. The Fe$_2$O$_3$ nanomaterials presented a high reversible capacity and the specific capacity of 732 mA h g^{-1} was retained after 50 cycles [138]. Li et al. demonstrated three-dimensional network structured α-Fe$_2$O$_3$ by a facile chemical corrosion of a stainless steel plate followed by thermal oxidation. The electrodes showed a reversible capacity of 858 mA h g^{-1} and maintained a stable capacity over 100 charge-discharge cycles [139]. Ogale et al. reported nano-assembled α-Fe$_2$O$_3$ spindles by the pyrolysis of iron based metal organic framework. The nanospindles obtained a reversible capacity of 1024 mA h g^{-1} at the current density of

100 mA g^{-1}. The electrode delivered excellent cycling performance with capacity retention over 90 % after 40 cycles and also exhibited good battery characteristics under high current cycling [140].

In addition to Fe$_2$O$_3$, Fe$_3$O$_4$ has also been investigated as anode materials for lithium ion batteries. Fe$_3$O$_4$ occurs in nature as the mineral magnetite and it adopts an inverse spinel structure. In 2006, Tarascon's group fabricated nanostructured Fe$_3$O$_4$ rods and films grown on copper substrates by electrodeposition [141]. When they were cycled in the potential range of 0.01-3.0 V, the capacities obtained in the range of 800-900 mA h g^{-1} at current rates of 0.25 C and 0.5 C. Good rate capability up to 8C was also achieved.
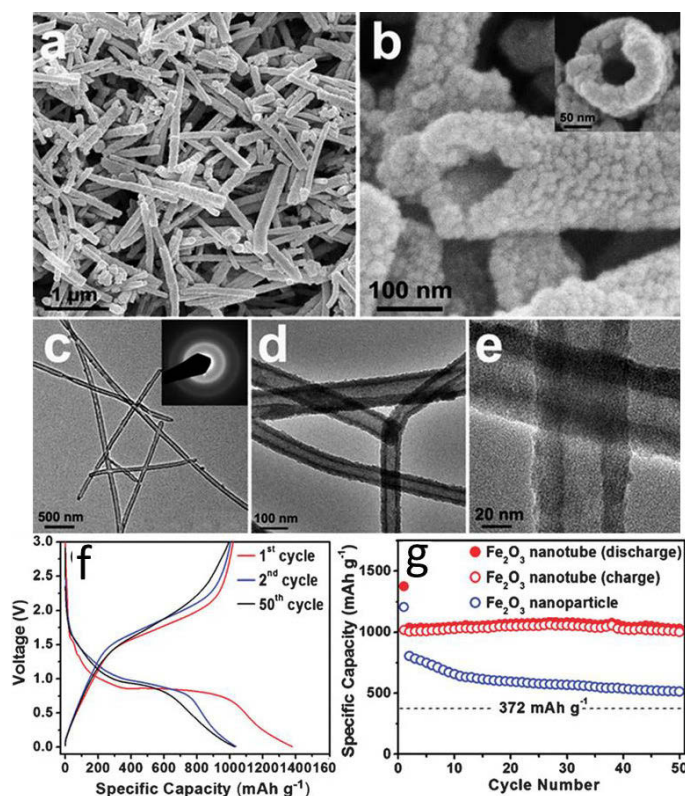
Figure 1.9 (a) Overview SEM image of Fe(OH)$_x$ nanotubes; (b) SEM image of cracked nanotubes showing exposed interior; (c and d) TEM images of Fe(OH)x nanotubes; (e) wall structure of the nanotubes. (f) Discharge/charge voltage profiles of α-Fe$_2$O$_3$ nanotubes cycled between 0.01–3.0 V at 0.5 C; (b) cycling performance of α-Fe$_2$O$_3$ nanotubes and nanoparticles at 0.5 C. All potentials are with reference to Li/Li$^+$ [135].

Interestingly, the measure capacity increased with an increase in the cycle number between 2 and 50 cycles. Uniform sub-micrometer sized Fe_3O_4 spherical particles were synthesized by using hydrothermal method, which reported by Chen et al. [142]. The Fe_3O_4 spherical particles presented a stable and reversible capacity of 900 mA h g^{-1} up to 60 cycles and good rate capability. We also synthesized α-Fe_2O_3 nanoparticles with two different sizes via a simple microwave method and will be discussed in Chapter 5.

Cobalt oxides

Cobalt oxide (Co_3O_4) possesses high theoretical capacity of 890 mA h g^{-1} and has been extensively investigated as anode materials for lithium ion batteries. Li et al. developed a template-free method for the large-area growth of self-supported Co_3O_4 nanowire arrays [143]. The nanowires were 500 nm in diameter and 15 μm in length and they grew almost vertically from the substrate. The nanowire Co_3O_4 arrays presented good capacity retention compared to other unsupported nanowires and commercial powders. Electrochemically active Co_3O_4 needle-like nanotubes have been synthesized by a one-step, self-supported transformation approach [144]. When evaluated as anode materials for lithium ion batteries, the Co_3O_4 nanotubes show excellent rate capability and ultrahigh capacity with nearly 100 % retention after 30 cycles. A simple solid-state formation of porous Co_3O_4 with a hexagonal sheet-like structure has been reported Zhan et al. [145]. The synthesis based on oil controlled thermal oxidative decomposition and recrystallization of precursor $Co(OH)_2$. Owing to their porous sheet-like structure and small size, the as-prepared material exhibited superior electrochemical performance with good cycling stability and high capacity of 1450 mA h g^{-1}.

Manthiram's group have developed a facile solution-phase route for the preparation of urchin-like hollow $Co(CO_3)_{0.5}(OH).0.11H_2O$ nanospheres [146]. The urchin like hollow nanospheres could readily be converted into hollow Co_3O_4 nanospheres assembled by

nanoplatelates by annealing at 300 ^{0}C. After 50 cycles, it maintained the capacity as high as 786 mA h g^{-1} and the Coulombic efficiency remained close to 100 % after the first cycle. A rational method was employed to synthesize mesoporous and single-crystal Co_3O_4 nanobelt array on a conducting substrate (via a thin layer of TiO_2), which provided an express pathway for charge transfer [147]. When applied as anode material without using any conductive agent and binder, the Co_3O_4 nanobelt array was capable of retaining the specific capacity of 770 mA h g^{-1} at the current density of 177 mA g^{-1}. When the charge-discharge rates were increased to 1670 and 3350 mA g^{-1}, the capacity still retained 510 and 330 mA h g^{-1} after 30 cycles. In-situ MWCNT/Co_3O_4 nanocomposites have also been demonstrated by a facile and effective method [148]. MWCNTs were mostly coated with a layer of Co_3O_4 with an average size of 8 nm. The nanocomposites showed higher lithium storage properties and cycling stability compared to the Co_3O_4 nanoparticles.

Recently, electrically conductive graphene anchored with Co_3O_4 nanoparticles as the advanced anode materials for high performance lithium ion batteries have been reported by Wu et al. [85]. The obtained nanoparticles were 10-30 nm in size and uniformly anchored as spacers to keep the neighbouring graphene sheets separated. The Co_3O_4/graphene composite was capable of effectively utilizing the good electrical conductivity, high surface area, mechanical flexibility. The composite exhibited a large reversible capacity of 935 mA h g^{-1} excellent cycling performance, high Coulombic efficiency (above 98 %) and good rate capability. Our group also fabricated Co_3O_4/graphene nanocomposite by an in-situ solution base method under reflux conditions [149]. The prepared material consists of uniform nanoparticles (15-25 nm), which are well dispersed on the surfaces of graphene nanosheets. The composite

material demonstrated an initial reversible capacity of 722 mA h g^{-1}, which is higher than pure graphene nanosheets and Co$_3$O$_4$ nanoparticles.

Molybdenum oxides

Molybdenum oxides (MoO$_3$, MoO$_2$) can also store lithium through conversion reaction and can deliver high theoretical specific capacities of 1111 and 830 mA h g^{-1}, respectively [150, 151]. Shi et al. prepared highly ordered mesoporous MoO$_2$ using a hard template method [152]. The material showed a reversible capacity of 750 mA h g^{-1} at the current rate of 0.05C in the range of 0.01-3.0 V with stable cycling performance up to 30 cycles. Recently, Bhaskar et al. reported a MoO$_2$/graphene composite by a one pot in-situ low-temperature solution phase reduction method [153]. The composite exhibited a reversible capacity of 550 mA h g^{-1} at the end of 1000 cycles at the current density of 540 mA g^{-1}. Chen et al. synthesized uniform α-MoO$_3$ nanorods with controlled aspect ratios through a fast hydrothermal route [154]. The interesting nanorods showed significantly enhanced lithium storage properties with higher reversible capacities and better rate performance compared to α-MoO$_3$ nanoparticles. A simple method was employed to prepare Na-doped MoO$_3$ (Na0.25MoO$_3$) by Nazar's group [155]. The material exhibited excellent cyclability and a high reversible capacity of 940 mA h g^{-1}. The lithium cycling properties of bare and carbon coated nanobelts of MoO$_3$ (150 nm diameter and 5-8 μm length) have been reported by Hassan et al. [156]. When the nanobelts were cycled at 0.1 C, the initial discharge capacity of ~1300 mA h g^{-1} for the bare MoO3 drastically faded to ~300 mA h g^{-1} at the end of 50 cycles. Under similar cycling conditions, carbon-coated MoO$_3$ displayed an initial capacity of ~1350 mA h g^{-1}, which decreased to 950 mA h g^{-1} after 10 cycles, and slowly increased to 1064 mA h g^{-1} after 50 cycles.

Other transition metal oxides

Other transition metal oxides such as manganese oxides [157, 158], copper oxides [159, 160] have also been studied as anode materials for lithium ion batteries. In practical LIBs, manganese oxides anodes are challenging because of their poor electrical conductivity and large volume change during cycling. In order to improve the lithium storage properties a one-step organic/aqueous interfacial method have been proposed to prepare porous hierarchical spheres assembled from polythiophene coated ultra thin nanosheets [161]. The prepared nanocomposite spheres demonstrated a promising lithium storage performance with a high reversible capacity of ~ 500 mA h g^{-1} retained after 100 cycles at a high current density of 500 mA g^{-1}. Wang et al. reported polycrystalline CuO nanowires by wet-chemical method through the reaction of $CuSO_4$, KOH and ammonia in aqueous solution and subsequent aging process [162]. The CuO nanowires exhibited a high reversible capacity of 720 mA h g^{-1}, and a capacity of 650 mA h g^{-1} was retained after 100 cycles. Ko et al. demonstrated a novel structure of the CuO/CNT nanocomposite in which the mesoporous CuO particles were threaded by CNTs [163]. The aqueous synthesis involved the precipitation of $Cu(OH)_2$ on the surface of CNTs and the chemical transformation of the $Cu(OH)_2$ into the mesoporous CuO particles wrapping the CNTs. The CuO/CNT nanocomposite electrode displayed a stable cycling performance up to 100 cycles and the reversible charge capacity retention was 650 mA h g^{-1} after 100 cycles. Graphene nanosheet (GNS) supported urchin-like CuO nanostructures were also synthesized by a facile low-temperature solution route [164]. Urchin-like CuO nanostructures were uniformly dispersed on GNS layer-by-layer network after stacking. Graphene supported CuO nanostructures showed a higher specific capacity of 826 mA h g^{-1} at the current density of 700 mA g^{-1}, long cycle life and excellent rate performance.

Mixed metal oxides

Several oxide systems containing two transition metals and crystallizing in a spinel structure namely, MMn_2O_4 (M = Co, Zn) [165, 166], MFe_2O_4 (M = Co, Ni) [167, 168], MCo_2O_4 (M = Fe, Cu, Ni) [169-171] have been reported. Many of these oxides can be prepared in nanosize form by various techniques and their lithium cycling behaviour has been examined in detail. The large and stable reversible capacity depends on the morphology, structure and particle size (micrometer/nanometer). Kim's group prepared one-dimensional $ZnMn_2O_4$ nanowires by a simple solid state reaction [172]. The highly crystalline $ZnMn_2O_4$ nanowires about 15 nm in width and 500 nm in length demonstrated a high specific capacity of about 650 mA h g^{-1} at the current density of 100 mA g^{-1} after 40 cycles. Qu *et al.* designed and fabricated feather-like 3D hierarchical nanostructures of $ZnCo_2O_4$ directly on Ni-foams current collectors and used it as binder-free electrodes (Fig. 1.10) [173]. The conductive agent and binder-free electrode delivered discharge capacities of at least 1100 mA h g^{-1} for 50 cycles at 0.5 A g^{-1} and 932 for 50 cycles at 1 A g^{-1}. Three-dimensional uniform mesoporous $ZnCo_2O_4$ microspheres have also been synthesized via a facile ethylene glycol (EG) mediated solvothermal method followed by subsequent annealing [174]. The uniform mesoporous $ZnCo_2O_4$ microspheres exhibited initial specific capacity of 1332 mA h g^{-1} at the current density of 100 mA g^{-1}. The capacity maintained 721 mA h g^{-1} after 80 cycles. Even at high current density of 1000 mA h g^{-1}, the initial specific capacity still showed 937 mA h g^{-1}.

Jadhav's group reported a simple and cost-effective urea-assisted chemical co-precipitation method for the synthesis of spinel $NiCo_2O_4$ [175]. The synthesized $NiCo_2O_4$ exhibited an urchin-like microstructure with polycrystalline and mesoporous nature. The mesoporous electrode delivered an initial discharge capacity of 1095 mA h

g^{-1} and maintained a reversible capacity of 1000 mA h g^{-1} for 400 cycles at 0.5 C-rate. An effective method of simultaneously etching and precipitation reactions was employed to synthesize hollow crossed NiCo$_2$O$_4$ nanocubes [176].
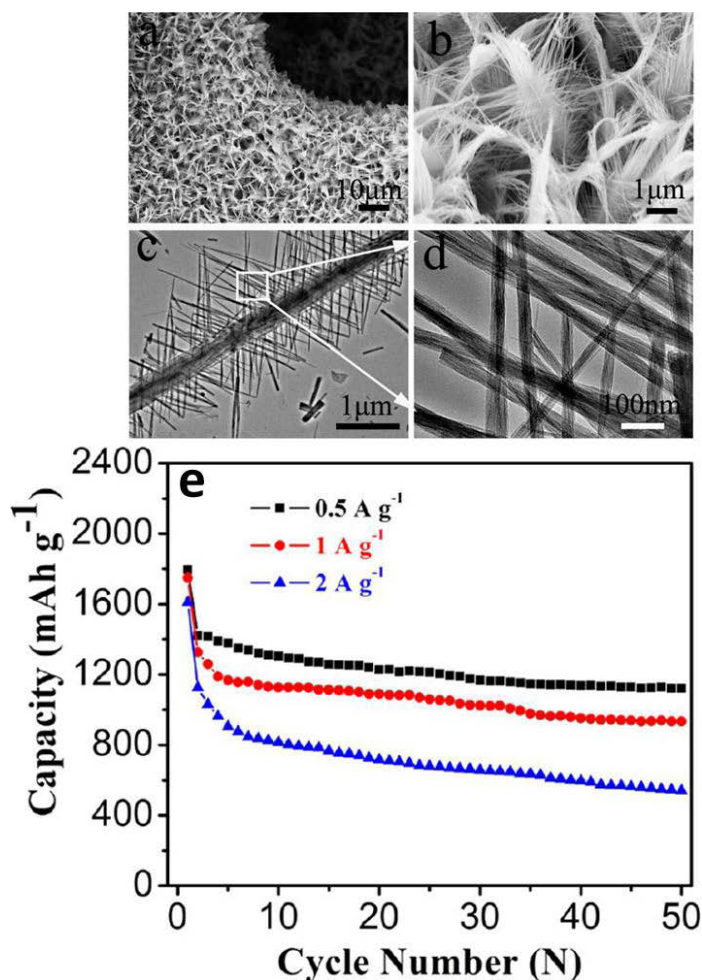
Figure 1.10 (a) Low-magnification SEM image, (b) high-magnification SEM image (c, d) TEM images and (e) Cycling performance of 3D-ZnCo$_2$O$_4$ nanostructures at different current densities [173].

First, amorphous hollow NiCo$_x$O(OH) nanoboxes were formed, and subsequent calcination results in the formation of NiCo$_2$O$_4$ nanocubes. The NiCo$_2$O$_4$ nanocubes displayed a stable reversible capacity of 1160 mA h g^{-1} at constant current density of 200 mA h g^{-1} with capacity retention of over 91 % after 200 cycles. A facile co-precipitation and annealing method has been developed for the synthesis of novel

double-shelled $CoMn_2O_4$ hollow microcubes with nanometer-sized building blocks [177]. When evaluated as an anode material for lithium ion batteries, the as-synthesized material exhibited a reversible capacity of 830 mA h g^{-1} at a current density of 200 mA g^{-1}, and retained 624 mA h g^{-1} after 50 cycles. A facile solvothermal route and a subsequent annealing treatment were employed to prepare hierarchical $Co_xMn_{3-x}O_4$ array micro/nanostructures with tunable morphology and compostion, which grown on conductive stainless steel with robust adhesion [178]. Owing to the unique structural feature, the resultant $CoMn_2O_4$ nanowires and $MnCo_2O_4$ nanosheets exhibited excellent electrochemical performance with remarkable specific capacities (540-207 mA h g^{-1}) at various current rates (1-10 C) and good cycling stability.

Chen's group also fabricated a $NiCo_2O_4$ nanoplates-reduced graphene oxide sheets ($NiCo_2O_4$-RGO) composite and applied as anode materials for lithium ion batteries [179]. It displayed a high reversible capacity of 816 mA h g^{-1} over 70 cycles with 80 % capacity retention of the second cycle and excellent rate capability. The enhanced cycling performance of the $NiCo_2O_4$-RGO nanocomposite could be attributed to the unique properties of the nanoplates anchored on the graphene nanosheets, which serve as the elastic substrate to buffer the volume expansion and provide room for the nanoplate cracking, helping to avoid aggregation upon cycling. The conductive graphene network can also facilitate the collection and transport of electrons during the cycling process, enabling a long cycle life. Wintersweet-flower-like $CoFe_2O_4$/MWCNTs hybrid materials were reported by Wang *et al.* [180]. The $CoFe_2O_4$/MWCNTs hybrid material delivered reversible lithium storage capacities of 809, 765, 539 and 359 mA h g^{-1} at current densities of 180, 450, 900 and 1800 mA g^{-1}, respectively. The good electrochemical performance of $CoFe_2O_4$/MWCNTs hybrid material could be credited to the synergistic effect, with contributions from $CoFe_2O_4$ nanocrystals and MWCNTs.

Sui *et al.* also explored a novel, inexpensive and simple one-step solvothermal route to synthesize monodisperse water-soluble MWCNT-ZnFe$_2$O$_4$ nanocomposites without any surface modification of MWCNTs [181]. The as-synthesized MWCNT-ZnFe$_2$O$_4$ nanocomposites showed a high reversible capacity of 1152 mA h g^{-1} after 50 cycles. A facile hydrothermal method has been developed for the preparation of hierarchical MnCo$_2$O$_4$ nanosheet arrays/carbon cloths as binder-free anodes for lithium ion batteries [182]. The electrode exhibited a high specific capacity, excellent cycling stability and good rate performances. We also synthesized NiCo$_2$O$_4$ nanoflakes, nanobelts and nanosheets and MnCo$_2$O$_4$ nanoflakes and will be discussed in Chapter 6, 7 and 8.

1.1.4.2 Cathode Materials

Since the discovery of the usefulness of layered LiCoO$_2$ in lithium ion cells, a number of cathode materials have been investigated. There are three intercalation compounds that are used commercially as cathode materials for lithium ion batteries: LiCoO$_2$, LiNiO$_2$ and LiMn$_2$O$_4$. Owing to the simplicity of preparation LiCoO$_2$ is the most well-known among the possible cathode materials [183]. It exhibits excellent cycling stability at room temperature. Although the theoretical capacity of LiCoO$_2$ is 273 mA h g^{-1}, it can only achieve a practical capacity of about 140 mA h g^{-1} [184]. The reversible capacity of LiNiO$_2$ is higher than that of LiCoO$_2$, since the amount of the extracted/inserted lithium during charge-discharge cycling is around 0.55, compared to the 0.5 for LiCoO$_2$, which results in the specific capacity to be more than 150 mA h g^{-1} with good cycling performance [185] Although it shows higher specific capacity, synthesis process of LiNiO$_2$ is more complicated. LiMn$_2$O$_4$ is another popular cathode material for lithium ion batteries because of its abundant materials source and less toxicity. However, its capacity restricted to120-125 to mA h g^{-1}, and significant capacity degradation observed at moderate temperature [186]. To improve the intercalation-

deintercalation kinetics of the material, it is necessary to downsize material to achieve short diffusion distance and large surface area.

Most of the lithium intercalation compounds suitable as positive electrodes in lithium ion batteries have been prepared in the form of nanostructures using different methods. The rate of lithium insertion/extraction is increased because of the shorter diffusion lengths and higher electrode/electrolyte contact area compared with microstructures. In recent years, nanostructured lithium metal oxides have been widely studied as cathode materials for lithium ion batteries. Li *et al.* reported open-ended $LiCoO_2$ nanotubes with uniform shape and size by a sol-gel template method using porous anodic aluminium oxide (AAO) as the template [187]. The obtained nanotubes exhibited higher discharge capacity and better rate performance. Cao's group demonstrated a surface modified $LiCoO_2$ cathode material obtained by coating it with a nano layer of amorphous carbon [188]. The carbon-coated $LiCoO_2$ showed lower charge transfer resistance, higher lithium ion diffusion coefficient and much better rate capability than pristine $LiCoO_2$. However, $LiCoO_2$ is very expensive and highly toxic, which limits its application in large-scale lithium power batteries for EVs and HEVs.

Spinel $LiMn_2O_4$ has been extensive studied by several groups [189, 24]. Schulz *et al.* synthesized nanoparticles of $LiMn_2O_4$ spinels through a sol-gel method followed by thermal treatment [190]. The $LiMn_2O_4$ nanoparticles were found to behave differently in different voltage ranges. The nanoparticle cathode showed improved capacity and cycling stability in the 3V discharge range, while in the 4 V discharge region it exhibited decreased capacity and improved cycling stability. Well-ordered mesoporous spinel-structured $LiMn_2O_4$ has been reported by Luo *et al.* [191]. Firstly, mesoporous MnO_2 was synthesized by using the ordered mesostructured KIT-6 as template. Mesoporous $LiMn_2O_4$ was obtained through chemical lithiation with LiI in acetonitrile

followed by annealing at a low temperature of 350 ^{o}C. The ordered mesoporous $LiMn_2O_4$ exhibited excellent cycling stability and high rate capability. It maintained 94 % of its initial capacity after 500 cycles. The major disadvantage of spinel $LiMn_2O_4$ is its slow dissolution of manganese ions in the electrolyte during cycling [192]. Spinel also suffers from low electronic conductivity and poor ionic conductivity, which limits its high-rate performance.

Recently, $LiFePO_4$ has been attracted enormous attention as new cathode materials for lithium ion batteries, particularly for high power applications [193]. It has been widely explored as a cathode material for lithium ion batteries due to its low cost, availability, environmental benignity, thermal stability in the fully charged state and large theoretical capacity (170 mA h g^{-1}). $LiFePO_4$ has relatively lower voltage against Li/Li$^+$ (3.4 V) compared to the other cathode materials, leading to higher electrochemical stability and less reactivity to the electrolyte. The intercalation mechanism of $LiFePO_4$ is shown in Fig. 1.11.
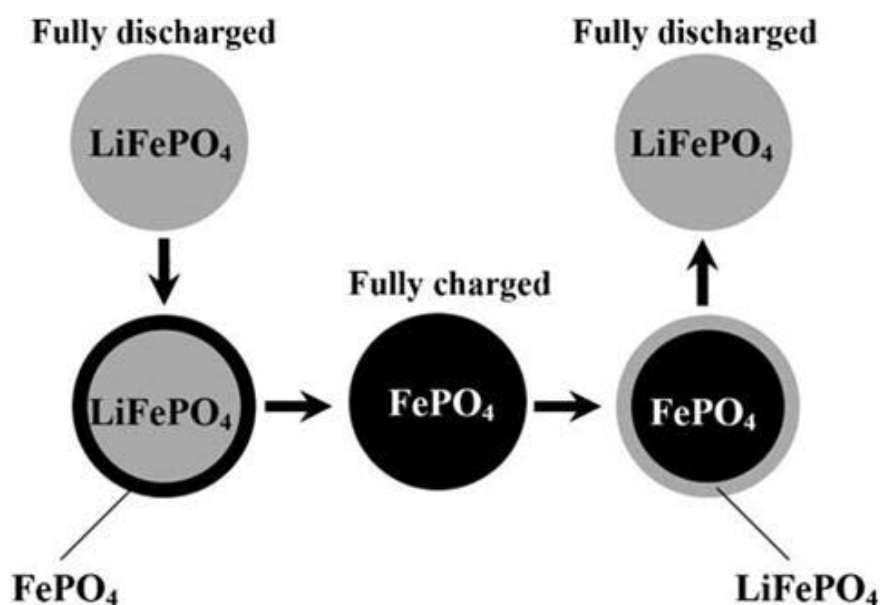
Figure 1.11 Schematic representation of the processes during charge/discharge of $LiFePO_4$ [20].

On charging, lithium is extracted from $LiFePO_4$, which results in the formation of a $FePO_4$ shell on the surface of the particles. On continuous charging, the boundary of the shell and the $LiFePO_4$ core move through the particle. As fully charged state, as lithium insertion commences, the $LiFePO_4$ shell gradually forms and then becomes fully discharged $LiFePO_4$ particles [194].

However, the low electrical conductivity has been limited the practical application of $LiFePO_4$ as the cathode material. Several nanotechnologies have been used to improve the electrochemical performance of $LiFePO_4$, including minimizing the particle size to the nanoscale and coating the particles with a thin carbon layer. Delacourt *et al.* prepared $LiFePO_4$ crystalline powders by a synthesis method based on direct precipitation under atmospheric pressure [195]. The particle size distribution is extremely narrow, centered on ca. 140 nm. After a soft thermal treatment under slight reducing conditions, the material showed the specific capacity of 147 mA h g^{-1} at 0.5 C and good cycling stability with no significant capacity loss after more than 40 cycles. To improve the electrical conductivity, Huang *et al.* fabricated $LiFePO_4$ composites by mixing raw materials with a carbon gel before heating and obtained nano-sized with particle sizes of 100-200 nm and 15 wt % carbon [196]. This composite showed excellent rate capability and stability and achieved 90 % theoretical capacity at C/2 at room temperature. The discharge capacity of 120 mA h g^{-1} was achieved even at high current rate of 5 C. They concluded that both particle size minimization and intimate carbon contact are essential to optimize the electrochemical performance of $LiFePO_4$.

To improve the electronic conductivity of $LiFePO_4$, MWCNT and graphene have also been used. A novel composite cathode was prepared by mixing $LiFePO_4$ particles with MWCNTs. $LiFePO_4$ particles were connected by MWCNTs to form a three-dimensional network wiring [197]. This structure can improve electron transport and

electrochemical activity effectively. The composite exhibited the initial discharge capacity of 155 mA h g^{-1} at C/10 rate and 146 mA h g^{-1} at 1C rate, high rate capability and good cycling stability. Ding *et al.* reported a LiFePO$_4$/graphene composite in a co-precipitation method, in which graphene nanosheets are used as additives [198]. The composite exhibited a discharge capacity of 160 mA h g^{-1} at 0.2 C and 109 mA h g^{-1} at 10 C. The high rate performance and good cycling stability could be ascribed to the fact that nanosize particle with high surface area and improved conductivity through a superior graphene conductor. LiFePO$_4$/graphene composite have also been prepared by hydrothermal method followed by thermal treatment [199]. It was found that the LiFePO$_4$ particles adhered to the surface of graphene and/or embedded in the graphene nanosheets. As a result, an effective three-dimensional conducting network was formed by bridging graphene nanosheets, which can facilitate electron transport effectively and thus improve the kinetics and rate performance of LiFePO$_4$. The composite cathode showed the capacities of 160 and 81 mA h g^{-1} at C/10 and 10 C rates, respectively.

1.2 Supercapacitors

1.2.1 History and Development

Supercapacitors (also called ultracapacitors or electrochemical capacitors) are passive and static electrochemical devices for storing and releasing energies rapidly and reversibly [200]. This is another form of energy storage devices with high power density and long life cycle. Supercapacitors have higher energy densites (about 5 Wh kg^{-1}) than conventional capacitors. Although supercapacitors have the lower energy densities than popular lithium ion batteries, their ultrafast charged and discharged capability lead to high power densities (10 kW kg^{-1}). The principle of energy storage in a supercapacitor is through the ion adsorption on an electrode/electrolyte interface which make electric double layer [electrical double layer capacitors (EDLC)] or due to electron transfer

between the electrolyte and electrode through fast Faradic redox reaction (pseudocapacitors) [201]. It shows potential applications in electronics, transportation, communication and aviation. It can also be used in a wide range of energy capture and storage applications either by themselves as a primary power source or in combination with batteries and fuel cells. Supercapacitors can be used as uninterrupted power supplies (back-up supplies used to protect against power disruption) and load-levelers (back-up power for memories, microcomputers, clocks, system boards etc.). In combination with batteries and fuel cells, supercapacitors are likely to be used for powering HEVs and EVs [202].

In 1957, General Electric first brought a capacitor, which store high capacitance by a double layer mechanism based on high surface area carbon and this innovation was filed as a patent by Becker [203]. In 1966, Stand Oil Company, Cleveland (SOIHO) invented the first supercapacitor device, which stored energy at the double layer interface [204]. After five years, in1971, NEC (Japan) developed the first supercapacitor device with an aqueous electrolyte capacitor under SOIHO's license, which is considered to be the first commercialized supercapacitor. A recent example is the use of supercapacitors in emergency doors on an Airbus A380, proving its reliability, safety and performance for large-scale applications [205]. The US Department of Energy has designated supercapacitors to be as important as batteries for future energy storage systems [206]. After 1990s supercapacitors began to draw some attention and significant research has been carried out to improve performance supercapacitor technology.

1.2.2 Energy Storage Mechanism

Supercapacitors are divided primarily by the charge storage mechanisms of their respective active material used for electrode construction. As we mentioned, two types

of supercapacitors exist. One is electric double layer capacitors and the other type is the pseudocapacitors [207].

Electric double layer capacitors

Electric double layer capacitors store electrical energy using reversible adsorption of ions from an electrolyte on the electrodes to form an electric double layer at an electrode/electrolyte interface. Supercapacitors that only involve physical adsorption, in which there is no electrochemical reactions on the electrode material (*e.g.* carbon) while charging and discharging process (Fig. 1.12 (a)) are called EDLC. In this type of supercapacitors, no charge transfers across the electrode/electrolyte interface, and no net ion exchanges occur between the electrode and the electrolyte [201]. This implies that the electrolyte concentration remains constant during the charging and discharging processes. Since there is no physical change in the electrodes during charge/discharge process, EDLCs can sustain millions of cycles. The model of energy storage could be defined by the following equation:

$$E = \frac{1}{2} CV^2 \tag{1.17}$$

Where E is the entire energy delivered, C denotes the specific capacitance, and V is the potential window.
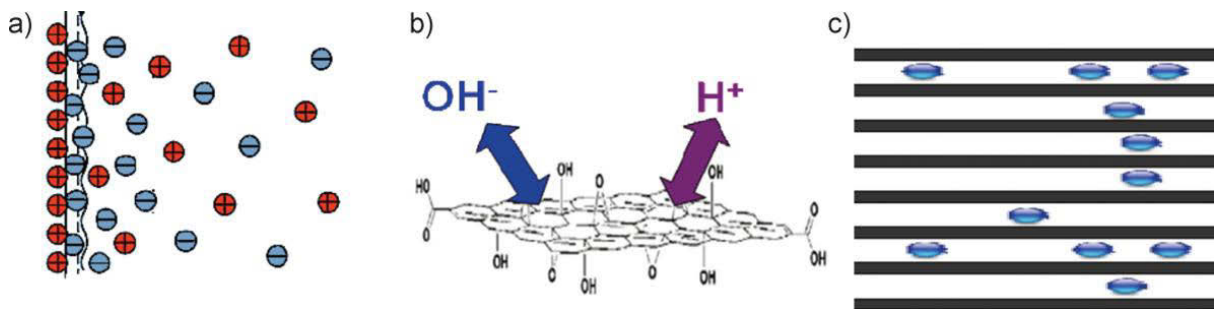
Figure 1.12 The working principle of supercapacitors, a) Electric double layer, b) redox reaction on the surface, and c) redox reaction in bulk [208].

However, due to the electrostatic surface charging mechanism, EDLCs suffer from a limited energy density and scientific research mainly emphasises to improve energy

performance. The materials for EDLCs should be highly conductive large specific surface area. Different carbon materials, such as activated carbon, carbon nanofibres, carbon nanotubes are considered to be best electrode materials for EDLCs.

Pseudocapacitors

The pseudocapacitors are different from EDLC in the way in which charge is stored. Pseudocapacitive charge storage fundamentally relies on redox reactions between electrode materials and electrolyte ions. The electric energy is generated by fast Faradic redox reaction, which produces pseudocapacitance. Materials undergoing such redox reactions include conducting polymers and several metal oxides (RuO_2, MnO_2, Co_3O_4 etc.) [209-211]. Depending on the location of these redox reactions, the pseudocapacitive charge storage can be categorized into surface charge storage and bulk charge storage (Fig 1.12 (b) and (c)). These pseudocapacitors can be superimposed on any electric double layer capacitors. In systems, where multiple oxidation states can be accessed, the pseudocapacitors often provide a higher energy density than EDLCs. Since the electrochemical processes occur both on the surface and in the bulk near the surface of the solid electrode, pseudocapacitors exhibit higher specific capacitance and energy density than EDLCs as [212]. Conway et al. has been reported that the specific capacitance is 10-100 times higher than the EDLCs [213]. However, pseudocapacitors suffer from relatively lower power density than EDLC because Faradic processes are normally slower than non-faradic processes. Moreover, due to the physical changes of the electrodes during redox reactions, pseudocapacitors have poor cycling stability compared with EDLCs [214].

1.2.3 Electrode Materials

The electrode materials mainly determine the performance of supercapacitors. Depending on the charge storage mechanism and active materials used, electrode

materials for supercapacitors can be classified into three categories: (i) carbon materials, (ii) metal oxides/hydroxides and (iii) conducting polymers. Different electrode materials and their electrochemical properties for supercapacitors will be reviewed in the following sections.

Carbon materials

Carbon materials are considered potential electrode materials for supercapacitors. As electrode materials, carbon materials have several advantages such as, higher specific surface area, good electronic conductivity, low cost, availability, chemical stability and wide operating temperature range. Carbon materials store charges in an electrochemical double layer formed at the interface between electrode and electrolyte. Therefore, the capacitance mainly depends on the surface area accessible to electrolyte ions. Carbon materials such as activated carbons (ACs) carbon nanofibers, carbon nanotubes, graphene have been extensively investigated as electrode material for EDLCs. Among them, ACs are the mostly used electrode materials for EDLCs. They are usually produced from the carbonization of pre-formed fibrous carbon precursors followed by activation process. Different types of activated carbon materials have been investigated as electrode materials for supercapacitors by Qu et al. [215]. Activated carbons with larger pores were found to be more suitable for high power applications. Xu et al. have been prepared activated carbon fibers (ACFs) with high surface area and highly mesoporous structure from polyacrylonitrile by NaOH activation [216]. Owing to the unique structural features, the ACFs exhibited high specific capacitances of 371, 213 and 188 F g^{-1} in aqueous, non-aqueous and ionic liquids, respectively. Beguin's group demonstrated a series of activated carbons with gradually changing nanotextural characteristics by heat treatment of a bituminous coal at temperatures ranging from 520 to 1000 ^{o}C and subsequent activation by KOH at 700°C or 800°C. The specific

capacitance on 6 M KOH varied almost linearly with the BET surface area, suggesting that the charge accumulation is controlled by the surface area development [217]. Although ACs have been commercially used as electrode materials for supercapacitors, their application still restricted because of the limited energy storage and rate capability. Carbon nanotubes are often regarded as high power electrode material because of their readily accessible surface area and good electrical conductivity. There high mechanical flexibility and open tubular network also make them a good support for active materials [218]. Futaba, and co-workers presented a method to fabricate a density packed aligned SWNT solid by using the zipping effect of liquids, which allowed the bulk materials to retain the intrinsic properties of the SWNTs [219]. The energy density of the obtained SWNT was about 35 Wh kg^{-1} in organic electrolyte. These studies demonstrated the importance of the aligned tubular structures and preserved intrinsic CNT properties on the electrochemical performance of the electrode materials. Recently, CNT-aerogel composite material was prepared by uniformly dispersing a carbon aerogel throughout the CNT host matrix without destroying the integrity of the CNT [220]. The composite material exhibited a high specific capacitance of 524 F g^{-1}. Manganese oxide nanoflower/carbon nanotube array (CNTA) composite electrodes with hierarchical porous structure large surface area and superior conductivity were prepared by combining electrodeposition technique and a vertically aligned CNTA framework. This binder-free manganese oxide/CNTA electrode presented excellent rate capability, high specific capacitance of 199 F g^{-1} and long cycle life (3 % capacity loss after 20000 cycles) [221]. Despite CNTs having excellent properties, their limited surface area restricted their use as high energy performance EDLCs.

Graphene with its maximal surface area of 2630 m^2 g^{-1} was an ideal medium for supercapacitors as the EDLC being directly proportional to the surface area. Ruoff et al.

pioneered the application of chemically reduced graphene (CRG) in supercapacitor [71]. The CRGs with a surface area of 705 m^2 g^{-1} exhibited specific capacitances of 135 F g^{-1} and 99 F g^{-1} in aqueous KOH and organic electrolytes, respectively. Improved specific capacitance (191 F g^{-1}) was obtained from reduction of GO to graphene (surface area 463 m^2 g^{-1}) using microwave-assisted reaction [222]. Wang's group also reported graphene materials from graphene oxide sheets and have been investigated as electrode materials for supercapacitors [223]. A maximum specific capacitance of 205 F g^{-1} with a power density of 10 kW kg^{-1} and energy density of 28.5 Wh kg^{-1} was obtained. The supercapacitor devices demonstrated excellent cycling stability along with 90 % specific capacitance retained after 1200 cycles.

Metal oxides/hydroxides

Metal oxides are generally considered the best candidates as electrode material for pseudocapacitors, because they have a variety of oxidation states available for redox charge transfer. They store energy not only like electrostatic carbon materials but also exhibit electrochemical redox reactions between electrode materials and ions within appropriate potential window [224].

Ruthenium oxides

Among the transition metal oxides, ruthenium oxide has been extensively studied because of its high theoretical capacitance of 2000 F g^{-1} in a wide potential window of 1.2 V, highly reversible redox reactions, good thermal stability, metallic type conductivity, and long cycle life [225]. Ruthenium oxides with different structure have offered improved specific capacitance and rate capability [226, 227]. Although ruthenium oxides have promising electrochemical properties, commercial applicability still limited due to its high cost and environmental harmfulness.

Manganese oxides

As an alternative approach, researchers have given significant attention to finding out cheaper and environmentally friendly materials for supercapacitors. Manganese oxide has attracted major attention and is considered a promising alternative class of materials because of its relatively low cost, low toxicity and environmental safety with high theoretical capacitances ranging from 1100 to 1300 F g^{-1} [228]. Lee's group synthesized amorphous MnO_2 and investigated as electrode material for faradic electrochemical capacitor cycled between -0.2 and +1.0 V versus SCE in 2 M KOH electrolyte [229]. In this potential range, it showed ideal capacitive behaviour with a specific capacitance of 200 F g^{-1} and good cycling stability. Nakayama *et al.* reported electrodeposition of the layered manganese oxide in a colloidal crystal template formed by self-assembly of polystyrene particles on an indium tin oxide substrate [230]. Owing to contributions of the surface of macropores and the interlayer space, the obtained macroporous film exhibited good pseudocapacitive behaviour in neutral electrolyte. Toupin et al. demonstrated an ultrahigh specific capacitance of 1380 F g^{-1} in platinum supported amorphous MnO_2 thin films electrodes at low charge-discharge rates [231]. Different nanostructured manganese oxides have also been prepared by a simple precipitation technique using $KMnO_4$ and different alcohols [232]. The nanostructured manganese oxides showed good pseudocapacitive performance in 1 M Na_2SO_4 electrolyte.

Nickel oxides/hydroxides

Nickel oxide is also considered as alternative electrode material for supercapacitors in alkaline electrolytes owing to its relatively higher specific capacitance (theoretical specific capacitance of 3750 F g^{-1}), low cost and environment friendliness [233]. The redox reaction of nickel oxide in a KOH electrolyte can be expressed as follows: [234]

$$NiO + OH^- \leftrightarrow NiOOH^- + e^- \tag{2.18}$$

Kang et. al repoted a simple chemical preparation method to prepare loose packed nickel oxide nanoflakes [235]. Author's demonstrated that the unique microstructure can accommodate the electroactive species in solid bulk electrode materials. Nickel oxide nanoflakes exhibited specific capacitance of 942 F g^{-1} at the current density of 5 mA g^{-1}. Ren's group prepared hierarchical and porous NiO nanoflowers with large BET surface area and controlled pore size distribution by microwave method.
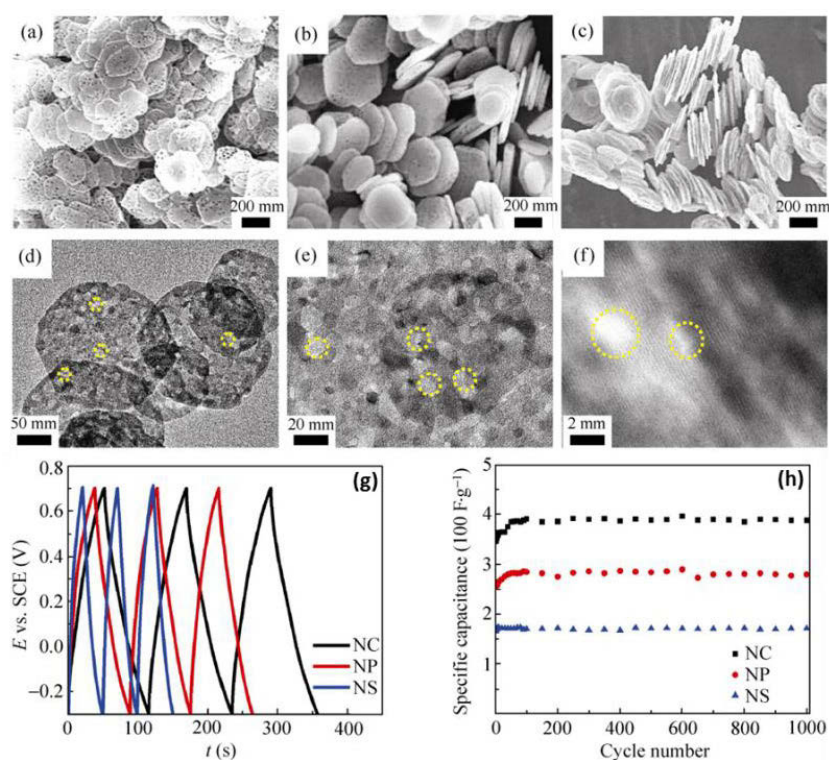
Figure 1.13 SEM images of the porous NiO nanocrystals: (a) nanoslices, (b) nanoplates, and (c) nanocolumns. HRTEM images of representative porous NiO nanocrystals: (d) nanoslices with pore sizes of 10–30 nm, (e) nanoplates with pore sizes of 10–25 nm, (f) nanocolumns with pore sizes of 2–5 nm. (g) Galvanostatic charge/discharge curves measured with a current density of 5 A/g for porous NiO nanocrystals. (h) Cycling performance for porous NiO nanocrystals at a current density of 5 A g^{-1} in 1M KOH. NS, NP, and NC denote nanoslices, nanoplates, and nanocolumns, respectively [238].

The obtained NiO nanoflowers have uniform size and are composed of sheet-like petals that are built up from nanocrystals [236]. The resultant NiO nanostructures presented a specific capacitance of 277 F g^{-1}, and good cycling stability. Shen *et al.* reported a practical and efficient strategy for synthesizing hierarchical (meso- and micro-) porous NiO nano/micro spherical superstructures. The obtained superstructures comprised 2D mesoporous NiO petal building blocks. The hierarchical porous NiO nano/micro superstructures delivered a specific capacitance of 710 F g^{-1} at 1 A g^{-1} and offered good specific capacitance retention of 98 % after 2000 continuous charge-discharge cycles [237]. Various porous NiO nanostructures including nanoslices, nanoplates and nanocolumns have also been reported by Yan *et al.* [238] (Fig. 1.13). The electrochemical results showed that the specific capacitance of porous NiO nanocolumns (390 F g^{-1}) is higher than that of nanoslices (176 F g^{-1}) or nanoplates (285 F g^{-1}) at a current density of 5 A g^{-1}. This illustrated that the performance of supercapacitor electrodes depends on structural properties of the material.

Nickel hydroxide is another pseudocapacitive material which showed much higher specific capacitance than NiO. Kong et al. synthesized mesoporous Ni(OH)$_2$ nanoflakes by a facile chemical precipitation method. The mesoporous Ni(OH)$_2$ delivered a specific capacitance of 2055 F g^{-1} at 0.625 A g^{-1} with the potential range of 0 to 0.4 V [239]. Xing's group reported mesoporous α-Ni(OH)$_2$ by a hydrothermal method. The mesoporous α-Ni(OH)$_2$ possessed a large specific surface area of 349 m^2 g^{-1} and narrow pore size distribution of 16 nm, which provide more electroactive sites and facilitate electrolyte transport. The mesoporous structure demonstrated specific capacitance of 1718 F g^{-1} at a scanning rate of 5 mV s^{-1} with good cycling stability [240]. Gong and co-workers proposed a facile template-free strategy to β-Ni(OH)$_2$ nanosheets via a solvothermal method using methanol and water as mixed solvents. The as-prepared β-

Ni(OH)$_2$ nanosheets showed high specific capacitance of 2342 F g^{-1} with stable cycling performance [241]. Three dimensional mesoporous β-Ni(OH)$_2$ film on nickel foam with ultra-thin (~6 nm) nanowalls were also constructed by Lu's group. The nanowalls presented high specific capacitance of 2675 F g^{-1} and 96 % specific capacitance retained after 500 cycles [242]. We also prepared Ni(OH)$_2$ nanospheres and will be discussed in Chapter 4.

Cobalt oxides/hydroxides

Cobalt oxides and hydroxides with unique morphology and microstructure also exhibt excellent reversible redox behaviour and long term cycle performance for supercapacitors. Hexagonal Co$_3$O$_4$ nanosheets were synthesized using a facile complex precursor solution process followed by thermal decomposition, which presented a specific capacitance of 227 F g^{-1} at 1 A g^{-1} [243]. Cobalt oxide nanotubes with an outer diameter of 300 nm have been synthesized by chemical deposition of cobalt hydroxide in anodic aluminium oxide templates and thermal annealing. It displayed a specific capacitance of 574 F g^{-1} at 0.1 A g^{-1} [244]. Mesoporous aerogel-like cobalt oxide has been successfully demonstrated with the addition of epoxide. Cobalt oxide aerogels showed a high specific capacitance of 600 F g^{-1} and good reversibility and cycling stability [245].

Cobalt hydroxide materials have also attracted much attention owing to their layered structure and large interlayer spacing, which provides high surface area and fast ion insertion/extraction rate [246]. Gupta et al. reported α-Co(OH)$_2$, which potentiostatically deposited onto a stainless-steel. The obtained nanolayered α-Co(OH)$_2$ sheets with the average thickness of 10 nm, delivered a high specific capacity of 860 F g^{-1} [247]. Zhou et al. reported one of the most impressive results, where an ordered mesoporous Co(OH)$_2$ film electrodeposited on foamed Ni mesh was used as electrode

material. The electrode presented a specific capacitance of 2646 F g^{-1}, which could be attributed to the special ordered mesoporous nanostructure [248].

Other metal oxides such as vanadium oxides, iron oxides have also been studied for supercapacitor applications. For example, Lee and Goodenough synthesized V_2O_5 by quenching V_2O_5 powders heated at 950 ^{o}C. The amorphous V_2O_5 showed a specific capacitance of 350 F g^{-1} in aqueous KCl solutions [249]. Srinivasan et al. prepared V_2O_5 nanofibers through a simple electrospinning method and the effect of calcination temperature on the structure and morphology of V_2O_5 was also investigated. When evaluated as electrode materials for supercapacitors, the highest specific capacitance of 190 F g^{-1} in aqueous electrolyte (2 M KCl) and 250 F g^{-1} in organic electrolyte (1 M LiClO$_4$ in PC) was achieved for sample annealed at 400 ^{o}C [250].

Iron oxide is another material for supercapacitor electrode, which offers low cost and minimal environmental impact. The electrochemical performance of Fe_3O_4 appears to be inferior in common neutral and basic electrolytes with a specific capacitance of only 5-7 F g^{-1} [251]. Chung et al. showed improved specific capacitance of 100 F g^{-1} by optimization of the porosity and crystallinity in electrodeposites hierarchical porous Fe_3O_4 thin films [252]. A Fe_3O_4 film with cubic morphology has also been demonstrated on stainless steel foil by hydrothermal method. The Fe_3O_4 film showed typical pseudocapacitive behaviour in 1 M Na_2SO_3 solution and exhibited a specific capacitance of 118.2 F g^{-1} at the current density of 6 mA g^{-1} with capacity retention of 88.75 % after 500 cycles [253]. However, poor electronic conductivity and low specific capacitance restricts its applications for supercapacitors.

Mixed metal oxides

In recent years, due to the available multiple oxidation state and higher electrical conductivity than single metal oxides process by mixed metal oxides spinel such as

AB_2O_4 (A = Mn, Ni, Co, Fe or Cu; B = Mn, Fe, Co, Ni) mixed metal oxides. They have attracted much research interest in the applications as supercapacitor. They offer the oxidation-state-rich redox reactions which are indispensable for pseudocapacitor possibly from their bi-metallic (both metal ions) contribution [254]. Different nanostructured mixed metal oxides with good electrochemical performances have been studied for supercapacitor applications [255-258].

Among them, $NiCo_2O_4$ has been conceived significant attention due to their higher electrical conductivity, environment friendliness, tunable structural features and low cost [259, 260]. Jiang et al. demonstrated a simple and scalable strategy for synthesizing hierarchical porous $NiCo_2O_4$ nanowires. The porous nanowires presented a high specific capacitance of 743 F g^{-1} at 1 A g^{-1} with excellent rate performance and cycling stability (only 6.2 % loss after 3000 cycles) [261]. A facile, low-cost co-precipitation process has been employed to prepare nanostructured $NiCo_2O_4$ spinel. The addition of ethylene glycol and the calcination time have signinificant impact on the size distribution, crystallinity, electronic conductivity and the electrochemical performances of the material. The $NiCo_2O_4$ spinel with 5-10 nm in size had excellent crystallinity and electric conductivity. It showed a specific capacitance of 671 F g^{-1} at a current density of 1 A g^{-1} and excellent cycling stability with the specific capacitance decay is less than 2 % after 7000 cycles [262]. Wang and Shen demonstrated urchin-like nanostructures via a hydrothermal method without using any template and catalyst. The syntheiszed $NiCo_2O_4$ urchins were uniform dimeters of 5 μm with numerous small nanorods radially grown from the center. With a porous and large surface area of 99.3 m^2 g^{-1}, the $NiCo_2O_4$ urchins exhibited superior specific capacitance of 1650 and 1348 F g^{-1} at the current density of 1 and 15 A g^{-1}. At the current density of 8 A g^{-1}, the specific capacitance loss was 9.2 % after 2000 cycles, which indicates excellent cycling stability (Fig. 1.14)

[263]. One dimensional ultralayered mesoporous $NiCo_2O_4$ nanowires, which constructed from lots of quasi-single crystalline $NiCo_2O_4$ nanosheet building blocks have also been reported. The ultralayered mesoporous nanowire electrode displayed high specific a capacitance and good cycling stability (10 % loss after 5000 cycles) [264].
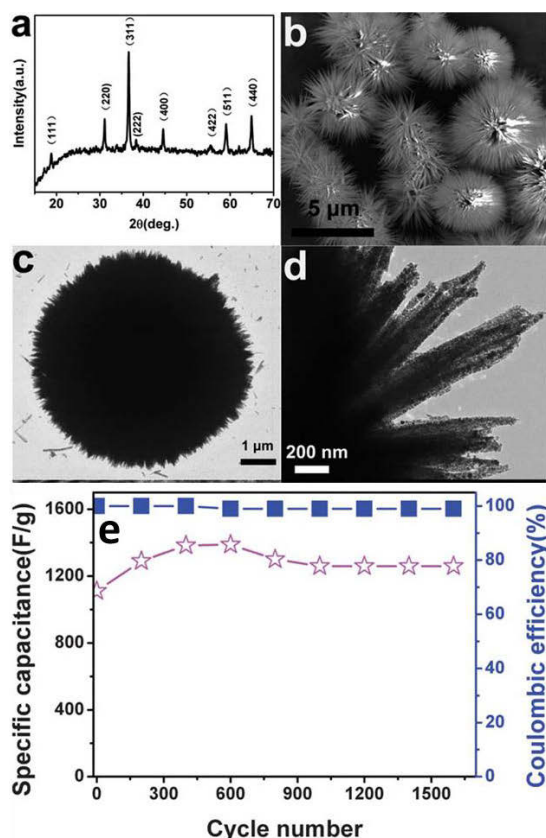
Figure 1.14 (a) XRD pattern, (b) SEM image, (c and d) TEM images and (e) Cycling performance and coulombic efficiency of the urchin-like $NiCo_2O_4$ nanostructures [263].

A hydrothermal method was employed to prepare porous urchin-like $MnCo_2O_{4.5}$ hierarchical structures with 4-6 μm in diameter. The urchin-like $MnCo_2O_{4.5}$ delivered a specific capacitance of 151.2 F g^{-1} with excellent long-term cycling stability [265]. Yuan et al. demonstrated two types of porous cobalt manganese oxide nanowires ($MnCo_2O_4$ and $CoMn_2O_4$) by thermal decomposition of Co-Mn-Nitrilotriacetic acid (Co-Mn-NA) polymer precursors at various Co-Mn molar ratios. The nanowires of

cobalt manganese oxides were composed of numerous nanoparticles. At the current density of 20 A g^{-1}, both the $MnCo_2O_4$ and $CoMn_2O_4$ nanowire electrodes displayed excellent specific capacitances of 2108 F g^{-1} and 1342 F g^{-1}, respectively [266]. Tang's group proposed a simple process composed of hydrothermal process and annealing directly to grow cobalt-manganese composite oxide nanostructures on 3D conductive nickel foam. When used as electrode materials for supercapacitors, the cobalt-manganese oxide electrode exhibited excellent specific capacitance of 840.2 F g^{-1} at the current density of 10 A g^{-1} and superior cycling stability over 7000 cycles [267]. Other mixed metal oxides such as, $ZnCo_2O_4$ and $CuFe_2O_4$ have also been studied as supercapacitor electrodes and obtained high specific capacitance and good cycling stability [268, 269].

However, the poor electrical conductivity of metal oxides largely limits their application in developing high performance supercapacitors. In order to improve the electrical conductivity of metal oxide electrodes, many attempts have been adopted by introducing carbon materials [270-273]. Among carbon materials graphene shows more advantages due to its excellent physical and chemical properties. For instance, Yan et al. synthesized graphene-MnO_2 composites through the self-limiting deposition of nanoscale MnO_2 on the surface of graphene by using a microwave method and investigated as electrode materials for supercapacitors. Graphene-MnO_2 composite (78 wt. % MnO_2) presented the specific capacitance of 310 F g^{-1} at 2 mV s^{-1} and 228 F g^{-1} at 500 mV s^{-1}, which is almost three time higher than that of pure graphene (104 F g^{-1}) and birnessite-type MnO_2 (103 F g^{-1}) [274]. Chen and co-worker's developed a technique for morphology transmission from graphene to metal oxide nanolamellas by in situ replacement with the framework of graphene. The process involves using graphene sheets as the starting agent, thus transmitting the morphology of layered

structurecfrom graphene to as-prepared metal oxides. The heteroconfiguration of the MnO$_2$ play an important role to prevent microstructure degradation in the electrochemical cycling process. The electrode showed excellent cycling stability with a less than 10 % decrease in specific capacitance after 3000 cycles [275]. MnO$_2$/graphene composite was also successfully prepared by CVD and electrodeposition. When studied as electrode materials for supercapacitors, the MnO$_2$/graphene composite electrode demonstrated a specific capacitance of 399.82 F g^{-1} at 10 mV s^{-1} and stable capacitance over 5000 redox cycles. Graphene layers improve the electrical conductivity of MnO$_2$ and the interaction between the electrode and electrolyte [276].

Xia et al. prepared graphene sheet/porous NiO hybrid film by the combination of electrophoretic deposition and chemical bath deposition. The graphene sheet/porous NiO hybrid film demonstrated excellent pseudocapacitive behavior with specific capacitances of 400 and 324 F g^{-1} at the current density of 2 and 40 A g^{-1}, respectively, which is higher than the porous NiO film (279 F g^{-1} and 188 F g^{-1} at 2 and 40 A g^{-1}). The improvement of the pseudocapacitive properties is attributed to the electrochemical activity of the graphene sheets [277]. Cao's group showed 3D graphene networks for the construction of graphene/NiO composite and used as electrode materials for supercapacitors. The unique 3D porous structure of the graphene network with a large specific surface area allows the rapid access of electrolyte ions to the NiO surface. The prepared NiO/graphene composite exhibited a high specific capacitance of 816 F g^{-1} at a scan rate of 5 mV s^{-1} and a stable cycling performance without any decrease of specific capacitance after 2000 cycles [278].

A series of Co$_3$O$_4$ nanoplates/graphene nanosheets (GNS) composites were fabricated using a simple and green method by hydrothermal treatment and subsequent calcinations in air. The Co$_3$O$_4$ nanoplates (length: 0.5-1 μm, width: 100-300 nm) are

homogeneously distributed on the surface of graphene nanosheets. The Co_3O_4 nanoplates/7.0 % GNS composite presented a specific capacitance of 667.9 F g^{-1} at 1.25 A g^{-1} and 412.5 F g^{-1} at 5 A g^{-1} in 2 M KOH aqueous solution. The composite electrode exhibited excellent cycling stability with 18.7 % capacitance increased after 1000 cycles [279]. Wang et al. reported a convenient method to fabricate a 3D Co_3O_4/graphene hydrogel composite and applied as electrode material for supercapacitors. The spherical Co_3O_4 particles act as a spacer to keep the adjacent graphene sheets separated. At the current density of 0.5 A g^{-1}, the Co_3O_4/graphene hydrogel composite material delivered a high specific capacitance of 757.5 F g^{-1}, which is much higher than that of Co_3O_4 (454.2 F g^{-1}) and graphene hydrogel (310 F g^{-1}) [280].

Conducting polymers

Conducting Polymers also provide capacitance behaviour through the redox process. They have many advantages including low cost, high conductivity, high potential window and low environmental impact. Polyaniline, Polypyrrole, polythiophene are typical conducting polymers for supercapacitor applications [281-283]. The most extensively investigated conducting polymers are polyaniline and polypyrrole. In both aqueous and non-aqueous electrolytes, polyaniline (PANI) can reach a specific capacitance of 150-190 F g^{-1} and polypyrrole (Ppy) a specific capacitance of 80-100 F g-1 [284, 285]. However, due to the swelling and shrinking problem of electrode, conducting polymers show poor cycling performance, which restrict its practical application for supercapacitors.

To enhance the cycling performance, the composite of conducting polymers and carbon materials provide a practical solution. Conductive polymer/CNT composites with high specific capacitance have been investgated extensively. Polyaniline/MWCNT was prepared by microwave-assisted polymerization. This composite was a core-shell

structure with PANI layers (50-70 nm). An improved specific capacitance of 322 F g^{-1} was achieved [286]. The composite films of electrically conducting polypyrole and single wall carbon nanotubes (SWCNTs) have been reported by Sun et al. the composite films were electropolymerized from homogeneous mixture of Ppy and SWCNTs, or suspension of Ppy and functionalized SWCNTs. The Ppy/SWCNTs and Ppy/functionalized SWCNTs delivered the specific capacitance of 144 F g^{-1} and 200 F g^{-1} at the scanning rate of 200 mV s^{-1}, respectively [287].

Graphene-conducting polymer composites have also received much interest owing to their flexibility and superior specific capacitance. A graphene nanosheets-PANI composite was synthesized by in situ polymerization [288]. The specific capacitance of 1046 F g^{-1} was obtained at a scanning rate of 1 mV s^{-1}. Conductive graphene nanosheets provided more active sites for nucleation and was coated by PANI nanoparticles on both sides, resulting it energy density of 39 kW h g^{-1} and a power density of 70 kW kg^{-1}. Zhang et al. used grapheneoxide instead of graphene as the starting material to prepare graphene oxide/PANI nanofiber composite, which was then reduced to graphe/PANI nanofiber composite [289]. This composite material showed high specific capacitance of 480 F g^{-1} at the current density of 0.1 A g^{-1}, and good rate performance. Stable aqueous dispersions of chemically converted graphene (CCG)/PANI composite were successfully prepared by mixing two purified components with the assistance of ultrasonication [290]. Both components were self- assembled through electrostatic interaction to form a uniform composite composed of the layered structure of PANI nanofibers sandwiching between CCG layers. It was flexible and mechanically stable. The conductivity of the composite film containing 44 % CCG (5.5×10^2 S m^{-1}) was about 10 times than PANI nanofiber film. When applied as electrode materials for

supercapacitors, the composite film demonstrated specific capacitance of 210 F g^{-1} at a discharge rate 0.3 A g^{-1} and improved electrochemical stability.

1.2.4 Electrolytes

Electrolytes are also one of the most important supercapacitor components. It plays a critical role in the development of the electric double layer in EDLCs and for the reversible redox processses in pseudocapacitors. The electrolytes for supercapacitors should have [214]:

1) high ionic concentration

2) wide potential window

3) high electrochemical stability

4) low resistivity and low toxicity

5) low viscosity and inexpensive

6) low solvated ionic radius

7) availability and high purity

The electrolytes used in supercapacitors can be categorized as: (i) aqueous electrolyte, (ii) organic electrolyte, and (iii) ionic liquid electrolyte (ILs)

Aqueous electrolytes

The main advantages of using aqueous electrolytes include its low cost and availability. Its high conductivity and low health concerns are also significant advantages. Aqueous electrolytes (such as H_2SO_4, Na_2SO_4, KOH, KCl, NH_4Cl aqueous solution) can provide lower resistance and higher ionic concentration. Supercapacitors containing aqueous electrolytes show higher specific capacitance than those of organic electrolyte, owing to its higher ionic concentration and smaller ionic radius. Moreover, the preparation and use of aqueous electrolytes are quite easy compared to organic electrolytes. However,

aqueous electrolytes have big disadvantages in terms of improving both energy and power density because of their narrow potential range (about 1.2 V).

Organic electrolytes

Organic electrolytes are currently used in commercial supercapacitors due to their potential window. They often operated above potentials above 2 V (2.2-2.7 V), which can be increased as high as 3.5 V [291]. Among organic electrolytes, acetonitrile and propylene carbonate (PC) are the most commonly used solvent. PC-based electrolytes are becoming more popular because of the low toxicity and can offer a wide electrochemical window, good conductivity and a wide range of operating temperature. Table 1.2 shows the common types of electrolytes and their difference in resistivity, density and voltage window used in supercapacitors.

Table 1.2 Density, resistivity and operating voltage window for different electrolytes [291].

Electrolyte	Density (g cm^{-3})	Resistivity (Ω cm)	Cell voltage (V)
KOH	1.29	1.9	1
H$_2$SO$_4$	1.2	1.35	1
Propylene carbonate	1.2	52	2.5-3.0
Acetonitrile	0.78	18	2.5-3.0
Ionic liquid	1.3-1.5	125 (25 ^{o}C)	4
		28 (100 ^{o}C)	3.25

Organic electrolytes in general suffer from a notable increase in resistivity, which is unfavourable to its power performance and safety issues that are associated with incorporating a toxic, flammable material into transportation vehicles. In addition,

organic electrolytes need restrict processes and conditions to obtain ultra-pure electrolytes. The water content in the electrolyte must be kept below 3-5 ppm.

Ionic liquid electrolytes

Ionic liquids exist solvent-free molten salt at room temperature and possess low vapour pressure and high thermal and chemical stability [292, 293]. It has wide electrochemical window ranging from 2 to 6 V, typically about 4.5 V, low flammability and conductivity at a level of 10 mS cm^{-1} [294]. The most studied ILs for supercapacitor applications are imidazolium pyrrolidinium, as well as asymmetric, aliphatic quaternary ammonium salts including tetrafluoroborate, trifluoromethanesulfonate and hexafluorophosphate [295]. Mesoporous nickel-based mixed rare-earth oxide/activated carbon composite was prepared as electrode materials in supercapacitor applications by using solvent-free1-butyl-3-methyl imidazolium hexafluorophosphate as electrolyte with good conductivity, low vapour pressure and wide potential window [296] The composite electrode delivered a real power density of 458 W kg^{-1}and higher energy density of 50 Wh kg^{-1} and excellent cycle life without any capacity decay up to 500 cycles. Such promising electrochemical performance can be ascribed to ionic liquid electrolyte with broad potential windows and high stable abilities.

Summary

In this chapter, the recent advances in nanostructured electrode materials for lithium ion batteries and supercapacitors have been reviewed. It is unquestionable that nanostructured materials play a key role in developing high-performance energy storage devices. The electrochemical performances of electrode materials are mainly depending on their morphology and size. Due to the high specific surface area of nanostructured materials, these materials can provide more active sites for electrochemical reactions, short diffusion pathways for both ions and electrons and effectively alleviate the volume

change during charge-discharge process, leading to enhanced electrochemical performance. Nanostructured electrode materials with high capacity, good safety, long cycle life and good reliability will undoubtedly boost the performance of lithium ion batteries and supercapacitors and facilitate their extensive application. In this doctoral study is emphasizing on electrode materials with improved electrochemical properties for lithium ion batteries and supercapacitors.

Chapter 2 Experimental

2.1 Overview

In this study, experimental work was performed in the laboratory. The overall experimental procedures for designing electrode materials are shown in Fig 2.1. This chapter refers to the preparation of materials followed by characterization of the prepared materials and evaluation of their electrochemical properties for lithium ion batteries and supercapacitors.
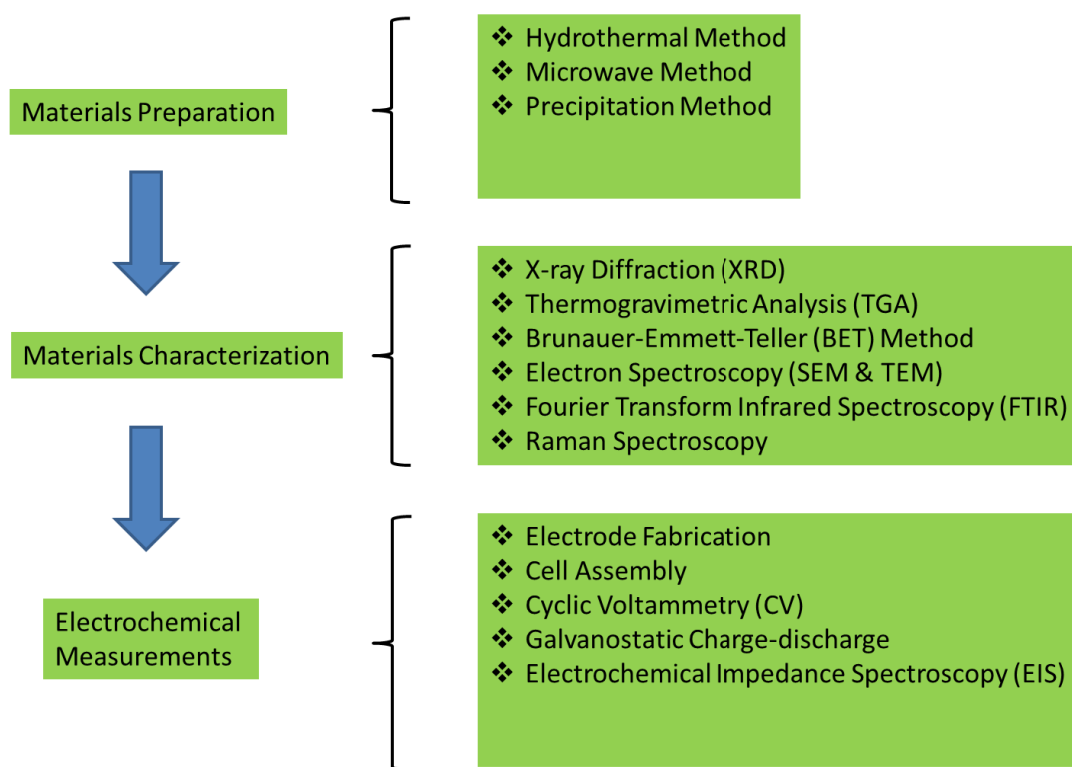
Figure 2.1 Schematic illustration of the overall experimental procedure.

2.2 Materials and Chemicals

A list of materials and chemicals used in this research are presented in Table 2.1.

Table 2.1 Materials and chemicals

Materials and Chemicals	Formula	Purity	Supplier
Acetone	CH_3COCH_3	99 %	Sigma-Aldrich
Carbon black	C	100 %	Sigma-Aldrich

Cobalt nitrate hexahydrate	$Co(NO_3)_2 \cdot 6H_2O$	98 %	Sigma-Aldrich
Dimethyl carbonate	$(CH_3)_2CO_3$	99 %	Sigma-Aldrich
Ethanol	CH_3CH_2OH	95 %	Chem Supply
Ethylene glycol	$OH(CH_2)_2OH$	99.8 %	Chem Supply
Ethylene carbonate	$(CH_2)_2CO_3$	99 %	Sigma-Aldrich
Ferric chloride	$FeCl_3$	97 %	Sigma-Aldrich
Graphite (natural flakes)	C	75 %	Aldrich
Glycine	$C_2H_5NO_2$	99 %	Sigma-Aldrich
Hydrochloric Acid	HCl	37 %	Sigma-Aldrich
Hydrogen peroxide solution	H_2O_2	50 %	Sigma-Aldrich
Hydrazine hydrate	$NH_2NH_2 \cdot xH_2O$	50-60 %	Sigma-Aldrich
Lithium foil	Li	99.999 %	Hohsen Corporation Japan
Lithium hexafluorophosphate	$LiPF_6$	99.99 %	Sigma-Aldrich
Manganese nitrate tetrahydrate	$Mn(NO_3)_2 \cdot 4H_2O$	97 %	Sigma-Aldrich
Nickel nitrate hexahydrate	$Ni(NO_3)_2 \cdot 6H_2O$	99%	Sigma-Aldrich
N-methyl pyrrolidinone (NMP, anhydrous)	C_5H_9NO	99.5 %	Aldrich
Nitric acid	HNO_3	68 %	Aldrich
Poly(vinylidene fluoride) (PVDF)	$(C_2H_2F_2)n$	99 %	Aldrich
Potassium bromide (FTIR grade)	KBr	99 %	Sigma-Aldrich
Potassium hydroxide	KOH	90 %	Sigma-Aldrich
Potassium permanganate	$KMnO_4$	99 %	Sigma-Aldrich
Propylene carbonate (PC, anhydrous)	$C_4H_6O_3$	99.7 %	Sigma-Aldrich
Polypropylene separator	$(C_3H_6)n$	100 %	Celgard
Polyvinylpyrrolidone (PVP)	$C_6H_9NO)_n$	99 %	Sigma-Aldrich

Sodium nitrate	NaNO$_3$	99 %	Sigma-Aldrich
Sodium sulfate (anhydrous)	Na$_2$SO$_4$	99 %	Sigma-Aldrich
Sodium hydroxide	NaOH	98 %	Sigma-Aldrich
Sulfuric acid	H$_2$SO$_4$	95-98 %	Sigma-Aldrich
Urea	H$_2$NCONH$_2$	98 %	Sigma-Aldrich

2.3 Materials Preparation

Different methods such as hydrothermal method, microwave method and precipitation method were used to synthesize nanostructured electrode materials. Each method has its advantages in tailoring the shape and sizes of the materials.

2.3.1 Hydrothermal Method

Hydrothermal method is a synthesis method of single crystals from high temperature aqueous solution at high vapour pressure. The crystal growth is performed in an apparatus consisting of a steel pressure vessel called an autoclave, in which a nutrient is supplied along with water. The crystal growth in hot solvent under high pressure depends on the solubility of the precursors. A temperature gradient is maintained at opposite ends of the growth chamber, so that the hotter end dissolves the nutrient and the cooler end facilitates the growth of the crystal seeds. Hydrothermal method can create crystalline phases that are unstable at the melting point temperatures. The hydrothermal method can also grow materials that have a high vapour pressure near their melting points. This method is particularly suitable for the growth of a lot of crystals with various morphologies. The disadvantages of these methods are the need for expensive autoclaves and the observation of in situ crystal growth is not possible. This method is widely used to prepare nanostructured materials. Synthesis conditions can affect the morphology, composition and crystal structure of the materials. These

include the temperature, the volume of the solvent, the concentration of the precursors and the use of a surfactant. The autoclave used in this study is made of stainless steel and the inside contains a polytetrafluoroethylene (PTFE) lined with 30 ml capacity, which is shown in Fig. 2.2(b). In this doctoral study hydrothermal method was employed to synthesize NiO nanosheets, $NiCo_2O_4$ nanoflakes and nanobelts and flake-like $MnCo_2O_4$, which are presentedin Chapter 3, Chapter 6 and Chapter 8, respectively.
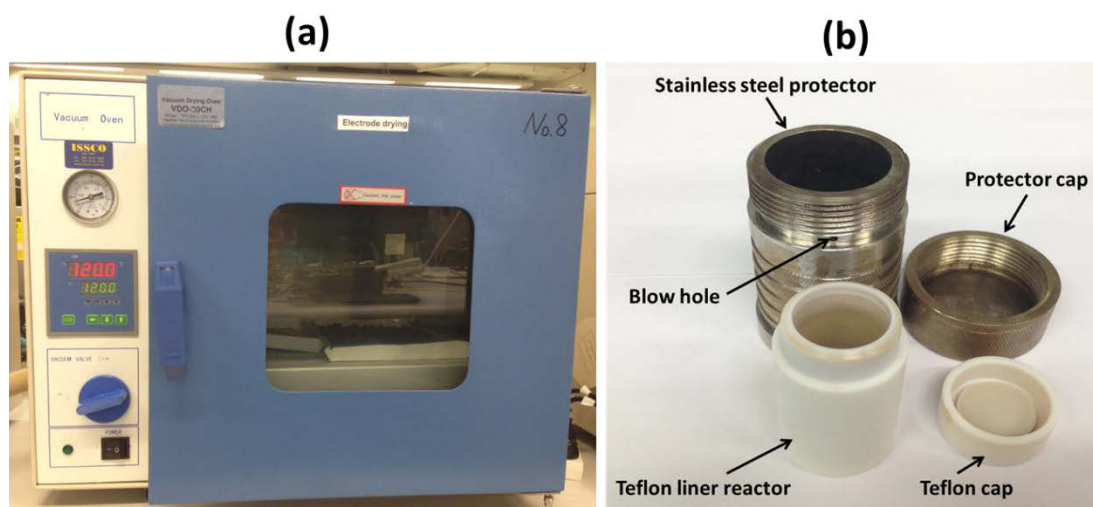
Figure 2.2 (a) Electric oven and (b) Autoclaves for hydrothermal synthesis.

2.3.2 Microwave Method

Microwave method is a recent technique to prepare nanomaterials in very short durations. In conventional thermal processing, energy is transferred to the material through convection, conduction and radiation of heat from the surfaces of the material. In contrast, microwave energy is delivered directly to materials through molecular interaction with the electromagnetic field. In heat transfer, energy is transferred due to the thermal gradients, but microwave heating is the transfer of electromagnetic energy to thermal energy and is energy conversion rather than heat transfer. This difference in the way of energy delivered can result in many potential applications including the preparation of nanomaterials. Since microwaves can penetrate materials and deposit

energy, heat can be generated throughout the volume of the material simultaneously and uniformly. Microwaves provide some atypical features that contribute to the acceleration of the reaction rates. Compared to solid state and other wet chemical approach, microwave processing is more facile for scaling up. The advantages of microwave process are as follows:

1) High heating rates, thus increasing the reaction rates

2) Extremely rapid kinetics of crystallization

3) No direct contact between the heating source and the reactants and solvents

4) Excellent control of the reaction parameters, which is very important with respect to the quality product and safety issues

5) Higher yields

6) Better selectivity due to reduced side reactions

Figure 2.3 Microwave Synthesizer (Model: NOVA-II).

Figure 2.3 shows the microwave synthesizer (Model: NOVA-II) used in this study. $Ni(OH)_2$ nanospheres, Fe_2O_3 nanoparticles and $NiCo_2O_4$ nanosheets, were prepared via microwave method as described in Chapter 4, Chapter 5 and Chapter 9, respectively.

2.3.3 Precipitation Method

Precipitation method is defined as the creation of a solid in a solution. In precipitation method, the chemical reaction occurs between the soluble reactants in a liquid solution. The precipitate that formed remains in the suspension, which can be separated by centrifuge or filtration. Graphene/MnO_2 nanosheets were synthesized by using precipitation method as presented in Chapter 9.

2.4 Materials Characterization

2.4.1 X-ray Diffraction (XRD)

X-ray diffraction is a non-destructive analytical characterization technique to determine the crystal phase and structure. It generates an X-ray beam hitting a sample as a function of incident and scattered angle, polarization and wavelength or energy. A certain sample has a particular arrangement within the unit cell and this will lead to particular relative intensities of the recorded diffraction peaks upon X-ray hitting. Therefore, the unit cell size and geometry may be resolved from the angular positions of the X-ray diffraction results. The resultant diffraction lines with obvious peaks together are called an XRD pattern. Since the wavelength of X-ray is comparable to the size of atoms, they are suited for examining the structural arrangement of atoms and molecules in a wide range of materials. Each crystal has its unique characteristic X-ray diffraction pattern based on Bragg's law:

$$n\lambda = 2d \sin \theta \tag{2.1}$$

Where d is the interplanar spacing, θ is the Bragg angle, n is the order of reflection and λ is the wavelength of the X-rays irradiation.

In this research work, the basic use of XRD was to determine the actual phase of the material by comparing the obtained XRD pattern to the known standard diffraction lines in the Joint Committee on Powder Diffraction Standards (JCPDS) database. Samples were prepared by mounting the sample powder onto a low background glass disk. As the XRD test is non-destructive, the material can be reused for other tests. An X-ray diffractometer (Simens D5000) is shown in Fig. 2.4(a).

2.4.2 Field-emission Scanning Electron Microscopy (FESEM)

The scanning electron microscope (SEM) is a type of the electron microscope that images a sample by scanning it in a raster scan pattern with the excited beam of electrons.
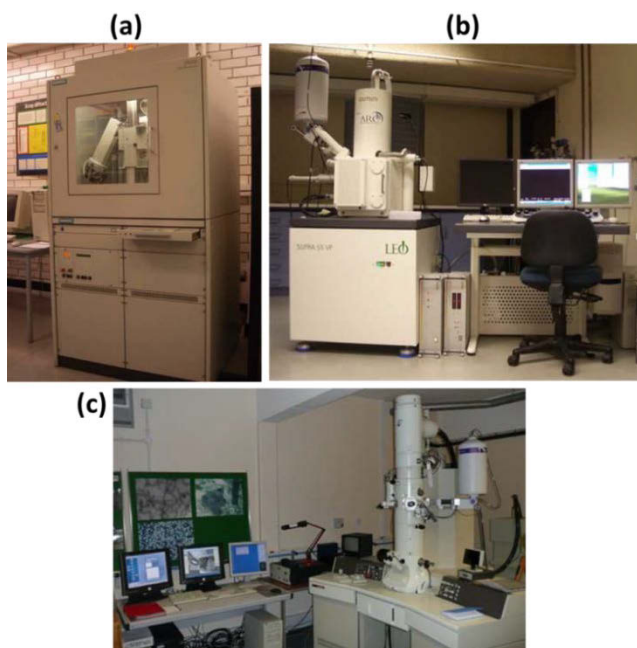
Figure 2.4 (a) An X-ray diffractometer (Simens D5000), (b) FESEM facility (Zeiss Supra 55 VP) and (c) A commercial TEM setup (JEOL 2011 model).

The electrons interact with the atoms that make up the sample producing signals that contain information about the sample's surface morphology. FESEM is often used to obtain high magnification images to examine the details within nanostructured materials

(around 1 nm in size). In this work, FESEM was employed to characterize the morphology and surface structure of as pre-pared electrode materials. Its high-efficiency in-lens detector produces exceptional quality scanning electron images. The FESEM specimens can be prepared by spreading sample powder directly onto the carbon tape or dropping the sample isopropanol solution onto the silicon substrates, and then air drying. Figure 2.4(b) displays a typical FESEM facility (Zeiss Supra 55 VP).

2.4.3 Transmission Electron Microscopy (TEM)

Transmission Electron Microscopy is a microscopy technique, where a beam of electrons is transmitted through an ultra thin sample on a copper grid, interacting with the sample as the electrons pass through to generate images.
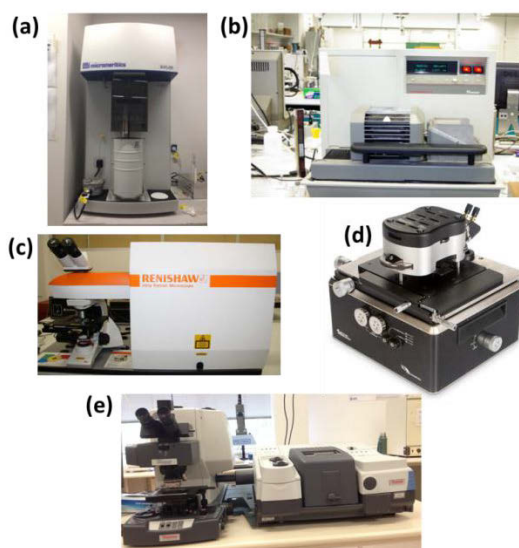
Figure 2.5 (a) A Micromeritics 3 Flex^{TM} surface characterization analyzer, (b) TGA Analyzer (SDT 2960 model, TA Instrument), (c) A Renishaw in Via Raman Microscope (d) A MFP-3D-SA AFM facility and (e) FTIR.

TEM is capable of imaging at a very high resolution. Thus, some detailed features of nanomaterials such as crystal orientation and electronic structure can be observed. In the electron diffraction patter, each ring represents the electron diffraction from different lattice planes. The lattice planes are indexed by matching the calculated d, the

inter-planer spacing, with the standard d-spacings from powder diffraction file (PDF) cards. Figure 2.4(c) presents a commercial TEM setup (JEOL 2011 model).

2.4.4 Brunauer-Emmett-Teller (BET) nitrogen adsorption-desorption isotherms

Brunauer-Emmett-Teller (BET) and Barrett-Joyner-Halenda (BJH) method are used to determine surface area, pore size and pore volume of the desired materials. The abbreviated terms BET and BJH are named from the initials of the family names of those inventors. Bet analysis examines the external area and pore area of the materials to determine the total specific surface area those developers. BET analysis examines the external area and pore area of the materials to determine the total specific surface area in m^2 g^{-1} by nitrogen multilayer adsorption isotherms. BJH analysis can also be employed to determine pore area and specific pore volume using nitrogen adsorption and desorption techniques to characterize pore size distribution of the sample. In this study, nitrogen adsorption and desorption isotherms were measured by using a Micromeritics 3 Flex^{TM} surface characterization analyzer at 77 K, as shown in Fig. 2.5 (a)

2.4.5 Thermogravimetric Analysis

Thermogravimetric analysis or thermal gravimetric analysis (TGA) is a type of measurement to determine the weight changes of samples associated with changes in temperature in a controlled atmosphere. This analysis accurately detects the weight of the sample as temperature elevates, drawing a continuous line to identify weight loss processes in relation to the chemical reactions occurring. TGA can be carried out in the air or noble gasses (e.g. N_2) for different applications. The temperature can increase up to 1000 ^oC with a speed of 5-10 ^oC min^{-1}. Figure 2.5(b) shows a typical TA instrument for TGA.

2.4.6 Raman Spectroscopy

Raman spectroscopy is a non-destructive spectroscopic technique used to study vibrational, rotational and other low-frequency modes in a molecular system. It relies on inelastic scattering, or Raman scattering of monochromatic light, such as laser. The laser light, in the Raman Microscope, is set to focuseon the test sample. This allows interactions of the sample with its vibrations or excitations at a molecular level in the system, resulting in the energy of the laser photons being shifted up or down. The shift in energy gives information about the vibrational modes in the system. The resolution of the Raman spectra can be enhanced by accumulated scans with a longer exposed time. Figure 2.5(c) a Renishaw in Via Raman Microscope.

2.4.7 Atomic Force Microscopy

Atomic force microscopy (AFM) is a very powerful high-resolution scanning probe microscopy. It can be used to examine any type of sample including ceramics, polymers, composites, as well as bio-samples in air or solutions with demonstrated nanoscale resolution. AFM uses electric potentials to detect surface features by conducting cantilevers, which are equipped with high-resolution silicon tips to engage with the sample surface, moving along it in different modes ad returning signals as electric potentials. AFM is used with a Tapping Mode to identify the sheet thickness and particle sizes, which can be evaluated by the relevant height differences upon scanning. Figure 2.5(d) presents one of the most advanced AFM (MFP-3D-SA model) manufactured by Asylum Research.

2.4.8 Fourier Transform Infrared Spectroscopy

Fourier Transform Infrared Spectroscopy (FTIR) is a technique used to obtain an infrared spectrum of absorption of a solid, liquid or gas sample. An FTIR spectrometer simultaneously collects spectral data in a wide spectral range. This confers a significant

advantage over a dispersive spectrometer that measures the intensity over a narrow range of wavelengths at time. Fourier transform infrared (FTIR) spectra were recorded on a Bruker Tensor 27 IR spectrometer using KBr as dispersant between 400 and 4000 cm^{-1}. Figure 2.5(e) shows a Bruker Tensor 27 IR spectrometer.

2.5 Electrode Fabrication and Cell Assembly

2.5.1 Electrode fabrication

The active materials (different nanomaterials in this study) carbon black and polyvinylidene fluoride (PVDF) powders are pre-weighed before mixing them together. The weight ratio of carbon black often varies, in relation to the conductivity of the active materials. The three ingredients are ground thoroughly in a mortar followed by the addition of a small amount of N-methyl pyrrolidinone (NMP) solution to form slurry. For lithium ion batteries, the slurry is then applied (area of coating: 1 cm^2, and a total mass of around 1 mg) uniformly onto a copper foil for anode materials by using a blade or spatula. For supercapacitors, the slurry is applied on pre-treated nickel foam or platinum/titanium foils. The active material loading is around 0.8 mg. The fabricated electrodes are immediately transferred to an electric oven and dried at 100 $^{\circ}$C under vacuum overnight. After the electrode was dried it is pressed at 200 kg cm^{-2} and weighed again before use.

2.5.2 Cell Assembly

2.5.2.1 Lithium ion batteries

The electrochemical tests were conducted under ambient temperature in two electrode coin cells (CR2032) which were assembled in a high purity argon-filled glove box (water and oxygen contents: <1 ppm) (UniLab, MBRAUN, Germany, Fig. 2.6(a)), using the working electrode and the battery grade lithium foil as the counter and reference electrodes. In this work, 1 M $LiPF_6$ in a mixture of ethylene carbonate and dimethyl

carbonate at 1:1 (v/v) was used as the electrolyte solution and a porous polypropylene (Celgard 2300) as the separator. The coin cell assembly was performed in the order of a battery shell, a working electrode with pasted mixture facing up, polypropylene separator, a few drops of the electrolyte, a lithium foil, a stainless steel gasket, a spring and a battery cover. This whole unit was then sealed completely by being crimped with a hand-operated crimping tool.

2.5.2.2 Supercapacitors

For supercapacitor test, beaker-type three-electrode cell was assembled with a working electrode facing a counter electrode (platinum foil) and reference electrode (saturated calomel electrode, SCE), which was placed close to working electrode. In this study 2 M KOH and 1 M Na_2SO_4 were used as an electrolyte. Before electrochemical testing, the three-electrode cell was left for one or two hours so that the electrolyte solution can penetrate into the working electrode.

2.6 Electrochemical Measurements

Electrochemistry is a branch of chemistry that studies chemical reactions that take place in a solution at the interface of an electron conductor and an ionic conductor, and which involve electron transfer between the electrode and the electrolyte or species in solution. In this doctoral study, the electrochemical properties were evaluated by cyclic voltammetry, galvanostatic charge-discharge and electrochemical impedance spectroscopy, which are discussed below.

2.6.1 Cyclic voltammetry

Cyclic voltammetry (CV) is an important tool to study electrochemical reactions (oxidation and reduction) and the electrochemical reversibility. It is a type of potentiodynamic neasurement that can be used to record a relationship of current *vs.* voltage. The measurement is taken when the potential at the working electrode is

ramped linearly versus time (at a particular scan rate) to a set potential and reversed

back to the original potential at the same scan rate.
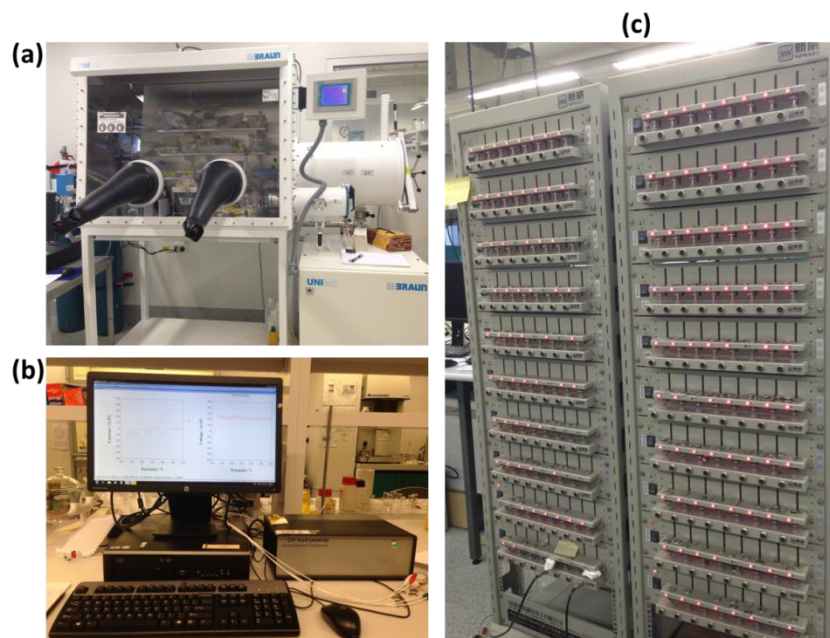
Figure 2.6 (a) A UniLab glove box, manufactured by MBraun, Germany (b) An electrochemistry workstation (CHI660D model) and (c) Neware battery testers.

For lithium ion batteries and supercapacitors, an ideal CV curve for a reversible reaction consists of two peaks opposite each other, as one process is anodic and the other is cathodic, and further confirm the energy storage mechanism involved. In this thesis, CV was conducted on an electrochemical workstation (CHI660C) at different scan rates and voltage ranges at room temperature, which is shown in Fig. 2.6(b).

2.6.2 Galvanostatic charge-discharge

For lithium ion batteries, galvanostatic charge-discharge testing is a commonly used technique to determine the specific capacity, cycling performance and coulombic efficiency of electrode materials. A closely sealed coin cell and a battery tester (Shenzen Neware Co. Ltd.) is often used for the galvanostatic charge-discharge test. Each cell is cycled at a constant current density within a certain voltage range, depending on the

materials used. The controlling software (Neware battery testing system) can monitor the accumulated capacity of each cell upon each cycle. The specific capacity of the electrode material can be calculated based on the specific mass of each electrode. The cycling performance and coulombic efficiency can also be obtained after certain cycles. Figure 2.6(c) presents Neware battery testers with multiple channels.

For three-electrode supercapacitors test cells, the galvanostatic charge-discharge performance is examined by a chronopotentiommetry technique on an electrochemistry work station with an aqueous electrolyte in open circumstances. More details are presented in the following chapters.

2.6.3 Electrochemical Impedance Spectroscopy

Electrochemical impedance spectroscopy (EIS) has been widely used to examine a complex sequence of coupled electrochemical processes, such as electron transfer and mass transfer. A very small amplitude signal is applied to the testing system over a range of frequencies from 0.01 Hz to 100,000 Hz. By monitoring the current response, the variation of resistance with frequency can be examined. The use of EIS often provides an estimation of the internal resistance with an open circuit potential or under other conditions. The data obtained by EIS measurement is expressed graphically in a Nyquist plot. A typical Nyquist plot of the working electrode is shown in Fig. 2.7. The Nyquist plot of lithium ion battery system consists of a compressed semicircle in the medium frequency region which is assigned to be charge transfer resistance (R_{ct}) and an inclined line is the low frequency range is assigned to be Warburg impedance.
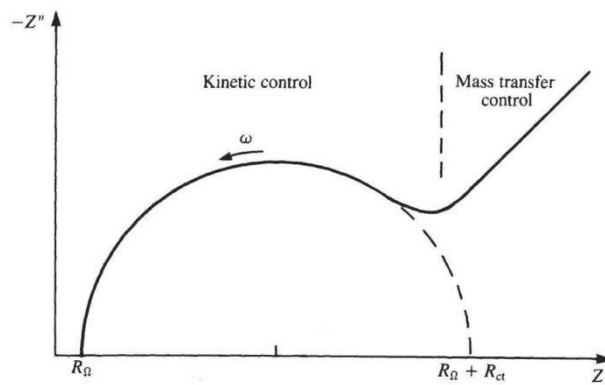
Figure 2.7 Typical Nyquist plot of a simple electrochemical system.

The charge transfer resistance (R_{ct}) qualitatively characterize the reaction speed of the electrode, which can be calculated from EIS measurements. The use of EIS tests to accompany other electrochemical results leads to be a better understanding of the internal electrochemical processes.

Chapter 3 Hydrothermal synthesis of nickel oxide nanosheets for lithium-ion batteries and supercapacitors with excellent performance

3.1 Introduction

The global economy and ecology have been severely affected due to the fast depletion of fossil fuels and climate change. As electrochemical energy storage and conversion devices, supercapacitors and lithium-ion batteries (LIBs) have attracted significant attentions owing to their high power and energy densities. Lithium-ion batteries are dominant power sources for portable electronic devices such as laptop computers, digital cameras and mobile phones [92, 297, 20, 21]. They are also important power sources for future electric vehicles and hybrid electric vehicles [114, 298, 5, 11]. Currently, supercapacitors are widely used in memory back-up systems, consumer electronics, industrial power and energy management [214]. Owing to high-power capability, the supercapacitors are considered to boost the performance of batteries or fuel cells in hybrid electric vehicles to provide the necessary power for acceleration [202, 205].

Recently, transition metal oxides have been extensively investigated as anode materials for lithium-ion batteries owing to their high theoretical capacity (500-1000 mA h g^{-1}) than commercial graphite anode materials [299-302]. Transition metal oxides have also been studied as electrode material for supercapacitors [303-305]. However, these oxides show reduced cycling performance due to their large volume variation during charge-discharge cycling. Nanostructured materials could solve this problem. The performance of nanostructured electrode materials mainly depends on size, shape, morphology and architecture. Among transition metal oxides, NiO has many attractive advantages such

as high theoretical capacity (718 mA h g^{-1}), natural availability, low cost and non-toxicity. The synthesis of nanostructured NiO in various morphologies has widely been reported by different techniques such as thermal decomposition, chemical precipitation, hydrothermal method and template-assisted carbothermal technique [306-311].

In this paper, we describe a simple and facile hydrothermal method to synthesize NiO nanosheets with uniform size distribution. The electrochemical properties of NiO nanosheets for lithium-ion batteries and supercapacitors were systematically investigated by cyclic voltammetry (CV) and the galvanostatic charge-discharge test.

3.2 Experimental

3.2.1 Preparation of NiO nanosheets

Nickel nitrate hexahydrate (Ni(NO$_3$)$_2$·6H$_2$O), urea, and ethylene glycol (EG) of analytical grade (Sigma-Aldrich) were used as received without further purification. In a typical synthesis process, 0.2 g of Ni(NO$_3$)$_2$·6H$_2$O and 0.0826 g urea (molar ratio : 1:2) were dissolved in 15 ml EG. 10 ml of de-ionized (DI) water was added into the above solution with stirring to form a homogeneous solution. The resulting solution was transferred into a 30 ml Teflon-lined stainless steel autoclave, sealed and then heated to 140 $^{\circ}$C for 12 h. After cooling to room temperature, the product was centrifuged, rinsed with DI water and absolute ethanol several times, respectively and finally dried at 60 $^{\circ}$C for 6 h. The NiO nanosheets were obtained by calcination of the as-prepared precursor in air at 300 $^{\circ}$C for 3 h.

3.2.2 Materials Characterization

The phase of NiO nanosheets were analyzed by a GBC MMA X-ray diffractometer (λ = 0.15405 nm). Specific surface area and pore size distribution were determined by

measuring Brunauer-Emmett-Teller (BET) nitrogen adsorption-desorption isotherms and using the Barret-Joyner-Halenda (BJH) method (Micromeritics 3 Flex^{TM} surface characterization analyzer). The morphology of NiO nanosheets was examined by field emission scanning electron microscope (FESEM, Zeiss Supra 55VP). The crystal structure of NiO nanosheets was analysed by transmission electron microscopy (TEM, JEOL 2011 TEM facility). AFM measurements were performed on Dimension 3100 SPM with a tapping mode.

3.2.3 Electrochemical testing

For electrochemical testing, NiO nanosheets were used as the working electrode and lithium metal foil was used as the counter and reference electrodes. 1 M LiPF$_6$ solution dissolved in a mixture of ethylene carbonate and dimethyl carbonate (1:1 by volume) was used as the electrolyte. The working electrodes were fabricated by mixing NiO nanosheets, acetylene black as conducting material and poly(vinylidene fluoride) (PVDF) as a binder in a weight ratio of 70:20:10 for lithium-ion batteries and 80:15:5 for supercapacitors in N-methyl-2-pyrrolidone (NMP) solvent. The slurry was coated uniformly on copper-foil substrate for lithium-ion batteries and nickel foam substrate for supercapacitors (area of loading: 1 cm^2, and active material is around 0.8 mg). The electrodes were then dried in a vacuum oven at 100 ^{o}C for 12 h. The actual mass loading of active material was 0.75 mg cm^{-2} and 0.62 mg cm^2 for lithium-ion batteries and supercapacitors, respectively. CR 2032 coin cells were assembled in a high purity argon-filled glove box (UniLab, MBRAUN, Germany). The cells were galvanostatically discharged and charged at different current densities within a voltage range from 0.01 to 3.0 V. Cyclic voltammetry (CV) test was carried out using a CHI 660C electrochemistry workstation at a scan rate of 0.1 mV s^{-1}. For the measurement of specific capacitance for

supercapacitors, beaker-type three-electrode cells were assembled with the working electrode, the platinum foil as a counter electrode and saturated calomel electrode (SCE) as the reference electrode in 2 M KOH solution. The electrochemical properties were evaluated by CV and galvanostatic charge-discharge using the CHI 660C electrochemistry workstation over the potential range of 0 to 0.5 V vs. SCE.

3.3 Results and Discussion

3.3.1 Structural and morphological analysis

Figure 3.1 shows X-ray diffraction (XRD) patterns of the as-synthesized NiO precursor and NiO nanosheets. Figure 3.1(a) shows the XRD pattern of the $Ni(OH)_2$ precursor.
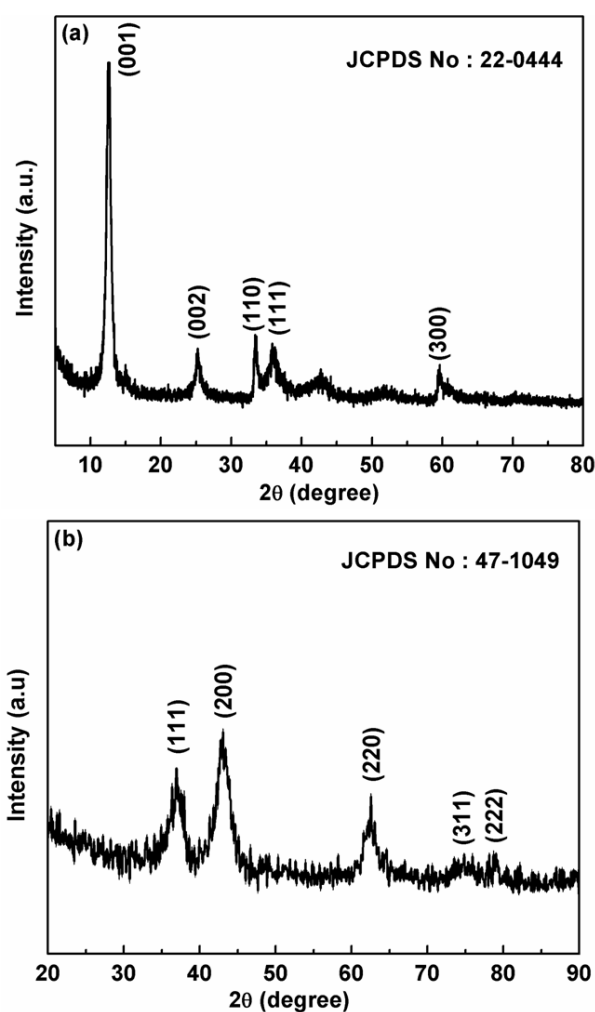
Figure 3.1 XRD patterns of as-synthesized (a) α-Ni(OH)$_2$ and (b) NiO nanosheets.

All diffraction peaks can be indexed to the α-Ni(OH)$_2$ structure (JCPDS card No. 22-0444). Figure 3.1(b) illustrates the XRD pattern of NiO nanosheets, which confirmed the face-centered cubic phase (JCPDS card No. 47-1049). The diffraction peaks can be readily indexed as (111), (200), (220), (311) and (222) crystal planes. The surface area and porosity of NiO nanosheets were investigated by measuring nitrogen adsorption-desorption isotherms and pore size distribution (as shown in Fig. 3.2). The specific surface area of NiO nanosheets was calculated to be 150 m^2 g^{-1} using the BET method. The pore size distribution (the inset in Fig. 3.2) was calculated by Barret-Joyner-Halenda (BJH) method. The pore size distribution displays a mean pore diameter of 27 nm, indicating mesoporous character of NiO nanosheets.
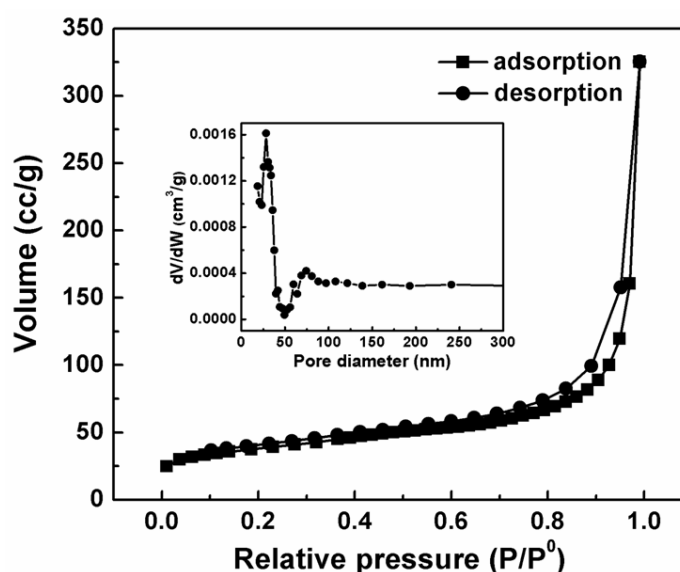
Figure 3.2 The Nitrogen adsorption/desorption isotherm of NiO nanosheets. The inset: corresponding pore size distribution curve.

The morphological characteristics of NiO nanosheets were observed by FESEM. Low magnification FESEM images (Fig. 3.3(a) and 3.3(b)) show the crumpled thin sheets of NiO. Higher magnification SEM images (Fig. 3.3(c) and 3.3(d)) reveal that NiO nanosheets are flexible and have abundant surfaces that resemble silk waves.

The detailed crystal structure of NiO nanosheets was analysed by transmission electron microscopy (TEM). Figure 3.4(a) shows a low magnification TEM image of NiO nanosheets. The as-prepared NiO nanosheets present a crumpled paper shape with large surface area. The corresponding SAED pattern is shown in Fig. 3.4(b) and can be fully indexed to the cubic NiO phase. The high magnification TEM image (Fig. 3.4(c)) displays the porous characteristic of NiO nanosheets.
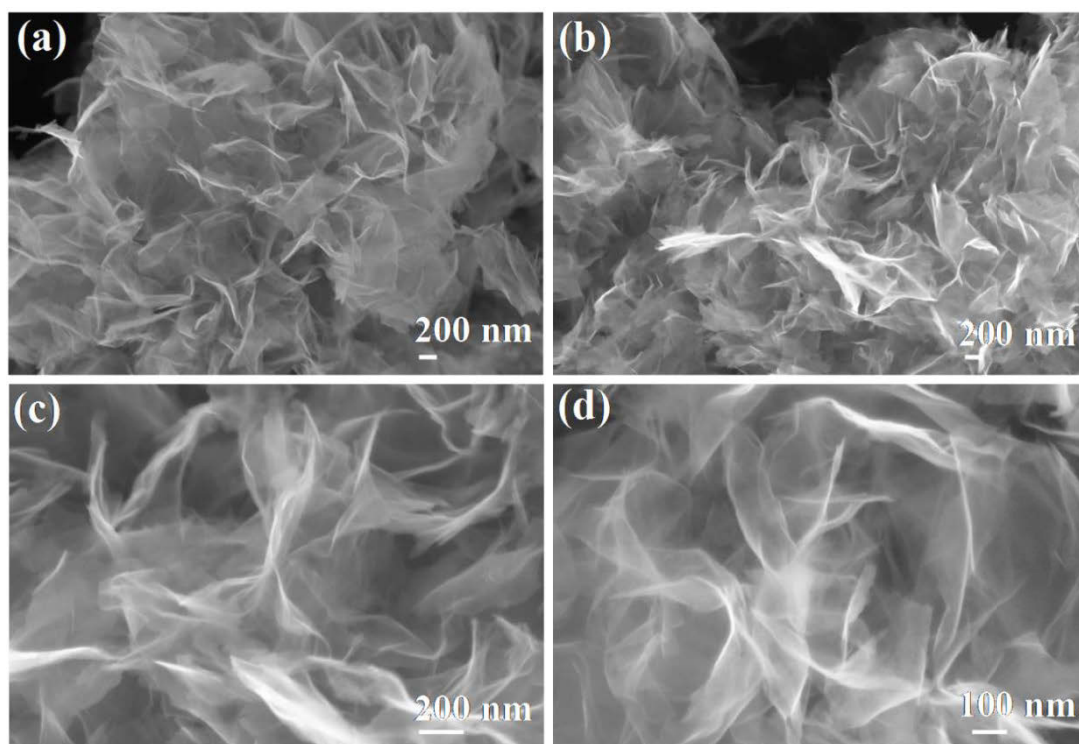
Figure 3.3 FESEM images of NiO nanosheets: (a) and (b) low magnification and (c) and (d) high magnification.

Figure 3.4(d) presents the lattice resolved HRTEM image of NiO nanosheet. The (111) and (200) crystal planes are clearly visible, having the lattice spacings of 0.24 and 0.21 nm, respectively.

In the hydrothermal process, the formation process of NiO precursor involves well-known hydrolysis-precipitation process. As a slow-released pH adjusting agent, urea generates OH^- ions in the reaction medium, which coordinate with Ni^+ to form $Ni(OH)_2$.

The controlled rate of OH⁻ ion generation influences the crystal growth process. The reactions involved in the formation of Ni(OH)$_2$ are as follow [320, 321]:

$$NH_2CONH_2 \rightarrow NH_4^+ + NCO^- \tag{3.1}$$

$$NCO^- + 3H_2O \rightarrow HCO_3^- + NH_4^+ + OH^- \tag{3.2}$$

$$Ni^+ + 2OH^- \rightarrow Ni(OH)_2 \tag{3.3}$$
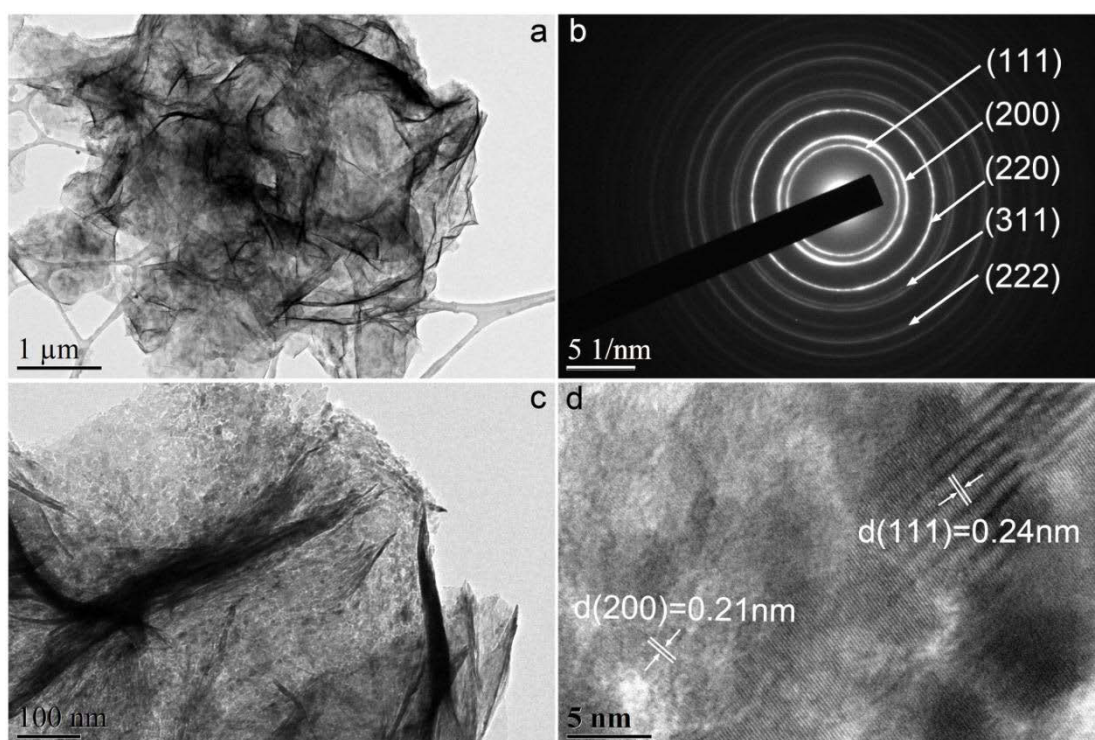
Figure 3.4 (a) Low magnification TEM image of NiO nanosheets. (b) Selected area electron diffraction pattern (SAED). (c) High magnification TEM image (d) Lattice resolved HRTEM image of NiO nanosheets.

With the assistance of ethylene glycol, the hydrothermal product presented the nanosheet structure. The porous thin NiO nanosheets were obtained by calcination of the precursor in air at 300 ^{o}C for 3 h. According to the atomic force microscopy (AFM) in Fig. 3.5, the thickness of the porous nanosheets is about 6 nm.
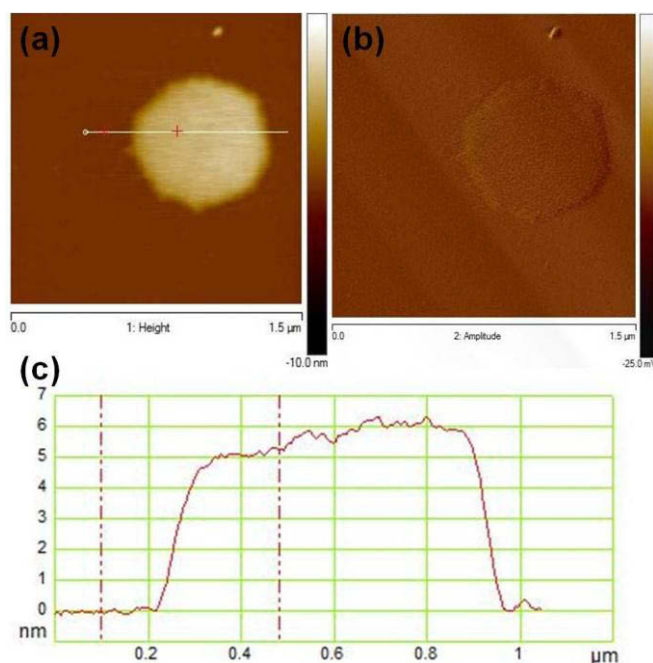
Figure 3.5 Atomic force microscopy images of NiO nanosheets obtained by tapping mode. The topography, amplitude and height profile in (a-c) are included, respectively. The height profiles obtained from the topography images are marked by white line with a red cross. Mica discs were used as the substrate.

3.3.2 Electrochemical performance of NiO nanosheets for lithium ion batteries and supercapacitors

The electrochemical performances of NiO nanosheets as anodes in lithium-ion cells and electrode materials for supercapacitors were evaluated by galvanostatic charge/discharge and cyclic voltammetry measurement. Figure 3.6(a) shows the discharge and charge curves of NiO nanosheet anode in the voltage range of 0.01 to 3.0 V at a current density of 500 mA g^{-1}. The NiO nanosheet electrode delivered the specific capacities of 2187, 1193 and 1096 mA h g^{-1}, in the first, second and fortieth cycles, respectively. In the first discharge process, the extra capacity could be originated from the formation of the solid electrolyte interface (SEI) layer [312, 313]. Figure 3.6(b) shows the capacity versus cycle number for the NiO nanosheet electrode. The NiO electrode maintained a stable capacity and retained 92 % of its initial reversible capacity. The electrode shows the specific capacity of 1096 mA h g^{-1} after 40 cycles,

which is much higher than the previous reports [314-316]. This result indicated that the unique two dimensional (2D) porous layered NiO nanosheet structure could enhance electrochemical properties, owing to the increased surface area.
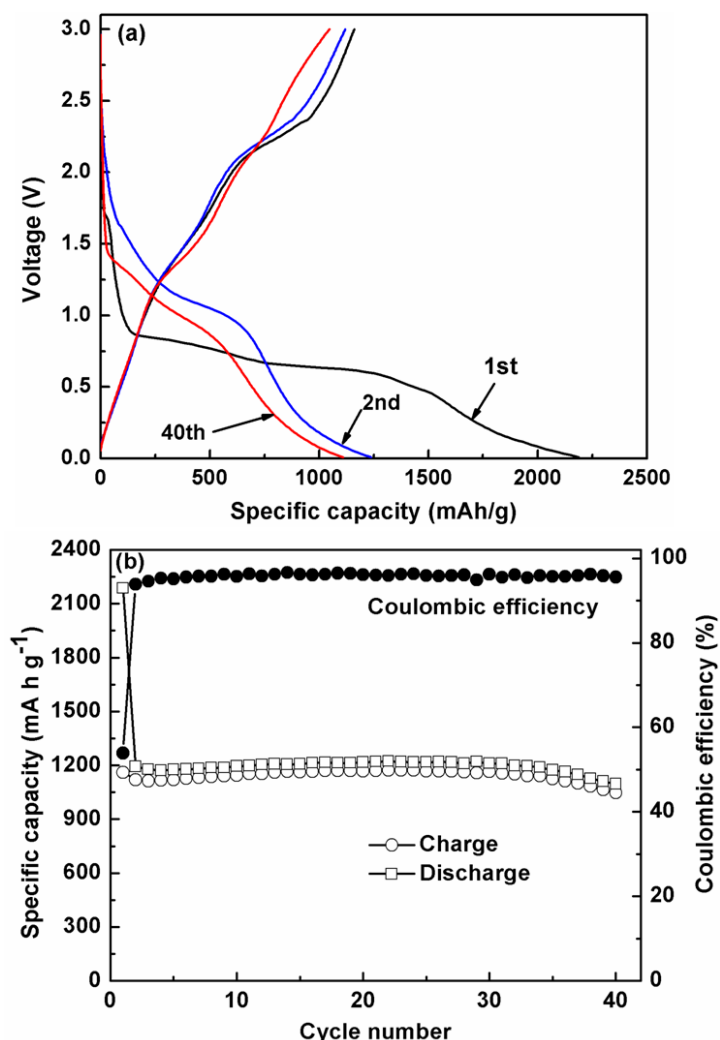
Figure 3.6 Discharge and charge curves (a) and cycle performance and Coulombic efficiency (b) of NiO nanosheet electrode at a current density of 500 mA g^{-1} between 0.01 and 3.0 V.

As a result, large contact interfaces between electrode and electrolyte facilitate the reaction between lithium ion and NiO. The layered nanosheet structure can also effectively alleviate the large volume expansion/contraction of the electrode during cycling. As shown in Fig. 3.6(b) the NiO nanosheet electrode shows an average Coulombic efficiency of 96 % from the second cycle.

The high rate capability of NiO nanosheets were further tested by cycling at different current densities from 100 mA g^{-1} to 2000 mA g^{-1}. As shown in Fig. 3.7, the NiO nanosheet electrode still delivered a lithium storage capacity of 481 mA h g^{-1} at the high current density of 2000 mA g^{-1}. This verified the exceptional rate performance of NiO nanosheets for high power lithium ion batteries.
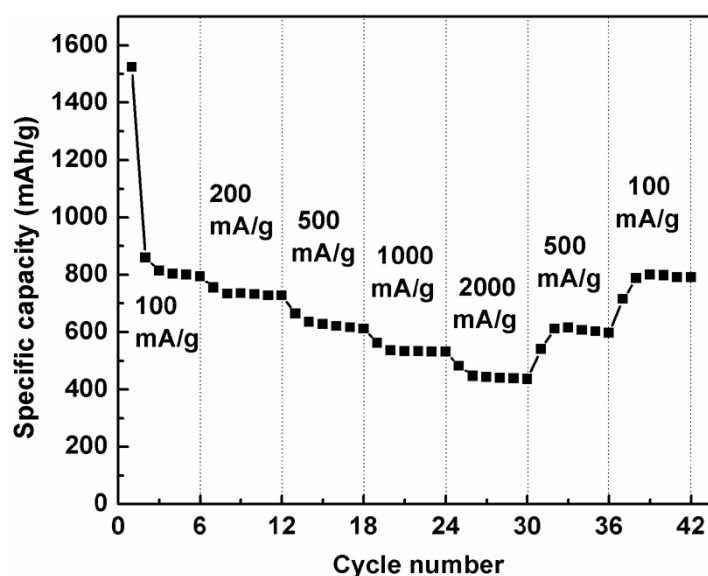
Figure 3.7 Rate capability of the NiO nanosheet electrode examined by multiple step galvanostatic testing at current densities of 100, 200, 500, 1000, 2000 mA g^{-1} and then reverse back to 500 and 100 mA g^{-1}.

When the currents reversed back to low current densities, the discharge capacities can recover to high values, indicating that the integrity of the electrode was maintained. The excellent electrochemical performances of the porous NiO nanosheets could be ascribed to the porous nanosheet architecture. The pores contained in thin nanosheets act as a buffer layer, which can effectively cushion the volume change to alleviate the pulverization during the charge-discharge cycling [312, 319]. Furthermore, 2-D thin nanosheets (6 nm in thickness) offer large electrode/electrolyte contact area and short diffusion path for lithium ions. Therefore, the unique porous nanosheet structure shows high specific capacity, excellent cycling stability and high rate capability.

NiO nanosheets were also tested as electrode materials for supercapacitors. Both galvanostatic charge/discharge and cyclic voltammetry were employed to determine the electrochemical capacitive properties of NiO nanosheets in 2 M KOH electrolyte.
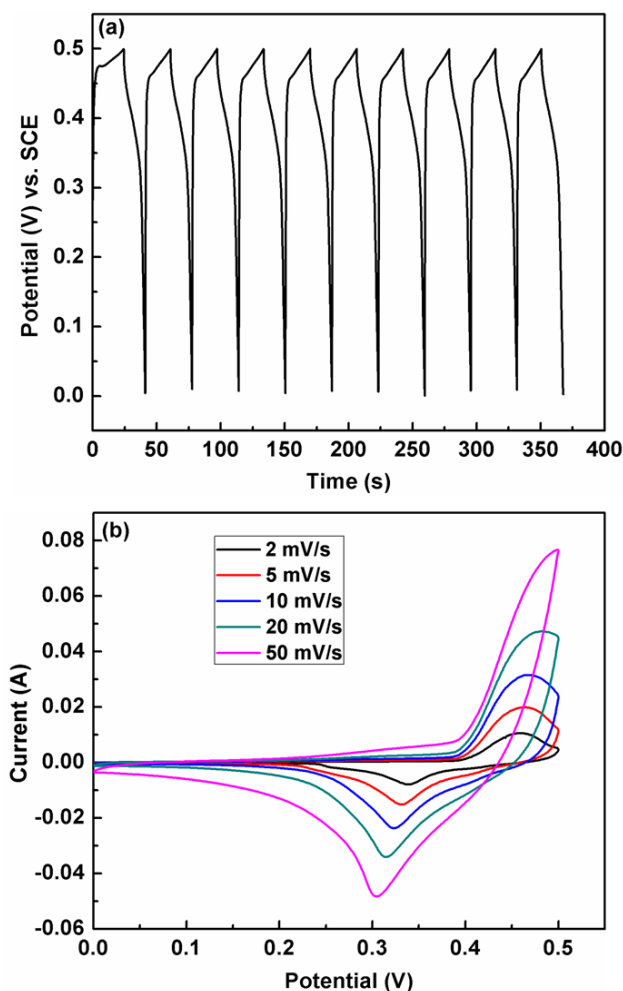
Figure 3.8 (a) Galvanostatic charge/discharge curves at the current density of 20 A g^{-1} and (b) cyclic voltammogram of the NiO nanosheet electrode at different scan rates in 2 M KOH electrolyte.

The galvanostatic charge/discharge cycling was recorded at different current densities within the potential window of 0-0.5 V vs. SCE. Figure 3.8(a) shows the charge-discharge curves for the first 10 cycles at a current density of 20 A g^{-1}. The non-linear shape of the curves indicates the pseudo-capacitance behaviour of the NiO electrode.

The specific capacitance can be calculated from the galvanostatic charge-discharge curve according to the following equation:

$$C = I\Delta t/\Delta Vm \tag{3.4}$$

where I is the applied current, Δt is the discharge time, ΔV is the voltage range and m is the mass of the prepared NiO nanosheets. The specific capacitance value of 999 F g^{-1} was achieved at 20 A g^{-1} for NiO nanosheets.

Figure 3.8(b) displays the CV curves of NiO nanosheet electrode at different scan rates in the potential range of 0-0.5 V. Obviously, a pair of strong redox peaks reveal the faradic pseudocapacitive property based on the surface redox mechanism of Ni^{2+} to Ni^{3+} that occurs at the surface of NiO nanosheets. This can be well expressed by the following mechanism:

$$NiO + OH^- \leftrightarrow NiOOH + e^- \tag{3.5}$$

Notably, as the scan rate increases from 2 to 50 mV s^{-1}, the shape of the CV curves basically remain unchanged, except for the small shift of the peak position, indicating excellent electrochemical reversibility and exceptional high-rate performance.

The specific capacitance of the NiO nanosheet was also calculated from the CV curves by using the equation:

$$C = Q/\upsilon m\Delta V \tag{3.6}$$

Where Q, υ, m and ΔV are the charges obtained by integrating the CV curves, the scanning rate, the mass of the electrode and the potential range of each scan, respectively. The average specific capacitance of NiO nanosheets reached as high as 997 F g^{-1} at a scanning rate of 10 mV s^{-1}. The calculated results from the charge-discharge and CV curves are much higher than previously reported results of NiO materials [317, 237, 318]. This excellent performance of NiO nanosheets could be credited to the high surface area and porous two-dimensional layered structure. The

large surface area and layered structure can provide rapid and effective diffusion paths for redox reactions. The interconnected porous nanosheets also offer additional reservoirs to absorb electrolytes. Moreover, the nanosheet morphology is ideal for fast electrochemical charge-discharge and full utilization of active surfaces. The electrolyte ions can diffuse between the layered structures of nanosheets, leading to the enhanced specific capacitance.

Since a long cycle-life is an important parameter for supercapacitors, long term electrochemical stability test of the NiO nanosheet electrode was conducted for 2000 cycles in 2 M KOH electrolyte at the scanning rate of 50 mV s^{-1}. The excellent cycle stability of the electrode is demonstrated in Fig. 3.9. The decay in specific capacitance is only 2.5 % after 2000 cycles, revealing the excellent stability of the electrode.
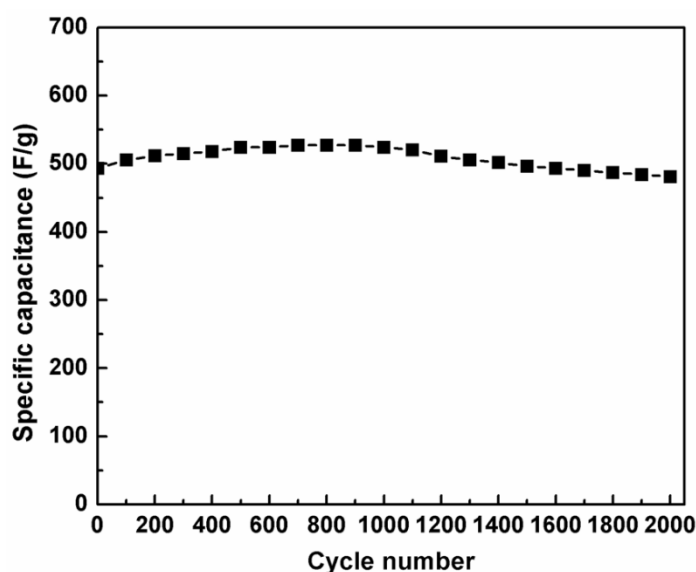
Figure 3.9 Cycling performance of the NiO nanosheet electrode at the scanning rate of 50 mV s^{-1} in 2 M KOH electrolyte.

3.4 Conclusions

We have successfully synthesized NiO nanosheets by a hydrothermal method. The crystal structure and morphology of NiO nanosheets were characterised by XRD,

FESEM, TEM and HRTEM analyses. BET measurement also confirmed the porous feature of NiO nanosheets. The as-synthesized NiO nanosheets were investigated as electrode materials for supercapacitors and as anode materials for lithium ion batteries. The NiO nanosheet electrode exhibited high specific capacitance of 999 F g^{-1} at 20 A g^{-1} and a specific lithium storage capacity of 1096 mA h g^{-1} even after 40 cycles at 500 mA g^{-1}. The results demonstrated that NiO nanosheets could be a promising electrode material for high-performance supercapacitors and lithium ion batteries.

Chapter 4 Microwave-assisted synthesis of spherical β-Ni(OH)₂ superstructures for electrochemical capacitors with excellent cycling stability

4.1 Introduction

It is now emergent demand for advanced electrochemical energy storage systems in parallel with the development of energy production from renewable and green energy sources. Among the different energy storage systems electrochemical capacitors (ECs) and batteries are two most investigated technological systems that lead the state-of-the-art electrochemical energy storage systems [21, 205, 27]. Batteries can store large amount of energy in a lightweight, compact structure and supply suitable power levels for many applications, virtually all mobile electronic devices store energy chemically in them. However, slow charge-discharge rates and short cycle life of current battery technologies limits high-power applications. Electrochemical capacitors (ECs) also known as supercapacitors offer transient but extremely high power for hybrid electric vehicles and mobile electrical systems. It has been considered as one of the most promising energy storage systems because of the higher power densities, faster recharge capabilities and longer cycle lives over batteries and it has the capability to store more energy than conventional capacitors [322, 214, 200]. In general, ECs store energy either between the electrode and electrolyte interfaces as electrical double layer capacitors (EDLCs) or fast and reversible redox reaction between electroactive species in electrolytes and electrodes as pseudo-capacitors [323, 324]. The practical applications of supercapacitors are mostly hampered owing to the lack of low-cost high-performance electrode materials. For instance, the specific capacitance of traditional EDLCs (carbon-based materials) are usually less than 200 F g^{-1}, which cannot meet the constantly

growing demand for peak-power support of electric vehicles and so on [214, 325]. On the other hand, the pseudocapacitors (metal oxides, hydroxides and conducting polymers) offer very high specific capacitance associated with reversible Faradic reactions occurring at the electrode surface and thus the energy density is several times greater than that of EDLCs [326, 202, 327].

To develop high-performance energy storage devices, one of the most advantageous approaches is the specific design of materials with advanced functions. Advancement in supercapacitor technology has mostly benefited from nanoscience. Major research efforts have focused in the design and fabrication of nanostructured electrode materials for high-performance energy storage devices due to the fast-rising demand for high-power applications such as electric vehicles and hybrid electric vehicles. The nanoscale structures create high surface area, which notably enhances the efficiency in utilizing the electrode material and thus improve the performance of the electrode [328]. The development of nanostructured materials, especially metal oxides and hydroxides are pseudocapacitive materials, which have multiple valence states that are capable of rich redox reactions. Various type of metal oxides and hydroxides, such as RuO_2 [329], NiO [330, 321] Co_3O_4 [331], MnO_2 [332, 333] and $Ni(OH)_2$ [334, 335] and their mixed oxides [336-338] are the most promising candidates for pseudocapacitor electrode materials. Among these materials $Ni(OH)_2$ is of particular interest due to its high specific capacitance, low cost and well-defined electrochemical redox activity [339-341]. Huang et al. fabricated nickel hydroxide electrodes with open-ended hexagonal nanotube arrays and achieved high specific capacitance of 1328 F g^{-1} at the current density of 1 A g^{-1} [334]. Mesoporous nickel hydroxide with a maximum capacitance of 1718 F g^{-1} has been reported by Xing et al. [240]. Ma et al. have described uniform $Ni(OH)_2$ nanostructures by using hydrothermal method. Among them, the flower-like

Ni(OH)$_2$ nanostructures assembled from ultrathin nanoflakes show the maximum specific capacitance of 1715 F g^{-1} at a scan rate of 5 mV s^{-1} [335]. Owing to its excellent electrochemical properties, it has extensive applications in alkaline rechargeable nickel-based batteries [342-345]. Different methods have been reported for the preparation of nanostructured β-Ni(OH)$_2$, such as hydrothermal [346, 347], solvothermal [348, 349], electrodeposition [340], chemical precipitation [350, 351] and sonochemical [352] methods. Recently, a microwave method has also gained tremendous attention due to its homogeneous thermal transmission and short heating time [353, 354]. Over the past few years, nano/micro superstructures constructed by nanometer-sized building blocks have been established to be one of the best materials for ECs. These hierarchical structures should take over the exclusive benefits of their main building blocks and acquire extra advantages from their superior secondary building blocks. These subunits should provide superstructures with fascinating properties such as increased surface area, easing mechanical stress, assisting the diffusion of foreign substances throughout the bulk material and so on [355, 356]. Therefore, an active material with superior surface properties and high capacitive performance is indispensable for the development of advanced supercapacitor device [357, 358].

In this paper, we reported the synthesis of uniform micro-sized spherical β-Ni(OH)$_2$, which is consisted of 2D nanosheets through a single step template free microwave method and investigated as electrochemical pseudo-capacitive materials for potential energy storage applications.

4.2 Experimental

4.2.1 Preparation of spherical β-Ni(OH)$_2$

In a typical preparation process of the spherical β-Ni(OH)$_2$, 0.2 g of Ni(NO$_3$)$_2$·6H$_2$O

was dissolved by adding deionized (DI) water (30 ml). The solution was stirred at room temperature, following the addition of 0.275 g of glycine and 0.275 g of Na_2SO_4 salt. Then 1.5 mL of NaOH solution (5 M) was added dropwise under magnetic stirring to form a clear blue solution. The solution was heated in a microwave synthesizer (Model: NOVA-II) at 180 ^{o}C for 30 min and then cooled down to room temperature. The products were collected by filtration, washed with DI water and absolute ethanol for several times and finally dried in an oven at 60 ^{o}C for 6 h.

4.2.2 Materials characterization

The crystallographic information and morphologies of the prepared spherical $Ni(OH)_2$ were investigated using GBC MMA X-ray diffractometer ($\lambda = 0.15405$ nm), a field emission scanning electron microscopy (FESEM, Zeiss Supra 55VP) and transmission electron microscopy (TEM, JEOL 2011 TEM facility). Thermogravimetric analysis (TGA) was carried out by using the 2960 SDT thermal analyser with a temperature ramp of 10 ^{o}C min^{-1} from room temperature to 700 ^{o}C under an air atmosphere. The measurements and analysis of the specific surface area and porosity were performed through Brunauer-Emmett-Teller (BET) nitrogen adsorption-desorption isotherms and Barret-Joyner-Halenda (BJH) method, respectively by using a Micromeritics 3 Flex^{TM} surface characterization analyzer at 77 K. Fourier transform infrared (FTIR) spectra were recorded on a Bruker Tensor 27 IR spectrometer using KBr as dispersant between 400 and 4000 cm^{-1}.

4.2.3 Electrochemical measurements

Electrochemical properties of the as-obtained spherical β-$Ni(OH)_2$ were conducted using a CHI 660C electrochemistry workstation using cyclic voltammetry and chronopotentiometry technology in a three electrodes cell. Where the as-prepared spherical $Ni(OH)_2$ was used as the working electrode, Pt foil as the counter electrode

and saturated calomel electrode (SCE) as the reference electrode in 2 M KOH solution. The working electrodes were prepared by mixing the as-prepared material as an active material, acetylene black as conducting material and polyvinylidene fluoride (PVDF) binder with a weight ratio of 70:20:10. A small amount of N-methyl-2-pyrrolidinone was added to the mixture to form a slurry. The slurry was coated (area of loading: 1 cm^2, and active material is around 0.8 mg) onto pre-treated nickel foam for electrical conductivity and dried under vacuum at 100 ^{o}C for 12 h. The specific capacitance was calculated from both cyclic voltammetry (CV) and galvanostatic charge-discharge measurements.

4.3 Results and discussion

4.3.1 Physical and structural characterization

The crystal structure and purity of the as-prepared spherical $Ni(OH)_2$ was examined by X-ray diffraction (XRD) as shown in Fig. 4.1. All diffraction peaks in Fig. 4.1 can be indexed perfectly to a hexagonal crystal phase of β-$Ni(OH)_2$ (JCPDS card No. 14-0117). No peaks of any other phases or impurities are detected, suggesting the high purity of the as-synthesized β-$Ni(OH)_2$.
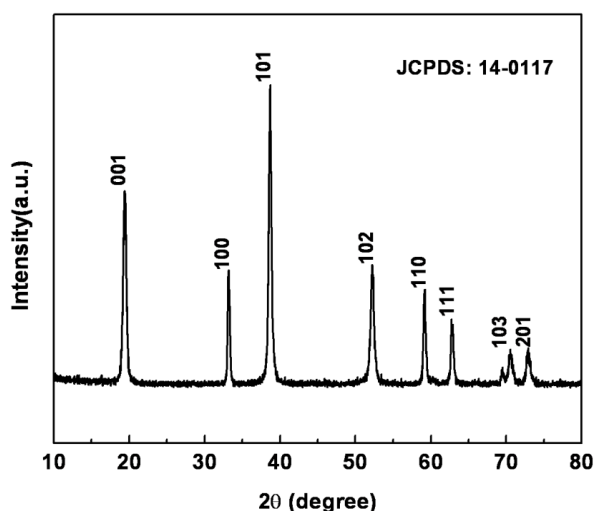
Figure 4.1 XRD pattern of spherical β-$Ni(OH)_2$.

The morphology of the as-prepared spherical β-Ni(OH)$_2$ was examined by FESEM. Figure 4.2(a) and 4.2(b) show the low magnification SEM images of the as-prepared sample, which indicating the formation of uniform numerous micro-sized spherical structures of β-Ni(OH)$_2$ with sizes around 2.0 μm. These micro-sized spheres have 3D hierarchical urchin-like nanostructures. These structures were constructed from 2D nanosheets interconnected with each other and have interior cavities as shown in the high magnification SEM images (Fig. 4.2(c) and 4.2(d)).

We further used transmission electron microscopy (TEM) and selected-area electron diffraction (SAED) patterns to identify the microstructure of as-prepared spherical β-Ni(OH)$_2$ as shown in Fig. 4.3. It can be clearly seen that in general the product is mainly micro-sized spherical shape with the uniform particle size from a low magnification TEM image (Fig. 4.3(a)).
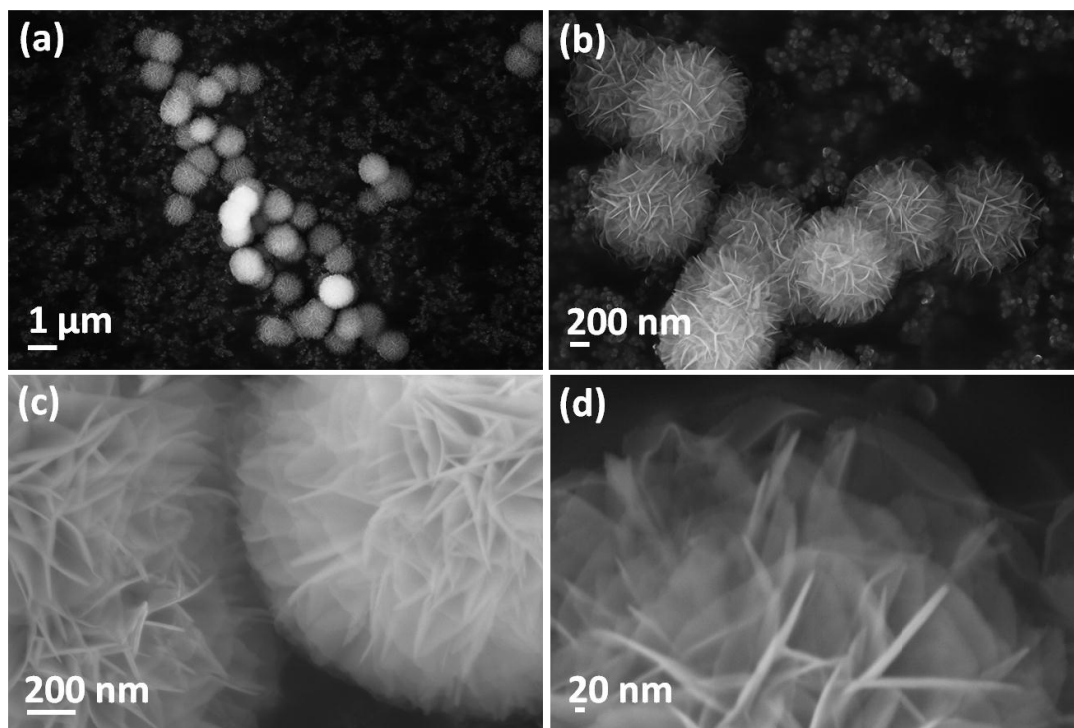
Figure 4.2 FESEM images of spherical β-Ni(OH)$_2$ (a and b) low magnification, (c and d) high magnification.

All the selected area electron diffraction (SAED) patterns rings (Figure 4.3(b)) which were taken from the corresponding single spherical Ni(OH)$_2$ can be readily indexed to the hexagonal Ni(OH)$_2$ crystal structure. The high magnification TEM image (Figure 4.3(c)) illustrated the spherical Ni(OH)$_2$ consisted of nanosheets. Figure 4.3(d) is the image of resolve HRTEM which shows the lattice of the Ni(OH)$_2$ nanocrystal, in which the (001) crystal plane with 0.46 nm d spacing can be observed directly, further confirming the crystal structure of the as-prepared Ni(OH)$_2$.
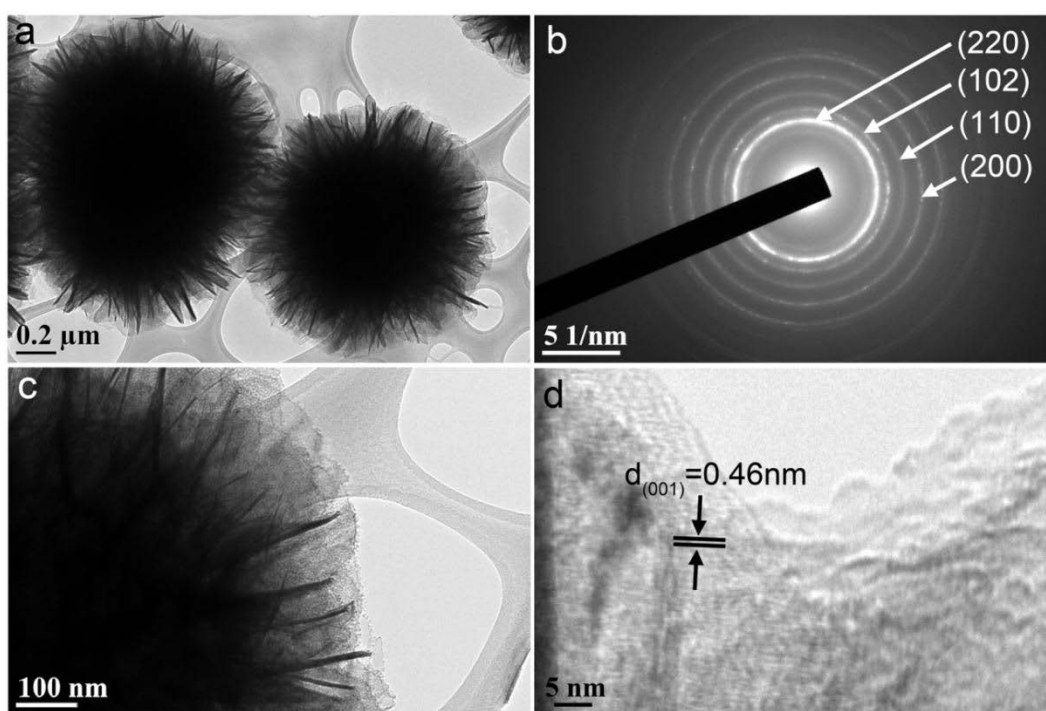
Figure 4.3 (a) Low magnification TEM image of spherical β-Ni(OH)$_2$ (b) is its corresponding selected area electron diffraction patterns (SAED) (c) High magnification TEM image and (d) Lattice resolved HRTEM image.

Thermogravimetric analysis (TGA) of the as-synthesized spherical β-Ni(OH)$_2$ was carried out between 25 and 700 $^{\circ}$C, as shown in Fig. 4.4. The first 5.3 % weight loss before 260 $^{\circ}$C can be ascribed to the loss of absorbed water. The rapid weight loss from 260 $^{\circ}$C to 322 $^{\circ}$C is assigned to the decomposition of Ni(OH)$_2$ to NiO. It is noted that at the temperature range between 500 $^{\circ}$C and 700 $^{\circ}$C there is no obvious weight loss

observed, which indicates the complete decomposition of Ni(OH)$_2$, the absence of any other phases and structural integrity.
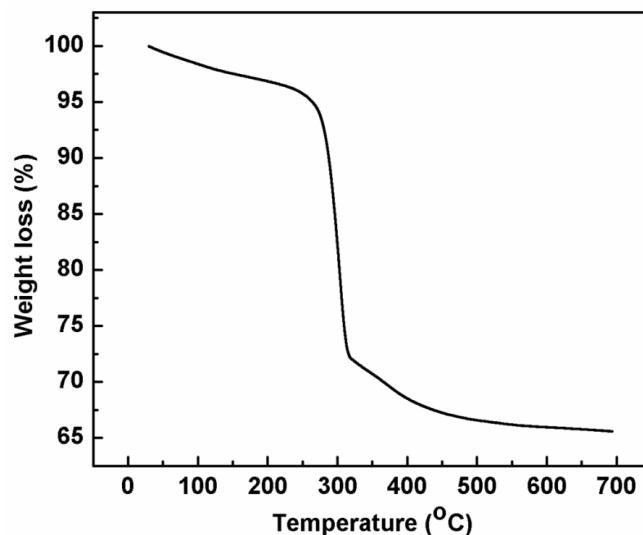
Figure 4.4 TGA curve of as-synthesized spherical β-Ni(OH)$_2$.

Figure 4.5 shows the FTIR spectrum, which reveals chemical information and major functional groups of the as-prepared spherical β-Ni(OH)$_2$. A narrow and sharp peak at 3640 cm^{-1} is related to the υ(OH) stretching vibration of non-hydrogen bonded hydroxyl groups, which confirms the brucite structure of β-Ni(OH)$_2$ phase. The broad band at 3444 cm^{-1} is assigned to the O-H stretching vibration of interlayer water molecules and hydrogen bound hydroxyl groups. A strong absorption at 1636 cm^{-1} can also be attributed to the stretching and bending modes of surface-adsorbed water molecules [359]. The peak at 624 cm^{-1} is characteristic of the hydroxyl group lattice vibration δ(OH) and the absorption 462 cm^{-1} corresponding to the stretching vibration of Ni-OH (υ $_{Ni-OH}$) [359]. The peak at 1383 cm^{-1} could be attributed to a trace surface adsorption of nitrate (NO$_3^-$) ions originating from the starting nickel nitrate. Due to the basicity of metal hydroxides, it is expected to absorb atmospheric carbon dioxide and the peaks

observed at 1636 cm^{-1}, 1479 cm^{-1} and 1064 cm^{-1} are assigned to the presence of carbonate anions on the surface of spherical β-Ni(OH)$_2$ [350].
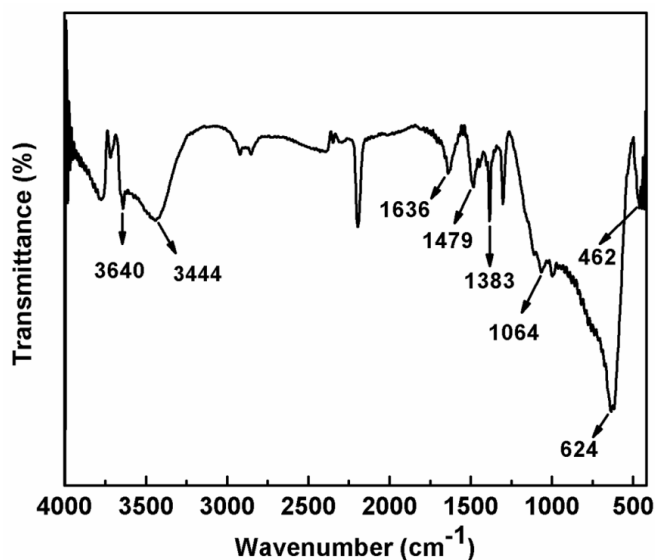
Figure 4.5 FTIR spectrum of the prepared spherical β-Ni(OH)$_2$.

The specific surface area and porous nature of the as-prepared spherical β-Ni(OH)$_2$ were studied by N$_2$ adsorption and desorption measurements, as presented in Fig. 4.6. From Fig. 4.6 we can observe that the curve can be classified as typical Langmuir type IV isotherms with an obvious hysteresis loop, indicating that the material has mesoporous structure [360]. The mesoporous structure was further supported by the BJH pore size distribution data shown in the inset of Fig. 4.6. The pore size distribution exposes with a mean pore diameter of 2.4 nm. The BET surface area of the spherical β-Ni(OH)$_2$ are calculated to be around 76 m^2 g^{-1}. Such large surface area and mesoporous structure can facilitate the transfer of ions and electrons at the electrode/electrolyte interface and are considered to be very suitable for application in supercapacitors.
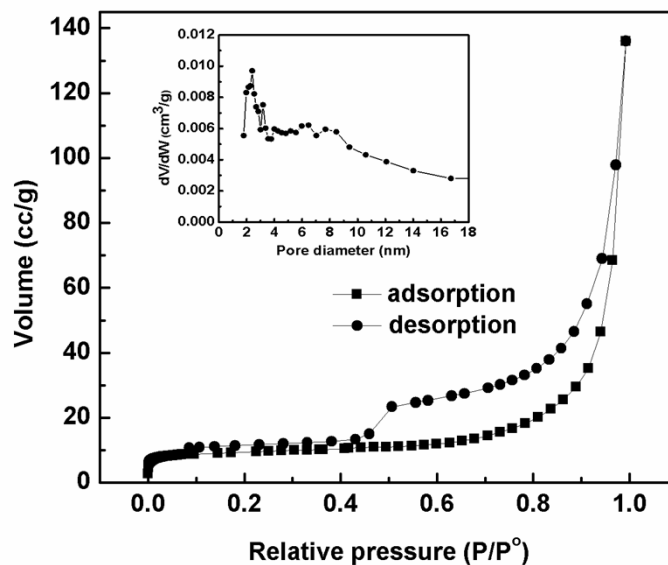
Figure 4.6 Nitrogen adsorption and desorption isotherm and pore size distribution curve of spherical β-Ni(OH)$_2$.

4.3.2 Electrochemical properties for supercapacitors

The electrochemical properties of spherical β-Ni(OH)$_2$ as electrode material for supercapacitors were investigated. To evaluate the electrochemical properties cyclic voltammetry (CV) and chronopotentiometry measurements were carried out in a three-electrode cell. Figure 4.7(a) gives the galvanostatic charge-discharge profiles in an aqueous 2 M KOH electrolyte between 0 and 0.4 V (*vs.* SCE) at different current densities ranging from 1 A g^{-1} to 10 A g^{-1}. The nonlinear shape of charge-discharge curves confirmed the pseudocapacitive behaviour of β-Ni(OH)$_2$. The specific capacitance can be calculated by the formula, $C = I\Delta t/m\Delta V$, in which I is the discharge current, Δt refers the discharge time, m denotes the mass of the active material and ΔV represents the voltage window. Hence, the calculated specific capacitances are 2147, 1775, 1437 and 975 F g^{-1} corresponding to discharge current densities of 1, 2, 5, 10 A g^{-1}, respectively. Figure 4.7(b) shows the representative CV curves of spherical β-Ni(OH)$_2$ electrode tested in an aqueous solution of 2 M KOH electrolyte at different scan rates within the potential window of 0 to 0.5 V (*vs.* SCE). In all of the CV curves, a

pair of redox peaks are clearly observed. Moreover, the shapes of the CV curves are well distinguished from that of the EDLC, which reveals the energy storage mechanism of β-Ni(OH)$_2$ primarily originates from faradic redox reactions. At the scan rate of 2 mV s^{-1} the anodic peak (positive current density) observed around 0.3V (*vs.* SCE) indicates an oxidation of Ni(OH)$_2$ to NiOOH, whereas the cathodic peak (negative current density) detected around 0.17 V (*vs.* SCE) corresponds to the reverse process. It is well recognized that the surface Faradic reaction for Ni(OH)$_2$ electrode material will proceed according to the following reaction: [361]

$$Ni(OH)_2 + OH^- \leftrightarrow NiOOH + H_2O + e^- \tag{4.1}$$
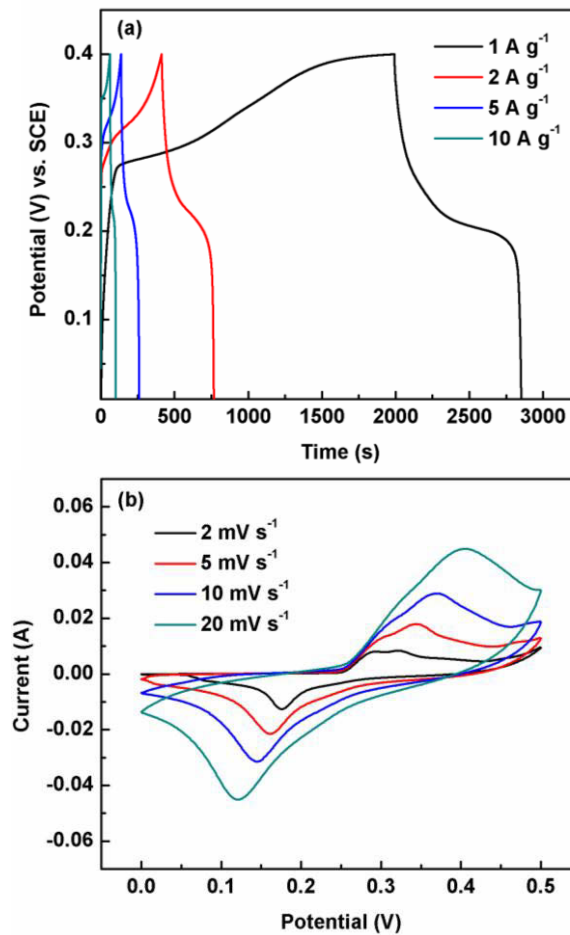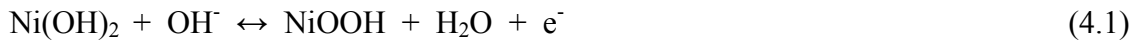
Figure 4.7 (a) Galvanostatic charge/discharge curves at different current densities (1 to 10 A g^{-1}) and (b) CV curves at various scan rates ranging from 2 to 50 mV s^{-1} for the spherical β-Ni(OH)$_2$ electrode in 2 M KOH electrolyte.

When the scan rates increase from 2 to 20 mV s^{-1} the shape of the CV curves does not change significantly, which reveals excellent electrochemical reversibility of the electrode owing to the facile ion diffusion and good adsorption behaviour of β-Ni(OH)$_2$ electrode. The corresponding specific capacitance was also calculated from the CV curves according to the equation, C = Q/υmΔV, where Q is the charge obtained by integrating the CV curves, υ is the scan rate, m is the mass of active material and ΔV is the potential window of each scan. According to the CV curves the calculated values to be 1909, 1720, 1369 and 1051 F g^{-1} at the scan rate of 2, 5, 10, and 20 mV s^{-1}, respectively.
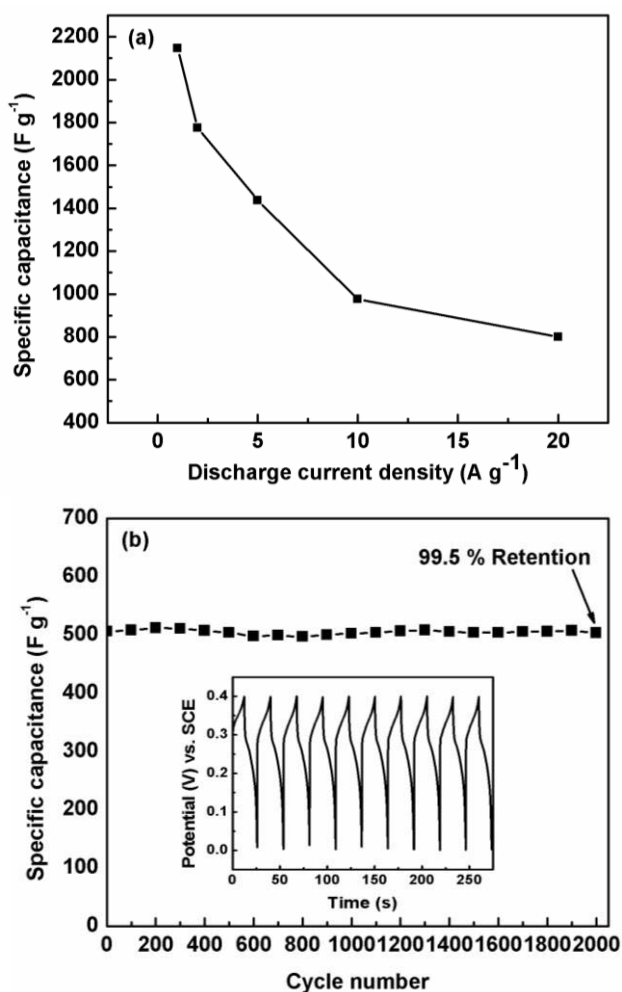
Figure 4.8 (a) Specific capacitance at various discharge current densities and (b) cycling performance of spherical β-Ni(OH)$_2$ at a scan rate of 50 mV s^{-1}. The charge and discharge curves of β-Ni(OH)$_2$ for the first ten cycles (the inset in Fig. 8(b)).

The specific capacitance determined from both charge-discharge and CV curves is much higher than the previously reported β-Ni(OH)$_2$ nanoflakes [335], β-Ni(OH)$_2$ nanoparticles [340] and mesoporous nickel hydroxide [240]. It is well-known that the morphologies of the material play an important role in electrochemical performances. The improved specific capacitance is mainly attributed to the effective utilization of spherical β-Ni(OH)$_2$. The high specific capacitance can be attributed to the unique micro-sized spherical structure constructed by nanosheets. The nanosheets provided high specific surface area and effective diffusion channels. These diffusion channels reduce the diffusion length for the electrolyte ions, guarantees rapid contact of electrolyte ions to the large surfaces of electroactive β-Ni(OH)$_2$. The β-Ni(OH)$_2$ consist of nanosheets connected with each other and interior cavities, which act as "ion-buffering reservoirs" and effectively mitigate the volume expansion during charge/discharge cycling. As a result, the unique spherical β-Ni(OH)$_2$ electrode can achieve a high electrochemical utilization even at high current densities and high scan rates.

Figure 4.8(a) shows the specific capacitances of spherical β-Ni(OH)$_2$ electrode at different current densities. When the current density increased from 1 A g^{-1} to 20 A g^{-1} the specific capacitances were noted to decrease. This was due to the presence of inner active sites that were incapable to take part complete redox transitions at high current densities. This suggests that the some areas of the electrode surfaces were unreachable at high current densities [362].

The long-term cycling performance is one of the most significant parameters for practical application of supercapacitors. The spherical β-Ni(OH)$_2$ was further tested by repeating CV tests over 2000 cycles at the scan rate of 50 mV s^{-1} as demonstrated in Fig. 4.8(b). Notably, capacitance deterioration was only 0.5 % after 2000 continuous

cycles, indicating the excellent long-term cycling stability. It is also worth noting that the charge and discharge curves of spherical β-Ni(OH)$_2$ (inset in Fig. 4.8(b)) for the first ten cycles were nearly same at the current density of 20 A g^{-1}, which also confirming the excellent electrochemical reversibility of the β-Ni(OH)$_2$ electrode. Thus, the spherical β-Ni(OH)$_2$ assembled from nanosheets demonstrate superior specific capacitance with excellent cycling stability, making them promising electrode materials for practical applications.

4.4 Conclusions

In summary, we have proposed a simple, but efficient strategy to prepare uniform spherical β-Ni(OH)$_2$ superstructures, which is composed of nanosheets. Such a unique morphology with mesoporous character could facilitate fast ion and electron transport. This could alleviate the volume expansion during OH$^-$ insertion and extraction process and ensures adequate Faradic reactions at high current densities for energy storage. Electrochemical results showed that the   spherical β-Ni(OH)$_2$ demonstrated a high specific capacitance of 2147 F g^{-1} at 1 A g^{-1} and excellent cycling stability (0.5 % capacitance loss after 2000 cycles). Importantly, this facile and cost-effective strategy could be extended to the preparation of other electroactive materials for electrochemical capacitors.

Chapter 5 Microwave synthesis of α-Fe₂O₃ nanoparticles and their lithium storage properties: A comparative study

5.1 Introduction

Among rechargeable batteries lithium-ion batteries (LIBs) have been widely used as a dominant power sources for different electronic devices, such as digital cameras, notebook PCs and cellular phones. There is an ever-increasing demand for high-power lithium-ion batteries (LIBs) for future large-scale applications (such as: electric vehicles, hybrid electric vehicles and plug-in hybrid electric vehicles). To meet this demand, there has been an emergent development of new generation electrode materials with high specific energy density, long cycle life and excellent rate capability [20, 5, 2]. In recent years, nanostructured materials have attracted much attention due to their exceptional shape and size dependant chemical, optical, magnetic and electrical properties [363-365]. Among all semiconductor nanomaterials, α-Fe₂O₃ is the most stable member of iron oxides with n-type semiconducting properties. It has been widely investigated in solar cells [366], water splitting [367], gas sensors [368], environmental treatment [369] and LIBs [370, 371]. Due to their high theoretical specific capacity compared to commercial graphite anode material, transition metal oxides have been widely studied as potential anode materials for LIBs. Among various transition metal oxides, α-Fe₂O₃ has attracted significant interest because of its huge abundance in nature, low cost, environmental benignity and high theoretical specific capacity (1007 mA h g⁻¹) [372-375, 140]. However, in practical application of LIBs, α-Fe₂O₃ suffers from a large volume variation and severe damage to the electrode during electrochemical cycling, which causes rapid capacity loss and poor rate performance.

In order to overcome these limitations, a lot of attempts have been taken to control structure, size and shape of electrode materials. Nanostructured materials have played a vital role in advancing the development to store energy. The nanostructures can not only shorten the transport distance of lithium ions but also increase the contact area between electrolyte and the electrode, which can provide fast electrochemical reactions. They also accommodate the structural strain created due to the Li^+ insertion [27]. Different nanostructures of α-Fe_2O_3 with various morphologies have been synthesized, such as nanosheets [376], nanoparticles [377], nanorods [378], nanotubes [379, 380] nanodiscs [381], nanoflakes [382, 383] and flower-like structures [384, 385]. However, most of these preparation processes are lengthy or quite complicated.

In this study, we synthesized α-Fe_2O_3 nanoparticles with two different sizes via a simple microwave method without further heat treatment. As anode materials for LIBs, the electrochemical properties of these two materials were investigated and compared on the basis of electrochemical performances.

5.2 Experimental

5.2.1 Preparation of Fe_2O_3 nanoparticles

In a typical synthesis of α-Fe_2O_3 small particles, 0.5 mmol of $FeCl_3$, and 5 mmol of urea were dissolved in 40 ml of water followed by the addition of 125 mg of PVP and stirred for 2 h. The resulting mixture was heated in a microwave synthesizer (Model: NOVA-II) at 180 ^{o}C for 30 min. After cooling to room temperature the materials were filtered, washed with de-ionised (DI) water and absolute ethanol several times, respectively. The red products were dried at 80 ^{o}C for 12 h under vacuum. In the synthesis of α-Fe_2O_3 large particles, the process was similar to the synthesis of α-Fe_2O_3 small particles. The

only change was the concentration of the precursor, where 5 mmol of $FeCl_3$ was used instead of 0.5 mmol.

5.2.2 Materials Characterization

The crystalline structure and morphology of the as-prepared materials were characterized by GBC MMA X-ray diffractometer (λ=0.15405 nm), field emission scanning electron microscopy (FESEM, Zeiss Supra 55VP) and transmission electron microscopy (TEM, JEOL 2011 TEM facility). The specific surface area and average pore size was calculated using the Brunauer-Emmett-Teller (BET) method and Barret-Joyner-Halenda (BJH) equation using a Micromeritics 3 Flex^{TM} surface characterization analyser at 77 K.

5.2.3 Electrochemical testing

The electrochemical performances were tested by using CR 2032 coin-type cells at room temperature. The working electrodes were fabricated by mixing 70 wt % of α-Fe_2O_3 (small and large particles) as the active material, 20 wt % of acetylene black as the conductive agent and 10 wt % of polyvinylidene fluoride (PVDF) as a binder in N-methyl-2-pyrrolidone (NMP). The mixed slurry was applied uniformly onto a copper foil substrate (area of loading: 1 cm^2, and active material is around 0.8 mg) and dried at 100 ^{o}C for 12 h under vacuum. The coin cells were assembled in an argon-filled glove box (UniLab, MBRAUN, Germany), where the moisture content and oxygen levels are less than 1 ppm. Battery grade lithium foil was used as the counter and reference electrodes. The electrolyte was 1 M $LiPF_6$ in ethylene carbonate (EC) and diethyl carbonate (DEC) (1:1 by volume). The cyclic voltammogram (CV) was measured using a CHI 660C electrochemistry workstation in the voltage range of 0.01 to 3.0 V (vs Li^+/Li) and at a scan rate of 0.1 mV s^{-1}. The galvanostatic charge-discharge tests were performed by the NEWARE-BTS battery tester with a potential window of 0.01-3.0 V.

The Electrochemical impedance spectra (EIS) were also measured on a CHI 660C electrochemistry workstation in the frequency range from 0.1 MHz to 0.01Hz.

5.3 Results and discussion

5.3.1 Structural and morphological analysis

The phase purities of α-Fe_2O_3 were examined by XRD. Figure 1(a) and 1(b) show the XRD patterns of nanoparticles, obtained from the precursor concentration 0.5 mmol and 5 mmol, respectively.
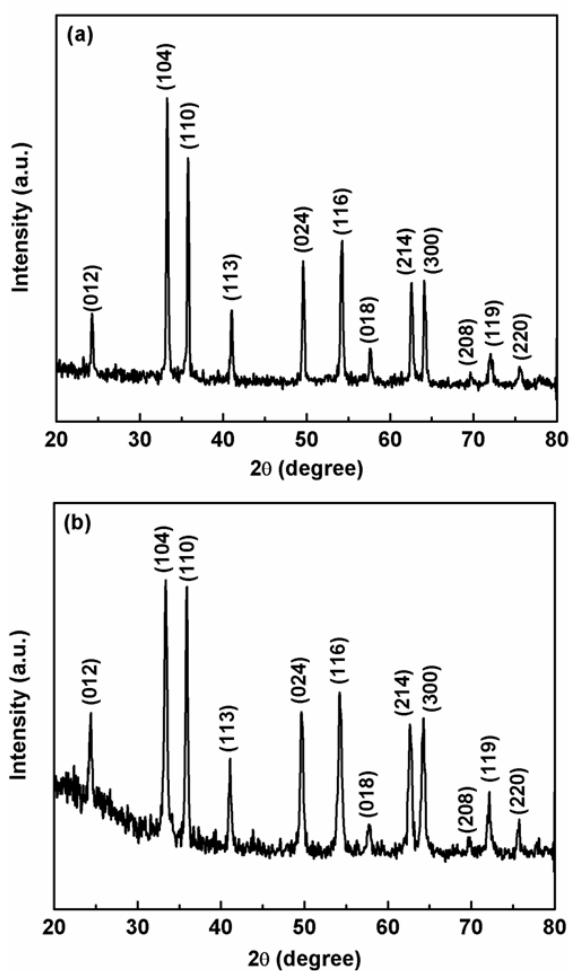
Figure 5.1 XRD patterns of α-Fe_2O_3 (a) small particles (precursor concentration 0.5 mmol) and (b) large particles (precursor concentration 5 mmol).

As shown in Fig. 5.1(a) and 5.1(b), twelve apparent diffraction peaks can be observed for the (012), (104), (110), (113), (024), (116), (018), (214), (300), (208), (119) and

(220) crystal planes of the rhombohedral phase of α-Fe$_2$O$_3$ crystalline structure (JCPDS No. 84-0307). No additional peaks of any other impurities were identified from Fig. 1(a) and (b), indicating that both the materials are pure phases of α-Fe$_2$O$_3$.
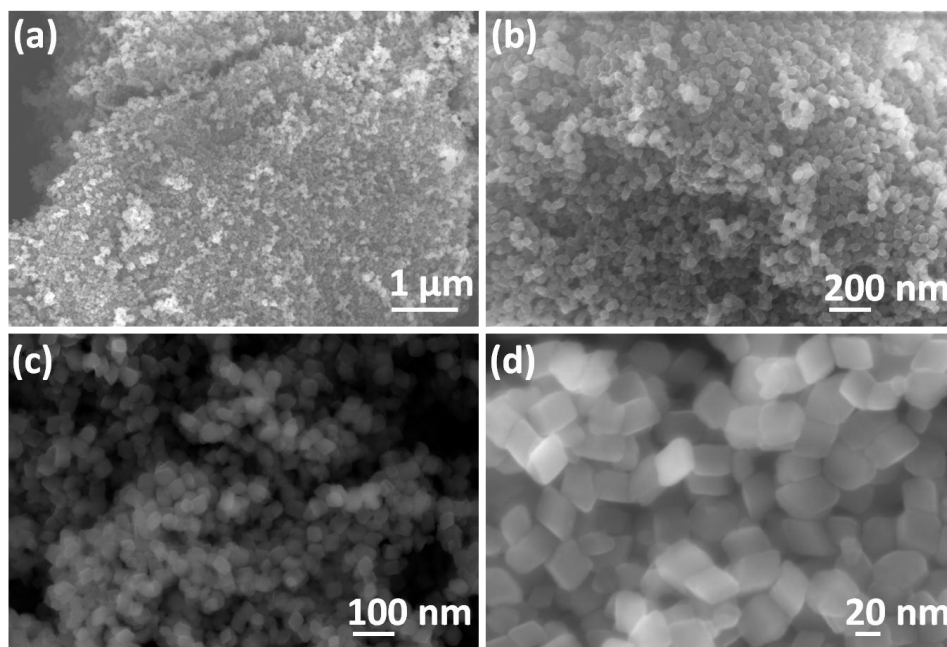
Figure 5.2 FESEM images of α-Fe$_2$O$_3$ small particles (precursor concentration 0.5 mmol) (a), (b) low magnification and (c), (d) high magnification.

The morphologies of the α-Fe$_2$O$_3$ nanoparticles (small and large) are shown in Fig. 5.2 and Fig. 5.3, respectively. The low magnification SEM images (Fig. 5.2(a) and 5.2(b)) show the uniform distribution of small particles. The nanoparticles are around 20-30 nm in size and there was some agglomeration of particles, as revealed by the high magnification SEM images (Fig. 5.2(c) and 5.2(d)). From the low magnification SEM images of large particles as illustrated in Fig. 5.3(a) and 5.3(b), homogeneous distribution of nanoparticles is observed. High magnification SEM images (Fig. 5.3(c) and 5.3(d)) show the particles with the size of 200-300 nm. The surface of the particles is quite rough and well separated from each other.

The influence of precursor concentration was investigated. As shown in Fig. 5.2 and Fig. 5.3, the precursor concentration has a significant impact on the quality of the nanoparticles in terms of size and dispersion. At the low concentration of the precursor (0.5mmol), the size of the particles is relatively small (20-30 nm) and some particles aggregate together, which is clearly observed in Fig. 5.2(c) and 5.2(d) (high magnification SEM images). In solution systems, the nucleation and growth of nanocrystals can be explained by the Von Weimarn theory. In the case of small particles, the precursor concentration (0.5 mmol) is too low compared to the concentration of the precipitation agent (5 mmol). In this low concentration of the precursor, a rush nucleation occurs, which results in aggregation of the small particles. When the precursor concentration increases, the diameter of the particles increased, as shown in Fig. 5.3. The size of the nanoparticles is associated to the formation process of the nanoparticles. It is well recognised that in the liquid system, the development of nanocrystals can be divided into two steps: nucleation and growth of nanocrystals. In general, the nucleation step takes place within a very short time, and the growth step takes a long time. At the same concentration of the precipitation agent (5 mmol), the amount of the nanocrystals entirely depends on the concentration of the precursor. As a result, more nanocrystal nuclei will be generated at the higher precursor concentration (5 mmol). Moreover, in the growth step, the amount of the precursor also increases with its concentration. Thus the sizes of the nanocrystals increased (200-300 nm), as shown in Fig. 5.3 [385].

In the microwave method, the formation process of Fe_2O_3 involves the well-known hydrolysis-precipitation process. Urea is a slow-released pH adjusting precipitation agent, which generates OH^- ions in the reaction medium and react with Fe^{3+} to form FeOOH. The crystal growth process is influenced by the controlled rate of OH^- ions.

The Fe_2O_3 nanoparticles are obtained by the dehydration of FeOOH. The PVP played a significant role, not only as a stabilizer to protect from agglomeration of nanoparticles but also as the structure-directing agent to control the size and morphology of the materials. The possible formation mechanism of Fe_2O_3 nanoparticles are described as follows: [386, 392]

$$NH_2CONH_2 \rightarrow NH_4^+ + NCO^- \tag{5.1}$$

$$NCO^- + 3H_2O \rightarrow HCO_3^- + NH_4^+ + OH^- \tag{5.2}$$

$$Fe^{3+} + 3OH^- \rightarrow FeOOH + H_2O \tag{5.3}$$

$$2FeOOH \rightarrow Fe_2O_3 + H_2O \tag{5.4}$$
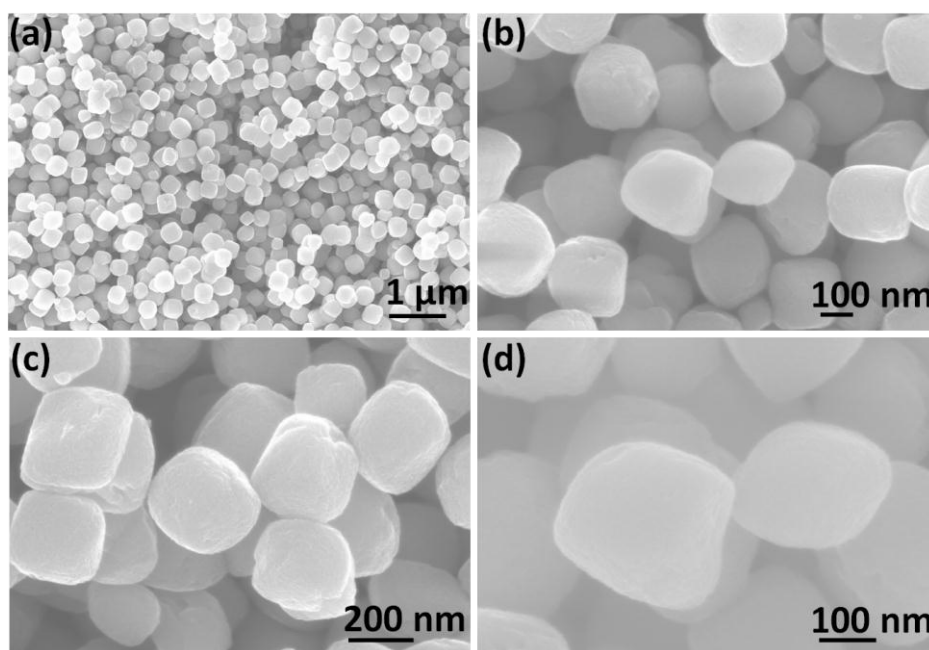
Figure 5.3 FESEM images of α-Fe_2O_3 large particles (precursor concentration 5 mmol) (a), (b) low magnification and (c), (d) high magnification.

Transmission electron microscopy (TEM) was employed to analyse detailed crystal structure of α-Fe_2O_3 nanoparticles. Figure 5.4(a) and 5.5(a) presents the low magnification TEM images of small and large particles. The uniform distribution of

particles is observed with the particle size of 20-30 nm and 200-300 nm, respectively. The selected area electron diffraction pattern (SAED) rings taken from the corresponding single α-Fe$_2$O$_3$ small and large particles (Fig. 5.4(b) and Fig. 5.5(b)) can be readily identified by the crystal structure of α-Fe$_2$O$_3$. As shown in Fig. 5.4(c) and 5.5(c), the high magnification TEM images clearly demonstrate the morphology of the small and large particles. High resolution TEM images (Fig. 5.4(d) and 5.5(d)) display the lattice fringes with the *d*-spacing of 0.29 nm and 0.48 nm with the crystal planes of (220) and (111) for the small and large particles, respectively, further confirming the crystalline feature of α-Fe$_2$O$_3$ nanoparticles.
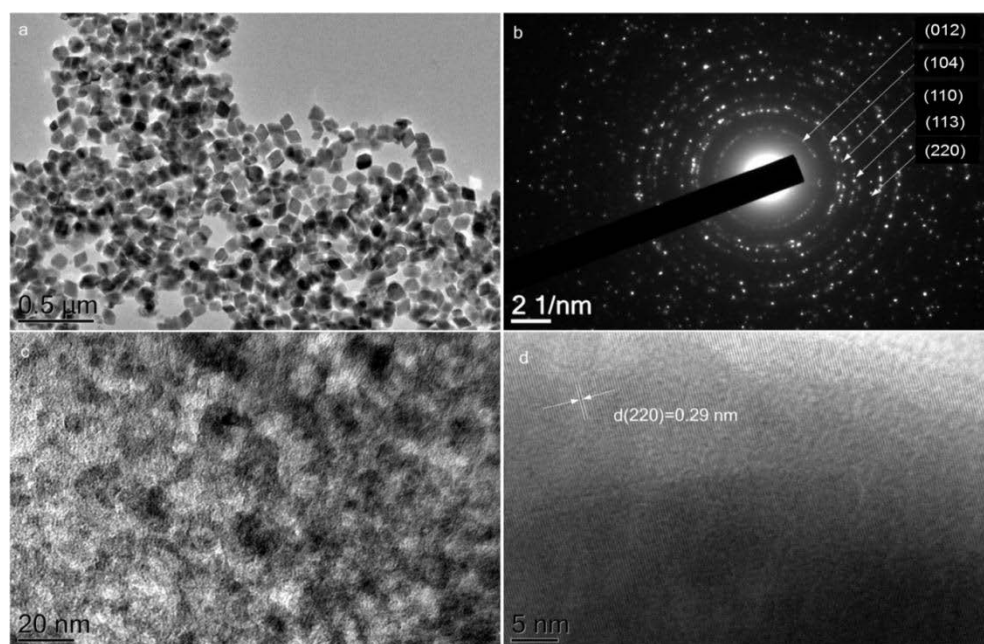
Figure 5.4 (a) Low magnification TEM image of α-Fe$_2$O$_3$ small particles (b) its corresponding selected area electron diffraction patterns (SAED), (c) high magnification TEM image, and (d) lattice resolved HRTEM image.

The nitrogen adsorption-desorption isotherm of α-Fe$_2$O$_3$ nanoparticles are demonstrated in Fig. 5.6. The isotherm of the α-Fe$_2$O$_3$ samples (small and large particles) can be classified as type IV with a distinct hysteresis loops (Fig. 5.6(a) and 5.6(b)) [387].
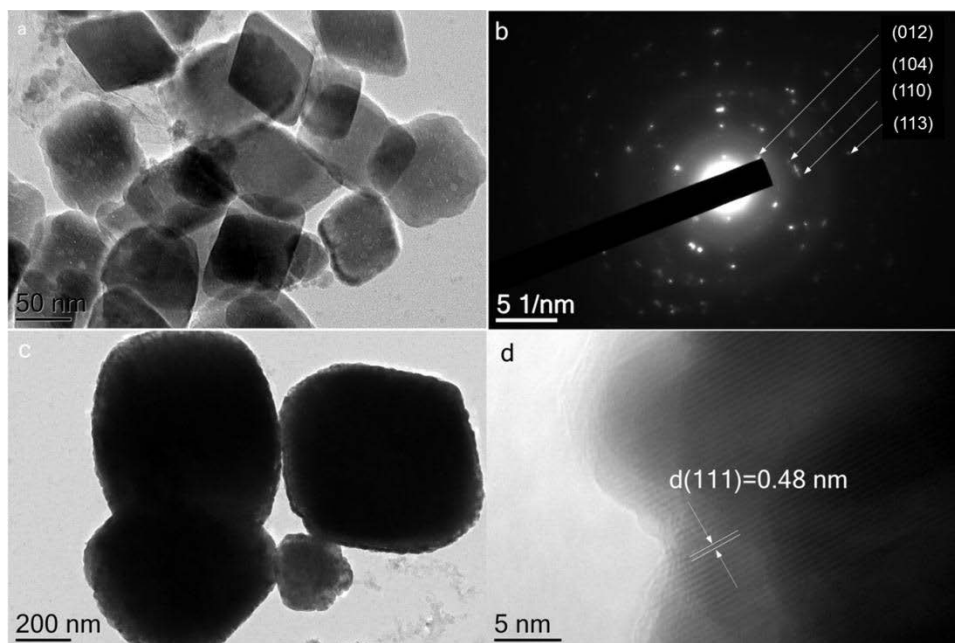
Figure 5.5 (a) Low magnification TEM image of α-Fe$_2$O$_3$ large particles (b) its corresponding selected area electron diffraction patterns (SAED), (c) high magnification TEM image, and (d) lattice resolved HRTEM image.

The small and large size particles show a relatively high specific surface area of 37 m^2 g^{-1} and 25 m^2 g^{-1}, respectively, which offers a sufficient interface to facilitate the electrochemical reactions.

5.3.2 Electrochemical performances

Cyclic voltammetry (CV), galvanostatic charge-discharge measurements and electrochemical impedance were employed to evaluate the electrochemical properties of the as-prepared α-Fe$_2$O$_3$ nanoparticles. Cyclic voltammetry is an important tool to understand the reaction mechanism during discharge and charge process. The CV curves of the α-Fe$_2$O$_3$ nanoparticles (small and large) for the initial three cycles are presented in Fig. 5.7. In the first cycle, the CV curves are clearly different from those for the subsequent cycles and there is no major change observed from the second cycles onwards for both the materials.
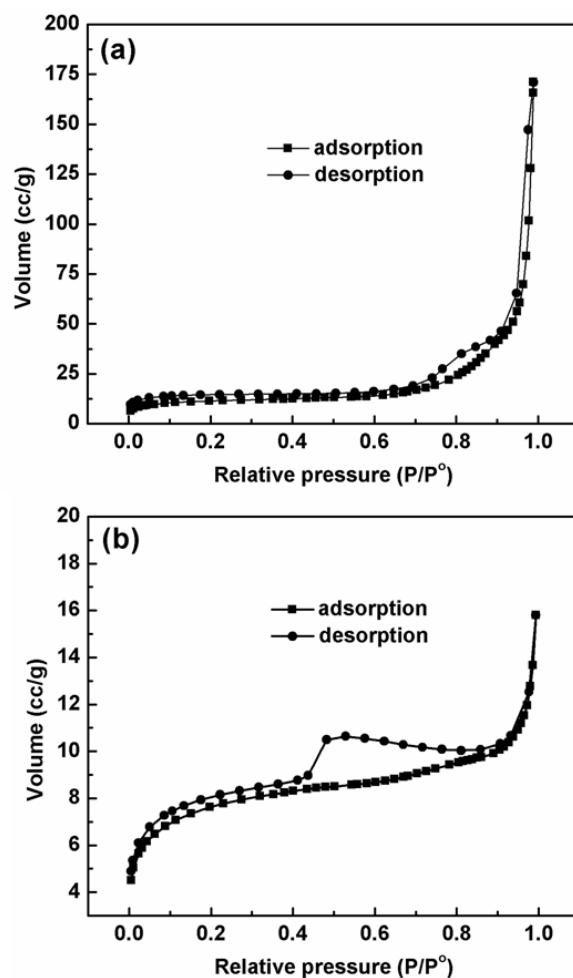
Figure 5.6 Nitrogen adsorption-desorption isotherms of α-Fe$_2$O$_3$ (a) small particles (b) large particles.

In the first cycle of α-Fe$_2$O$_3$ small particles, as shown in Fig. 5.7(a), there is a broad peak at ~0.98 and a sharp reduction peak at ~0.70 V, in the cathodic scan, which is due to the Li$^+$ intercalation into the α-Fe$_2$O$_3$ crystal lattice, the reversible conversion reaction of α-Fe$_2$O$_3$ with metallic lithium to form Li$_2$O and metallic Fe^o and the electrolyte decomposition to form SEI films [140, 388]. In the first anodic scan a broad peak at around 1.80 V is ascribed to the oxidation of Fe^o to Fe^{3+} to re-form the crystalline α-Fe$_2$O$_3$ phase [140].
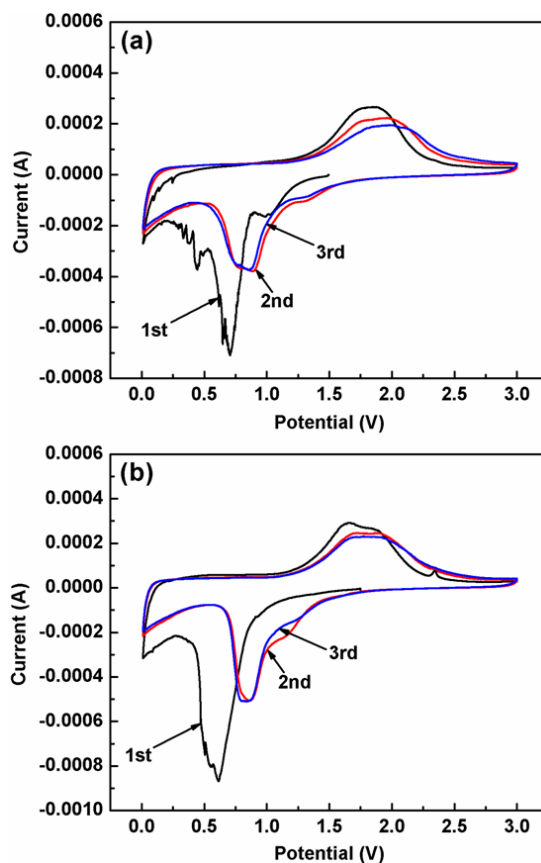
Figure 5.7 Cyclic voltammograms of the electrodes made from α-Fe$_2$O$_3$ (a) small particles (b) large particles at a scan rate of 0.1 mV s^{-1} in the voltage range of 0.01-3.0 V.

During the successive cycles, CV curves overlapped well, indicating good reversibility of α-Fe$_2$O$_3$ nanoparticles during electrochemical reactions. In the first cathodic scan, the α-Fe$_2$O$_3$ large particle electrode (Fig. 5.7(b)) displays a sharp peak at ~0.61 V. Meanwhile, in the anodic process, a broad peak is observed at ~1.64 V. In the following cycles, the CV curves remain unchanged, which also indicates the good reversibility of the electrode.

The first, second and fiftieth charge-discharge voltage profiles of the α-Fe$_2$O$_3$ small particles and large particles are shown in Fig. 5.8. Small particles of α-Fe$_2$O$_3$ show the first discharge capacity of 1649 mA h g^{-1} (Fig. 5.8(a)). The extra capacity possibly comes from the formation of solid electrolyte interphase (SEI) layer on the surface of

the working electrode [389, 390]. The initial charge capacity was measured to be 1103 mA h g^{-1}, corresponding to a coulombic efficiency of 67 %. The charge-discharge profiles of the 2nd and 50th cycle are quite similar to each other, which indicates good reversibility during lithium insertion and extraction processes.
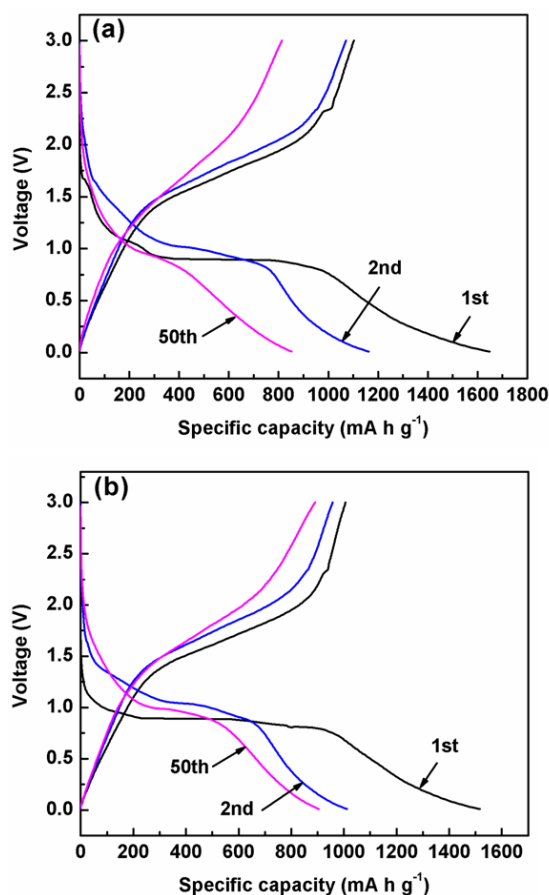
Figure 5.8 Discharge/charge profiles of α-Fe$_2$O$_3$ (a) small particles and (b) big particles at a current density of 100 mA g^{-1}, in the potential range of 0.01-3.0 V.

The electrodes made of α-Fe$_2$O$_3$ large particles also show the similar phenomenon, as presented in Fig. 5.8(b). From the second cycle the average coulombic efficiency is 97 % for both the nanoparticles.

The cycling performances of the electrodes made from small and large particles of α-Fe$_2$O$_3$ are shown in Fig. 5.9. Although, the small particles (Fig. 5.9(a)) showed a very high reversible capacity of 1163 mA h g^{-1} at the current density of 100 mA g^{-1}, the

capacity decreases quickly and after 80 cycles the capacity retained 569 mA h g^{-1}, which is only 49 % of the initial reversible capacity.
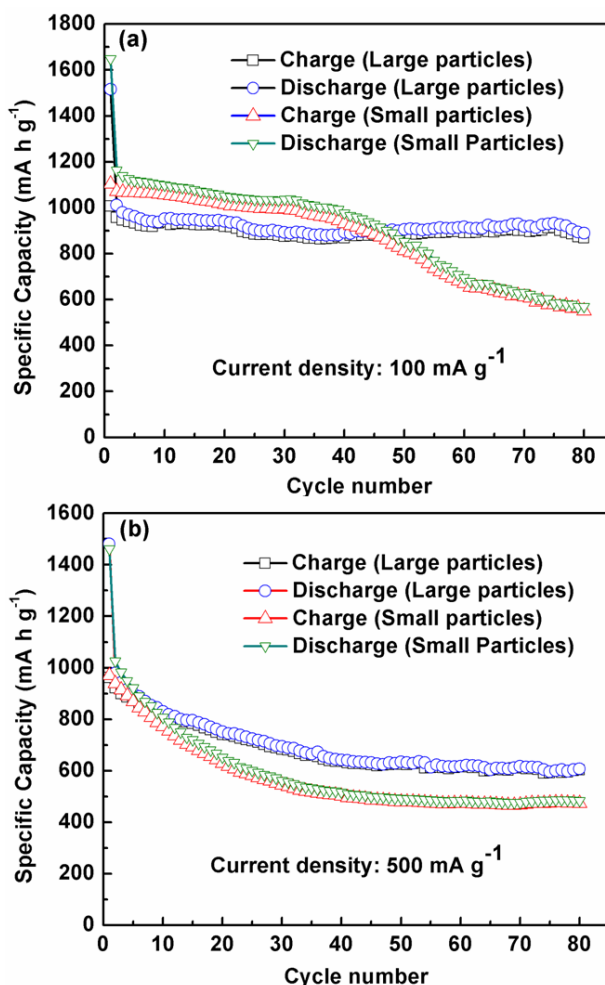
Figure 5.9 Cycling performances of the electrodes made of small and large particles of α-Fe$_2$O$_3$ at the current density of (a) 100 mA g^{-1} and (b) 500 mA g^{-1}.

Compared with the small particles, the large particles of α-Fe$_2$O$_3$ exhibit the lower initial reversible capacity of 1012 mA h g^{-1} and maintained stable cycling performance over 80 cycles. The reversible capacity still retained 889 mA h g^{-1} after 80 cycles, which is 88 % of the initial reversible capacity. As shown in Fig. 5.9(b), the cycling performances of small and big particles of α-Fe$_2$O$_3$ at the high current density of 500 mA g^{-1} were also evaluated. Both electrodes showed a rapid decrease in reversible

capacities but the electrode made of large particles still showed the reversible capacity of 607 mA h g^{-1} compared to the small particles (484 mA h g^{-1}) after 80 cycles.
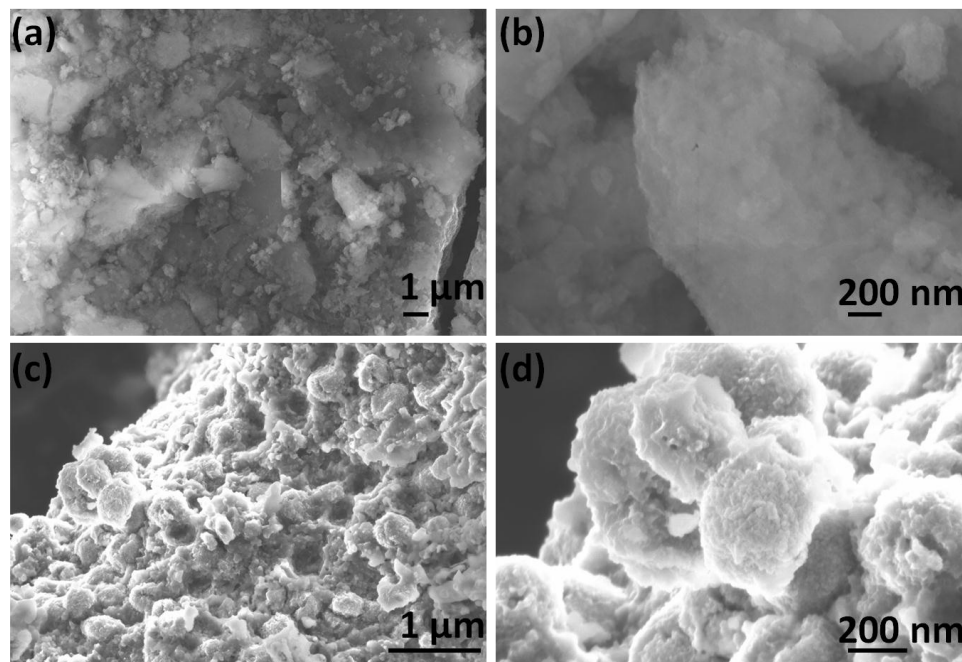
Figure 5.10 FESEM images of α-Fe$_2$O$_3$ nanoparticles after charge-discharge cycling (a), (b) small particles and (c), (d) large particles.

In general, the small particles having larger specific surface area should result in better electrochemical performances than that of the large particles. However, large particles of α-Fe$_2$O$_3$ show better electrochemical performances than small particles. In order to explain this phenomenon, we further examined the electrode after cycling. Figure 5.10 shows the SEM images of small and large particles of α-Fe$_2$O$_3$ after 80 times charge-discharge cycling at the current density of 500 mA g^{-1}. From the Fig. 5.10(a) and 5.10(b), we can see the small particles aggregated together during cycling. Due to the agglomeration, the surface area of small particles decreases, resulting in the insufficient electro active sites for electrochemical reaction. Under this circumstance, the electrolyte cannot enter to the inner side of the electrode leading to a poor electrical contact between the active material and electrolyte, which results in a rapid decrease in specific

capacity. In contrast, the large particles of α-Fe$_2$O$_3$ still preserve their morphology, although they display a little deformation (Fig. 5.10(c) and 5.10(d)). Therefore, when compared to the electrode made of small particles, the large particles of α-Fe$_2$O$_3$ could provide enough spaces to connect electrode and electrolyte. This gave more active sites for Li$^+$ diffusion, shortened the lithium ions transportation paths and efficiently mitigated the volume expansion during lithium intercalation/extraction processes, leading to enhanced electrochemical performance.

The rate capability is also critical in the practical application for LIBs. The rate capabilities of the small and large particles α-Fe$_2$O$_3$ are demonstrated in Fig. 5.11. The electrodes made of small and large particles of α-Fe$_2$O$_3$ were cycled at different current densities from 100 mA g^{-1} to 2000 mA g^{-1}. As shown in Fig. 5.11(a) and 5.11(b), the reversible capacities decrease gradually with the increasing current densities. At the high current density of 2000 mA g^{-1}, the electrodes made of large particles still shows the specific capacity of 619 mA h g^{-1} compared to the small particles (483 mA h g^{-1}). When the current density returns to 500 mA g^{-1} and 100 mA g^{-1}, the capacity of the electrodes did recover almost to the same levels as the previous cycles. However, a little decreasing tendency is observed in the case of small particles (Fig. 5.11(a)), when the current density is reduced back to 500 mA g^{-1} and 100 mA g^{-1}. It is important to note that, the small particles show the less tolerance to high current charge-discharge than the large particles. This further confirms the structural stability of the big particles.

Electrochemical impedance spectra (EIS) were performed to understand the performance of small and large particles of α-Fe$_2$O$_3$. As shown in Fig. 5.12(a) and 5.12(b), the Nyquist plots of α-Fe$_2$O$_3$ electrodes (small and large particles) for fresh cells and after 80 cycles were collected for comparison. The EIS spectra of the

electrodes consist of a depressed semicircle in the high and medium frequency region and a straight line in the low-frequency region. The straight line in the low-frequency region represents the Warburg impedance (Zw), which is related to the solid state diffusion of lithium ions into the bulk of the electrode materials [391].
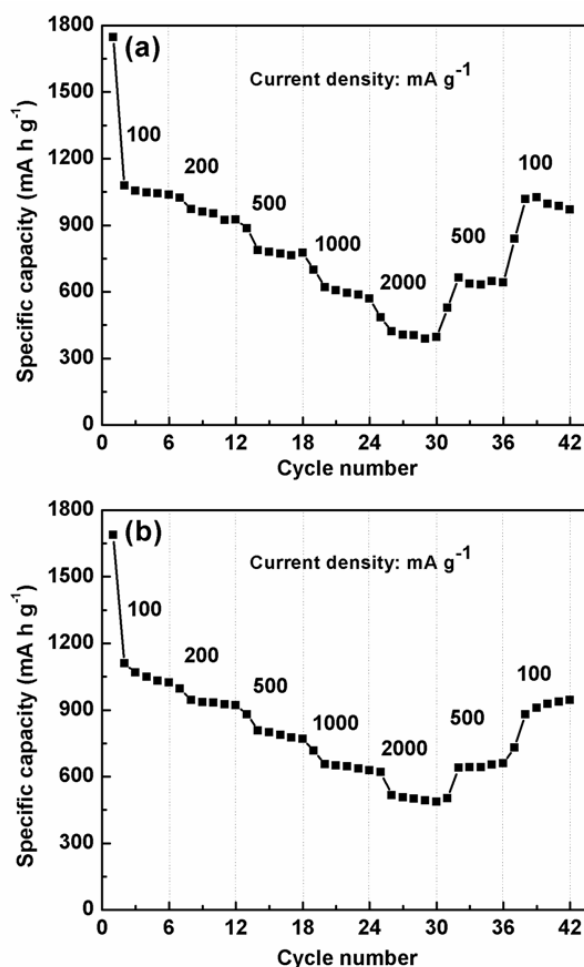
Figure 5.11 Rate performances of the α-Fe$_2$O$_3$ electrodes at different current densities (a) small particles and (b) big particles.

The semicircle in the high to medium frequency region indicates the interfacial charge transfer resistance (R$_{ct}$), relating to charge transfer throughout the electrode-electrolyte interface. For the fresh cells, the R$_{ct}$ of the small particles is lower than that of the big particles as shown in Fig. 5.12(a). In the initial stage, small particles with larger surface area showed better electrochemical performance than large particles. Upon prolonged

cycling, the small particles aggregate together as observed in Fig. 5.10(a) and 5.10(b), which lead to a decrease of electrical conductivity. From the Fig. 5.12(b) we can clearly observe that the R_{ct} of the small particles substantially increased and the R_{ct} of the big particles decreased during cycling.
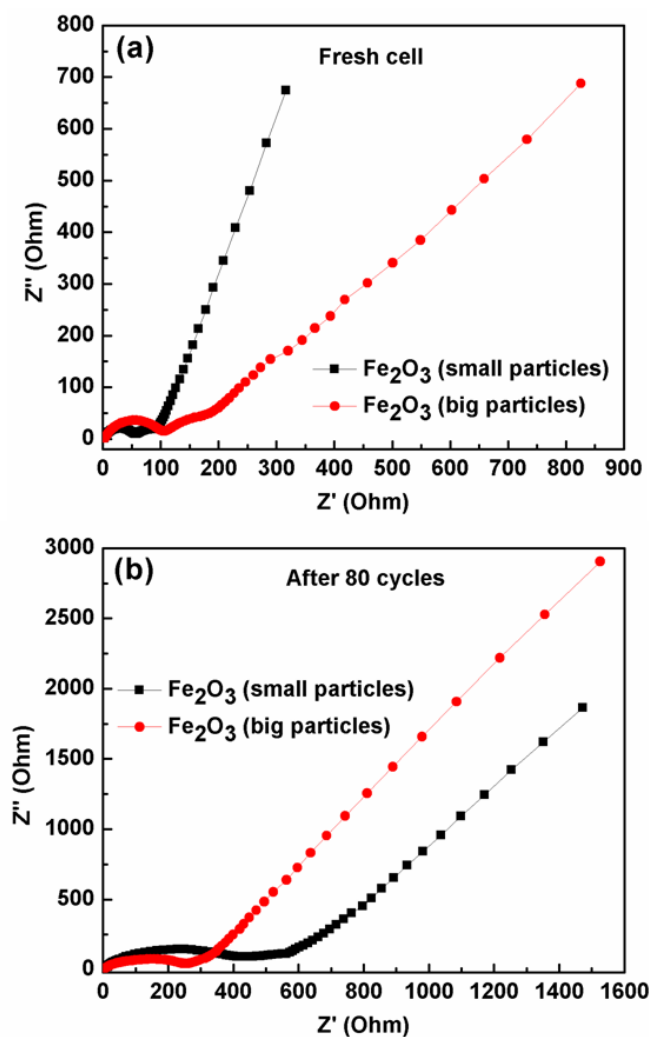
Figure 5.12 Electrochemical impedance spectra of the α-Fe$_2$O$_3$ electrode (small and large particles) (a) fresh cell (b) after 80 cycles.

The R_{ct} of big particles is much lower than that of small particles after 80 cycles, as shown in Fig. 5.12(b). These results indicate that the electrons can transfer more quickly in the electrode made of large particles of α-Fe$_2$O$_3$ and therefore, enhance the lithium storage properties and cycling performance.

5.4 Conclusions

We successfully synthesised α-Fe_2O_3 nanoparticles with two different sizes via a simple microwave method without further thermal treatment. The particle size can be easily controlled by changing the precursor concentration. When used as anode materials for lithium ion batteries both the materials show excellent electrochemical performances. Importantly, large particles of α-Fe_2O_3 exhibited high rate capability and excellent cycling stability (88 % retention after 80 cycles) when compared to the small particles (49 % retention after 80 cycles). The better lithium storage properties of the large particles are attributed to their structural integrity during cycling that has offered adequate spaces for volume expansion during Li^+ insertion/extraction and shortens the diffusion paths of lithium ions.

Chapter 6 Highly porous NiCo$_2$O$_4$ nanoflakes and nanobelts as anode materials for lithium ion batteries with excellent rate capability

6.1 Introduction

The limited traditional energy resources, and the increasing concerns on environmental pollution are the major drive for the development of sustainable and clean energy sources [393-395]. As one of the most promising energy storage devices, the lithium ion batteries have progressively attracted extensive interests within the industrial and scientific communities. It is now the dominate power source for portable electronics and electric/hybrid electric cars [20, 27, 92]. The ever-increasing energy demand has inspired current research to develop new high-performance electrode materials with various morphologies, from micro to nanoscales, for lithium ion batteries. Owing to their higher theoretical specific capacity (500 to 1000 mA h g^{-1}) and reversible conversion mechanism for lithium storage, nanostructured transition metal oxides have been considered as a possible alternative anode material for lithium ion batteries [299, 396-399, 373, 422, 423]. However, poor cycling performance and low electrical conductivity limits their practical application. Among transition metal oxides, cobalt oxide exhibited capacity 3 times higher than that of conventional graphite. However, because of the high cost and toxic nature of cobalt, it has not been recognized as an alternative anode material. Many efforts have been devoted to partially replacing cobalt oxide with other inexpensive and environmentally friendly metals oxides [170, 400-402].

Binary metal oxides such as CuCo$_2$O$_4$, MnCo$_2$O$_4$, ZnCo$_2$O$_4$, NiCo$_2$O$_4$ and ZnMn$_2$O$_4$ have also been reported as anode materials for lithium ion batteries [170, 400-403].

Among various binary metal oxides $NiCo_2O_4$ is a very promising electrode material because of its high theoretical capacity (890 mA h g^{-1}). More importantly, it has been reported that $NiCo_2O_4$ has much higher electrical conductivity than nickel oxides and cobalt oxides [337]. The higher electronic conductivity is favorable for the rapid transfer of electron in an electrode. Because of the synergistic effect from higher electronic conductivity and porous structure, $NiCo_2O_4$ nanoflakes and nanobelts show much better electrochemical performances than that of nickel oxide and cobalt oxide. Owing to its intriguing properties, it emerges as a promising material for diverse applications such as photodetectors [404], electrocatalytic water splitters [405], supercapacitors [261] and lithium ion batteries [402, 406]. In order to develop high performance lithium ion batteries, electrode materials play a very important role in terms in determining the performance of batteries. Generally, porous electrode materials exhibit several beneficial properties, which are preferable for the enhancement of electrochemical performances, these include that (i) the porous structure can offer space for volume change throughout the cycling process, and (ii) the high specific surface area can greatly improve the interface contact between the active materials and electrolyte, facilitating fast Li$^+$ and electron transport [407, 312]. It is also well-recognized that the rate performance of electrode materials is generally determined by electronic conductivity and the kinetics of ion diffusion. Thus, the design of electrode materials with different shapes and sizes are essential to improve electrochemical performances of lithium ion batteries. $NiCo_2O_4$ has been widely studied as an electrode material for supercapacitors owing to its remarkable electrical conductivity and electrochemical activities [408-410, 254]. However, there have been only a few reports on the application of $NiCo_2O_4$ as anode materials for lithium ion batteries. Qian et al. have reported monodisperse $NiCo_2O_4$ mesoporous microspheres by a solvothermal method

with subsequent annealing of precursor, which displayed good battery performance [402]. Porous flower-like $NiCo_2O_4$ was synthesized through a hydrothermal method followed by calcination in air. The flower-like $NiCo_2O_4$ exhibited improved lithium storage properties and good cycling performance [406]. Li and co-workers have fabricated well-aligned nanorod arrays on Cu substrates by using a one-pot hydrothermal decomposition followed by calcination in air. The nanorod arrays demonstrated higher lithium storage performances [411].

Herein, we reported the preparation of highly porous $NiCo_2O_4$ nanoflakes and nanobelts by a simple template-free hydrothermal method. The as-prepared $NiCo_2O_4$ nanostructures demonstrated high specific capacity, excellent rate capability and a good cycling stability.

6.2 Experimental

6.2.1 Synthesis of $NiCo_2O_4$ Nanoflakes and Nanobelts

In a typical synthesis process of $NiCo_2O_4$ nanoflakes, 0.687 mmol of $Ni(NO_3)_2 \cdot 6H_2O$ and 1.375 mmol of $Co(NO_3)_2 \cdot 6H_2O$ are dissolved in 25 ml of deionized (DI) water followed by the addition of 0.516 g glycine and 0.585 g Na_2SO_4 salt. The mixture was slowly adjusted to pH 11 by the drop wise addition of 5 M NaOH solution and stirred for 1 h. The resultant mixture was transferred into a 30 ml Teflon-lined stainless steel autoclave and heated at 180 ^{o}C for 20 h. After cooling to room temperature, the precipitates were collected by filtration, washed with DI water and ethanol and dried in a vacuum oven at 80 ^{o}C for 12 h. Finally, to obtain the porous nanoflakes, the precursor was annealed at 500 ^{o}C for 3 h in air. For the synthesis of $NiCo_2O_4$ nanobelts, the process was almost identical to the synthesis of $NiCo_2O_4$ nanoflakes described above. The only difference is the addition of 50 % ethanol and 50 % water instead of 100 % water.

6.2.2 Materials Characterization

The as-synthesized $NiCo_2O_4$ nanoflakes and nanobelts were characterized using GBC MMA X-ray diffractometer (λ = 0.15405 nm), a field emission scanning electron microscopy (FESEM, Zeiss Supra 55VP) with an energy dispersive X-ray (EDX) attachment and a transmission electron microscopy (TEM, JEOL 2011 TEM facility). The specific surface area was calculated using the Brunauer-Emmett-Teller (BET) method. The pore size distribution and average pore diameter were calculated by the Barrett-Joyner-Halenda (BJH) equation using a Micromeritics 3 Flex^{TM} surface characterization analyser at 77 K. Fourier transform infrared (FTIR) spectroscopy was performed on a Bruker Tensor 27 IR spectrometer using KBr as dispersant between 400 to 4000 cm^{-1}. Thermogravimetric analysis (TGA) was carried out at a heating rate of 10 ^{o}C min^{-1} from room temperature to 600 ^{o}C with an air flow rate of 30 mL min^{-1} by using the 2960 SDT thermal analyser.

6.2.3 Electrochemical Measurements

The electrochemical performances of the as-prepared $NiCo_2O_4$ nanoflakes and nanobelts were measured under room temperature by using coin cells (CR 2032), in which lithium was used as the counter electrode as well as the reference electrode. The working electrode was prepared using the active material ($NiCo_2O_4$ nanobelts and nanoflakes), acetylene carbon black (conductive agent) and polyvinylidene fluoride (PVDF) binder in a weight ratio of 60:20:20. The slurry was pasted onto a copper foil substrate (area of loading: 1 cm^2, and active material is around 0.8 mg) and dried in a vacuum oven at 100 ^{o}C overnight. A thin round sheet of microporous polythene (Celgard 2400) was used as separator and 1 M $LiPF_6$ in ethylene carbonate (EC) and diethyl carbonate (DEC) (1:1 by volume) was used as the electrolyte (20 μL for each cell). The cells were assembled in an argon-filled glove box (UniLab, MBRAUN,

Germany) with water and oxygen contents of less than 1 ppm. The galvanostatic charge-discharge cycling was evaluated by the NEWARE-BTS battery tester with a voltage window of 0.01-3.0 V. The cyclic voltammetry (CV) experiment was carried out using a CHI 660C electrochemistry workstation in the voltage range of 0.01 to 3.0 V (vs Li^+/Li) and at a scan rate of 0.1 mV s^{-1}. Electrochemical impedance spectroscopy (EIS) was conducted on the CHI 660C electrochemistry workstation in the frequency range from 0.1 MHz to 0.01Hz.

6.3 Results and Discussion

6.3.1 Physical and structural characterization

The crystalline structure and phase purity of the $NiCo_2O_4$ materials were characterized by XRD. Figure 6.1(a) and 6.1(b) shows the XRD patterns of $NiCo_2O_4$ nanoflakes and nanobelts.
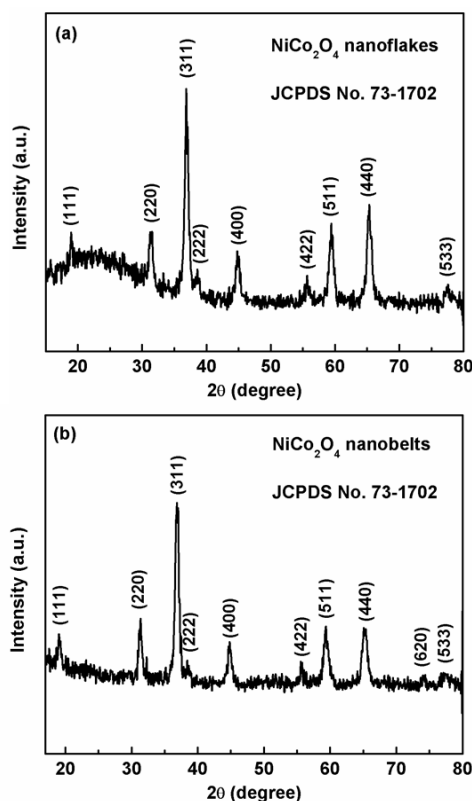
Figure 6.1 XRD patterns of $NiCo_2O_4$ calcinated at 500 ^{o}C for 3 h (a) nanoflakes (b) nanobelts.

Nine distinct diffraction peaks are observed at 2θ values of 19.3°, 31.2°, 36.8°, 38.5°, 44.8°, 55.8°, 59.3°, 65.2° and 77.2°, respectively (Fig. 1(a)). All of these diffraction peaks can be indexed to (111), (220), (311), (222), (400), (422), (511), (440) and (533) crystal planes and assigned to cubic $NiCo_2O_4$ with spinel crystalline structure (JCPDS card no. 73-1702). In Fig. 6.1(b), the small peak at around 74° can be indexed to the (620) crystal plane of $NiCo_2O_4$. All diffraction peaks in Fig. 1(b) can also be ascribed to the cubic $NiCo_2O_4$ with spinel crystalline structure (JCPDS card no. 73-1702) [408]. No other impurity peaks were observed, which indicates that the pure $NiCo_2O_4$ nanoflakes and nanobelts were formed after thermal treatment.

The morphologies of the as-synthesized Ni-Co based intermediate products and $NiCo_2O_4$ nanoflakes and nanobelts were determined by FESEM. Figure 6.2(a) and 6.2(b) shows the SEM images of Ni-Co based intermediate products (nanoflakes). From the low and high magnification images, the uniform distribution of nanoflakes is observed. Figure 6.2(c) and 6.2(d) shows the nanobelts of Ni-Co based intermediate with regular distribution. Remarkably, the nanoflake and nanobelt structures were maintained even after thermal treatment of the precursors. There is no obvious morphology change, which demonstrates excellent structural stability (Fig. 6.3 and Fig. 6.4). Figure 6.3 displays different magnification SEM images of $NiCo_2O_4$ nanoflakes. From the low magnification SEM images, uniform distribution of $NiCo_2O_4$ nanoflakes is observed (Fig. 6.3(a) and 6.3(b)). The high magnification SEM images show the nanoflake structure with clearly visible small pores on the surface of nanoflakes (Fig. 6.3(c) and 6.3(d)). Figures 6.4(a) and 6.4(b) show the low magnification SEM images of $NiCo_2O_4$ nanobelts, in which nanobelts are homogeneously distributed. From the high magnification SEM images, we can clearly observe that there are many mesopores on the surface of the nanobelts (Fig. 6.4(c) and 6.4(d)).
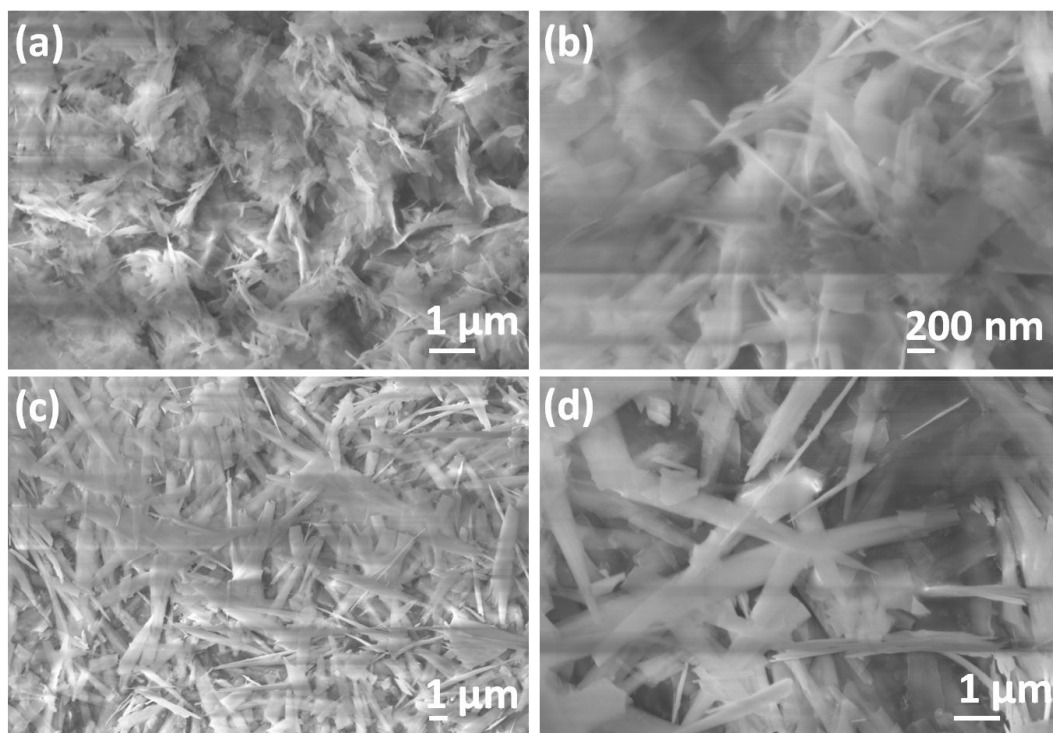
Figure 6.2 FESEM images of the Ni-Co based intermediate (a and b) nanoflakes (low and high magnification), (c and d) nanobelts (low and high magnification).

We investigated the morphology development of Ni-Co based precursors and $NiCo_2O_4$ nanoflakes and nanobelts. Strong alkaline conditions and the presence of glycine were essential for the growth of nanoflakes and nanobelts. In the absence of glycine and without alkaline conditions, nanoparticles were formed. Glycine is applied as a hydrolysis controlling agent for the formation of $NiCo_2O_4$ nanoflakes and nanobelts. Assisted by amphiphilic glycine, the $NiCo_2O_4$ precursors tend to form a layered structure, which was uniformly wrapped by the hydrophobic part of glycine. Meanwhile, the hydrophilic part of glycine was dissolved in the aqueous solution. Through the hydrolysis of glycine during the hydrothermal process, more OH^- ions generate in the solution and the pH value of the solution significantly increases, leading to the formation of a nanoflake or nanobelt structure rather than nanoparticles. The temperature also has a significant effect on morphology development. The nanoflakes and nanobelts were not achieved if the temperature is less than 180 ^{o}C.
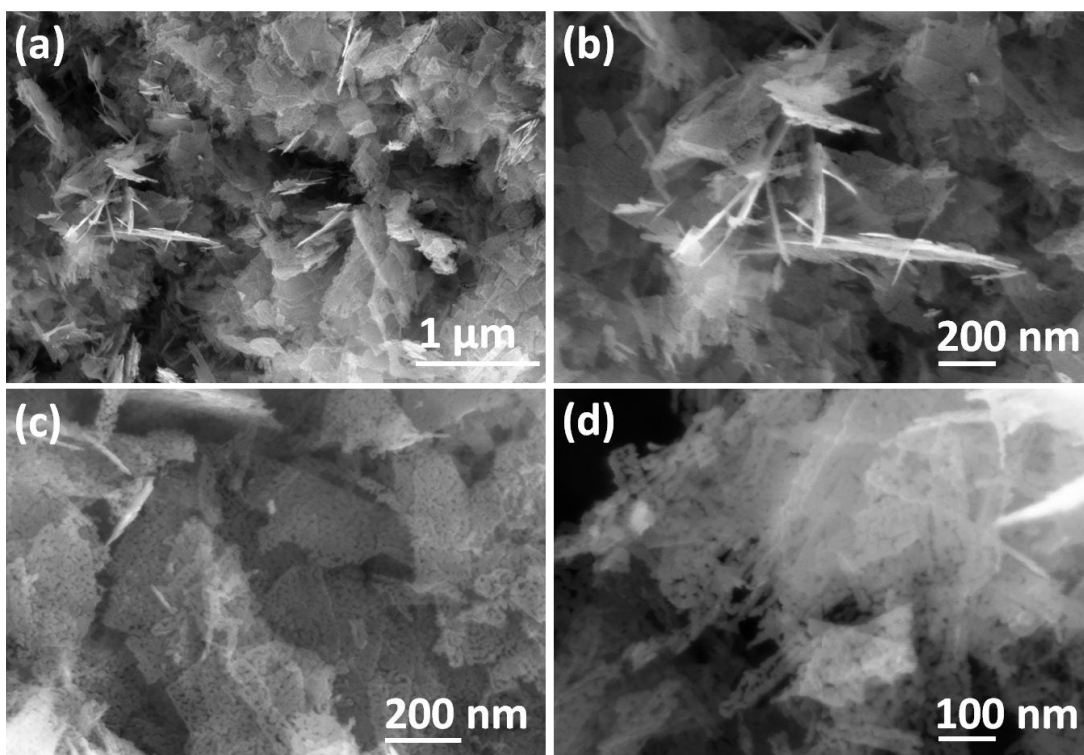
Figure 6.3 FESEM images of porous NiCo$_2$O$_4$ nanoflakes (a and b) low magnification, (c and d) high magnification.

When the temperature is increased to 200 ^{o}C, the similar morphology of nanoflakes and nanobelts can be obtained. The Ni-Co based precursors are calcined at 500 ^{o}C for 3 h to obtain porous NiCo$_2$O$_4$ nanoflakes and nanobelts. The surface composition of NiCo$_2$O$_4$ nanoflakes and nanobelts were also determined by energy-dispersive X-ray spectroscopy (EDX), which confirms the presence of Ni, Co and O atoms (Fig. 6.5). The peaks of carbon originated from the C substrate.

We further used transmission electron microscopy (TEM) and selected-area electron diffraction (SAED) patterns to identify the microstructure of as-prepared NiCo$_2$O$_4$ nanoflakes and nanobelts as shown in Fig. 6.6 and Fig. 6.7, respectively. In Fig. 6.6(a), it can be clearly seen that, in general, the product is mainly flakes with the size of ~500 nm which is similar to the calculated value based on the width of the peaks in the XRD profiles. In the low magnification TEM image of NiCo$_2$O$_4$ nanobelts (Fig. 6.7(a)), the

nanobelt feature of the as-prepared $NiCo_2O_4$ can be observed. All the selected area electron diffraction (SAED) pattern rings (Fig. 6.6(b) and Fig. 6.7(b)) taken from the corresponding single $NiCo_2O_4$ nanoflake and $NiCo_2O_4$ nanobelt can be readily indexed to the $NiCo_2O_4$ crystal structure. The high magnification TEM image (Fig. 6.6(c) and Fig. 6.7(c)) illustrate that the as-prepared $NiCo_2O_4$ nanocrystals are consistent with the porous structure. Fig. 6.6(d) and Fig. 6.7(d) show the lattice resolved HRTEM images of the $NiCo_2O_4$ nanoflakes and $NiCo_2O_4$ nanobelts, respectively, in which the (220) crystal plane with a d spacing of 0.28 nm can be directly observed. This further confirmed the crystal structure of the as-prepared $NiCo_2O_4$.
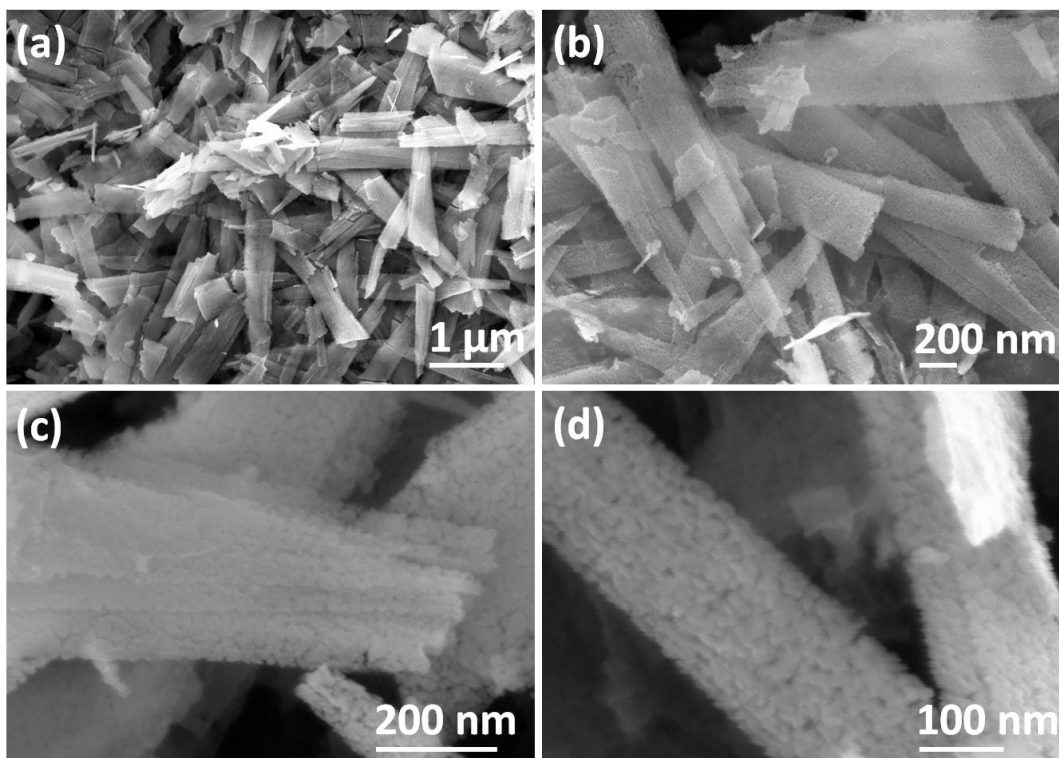
Figure 6.4 FESEM images of porous $NiCo_2O_4$ nanobelts (a and b) low magnification, (c and d) high magnification.

Figure 6.8 shows the N_2 adsorption and desorption isotherms of $NiCo_2O_4$ nanoflakes and nanobelts. All of the isotherms in Fig. 6.8(a) and 6.8(b) can be categorized as type IV isotherms with H1 hysteresis loops, which indicates a characteristic mesoporous structure [360].
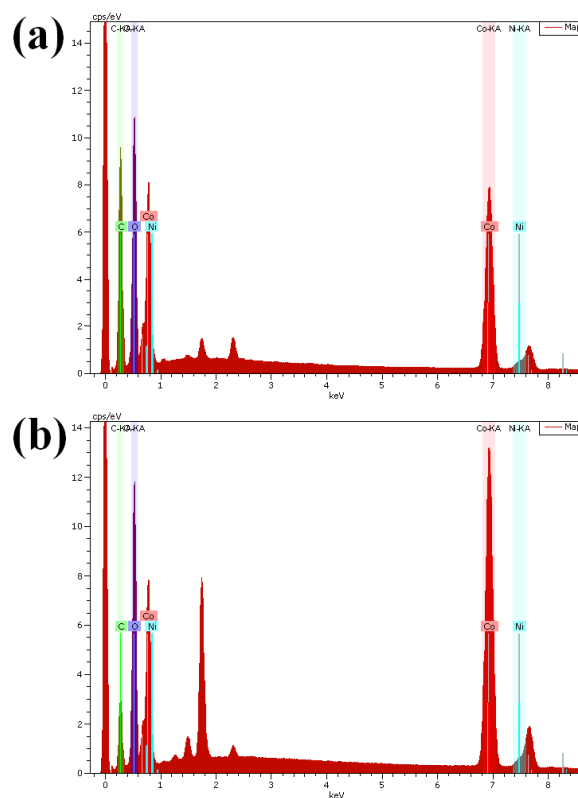
Figure 6.5 SEM-EDX pattern of (a) NiCo$_2$O$_4$ nanoflakes and (b) NiCo$_2$O$_4$ nanobelts.
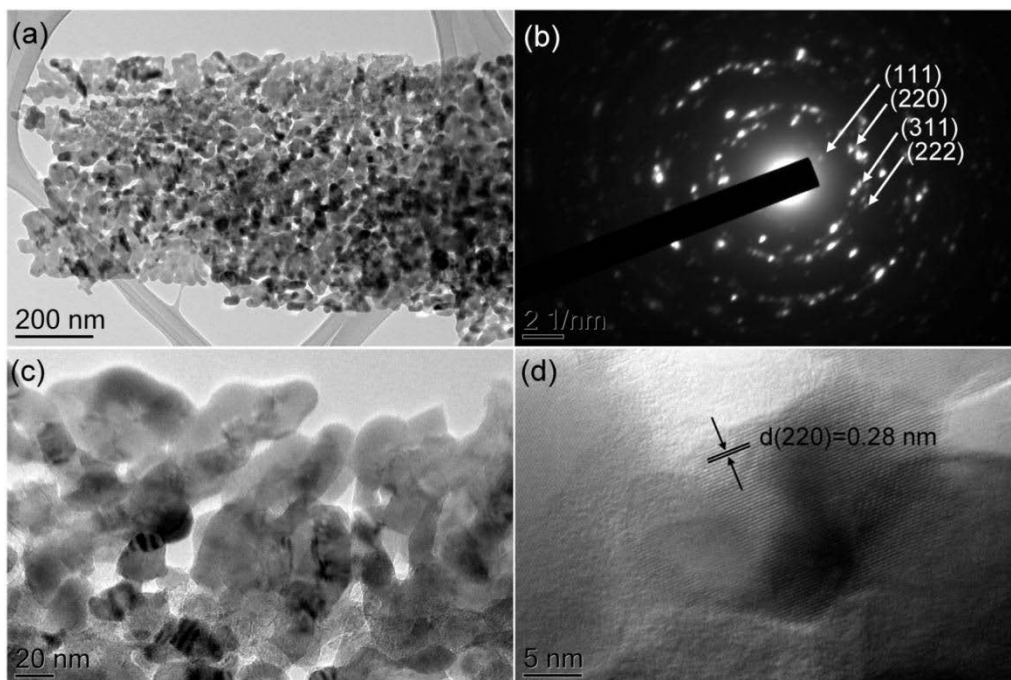
Figure 6.6 (a) Low magnification TEM image of NiCo$_2$O$_4$ nanoflakes (b) its corresponding selected area electron diffraction patterns (SAED), (c) high magnification TEM image, and (d) lattice resolved HRTEM image.
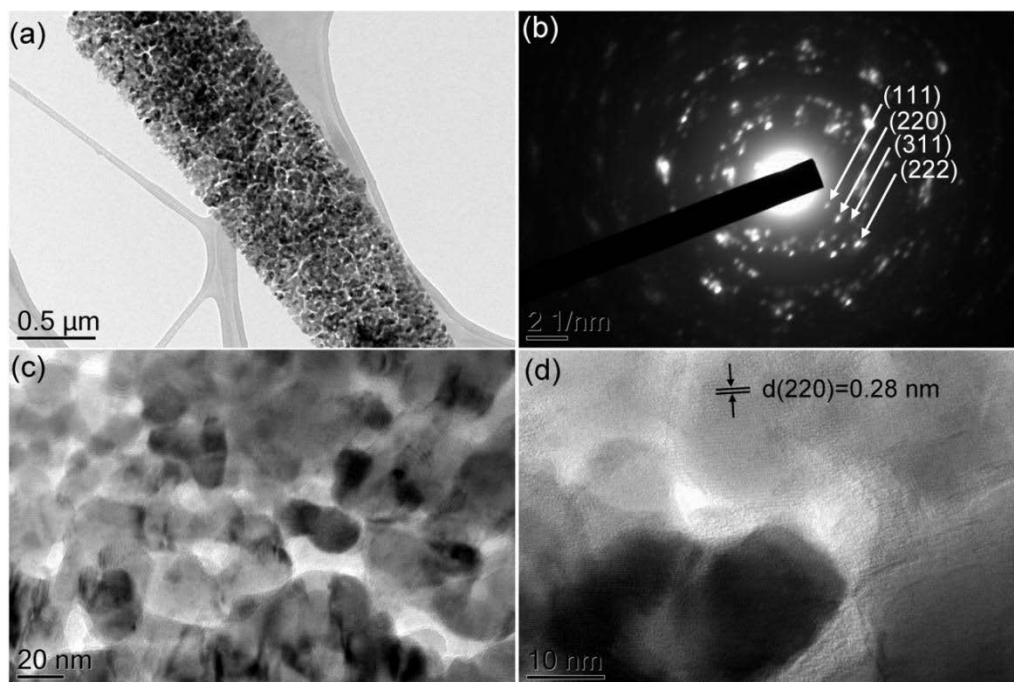
Figure 6.7 (a) Low magnification TEM image of NiCo$_2$O$_4$ nanobelts (b) its corresponding selected area electron diffraction patterns (SAED), (c) high magnification TEM image, and (d) lattice resolved HRTEM image.

Moreover, the BET surface area of NiCo$_2$O$_4$ nanoflakes and nanobelts are calculated to be around 54 m^2 g^{-1} and 66 m^2 g^{-1}, respectively. As shown in the insets of Fig. 6.8(a) and 6.8(b), the mesoporous structure of NiCo$_2$O$_4$ nanoflakes and nanobelts are further confirmed by the Barrett-Joyner-Halenda (BJH) pore size distribution data. The pore size distributions are relatively narrow, with most of the pores basically in the range of 3-5 nm for nanoflakes and 2-4 nm for nanobelts. Since the mesoporous feature and large surface area facilitate the Li$^+$ diffusion and electrode-electrolyte contacts throughout the electrochemical process, the NiCo$_2$O$_4$ nanoflakes and nanobelts could have enhanced electrochemical properties.
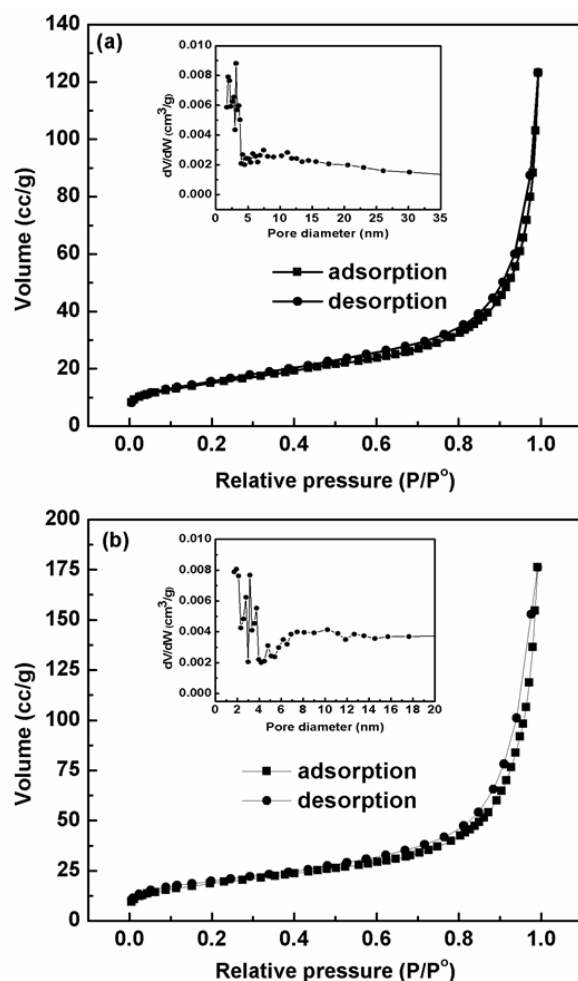
Figure 6.8 Nitrogen adsorption/desorption isotherms and corresponding BJH pore size distributions (inset) of (a) $NiCo_2O_4$ nanoflakes and (b) $NiCo_2O_4$ nanobelts.

Thermogravimetric analysis of Ni-Co based precursors (nanoflakes and nanobelts) were carried out between room temperature and 600 ^{o}C. As illustrated in Fig. 6.9(a) and 6.9(b), the 3.5 % weight loss that occurs before 286 ^{o}C can be ascribed to the dehydration of Ni-Co based precursors. The second step (18.5 % weight loss) in the TGA curves, corresponds to the conversion process of Ni-Co based precursors to $NiCo_2O_4$ nanoflakes and nanobelts. In the temperature range between 500 ^{o}C and 600 ^{o}C, there is no obvious weight loss is observed, which is inferred as the thorough decomposition of the precursors, structural integrity and absence of any other phases. Therefore, the calcination temperature of 500 ^{o}C was applied in order to achieve single phase $NiCo_2O_4$ nanoflakes and nanobelts.
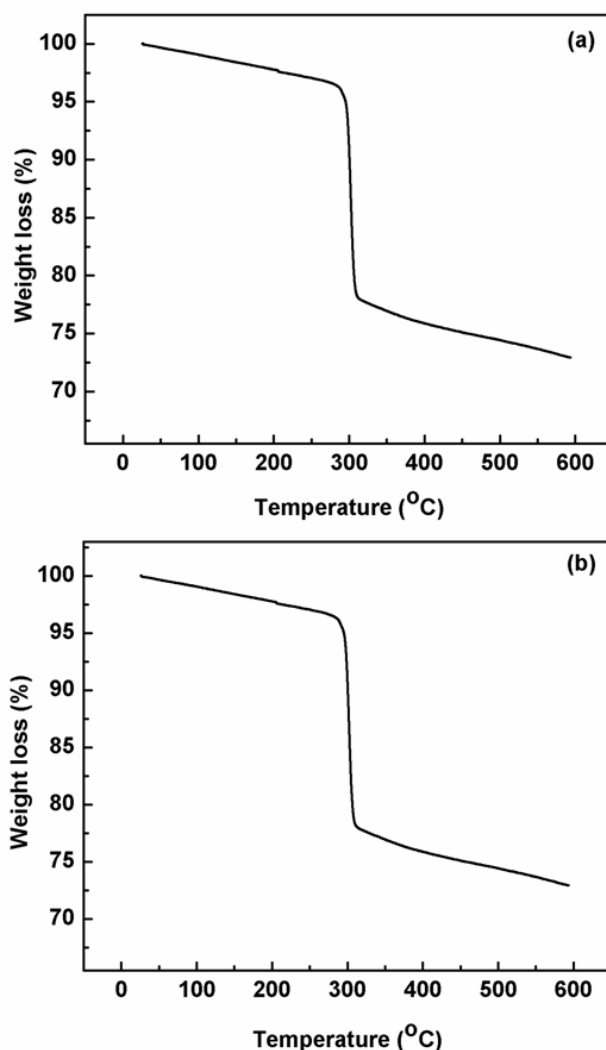
Figure 6.9 TGA curves for the NiCo$_2$O$_4$ nanoflakes (a) and NiCo$_2$O$_4$ nanobelts (b).

Figure 6.10 shows the FTIR spectra of NiCo$_2$O$_4$ nanoflakes and NiCo$_2$O$_4$ nanobelts. For the nanoflakes (Fig. 6.10(a)), the peaks at around 662 cm^{-1} and 565 cm^{-1} are arising from the metal-oxygen (M-O) vibrations of the NiCo$_2$O$_4$. The bands at around 662 cm^{-1} and 557 cm^{-1} in the Fig. 6.10(b) are also ascribed to the M-O vibrations of the NiCo$_2$O$_4$ nanobelts [412].
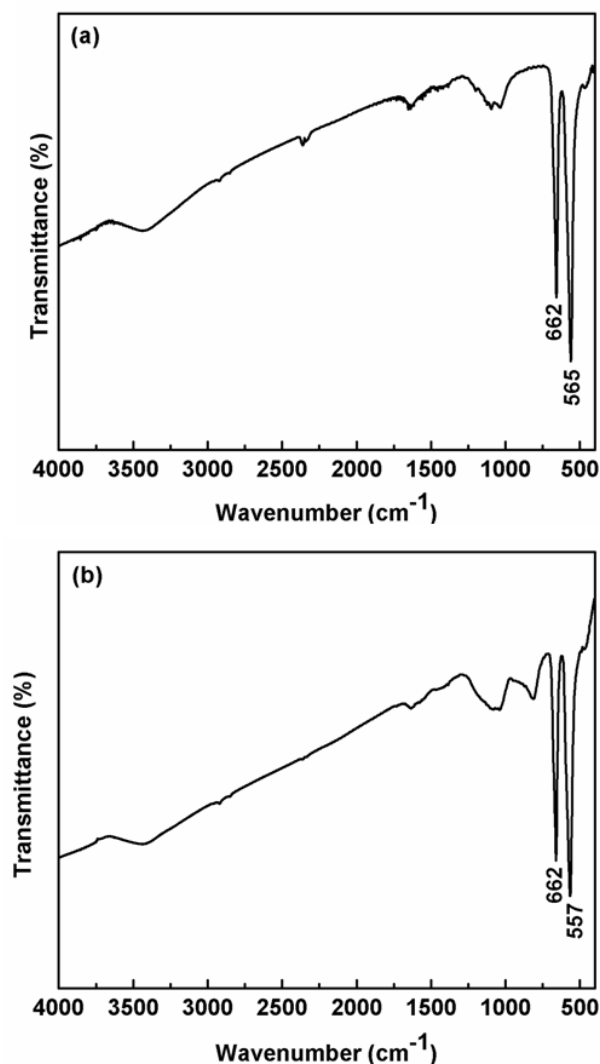
Figure 6.10 FTIR spectra of the $NiCo_2O_4$ nanoflakes (a) and $NiCo_2O_4$ nanobelts (b).

6.3.2 Electrochemical performances for lithium ion batteries

The lithium storage properties of the as-synthesized $NiCo_2O_4$ nanoflakes and nanobelts were initially evaluated by cyclic voltammetry (CV). Figure 6.11(a) and 6.11(b) shows the first three CV curves of the $NiCo_2O_4$ nanoflakes and nanobelts. In the first cycle of $NiCo_2O_4$ nanoflakes, as shown in Fig. 6.11(a), the intense cathodic peak located at ~0.95 V, results from the reduction of Co^{3+} and Ni^{2+} to metallic Co and Ni, respectively. However, the broad peak at ~0.68 V corresponds to the formation of a solid electrolyte interface (SEI) layer. The anodic peak is observed at ~2.1 V, which could be attributed to the oxidation of metallic Ni and Co to nickel oxides and cobalt oxides. In the second

and third cycles, the redox peaks at ~1.17 and ~2.16 V, corresponded to the reduction and oxidation of the nickel oxides and cobalt oxides [402, 406]. Unlike nanoflakes, the NiCo$_2$O$_4$ nanobelt electrode displays three cathodic peaks in the first cycle (6.11(b)). A minor peak at ~1.17 V can be ascribed to the devastation of crystalline structure, which is clearly different from the other cycles [406]. A strong irreversible cathodic peak at ~0.99 V, could be attributed to the reduction of Co^{3+} and Ni^{2+} to metallic Co and Ni, respectively. A broad peak at ~0.68 V can be attributed to the formation of SEI. The anodic peak at ~2.08 V, corresponds to the oxidation of metallic Ni and Co to nickel oxides and cobalt oxides. In the subsequent cycles, the continual reduction-oxidation of NiO and CoO results in redox peaks at ~1.18 V and 2.10 V, respectively.
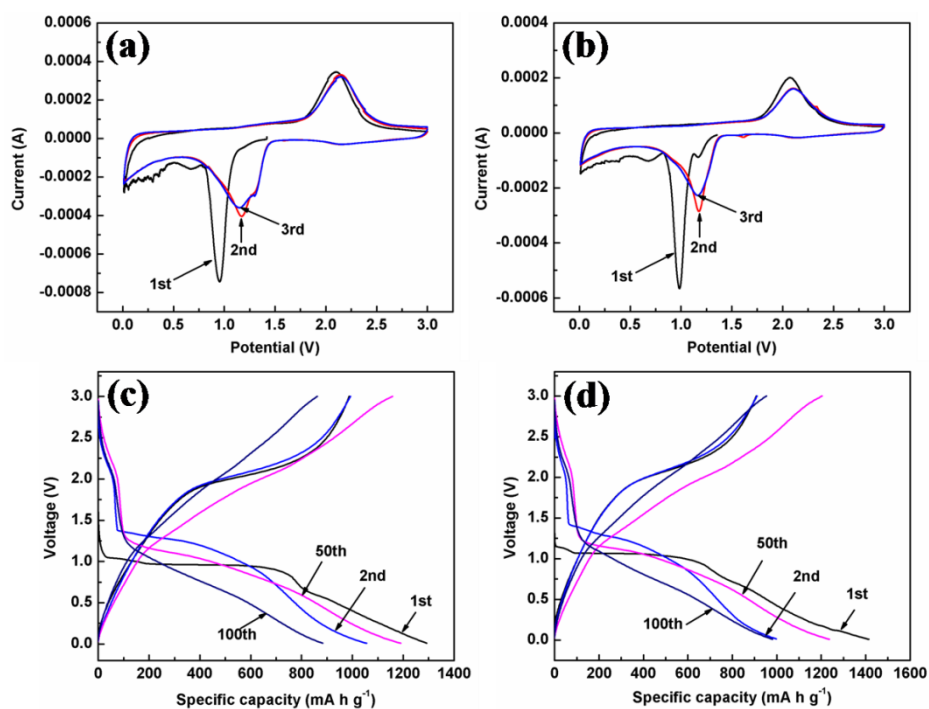
Figure 6.11 The first three consecutive CV curves of NiCo$_2$O$_4$ (a) nanoflakes and (b) nanobelts at a scan rate of 0.1 mV s^{-1} in the voltage range of 0.01-3.0 V, and galvanostatic discharge and charge profiles for the 1st, 2nd, 50th and 100th cycles of NiCo$_2$O$_4$ (c) nanoflakes and (d) nanobelts.

From the second cycle, there is no obvious change of the redox peaks for the NiCo$_2$O$_4$ nanoflake and nanobelt electrodes. This demonstrated that there is good electrochemical

reversibility. On the basis of the previous reports [402, 413, 414, 179], the redox reactions can be described as follows:

$$NiCo_2O_4 + 8\ Li^+ + 8e^- \rightarrow Ni + 2Co + 4Li_2O \tag{6.1}$$

$$Ni + Li_2O \leftrightarrow NiO + 2Li^+ + 2e^- \tag{6.2}$$

$$Co + Li_2O \leftrightarrow CoO + 2Li^+ + 2e^- \tag{6.3}$$

$$CoO + 1/3Li_2O \leftrightarrow 1/3Co_3O_4 + 2/3Li^+ + 2/3e^- \tag{6.4}$$
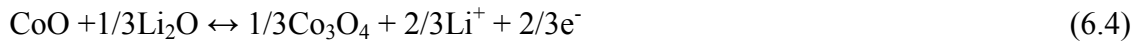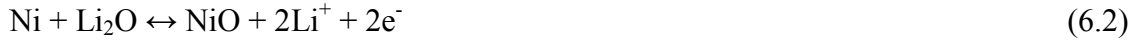
The galvanostatic discharge-charge profiles of the as-prepared $NiCo_2O_4$ nanoflake and nanobelt electrodes at the current density of 500 mA g^{-1} are presented in Fig. 6.11(c) and 6.11(d). In the first discharge process, the $NiCo_2O_4$ nanoflake and nanobelt electrodes show a wide and steady potential plateau at 1.1 V, followed by a gradual voltage decrease. The first discharge capacity reached about 1292 mA h g^{-1} and 1414 mA h g^{-1} for $NiCo_2O_4$ nanoflakes and nanobelts, respectively. The formation of a solid electrolyte interface (SEI) may contribute to the initial extra capacity at the first discharge [402, 415]. The potential plateaus in the subsequent discharge curves were shifted to the higher voltage than those of the first cycle, which can be ascribed to the irreversible reaction of $NiCo_2O_4$ and Li$^+$ as equation (1) [421]. The consequent charge curves show a steady potential increase, which are associated with the different electrochemical mechanism. The increase of the overpotential could be ascribed to the polarization related to the ion transfer during charge-discharge process, which is often observed in many metal oxides [406, 415]. The $NiCo_2O_4$ nanoflake and nanobelt electrodes delivered a capacity of 934 and 1018 mA h g^{-1}, respectively, in the first charge process with the capacity retention ratio of around 72 %. The large irreversible capacity loss in the first cycle can be ascribed to the formation of the SEI layer that cannot fully decompose during the first charge [402]. The increased capacity retention

ratios of 90 %, 97 % and 97.5 % were observed in the second, 50th and 100th cycle, respectively.

Figure 6.12(a) and (b) shows the reversible capacities versus cycle number of the $NiCo_2O_4$ nanoflake and nanobelt electrode at the current densities of 500 mA g^{-1} and 800 mA g^{-1}. The second discharge capacities of $NiCo_2O_4$ nanoflakes and nanobelts are 1033 mA h g^{-1} and 1056 mA h g^{-1}, respectively, at the current density of 500 mA g^{-1}. It is interesting to note that there is a trend of the gradual increased capacities before 40 cycles for both materials, which is ascribed to the reversible formation of a polymeric gel-like film originating from the slow kinetic activation process of the electrode.
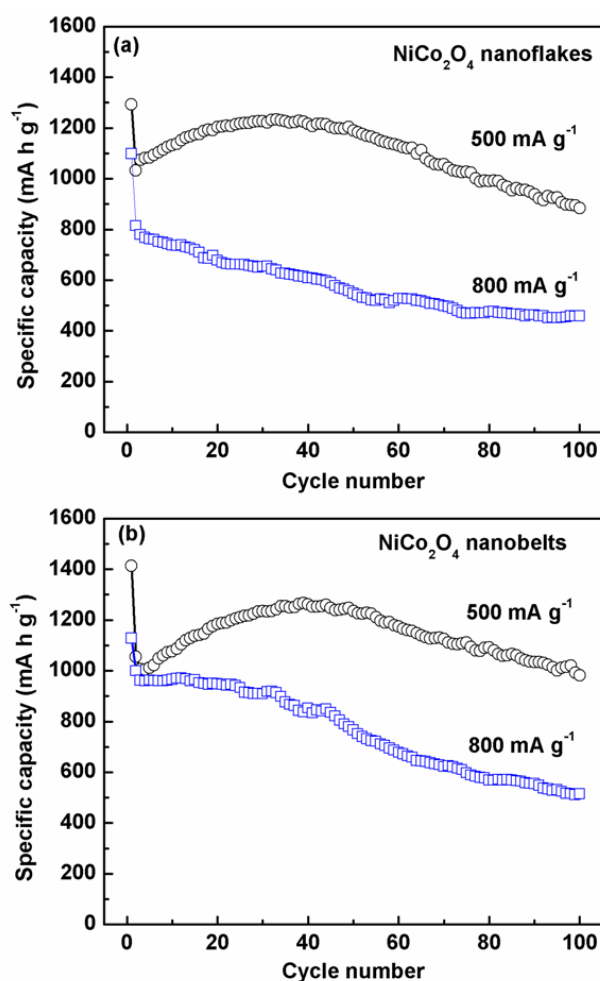
Figure 6.12 Cycling performance of $NiCo_2O_4$ electrode at the current densities of 500 and 800 mA g^{-1} (a) nanoflakes (b) nanobelts.

This is a general observation for transition metal oxides and it has been well-documented in previous reports [406, 416-418]. After 100 cycles, the discharge capacities are retained 884 mA h g^{-1} for nanoflakes and 981 mA h g^{-1} for nanobelts, which are almost 85.5 % and 93 % of the second reversible capacities. At the high current density of 800 mA g^{-1}, the NiCo$_2$O$_4$ nanoflake and nanobelt electrodes still show the reversible capacity of 814 mA h g^{-1} and 998 mA h g^{-1}, respectively. NiCo$_2$O$_4$ nanobelts exhibit better cycling stability than that of nanoflakes over 100 cycles.

The rate performances were also evaluated to investigate the high power performance of the porous NiCo$_2$O$_4$ nanoflakes and nanobelts, which is shown in Fig. 6.13(a) and 6.13(b).
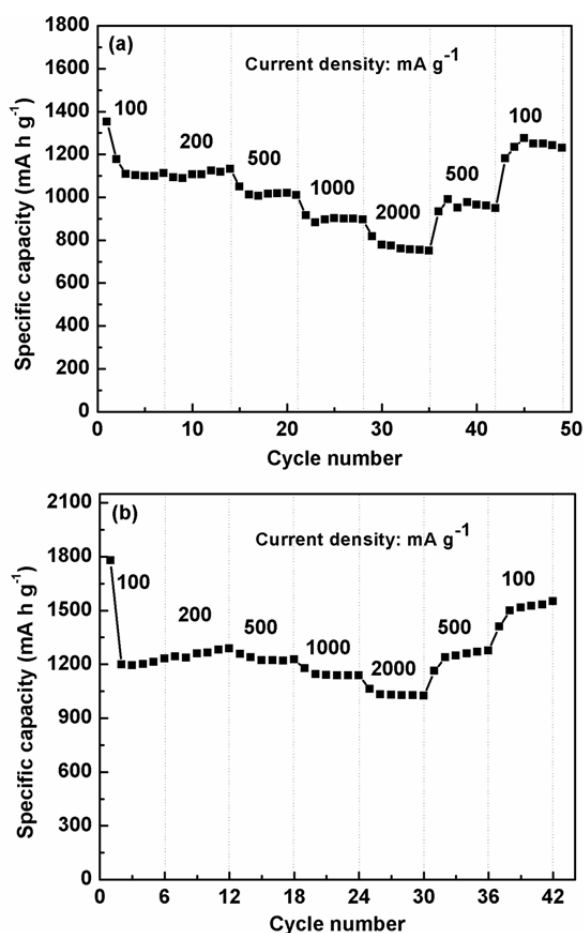
Figure 6.13 Rate performances for the NiCo$_2$O$_4$ electrode at various current densities (a) nanoflakes and (b) nanobelts.

The $NiCo_2O_4$ nanoflake electrode was cycled at different current densities ranging from 100 to 2000 mA g^{-1} (Fig. 6.13(a)). The electrode shows an excellent cycling performance at differed current densities. At the current density of 2000 mA g^{-1}, the electrode still delivered a reversible capacity of 902 mA h g^{-1}. Figure 6.13(b) presents the rate capability of $NiCo_2O_4$ nanobelts. The nanobelt electrode also shows the capacity of 1062 mA h g^{-1}, at the high current density of 2000 mA g^{-1}. This verified the excellent rate performance of $NiCo_2O_4$ nanoflakes and nanobelts for high power lithium ion batteries. Interestingly, when the currents reversed back to low current densities (500 and 100 mA g^{-1}), the discharge capacities recovered to the higher values than previous cycles for both $NiCo_2O_4$ nanoflakes and nanobelts. This high rate capability demonstrates that the porous $NiCo_2O_4$ nanoflake and nanobelt structures have potentials for high-rate anode in lithium ion batteries. To explain the higher values than previous cycles at the low current densities, we further demonstrate SEM images of $NiCo_2O_4$ nanoflake and nanobelt electrodes after rate capability testing. From Fig. 6.14(a) and (b), we can see that the $NiCo_2O_4$ nanoflake structure re-organised during charge-discharge cycling at different current densities and converted to nanoparticles. The nano-sized particles may have provided a larger specific surface area, which effectively maximises the $NiCo_2O_4$/electrolyte contact area and offer more reaction sites for Li^+ diffusion. Owing to the re-organisation during high current density cycling, the $NiCo_2O_4$ nanobelt structure (Fig. 6.14(c)) and (d)) also converted to nanoparticles, providing a high specific surface area to increase the contact area between active electrode materials and electrolyte. The high contact area can provide more active sites for lithium ion insertion/extraction. Those factors could induce the increase of specific capacity. To the best of our knowledge, reports on unique rate capabilities of porous $NiCo_2O_4$ nanoflakes and nanobelts are quite rare.
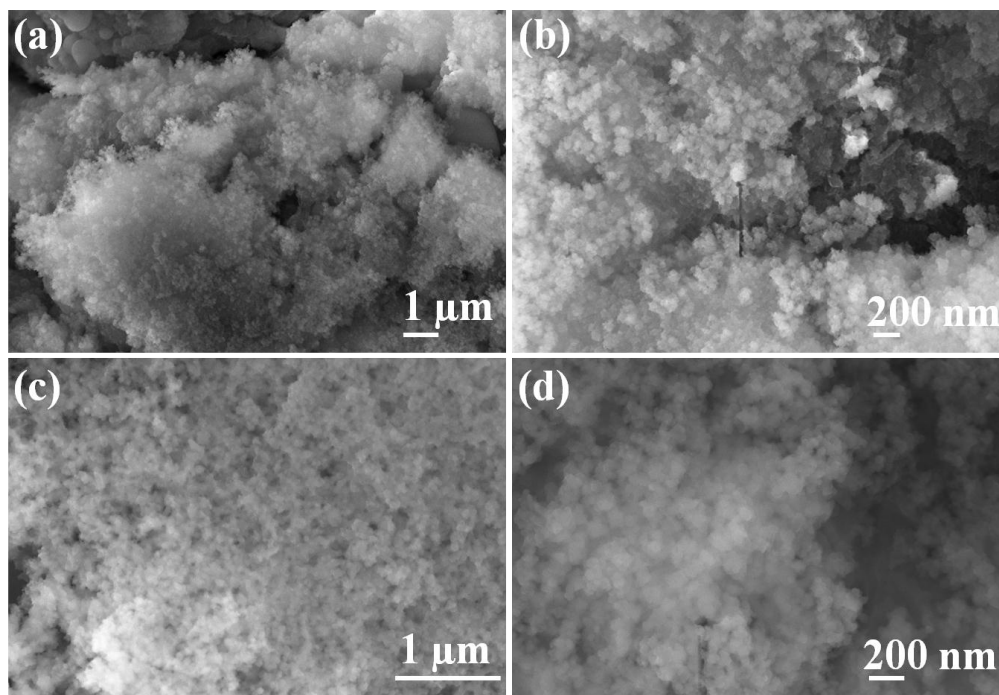
Figure 6.14 FESEM images of $NiCo_2O_4$ after rate capability test: (a, b) nanoflakes and (c, d) nanobelts.

Electrochemical impedance spectra (EIS) were measured to understand the performance of the as-prepared porous $NiCo_2O_4$ nanoflakes and nanobelts. Figure 6.15(a) and (b) presents the Nyquist plots obtained from the $NiCo_2O_4$ nanoflake and nanobelt electrodes for fresh cells and after rate capability test. Both the Nyquist plots exhibit two depressed semicircles in the high and medium frequency regions and a straight line in the low frequency region. The straight line in the low frequency region corresponds to the Warburg behaviour, reflecting the solid state diffusion of lithium ions into the bulk of the electrode materials [391]. The semicircle in the medium frequency region is probably ascribed to the charge-transfer process. As shown in Fig. 6.15(a), there are obvious increases of charge-transfer resistance (R_{ct}) after the rate capability test for $NiCo_2O_4$ nanoflakes. On the other hand, the R_{ct} value of the $NiCo_2O_4$ nanobelt electrode (Fig. 6.15(b)) is lower than that of the $NiCo_2O_4$ nanoflake after rate capability test. This shows that the lithium ions and electrons can transfer more freely in the

electrode/electrolyte interface and, therefore, enhance the electrode reaction kinetics and cycling stability throughout the cycling. Moreover, according to the electrochemical impedance data of the $NiCo_2O_4$ nanobelt electrode (Fig. 6.15(b)), we can observe that the radius of the semicircle before and after rate capability test is almost similar, demonstrating that there is no significant change in electrochemical resistance after the rate capability test. Furthermore, compared with the $NiCo_2O_4$ nanoflakes, the high specific surface area of porous $NiCo_2O_4$ nanobelts maximise the contact area between active materials and electrolyte, which can provide more reaction sites [419].
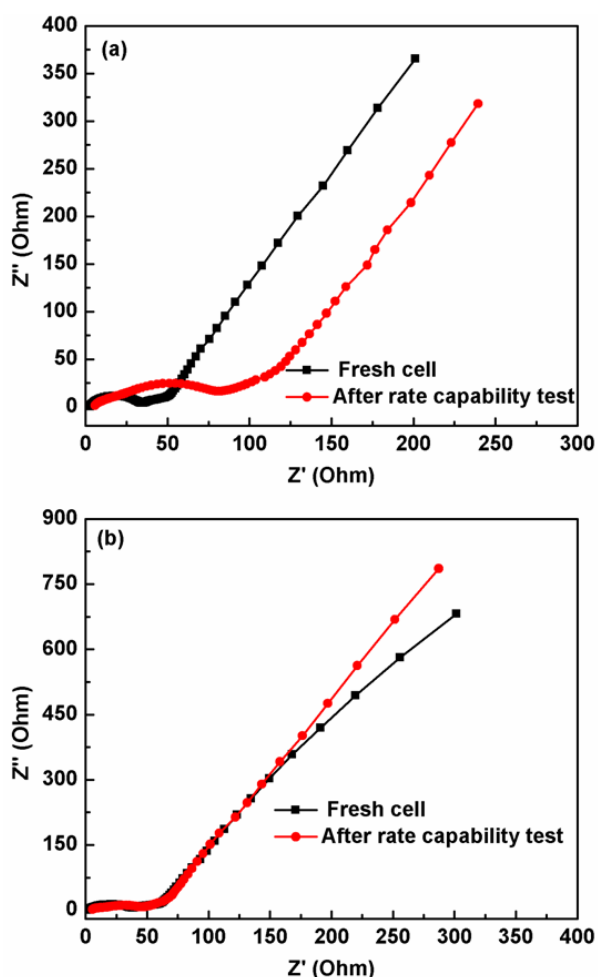
Figure 6.15 Electrochemical impedance spectra of the as-prepared $NiCo_2O_4$ before and after rate capability test (a) nanoflakes and (b) nanobelts.

Thus, NiCo$_2$O$_4$ nanobelts show better high specific capacity, good cycling performance and high rate capability than that of the NiCo$_2$O$_4$ nanoflakes.

The following factors could be responsible for the observed good electrochemical performance of these two materials. First, their higher specific surface area offers a large contact area between electrode and electrolyte for more Li$^+$ diffusion through the interface, thus improving the high specific capacity and also benefiting the charge-transfer rate, and enhancing the rate capability [418, 420]. Second, the existence of pores in the NiCo$_2$O$_4$ nanoflakes and nanobelts could cushion the volume change associated with the Li$^+$ intercalation/de-intercalation process during the long-term charge-discharge cycling, and alleviate the aggregation and pulverization of the electrode material, thereby improving cycling stability.

6.4 Conclusions

We established a facile hydrothermal method to produce both NiCo$_2$O$_4$ nanoflakes and NiCo$_2$O$_4$ nanobelts, followed by annealing in air. The materials have high specific surface area and a mesoporous structure, which facilitates the fast transportation of Li$^+$ and also accommodates the volume variation based on the conversion reaction during the charge/discharge process. When applied as an anode material for LIB applications, the NiCo$_2$O$_4$ nanoflake and nanobelt electrodes retained reversible capacities of 884 mA h g^{-1} and 981 mA h g^{-1}, respectively, at the current density of 500 mA g^{-1}, even after 100 cycles, which is 85.5 % and 93 % of the second discharge capacities. When the NiCo$_2$O$_4$ nanoflake and nanobelt electrodes were cycled at different current densities (100-2000 mA g^{-1}), both the materials still delivered the capacity of 902 mA h g^{-1} and 1062 mA h g^{-1}, respectively, even at a high current density of 2000 mA g^{-1}, demonstrating an excellent high rate capability. The simple preparation process and

excellent electrochemical performances render porous $NiCo_2O_4$ nanoflakes and nanobelts to be attractive anode materials for lithium ion batteries.

Chapter 7 Graphene/MnO$_2$ hybrid nanosheets as high performance electrode materials for supercapacitors

7.1 Introduction

To address the ever-increasing global energy demand and the critical issue of climate change, one of the most essential tasks is to develop sustainable and efficient energy storage systems. Significant efforts have been devoted towards developing advanced, low-cost and environmentally friendly energy storage/conversion devices with high power and high energy densities that can be used in hybrid electric vehicles and electric vehicles [27, 424, 425]. Among the different energy storage systems, supercapacitors (also known as ultracapacitors) have attracted much interest because of their higher power density and longer cycle life than batteries. The power density is several orders of magnitude higher than that of conventional dielectric capacitors. These exceptional properties make them promising energy storage devices for a broad range of applications where high power density and long cycle life are required, such as mobile electronic devices, large industrial equipment, hybrid electric vehicles, memory backup systems and military devices [21, 205, 201, 337, 208].

The electrochemical performance of supercapacitors is mainly determined by the electrode materials, which can be divided into two categories. The first is carbon-based materials such as activated carbon [323], carbon nanotubes [219] and graphene [426, 71]. Carbon materials deliver capacitance based on the mechanism of electrical double layer capacitance (EDLC), which stores electric charge through reversible adsorption of ions in the electrolyte to form an electric double layer at the electrode/electrolyte interface. This process involves only physical adsorption of ions without any chemical reaction. The second is redox-based electrochemical capacitors, where transition metal

oxides [324, 427-429] such as MnO_2 and RuO_2 are used for fast and reversible redox reactions at the surface of active materials.

Transition metal oxides are usually considered the best candidates for electrode materials in supercapacitors owing to their large capacitance and fast redox kinetics. For instance, ruthenium oxide presents an exciting specific capacitance as high as 720 F g^{-1} [430]. However, the high cost and toxicity circumvent its practical and extensive applications. Thus, much attention has been given to metal oxides which are environmentally friendly and inexpensive [431-433]. Manganese dioxide (MnO_2) has been extensively investigated as an electrode material for supercapacitors [231, 434-437]. However, its performance is limited by poor electrical conductivity and densely packed structures with small surface area. Many approaches have been developed to improve the electrochemical performance of MnO_2, such as hybrid electrode materials incorporating MnO_2 with either CNTs [438] or conducting polymers [439]. The problems, such as mechanical instability and low cycle life of MnO_2 hybrid materials, still remain [440], therefore, it is essential to investigate new strategies to synthesize hybrid MnO_2 materials with high electrochemical performances.

Graphene has attracted considerable attention due to its remarkable mechanical stiffness, high electrical and thermal conductivities and an exceptionally high specific surface area (2630 m^2 g^{-1}) [65, 64, 68]. In particular, graphene could have significant potential for energy storage and conversion. However, poor utilization of high surface area owing to the irreversible re-stacking nature of graphene nanosheets (GNS) induces low specific capacitance. In order to overcome this problem, researchers are trying to explore composite materials with high specific capacitance and long cycle life. Graphene/metal oxide composite materials are very promising as electrode materials

with a potential application in energy conversion devices. In these composite materials, graphene acts as a highly porous conducting network, which enable readily access to ions and electrons to the active surfaces of metal oxides. Well dispersed metal oxides on the graphene nanosheets can efficiently inhibit the agglomeration and re-stacking of graphene and therefore increase the accessible surface area. Moreover, graphene can contribute double-layer capacitance to the overall energy storage as well as provide efficient electron transfer networks to improve electrochemical performance. Graphene/MnO_2 nanocomposites have been investigated by several groups using different methods. J. Yan *et al.* has reported graphene-MnO_2 composite through the self-limiting deposition of nanoscale MnO_2 on the surface of graphene under microwave irradiation and obtained specific capacitance of 310 F g^{-1} [274]. MnO_2 nanoparticles/graphene was synthesized by Qian et al. via polymer-assisted chemical reduction method and achieved good electrochemical performance as electrode material for supercapacitor [441]. Huang et al. fabricated Graphene nanoplate-MnO_2 composites by changing the corrosion reaction time at ambient temperature. The hybrid graphene nanoplate-MnO_2 prepared at 3 h showed the best performance [442]. Sow et al. had demonstrated a facile route for fabrication of α-Fe_2O_3 nanotubes-reduced graphene oxide nanocomposites. The nanocomposites showed high specific capacitance and excellent cycling life [447]. However, to the best of our knowledge, nanosheet morphology of MnO_2 and graphene nanosheets hybrid as electrode material for supercapacitors with good electrochemical performance remains limited. In this paper, we have successfully prepared MnO_2 nanosheets and graphene nanosheets separately without any surfactant and fabricated the graphene/MnO_2 hybrid nanosheets using ethylene glycol as dispersing agent. When applied as electrode materials for supercapacitors, graphene/MnO_2 hybrid materials showed a high specific capacitance of

320 F g^{-1} with an excellent cycle stability of over 2000 cycles.

7.2 Experimental

7.2.1 Synthesis of graphene nanosheets

In a typical synthesis process, natural graphite powders were oxidized to graphite oxide using a modified Hummers method [443]. 1.0 g graphite powder and 0.5 g sodium nitrate were poured to 25 mL concentrated H_2SO_4 (under ice bath). 4.0 g $KMnO_4$ was gradually added and stirred for 2.5 h. The mixture was diluted with 150 mL de-ionised (DI) water. Then 5% H_2O_2 was added into the solution until the colour of the mixture changed to brilliant yellow. The solution was washed with 5% HCl and DI water until the pH = 7. Then the obtained graphite oxide was dried in a vacuum oven overnight at 60 ^{o}C. The dry graphite oxide was re-dispersed in DI water and exfoliated to generate graphene oxide nanosheets by ultrasonication using a Brandson Digital Sonifier. The brown graphene oxide nanosheet dispersion was poured into a round bottom flask and then 60 μL hydrazine monohydrate (reducing agent) was added to the dispersion. The mixed solution was then refluxed at 100 ^{o}C for 3 h and the colour of the solution gradually changed to dark black as the graphene nanosheet dispersion was formed. The dispersion was then filtered and washed with DI water and ethanol and dried in a vacuum oven at 60 ^{o}C overnight to obtain bulk graphene nanosheets.

7.2.2 Synthesis of MnO_2 nanosheets

MnO_2 nanosheets were synthesized using a redox reaction of manganese nitrate tetrahydrate and potassium permanganate. 80 mL DI water was added to a flask and heated to 80 ^{o}C. 0.0885 g $Mn(NO_3)_2 \cdot 4H_2O$ and 0.1621 g $KMnO_4$ were dissolved in 30 mL hot water (80 ^{o}C), separately. Both the solutions were added to the flask drop by

drop under magnetic stirring and kept at 80 ^{o}C for 2 h. The resulting product was filtered and washed with DI water and ethanol several times and then dried at 100 ^{o}C overnight under vacuum.

7.2.3 Preparation of graphene-MnO$_2$ hybrid nanosheets

Graphene nanosheets (10 mg) were dispersed in 15 mL ethylene glycol and sonicated in digital sonicator for 5 h. 40 mg MnO$_2$ nanosheets were added in 50 mL ethylene glycol and sonicated in a bath sonifier for 1 h. Then the two dispersions were mixed by vigorous stirring. The two dispersions were interacted by the Van der Waals forces during vigorous stirring to make homogeneous composite. The mixture was filtered and washed with DI water and ethanol several times and dried in a vacuum oven at 80 ^{o}C overnight. Three hybrid nanosheets were prepared with the weight ratios of graphene:MnO$_2$ equalling 1:4, 1:9 and 3:2.

7.2.4 Materials Characterization

X-ray diffraction (XRD) patterns of the as-prepared materials were measured using a GBC MMA X-ray diffractometer (λ = 0.15405 nm). The morphologies and crystal structure of materials were analysed by the field emission scanning electron microscope (FESEM, Zeiss Supra 55VP) and transmission electron microscopy (TEM, JEOL 2011 TEM facility). The Raman spectrum was measured by using a Jobin Yvon HR800 confocal Raman system with 632.81 nm diode laser excitation on a 300 lines/mm grating at room temperature.

7.2.5 Electrochemical testing

The working electrodes were fabricated by mixing graphene/MnO$_2$ nanosheets, carbon black and polyvinylidene difluoride (PVdF) in a weight ratio of 65:25:10 and dispersed in N-methyl pyrrolidinone (NMP) solvent. The resulting slurry was then pasted onto titanium foil substrates (area of loading: 1 cm^2, and active material is around 0.8 mg)

and dried overnight at 100 °C in a vacuum oven. The electrodes were immersed in the electrolyte solution for 1 h in order to enhance the electrolyte diffusion into the bulk material before electrochemical measurement. A beaker-type three-electrode cell was assembled with platinum foil and a saturated calomel electrode (SCE) as counter and reference electrodes, respectively. 1 M Na_2SO_4 aqueous solution was used as the electrolyte. The electrochemical properties were examined by the cyclic voltammetry (CV) technique using the CHI 660C electrochemistry workstation. The CV measurement was conducted in the potential range of -0.1 to 0.9 V at scan rates of 5, 10, 20, 50 and 100 mV s^{-1}. Galvanostatic charge-discharge measurements were carried out between 0 to 1.0 V at a current density of 500 mA g^{-1}.

7.3 Results and discussion

7.3.1 Structural and morphological characterization

Figure 7.1 shows the XRD patterns of graphene nanosheets and graphene/MnO_2 hybrid nanosheets.
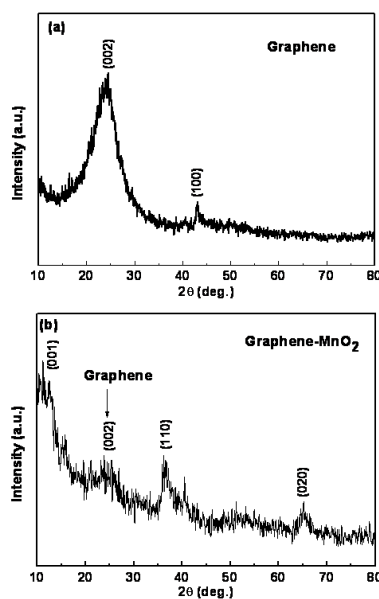
Figure 7.1 XRD patterns of (a) graphene nanosheets and (b) graphene/MnO_2 hybrid nanosheets (1:4 in weight ratio).

The broad diffraction peak in Fig. 7.1 (b) at 2θ between 20 $^{\circ}$ and 30 $^{\circ}$ indicates the graphene sheets and the other three peaks at around 12 $^{\circ}$, 37 $^{\circ}$ and 66 $^{\circ}$ can be indexed to (001), (110) and (020) crystal planes of the birnessite-type MnO_2, which is in agreement with Joint Committee on Powder Diffraction Standards (JCPDS) card 42-1317 [444].

The morphologies of graphene nanosheets, MnO_2 nanosheets and graphene/MnO_2 hybrid nanosheets were examined by FESEM observation. As shown in Fig. 7.2(a), graphene nanosheets are wavy and have a layered structure. MnO_2 nanosheets showed in Fig. 7.2(b), which demonstrates wrinkled thin sheets with abundant surface.
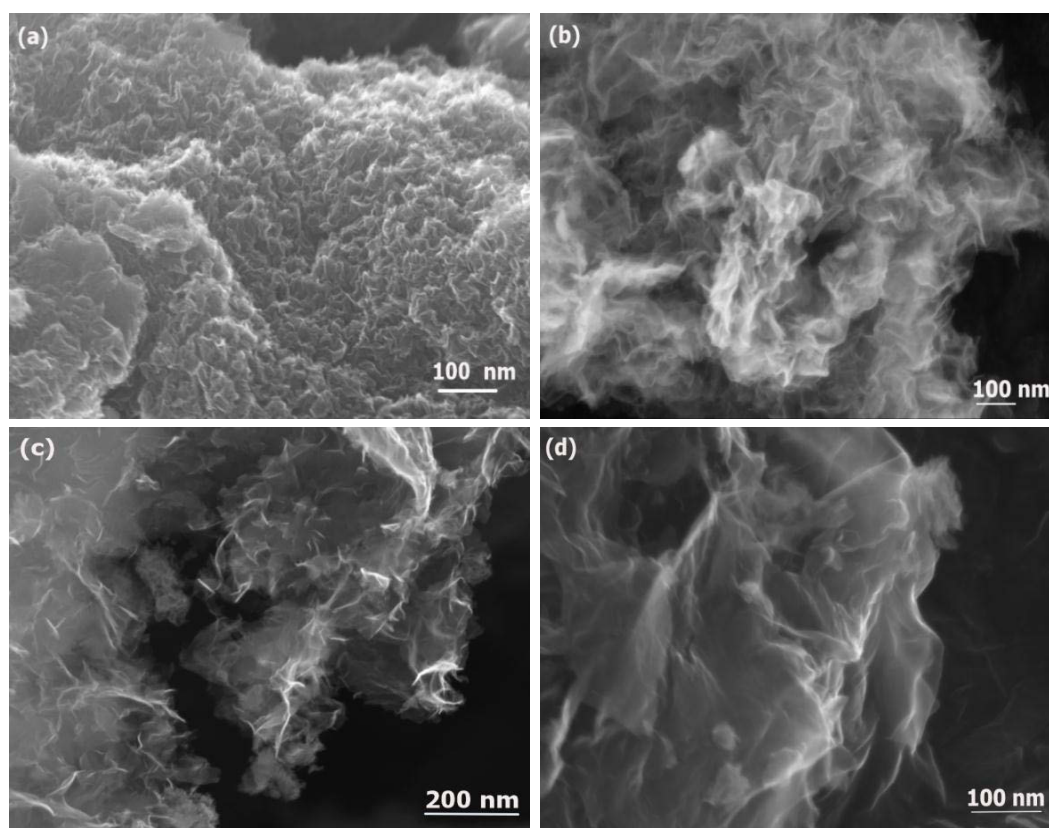
Figure 7.2 FESEM images of (a) graphene nanosheets, (b) MnO_2 nanosheets, (c) graphene/MnO_2 (1:4 in weight ratio) hybrid nanosheets (low magnification), and (d) graphene/MnO_2 (1:4 in weight ratio) hybrid nanosheets (high magnification).

Figure 7.2(c) and 7.2(d) show low and high magnification SEM images of graphene/MnO$_2$ hybrid nanosheets, respectively. In order to clarify the uniformity of graphene/MnO$_2$ hybrid nanosheets, energy dispersive X-ray (EDX) mapping was carried out by using scanning transmision electron microscope (STEM) (Fig. 7.4). The results confirmed that the C, Mn and O elements are homogeneously distributed throughout the entire surface of the hybrid nanosheets. The surface composition of graphene/MnO$_2$ hybrid nanosheets, was distinctly determined with SEM-EDX spectrum. It confirms the presence of C, Mn and O atoms (Fig. 7.5).
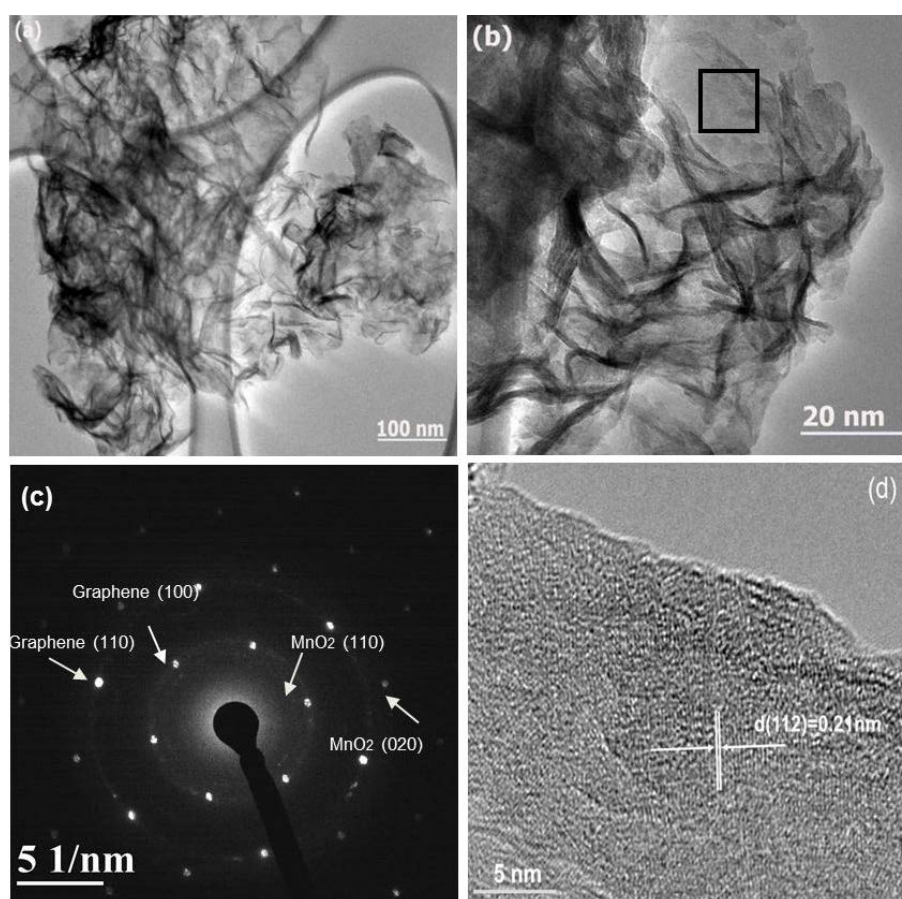
Figure 7.3 (a) Low magnification TEM image of graphene/MnO$_2$ hybrid nanosheets (1:4 in weight ratio), (b) high magnification TEM image of graphene/MnO$_2$ hybrid nanosheets, (c) selected area electron diffraction patterns taken from the black rectangle section in Fig. 3b of the hybrid nanosheets, and (d) HRTEM image of graphene/MnO$_2$ (1:4 in weight ratio) hybrid nanosheets.

The morphology and crystal structure of graphene/MnO$_2$ hybrid nanosheets were further analysed by TEM and HRTEM. Figure 7.3(a) shows a low magnification TEM image of graphene/MnO$_2$ hybrid nanosheets, in which MnO$_2$ nanosheets are homogeneously distributed in graphene nanosheets. A high magnification TEM image (Fig. 7.3(b)) also confirmed uniform mixing of both nanosheets with the layered nano structure. Figure 7.3(c) presents the corresponding selected area electron diffraction (SAED) pattern. The diffraction rings can be indexed to the birnesite-type (110), (020) crystal planes of MnO$_2$ nanosheets and (100) and (110) of graphene nanosheets [75]. The HRTEM image (Fig. 7.3(d)) shows the (112) crystal plane with the 0.21 nm d-spacing of MnO$_2$, indicating good crystallinity of the as-prepared MnO$_2$ nanosheets [444].
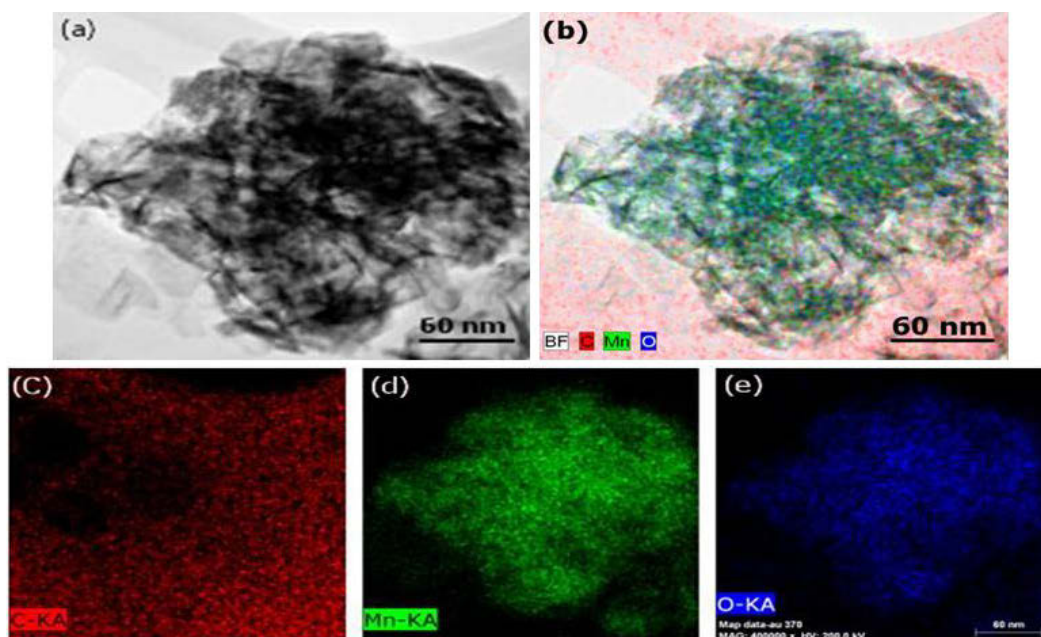
Figure 7.4 (a) TEM image of graphene/MnO$_2$ (1:4 in weight ratio) hybrid nanosheets (b) STEM-EDX mapping of graphene/MnO$_2$ hybrid nanosheets (c-e) mapping of C, Mn and O elements.

Figure 7.6 shows Raman spectrum of graphene/MnO$_2$ hybrid nanosheets. Two typical Raman peaks of carbon, the D line and G line are observed at 1333 cm^{-1} and 1589 cm^{-1}, respectively, which could be attributed to the Raman spectrum of pure graphene nanosheets [75].
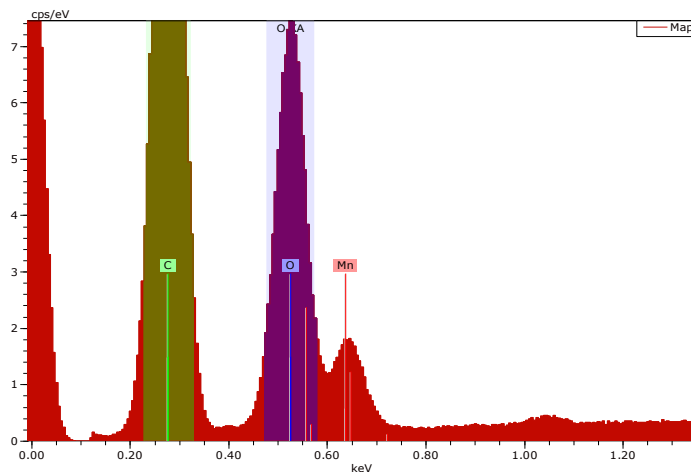
Figure 7.5 SEM-EDX elemental analysis of graphene/MnO_2 (1:4 in weight ratio) hybrid nanosheets.

From the Raman spectrum of graphene/MnO_2 hybrid nanosheets a new peak appears at 645 cm^{-1}, which can be ascribed to the symmetric stretching vibration (Mn-O) of the MnO_6 group and Mn-O stretching vibration in the basal plane of MnO_6 [448].
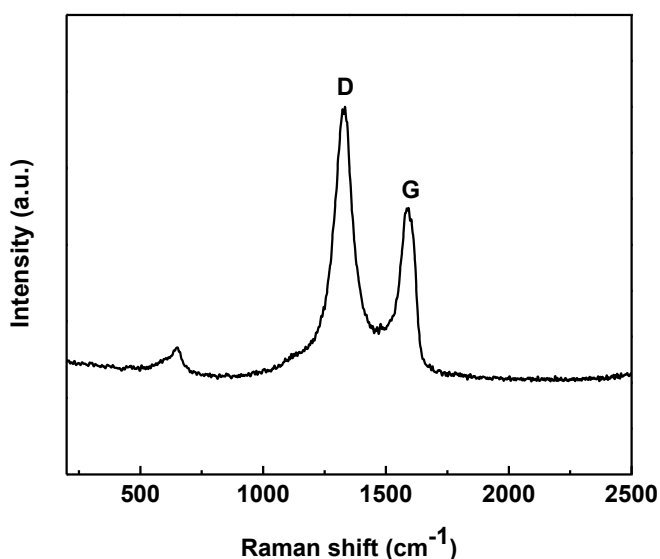
Figure 7.6 Raman spectrum of graphene/MnO_2 (1:4 in weight ratio) hybrid nanosheets.

7.3.2 Electrochemical performances for supercapacitors

Cyclic voltammetry (CV) and galvanostatic charge-discharge were used to investigate

the electrochemical properties of graphene/MnO_2 hybrid nanosheets. Figure 7.7 shows the CV curves of graphene/MnO_2 hybrid nanosheets measured at different scan rates in 1 M Na_2SO_4 solution. It is well known that the shape of CV of a supercapacitor should be rectangular over a wide range of scan rate, which indicates that there are low contact resistances and ideal capacitive behaviour. The CV curves of graphene/MnO_2 hybrid nanosheets exhibit ideal rectangular shapes over the potential range, even at high scan rate of 100 mV s^{-1}. The perfect symmetry in anodic and cathodic directions indicates an excellent capacitive behaviour of the electrode materials and low contact resistance in the capacitors [201]. There are also small humps at around 0.5 V, which is related to the redox behaviour of MnO_2. The specific capacitance was calculated from the CV curves by the following equation:

$$C = Q/\upsilon m \Delta V \qquad (7.1)$$

Where Q is the charge obtained by integrating the CV curves, υ is the scan rate, m is the mass of active material and ΔV is the voltage range of each scan.
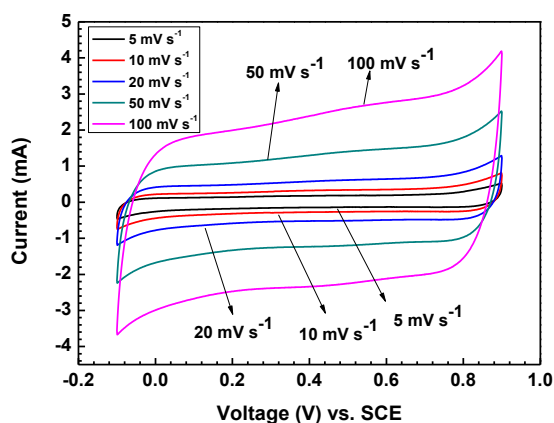
Figure 7.7 CV curves of graphene/MnO_2 (1:4 in weight ratio) hybrid nanosheets at different scan rates of 5 mV s^{-1}, 10 mV s^{-1}, 20 mV s^{-1}, 50 mV s^{-1} and 100 mV s^{-1} in 1 M Na_2SO_4 solution.

The corresponding specific capacitances are 268, 241, 212, 185 and 170 F g^{-1} at the scan rates of 5, 10, 20, 50 and 100 mV s^{-1}, respectively.

In order to evaluate the capacitive behaviour of graphene/MnO$_2$ hybrid nanosheets, galvanostatic charge-discharge measurements were performed at a constant current density of 500 mA g^{-1} within the potential range of 0 - 1 V. As shown in Fig. 7.8, the charge-discharge curves are highly linear and symmetrical in the potential range. This indicates that the electrode has an excellent electrochemical reversibility with a typical capacitive behaviour of supercapacitors [201, 200].
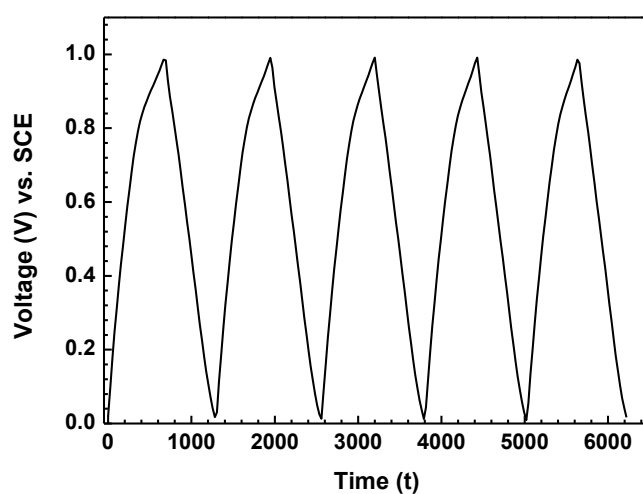
Figure 7.8 Charge/discharge profiles of graphene/MnO$_2$ (1:4 in weight ratio) hybrid nanosheets at the current density of 500 mA g^{-1} in 1 M Na$_2$SO$_4$ solution.

The specific capacitance (SC) was calculated from galvanostatic charge-discharge cycling using the following equation:

$$SC = I\Delta t/(\Delta Vm) \tag{7.2}$$

Where I is the current, Δt is the discharge (or charge) time, ΔV (=1.0 V) is the potential window of cycling and m is mass of active materials. The calculated SC value is 320 F g^{-1}, which is much higher than that of the previously reported values of pure graphene (205 F g^{-1} and 135 F g^{-1}) [426, 71]. The specific capacitance of 291, 272, 249 and 191 F g^{-1} was achieved at the current density of 1, 2, 4 and 8 A g^{-1}, respectively. This high specific capacitance demonstrates that the graphene/MnO$_2$ hybrid nanosheets could be

an attractive electrode material for supercapacitors. The pseudocapacitance of MnO_2 in aqueous neutral electrolytes could be ascribed to reversible insertion-deinsertion of alkali cations (Li^+, Na^+, K^+) or protons (H^+) [231, 435].

$$MnO_2 + M^+ + e^- \leftrightarrow MnOOM \ (M^+ = Li^+, Na^+, K^+ \ or \ H^+) \tag{7.3}$$
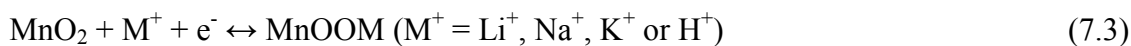
It should be noted that, the proposed charge storage mechanism involved a redox reaction between the III and IV oxidation states of Mn ions.
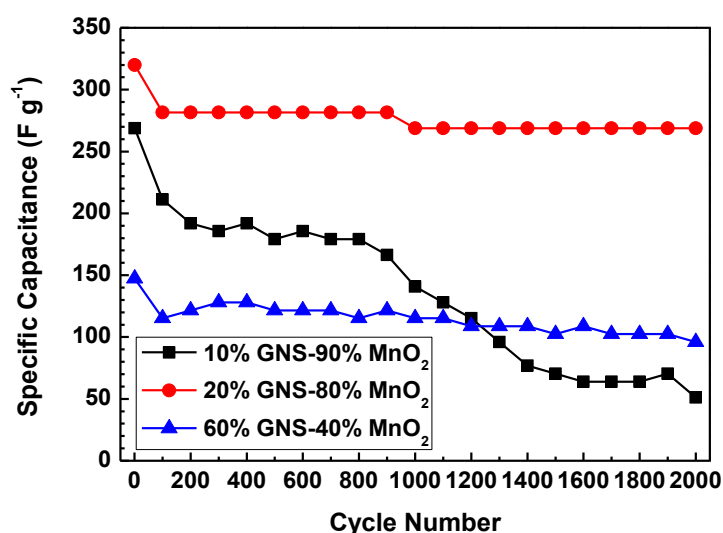
Figure 7.9 Comparison of cycling performance of graphene/MnO_2 hybrid nanosheets with different ratios in 1 M Na_2SO_4 at the current density of 500 mA g^{-1}.

Long cycle life is an essential requirement for supercapacitors. Figure 7.9 shows specific capacitance versus cycle number for graphene/MnO_2 hybrid nanosheets with different ratios. The initial specific capacitance of graphene/MnO_2 (60-40 %) sample was 150 F g^{-1} and 66% of the initial capacitance was retained after 2000 cycles. When the amount of MnO_2 was increased to 80% in the hybrid nanosheets, the electrode shows a high initial specific capacitance of 320 F g^{-1} with a slight decrease to 280 F g^{-1} after 1000 cycles. The electrode maintained 84% of the initial capacitance after 2000 cycles. The initial specific capacitance of the sample with a ratio of 1:9 was 270 F g^{-1},

but the capacitance retention was only 19 % after 2000 cycles. In this sample, the low percentage of graphene nanosheets resulted in fewer spaces to anchor MnO_2 nanosheets. Therefore, the utilization of MnO_2 is low, which results in the decrease of specific capacitance and low capacitance retention. The significant improvement of specific capacitance can be ascribed to the contributions of both graphene and MnO_2 nanosheets.
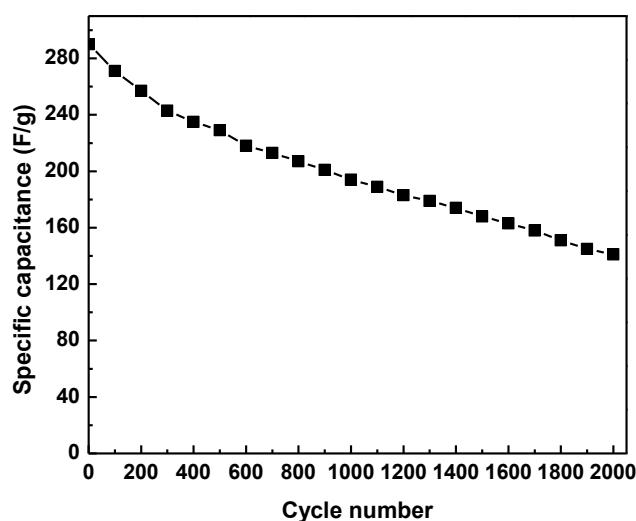
Figure 7.10 Cycling performance of MnO_2 nanosheets at the current density of 500 mA g^{-1} in 1 M Na_2SO_4.

The morphology and surface area of the material are important factors to enhance the specific capacitance and cycle stability. If the arrangement of the material does not possess adequate gaps to accommodate electrolyte ions then low value of capacitance will be achieved. Among all the polymorphs of the manganese dioxides birnessite-type two-dimensional (2D) layered nanaostructures, reveal an exceptional surface morphology, particularly their two-dimensionality and high surface area. Birnessite is an attractive layered 2D sheets displays edge-sharing MnO_6 octahedra separated from each other by exchangeable cations and water molecules in the interlayer region [434, 445, 446]. Metal cations can readily move into or out of the interlayer space. In our

hybrid material MnO_2 nanosheets are birnessite-type two dimensional (2D) layered structure. This 2D layered structure is favourable for the intercalation of electrolyte ions and protons. Both graphene and MnO_2 have nanosheet morphology. The electrolyte ions and protons can facilely diffuse into the 2D layered structure of hybrid nanosheets and therefore enhance the specific capacitance. Although the specific capacitance of MnO_2 nanosheets is close to the value of the graphene/MnO_2 hybrid nanosheets however, its cycling performance is very poor (Supplementary information Fig. 7.10). The capacitance of the bare MnO_2 nanosheets decreases dramatically on cycling. The specific capacitance retained only 49% after 2000 charge-discharge cycling. In the hybrid material, graphene nanosheets provide a highly conductive network for electron transfer. Meanwhile, MnO_2 nanosheets can efficiently inhibit the stack of graphene nanosheets, and therefore, increases the accessible surface area and facilitate the transport of ions in the electrode material, which improves the electric double layer capacitance. The effective charge transfer played a significant role in enhancing the specific capacitance. Therefore, graphene/MnO_2 hybrid nanosheets achieved a significant improvement of specific capacitance and cyclability.

7.4 Conclusions

Graphene/MnO_2 hybrid nanosheets were successfully prepared and their applications as electrode materials for supercapacitors were investigated. The as-prepared hybrid nanosheets were characterized by XRD, FESEM, TEM and EDX analyses. Cyclic voltammetry and charge-discharge measurements showed ideal capacitive behaviour of graphene/MnO_2 hybrid nanosheets. The specific capacitance of graphene/MnO_2 hybrid electrode (1:4) was 320 F g^{-1} at a discharge current density of 500 mA g^{-1}. The electrode retained 84% of the initial specific capacitance after 2000 cycles, indicating excellent

cycle stability. Graphene/MnO$_2$ hybrid materials could be a promising electrode material for high-performance supercapacitors.

Chapter 8 A microwave synthesis of mesoporous NiCo$_2$O$_4$ nanosheets as electrode materials for lithium ion batteries and supercapacitors

8.1 Introduction

The ever-increasing energy consumption and the limited supply of fossil fuels combined with the urgent need to reduce CO_2 emissions are driving the development of energy storage and conversion technologies to store energy from renewable and alternative sources. In recent years, we have seen notable improvement in the development of technologies for renewable energy harvesting, such as fuel cells, wind turbines and photovoltaic cells [449-451]. However, the production of renewable energy significantly relies on environmental conditions, e.g., the day time, the night time and the wind. Therefore, the availability of appropriate technologies is required to capture and store the energy generated and to stabilize the electricity grid. Electrochemical energy storage systems are promising to serve as such supporting facilities, namely, lithium-ion batteries and supercapacitors [452, 4, 453]. Lithium-ion batteries have been successfully incorporated in mobile electronics as clean and reliable energy storage devices. They are becoming a key-empowering technology for hybrid electric vehicles (HEV), plug-in hybrid electric vehicles (PHEV) and full electric vehicles [3]. Recently, supercapacitors also known as electrochemical capacitors have attracted enormous attention due to their high power density and longer cycle life. Supercapacitors can play a significant role as voltage support for systems during increased loads from portable electronics to electric vehicles [454, 201].

The performance of lithium-ion batteries and supercapacitors significantly depends on the applied electrode materials. These two electrochemical energy storage technologies

163

have been intensely impacted by nano-science and technology [455, 224]. Nanostructured materials are attractive because of their large specific surface area, which provides numerous electroactive sites and can efficiently accommodate the mechanical strain caused by the volume variation during the cycling process. Larger surface area can enhance the capacities through the surface lithium storage mechanism [34]. The smaller size can also shorten the ion and electron transport pathways and improve phase transformation. Nanostructured transition metal oxides have been renowned as one type of promising material for applications in energy-related systems. They are widely investigated resulting in increased electrochemical performance for lithium-ion batteries and supercapacitors [140, 456-458, 392, 459].

Mixed metal oxides such as $CuFe_2O_4$, $ZnCo_2O_4$, $CoFe_2O_4$, $ZnMn_2O_4$, $MnCo_2O_4$, and $NiCo_2O_4$ have been reported as electrode materials for lithium ion batteries and supercapacitors with better performance than single metal oxides due to their high electrical conductivity and variable oxidation state [460, 174, 461-463, 256, 254, 176]. Among different nanostructured mixed metal oxides, $NiCo_2O_4$ is considered as a promising electrode material because of its good electronic conductivity [337, 464-466]. Various synthesis techniques have been employed to prepare $NiCo_2O_4$ with different shapes and sizes [467-470]. In particular, electrode materials with porous structures have many advantages that are favourable to enhance the electrochemical performances of lithium-ion batteries and supercapacitors. These include: (i) Porous materials have the ability to alleviate volume variation throughout the cycling process and therefore, enhance the structural integrity; (ii) Porous materials can provide short ion pathway for lithium ion diffusion and (iii) Large surface area for the electrode/electrolyte contact [415]. Shen *et al.* have reported a simple surfactant-assisted hydrothermal method with a post annealing treatment to grow mesoporous $NiCo_2O_4$ nanowire arrays on carbon

textiles with firm adhesion [471]. As a binder-free electrode, the mesoporous flexible $NiCo_2O_4$/carbon electrode demonstrated high capacitance/capacity, good cycling stability and excellent rate performance for lithium-ion batteries and supercapacitors. Zhang's group also showed interconnected mesoporous $NiCo_2O_4$ nanosheets grown on different conductive substrates through a general solution method combined with a simple post heat treatment [472]. The $NiCo_2O_4$ nanosheets-Ni foam electrode exhibited enhanced electrochemical properties with high specific capacitance and better cycling stability.

Among the different synthesis techniques, the microwave method has attracted much attention owing to its intrinsic advantages, including short heating time and homogeneous thermal transmission [353, 354]. In this paper, we report the synthesis of porous $NiCo_2O_4$ nanosheets through a facile microwave method followed by annealing in air. When applied as anode materials for lithium ion batteries and electrode materials for supercapacitors, the as-prepared porous $NiCo_2O_4$ nanosheets present a high specific capacity/capacitance and excellent cycling stability over long term cycling.

8.2 Experimental

8.2.1 Synthesis of $NiCo_2O_4$ nanosheets

In the typical synthesis process, 0.2 g $Ni(NO_3)_2 \cdot 6H_2O$ and 0.4 g $Co(NO_3)_2 \cdot 6H_2O$ were dissolved in 10 mL de-ionized (DI) water to form a homogeneous solution. 0.2 g urea and 35 mL ethylene glycol (EG) were added to the above solution and stirred for 2 h. The solution was then heated to 140 ^{o}C for 30 min in a microwave synthesizer (Model: NOVA-II). After cooling to room temperature, the green precipitate was filtered, washed with DI water and ethanol several times and dried at 80 ^{o}C in an oven for 12 h.

In order to obtain porous NiCo$_2$O$_4$ nanosheets, the dried material was annealed with a heating rate of 1 ^{o}C/min at 300 ^{o}C, in the air for 3 h.

8.2.2 Materials characterization

The crystallographic information of the synthesized NiCo$_2$O$_4$ nanosheets were studied using the GBC MMA X-ray diffractometer (λ = 0.15405 nm). Field emission scanning electron microscopy (FESEM, Zeiss Supra 55VP) with an energy-dispersive X-ray (EDX) attachment and transmission electron microscopy (TEM, JEOL 2011 TEM facility) were employed to examine the morphology and structure of the material. The specific surface area and the porosity distributions were calculated using Brunauer-Emmett-Teller (BET) nitrogen adsorption-desorption isotherms and Barrett-Joyner-Halenda (BJH) method, respectively by using a Micromeritics 3 Flex^{TM} surface characterization analyzer at 77 K. Thermogravimetric analysis (TGA) was carried out on a 2960 SDT thermal analyzer with a heating rate of 10 ^{o}C min^{-1}, from room temperature to 600 ^{o}C in air.

8.2.3 Electrochemical testing

All the electrochemical tests were conducted under ambient temperature in two electrode coin cells (CR2032) were assembled in a high purity argon-filled glove box (water and oxygen contents: <1 ppm) (UniLab, MBRAUN, Germany). NiCo$_2$O$_4$ nanosheets were used as the working electrode and the battery grade lithium foil as the counter and reference electrodes for lithium ion batteries. 1 M LiPF$_6$ in a mixture of ethylene carbonate and dimethyl carbonate at 1:1 (v/v) was used as the electrolyte solution. For supercapacitors, a beaker-type three-electrode cell was assembled with a working electrode, a platinum foil as a counter electrode and saturated calomel electrode (SCE) as a reference electrode in 2 M KOH solution. The working electrodes

were fabricated by mixing 70 wt % $NiCo_2O_4$ nanosheets (active material), with 20 wt % conductive additive (acetylene carbon black) and 10 wt % binder (poly(vinylidene fluoride), PVDF) in *N*-methyl-2-pyrrolidone. The slurry mixture was then uniformly coated (area of loading: 1 cm^2, and active material is around 0.8 mg) uniformly onto a copper foil and pre-treated nickel foam substrate for lithium-ion batteries and supercapacitors, respectively. The electrodes were dried at 100 ^{o}C under vacuum for 12 h. For LIBs, the galvanostatic charge-discharge was conducted by the NEWARE-BTS battery tester with a potential window of 0.01-3.0 V. A cyclic voltammetry (CV) experiment was carried out using a CHI 660C electrochemistry workstation in the voltage range of 0.01 to 3.0 V (vs Li^+/Li) and at the scan rate of 0.1 mV s^{-1}. For supercapacitors, the electrochemical properties were evaluated by the CV technique and galvanostatic charge-discharge measurements.

8.3 Results and discussion

8.3.1 Structural analysis and surface characterization

Two steps were employed to prepare $NiCo_2O_4$ nanosheets. Firstly, green mixed metal (Ni, Co) hydroxide precursors were formed. In the second step, the hydroxide precursors were thermally converted to black $NiCo_2O_4$ nanosheets.
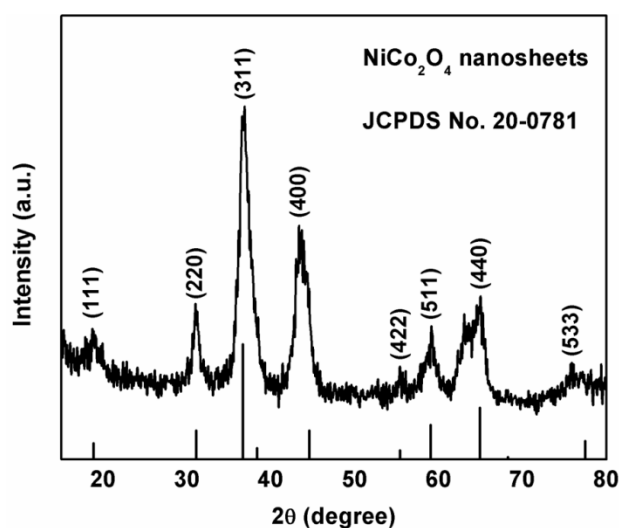
Figure 8.1 XRD pattern of $NiCo_2O_4$ nanosheets.

The XRD pattern (Fig. 8.1) reveals the phase purity and crystalline structure of the as-prepared $NiCo_2O_4$ nanosheets. The representative peaks can be indexed to (111), (220), (311), (400), (422), (511), (440) and (533) crystal planes and are in good agreement with the spinel $NiCo_2O_4$ crystalline structure (JCPDS card no. 20-0781). No any others impurity peaks can be identified.
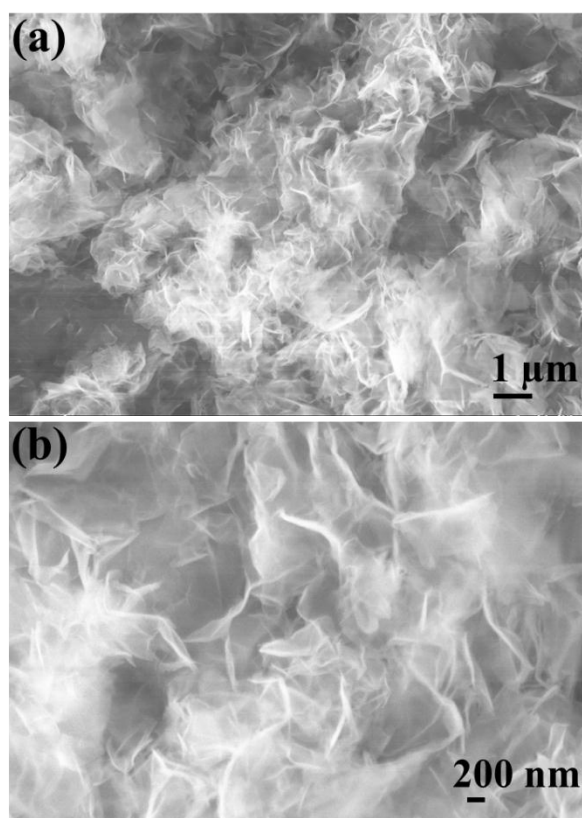
Figure 8.2 FESEM images of the Ni-Co based intermediate (a) low magnification and (b) high magnification.

The morphologies of the Ni-Co based precursor and $NiCo_2O_4$ nanosheets were observed by FESEM. Figure 8.2(a) and 8.2(b) show the low and high magnification FESEM images of the Ni-Co based precursor. The precursor possesses a nanosheet structure and the nanosheets are interconnected with each other with a rippled silk morphology. The Ni-Co based precursors were converted to black crystalline $NiCo_2O_4$ nanosheets with well-conserved morphology after thermal treatment at a relatively low temperature of

300 °C (Fig. 8.3(a) and 8.3(b)). These nanosheets contain numerous mesopores with abundant open space and electroactive sites (Fig. 8.3(c) and 8.3(d)). The surface composition of $NiCo_2O_4$ nanosheets were also determined by energy-dispersive X-ray spectroscopy (EDX), which confirms the existence of Ni, Co and O atoms (Fig. 8.4). The molar ratio of Ni and Co is approximately 1:2 which is very close to that in the precursor solution. The peaks of carbon are originated from the C substrate.
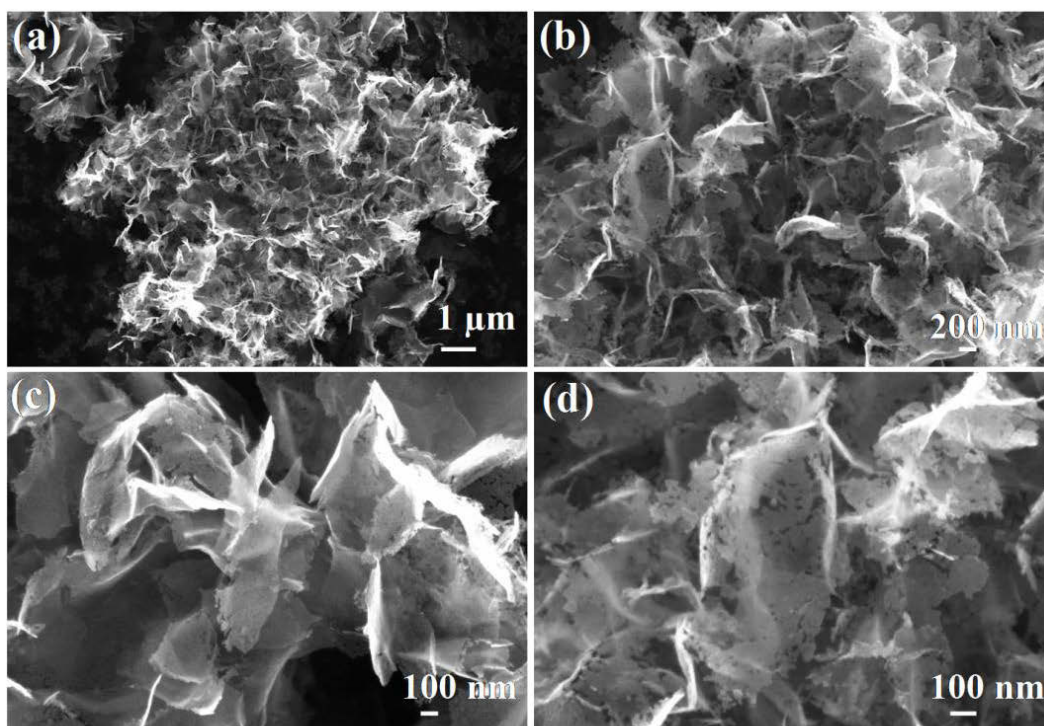
Figure 8.3 FESEM images of $NiCo_2O_4$ nanosheets (a) and (b) low magnification; (c) and (d) high magnification.

To provide a detailed crystal structure, we further analysed $NiCo_2O_4$ nanosheets used TEM techniques, selected area electron diffraction (SAED) and high-resolution TEM (HRTEM). Figure 8.5(a) shows the low magnification TEM image of $NiCo_2O_4$ nanosheets. The as-synthesized $NiCo_2O_4$ nanosheets present wrinkled silk-like thin sheets with high surface area. The selected area electron diffraction pattern (Fig. 8.5(b)) shows distinct diffraction rings, which can be fully indexed to the $NiCo_2O_4$ crystal

structure. The high magnification TEM image (Fig. 8.5(c)) demonstrates the porous nature of $NiCo_2O_4$ nanosheets.
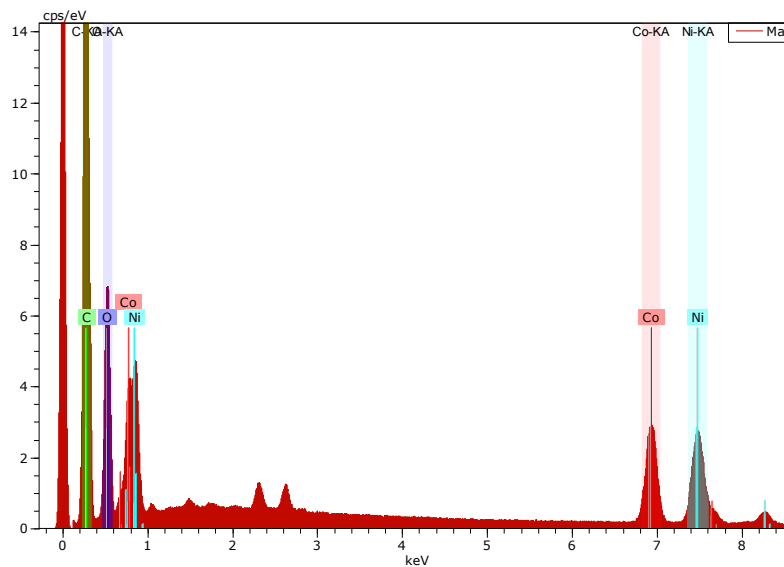
Figure 8.4 SEM-EDX pattern of $NiCo_2O_4$ nanosheets.
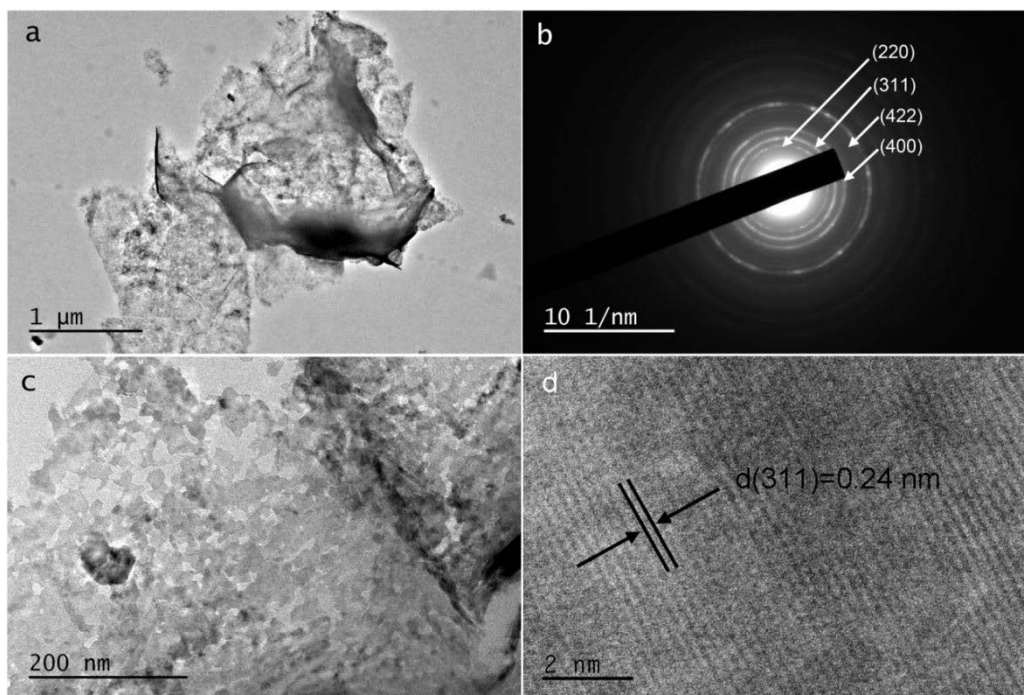
Figure 8.5 Low magnification TEM image of $NiCo_2O_4$ nanosheets (b) its corresponding selected area electron diffraction patterns (SAED), (c) high magnification TEM image, and (d) lattice resolved HRTEM image.

The lattice resolved HRTEM image (Fig. 8.5(d)) reveals the $NiCo_2O_4$ nanocrystal, in which the (311) crystal plane is indexed with an interplane spacing of 0.24 nm of the $NiCo_2O_4$ spinel phase.

During the microwave synthesis process, the formation of the Ni-Co based precursor involves the well-known hydrolysis-precipitation process. Urea was used as a slow-released pH adjusting precipitation agent, it generates OH^- ions in the reaction medium, which then react with Ni^{2+} and Co^{2+} to form Ni-CoOOH. The crystal growth is influenced by the controlled rate of OH^- ions. With the assistance of ethylene glycol, the generated material formed a nanosheet structure. The porous $NiCo_2O_4$ nanosheets were obtained by calcination of the Ni-CoOOH at 300 ^{o}C in air for 3 h. The reactions involved in the formation of $NiCo_2O_4$ nanosheets can be described as follows: [392, 320]

$$NH_2CONH_2 \rightarrow NH_4^+ + NCO^- \tag{8.1}$$

$$NCO^- + 3H_2O \rightarrow HCO_3^- + NH_4^+ + OH^- \tag{8.2}$$

$$Ni^{2+} + Co^{2+} + 3OH^- \rightarrow Ni\text{-}CoOOH + H_2O \tag{8.3}$$

$$2Ni\text{-}CoOOH \rightarrow 2NiCo_2O_4 + H_2O \tag{8.4}$$

The specific surface area and porous nature of the $NiCo_2O_4$ nanosheets were also examined by nitrogen adsorption-desorption measurements, which is shown in Fig. 8.6. Figure 8.6 revealed a typical Langmuir type IV isotherm with an apparent hysteresis loop, indicating the characteristics of the mesoporous nature [360]. The porous $NiCo_2O_4$ nanosheets show a high BET specific surface area of 143 $m^2\,g^{-1}$ with a narrow pore size distribution (2-5 nm) (inset Fig. 8.6) and a pore volume of 0.35 $cm^3\,g^{-1}$. Since mesoporous structures can facilitate ion diffusion at the electrode/electrolyte interface

during electrochemical processes, $NiCo_2O_4$ nanosheets could have enhanced electrochemical performances. Thermogravimetric analysis (TGA) was carried out between room temperature to 600 ^{o}C to investigate the thermal behaviour of the Ni-Co based precursor. As shown in Fig. 8.7, the first weight loss below 250 ^{o}C is ascribed to the loss of physically and chemically adsorbed water. While the second notable weight loss is caused by the thermal decomposition of the precursor to $NiCo_2O_4$ nanosheets. There is no obvious weight loss observed in the temperature range between 500 ^{o}C and 600 ^{o}C, indicating the complete decomposition of the precursor.
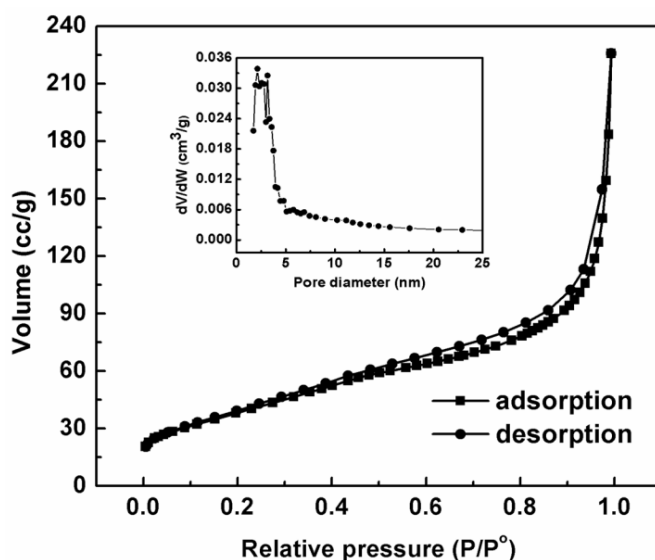
Figure 8.6 Nitrogen adsorption/desorption isotherm and corresponding BJH pore size distributions (inset) of $NiCo_2O_4$ nanosheets.

8.3.2 Electrochemical performances for lithium-ion batteries and supercapacitors

In order to demonstrate the benefits of this porous nanosheet structure and high specific surface area, the electrochemical properties of $NiCo_2O_4$ nanosheets were evaluated as an anode material for lithium ion batteries. Figure 8.8(a) shows the first three cyclic voltammetry (CV) curves of the $NiCo_2O_4$ nanosheet electrode at the scan rate of 0.1 mV s^{-1}. Three peaks were observed in the first cathodic sweep. The peak at ~0.60 V can be attributed to the formation of the solid electrolyte interface (SEI) layer. The sharp

peak at ~0.93 V was assigned to the reduction of Ni^{2+} and Co^{3+} to metallic Ni and Co, respectively, whereas the broad peak at ~1.23 V can be ascribed to the formation of Li_2O [406, 473]. In the first anodic sweep, two oxidation peaks at ~1.36 V and ~2.23 V are observed, which can be ascribed to the oxidation of the metallic Ni and Co to nickel oxides and cobalt oxides. From the second cycle there is no apparent change in oxidation and reduction peaks, indicating a good electrochemical reversibility.
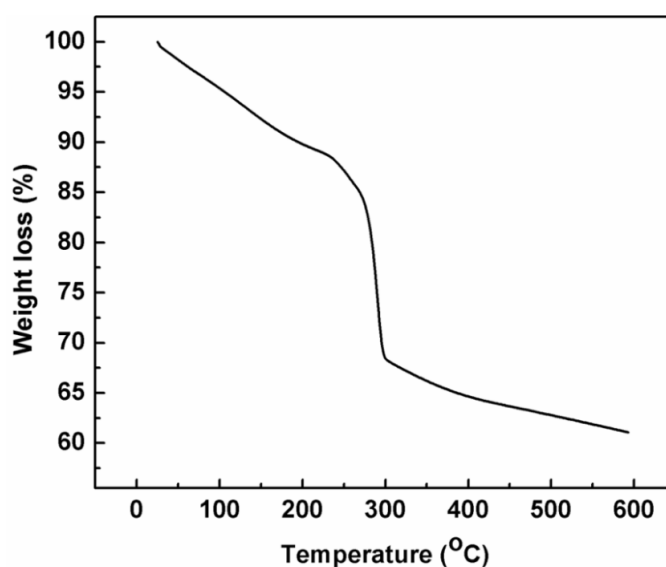
Figure 8.7 TGA curve for the Ni-Co based intermediate.

Based on the previous reports the complete electrochemical reactions are believed to proceed as follows: [413, 474, 402]

$$NiCo_2O_4 + 8\ Li^+ + 8e^- \rightarrow Ni + 2Co + 4Li_2O \tag{8.5}$$

$$Ni + Li_2O \leftrightarrow NiO + 2Li^+ + 2e^- \tag{8.6}$$

$$Co + Li_2O \leftrightarrow CoO + 2Li^+ + 2e^- \tag{8.7}$$

$$CoO + 1/3Li_2O \leftrightarrow 1/3Co_3O_4 + 2/3Li^+ + 2/3e^- \tag{8.8}$$
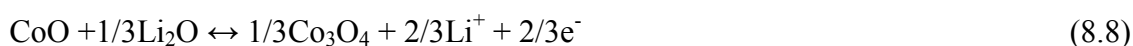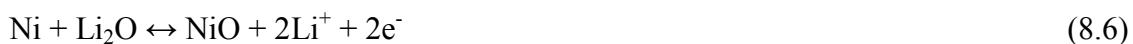
Figure 8.8(b) presents the galvanostatic discharge-charge profiles of the porous NiCo$_2$O$_4$ nanosheet electrode for the first, second and fiftieth cycle in the voltage range of 0.01-3.0 V. In the first cycle, the discharge capacity reached about 1520 mA h g^{-1}, which is associated with the formation of a solid electrolyte interface (SEI) layer [402]. In the first charge process, the electrode shows the capacity of 798 mA h g^{-1}. The large irreversible capacity loss in the first cycle can be attributed to the formation of the SEI layer that cannot fully decompose during the first charge [402]. In the subsequent charge-discharge curves, a significant deviation of voltage is observed.
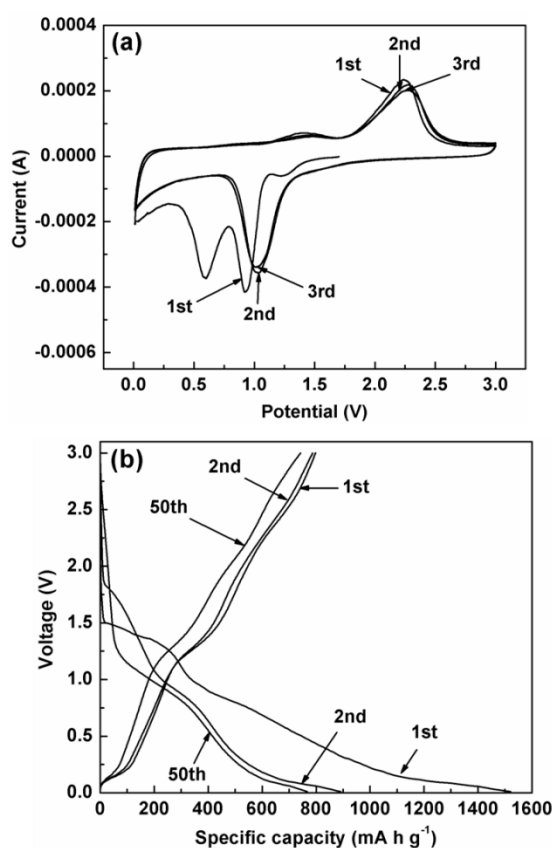
Figure 8.8 (a) The first three consecutive CV curves in the potential range of 0.01-3.0 V and (b) galvanostatic discharge and charge profiles for the selected cycles of NiCo$_2$O$_4$ nanosheets at the current density of 100 mA g^{-1}.

This may be due to the polarization related to ion transfer during the cycling process, which is often found in many transition metal oxides [415, 475]. The NiCo$_2$O$_4$

nanosheet electrode delivered discharge capacities of 891 and 767 mA h g^{-1} in the second and fiftieth cycles, respectively.

The rate capability is an important parameter for lithium ion batteries. The NiCo$_2$O$_4$ nanosheet electrode was cycled at different current densities (100-1000 mA g^{-1}), as shown in Fig. 8.9. The electrode delivered discharge capacities of 1149, 936, 701 and 487 mA h g^{-1} at the current densities of 100, 200, 500 and 1000 mA g^{-1}, respectively, demonstrating good cycling performance at varied current rates. When the current density reversed back to 500 and 100 mA g^{-1}, the discharge capacities almost recovered to the previous values. This indicates that the mesoporous NiCo$_2$O$_4$ nanosheet electrodes tolerate the high current charge/discharge.
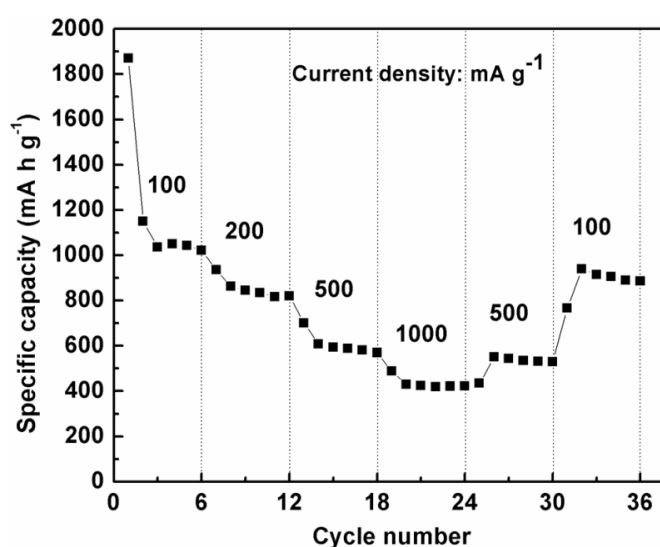
Figure 8.9 (a) Rate performance of NiCo$_2$O$_4$ nanosheets.

Figure 8.10 presents the discharge capacity versus cycle number at the current density of 100 mA g^{-1}. After 50 cycles, the NiCo$_2$O$_4$ nanosheet electrode still shows a discharge capacity of 767 mA h g^{-1}, which is almost 86 % of the discharge capacity in the second cycle. This demonstrates that the porous structure is beneficial for enhanced electrochemical performance. During the cycling process, the porous nanosheet

structure can cushion the volume variation of the electrode and effectively alleviate the pulverization problem, thus improve cycling stability. As shown in Fig. 8.10, the electrode shows an average Coulombic efficiency of 97 % form the second cycle.
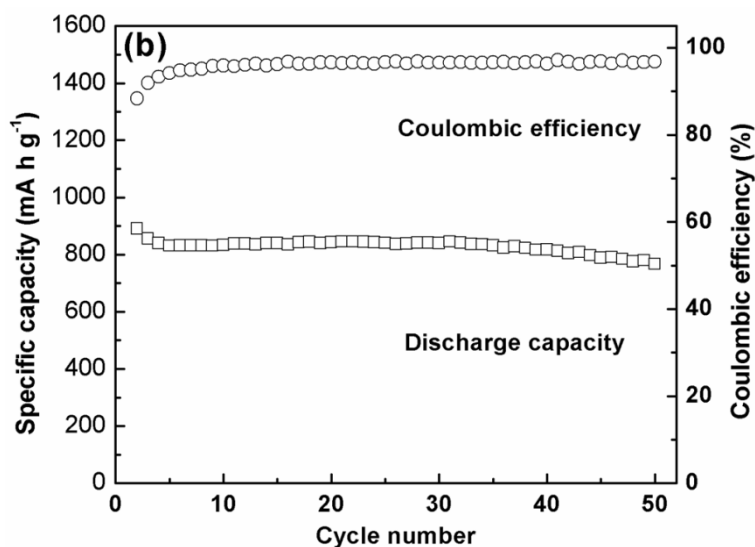
Figure 8.10 Cycling performance and Coulombic efficiency of $NiCo_2O_4$ nanosheets.

The porous $NiCo_2O_4$ nanosheets were also investigated as electrode materials for supercapacitors. The galvanostatic charge-discharge tests were carried out in 2 M KOH electrolyte at different current densities within the voltage range of 0-0.6 V, which is shown in Fig. 8.11(a). The non-linear charge-discharge curves indicate the pseudocapacitive behaviour of $NiCo_2O_4$ nanosheets. The specific capacitance could be calculated by using the following formula:

$$C = I\Delta t/\Delta Vm \qquad (8.9)$$

In which, I refers to the discharge current, Δt represents the discharge time, ΔV denotes the voltage interval and m is the mass of the active material. Thus the calculated specific capacitances of mesoporous $NiCo_2O_4$ nanosheets are 560, 525, 467 and 400 F g^{-1} at the current densities of 2, 5, 10 and 20 A g^{-1}, respectively. When the current density is

increased from 2 to 20 A g^{-1} the specific capacitance still retained 71 %, which suggests the stable reversibility of the porous $NiCo_2O_4$ nanosheets.

The cyclic voltammetry (CV) of the as-synthesized $NiCo_2O_4$ nanosheets were measured at different scan rates in a potential range of -0.2 to 0.6 V (*vs.* SCE). The corresponding CV curves are shown in Fig. 8.11(b). All curves exhibit well-defined redox peaks, which further confirmed the capacitive behaviour mainly originating from the Faradic reaction.
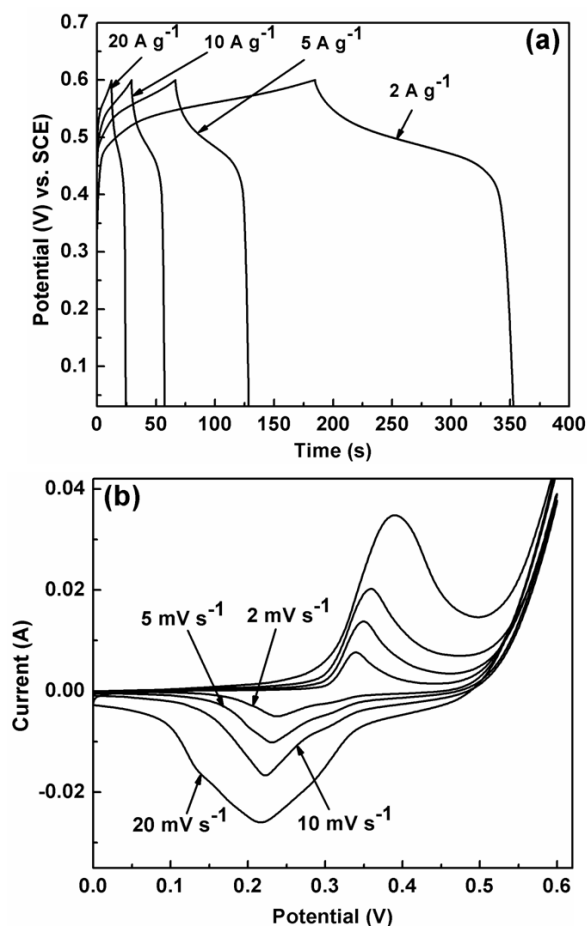
Figure 8.11 (a) Galvanostatic discharge and charge curves at different current densities (2 to 20 A g^{-1}) and (b) CV curves at various scan rates ranging from 2 to 20 mV s^{-1} for the porous $NiCo_2O_4$ nanosheet electrode in 2 M KOH electrolyte.

Figure 8.12 presents the cycling stability of the $NiCo_2O_4$ nanosheet electrode at a current density of 10 A g^{-1}. The electrode maintained a stable cycling performance, and

95.2 % specific capacitance is retained even after 5000 charge-discharge cycles, demonstrating excellent long-term electrochemical stability. The good electrochemical performances could be ascribed to the exceptional structural feature of the material. In particular, the large specific surface area and the porous structure are beneficial for the improvement of electrochemical properties. The large specific surface area provides numerous electro-active sites for electrochemical reactions. The existing pores in the nanosheets can act as a reservoir for ions, provide efficient transport pathways and ensure adequate contact between the electrode and electrolyte [408]. The porous feature also buffers the volume change originating from the high rate insertion/extraction of OH^- ions during cycling, thereby improving cycling stability. The inset in Fig. 8.12 shows the charge-discharge curves of $NiCo_2O_4$ nanosheets at the current density of 20 A g^{-1}. All curves show high similarity, which further confirms the excellent electrochemical reversibility.
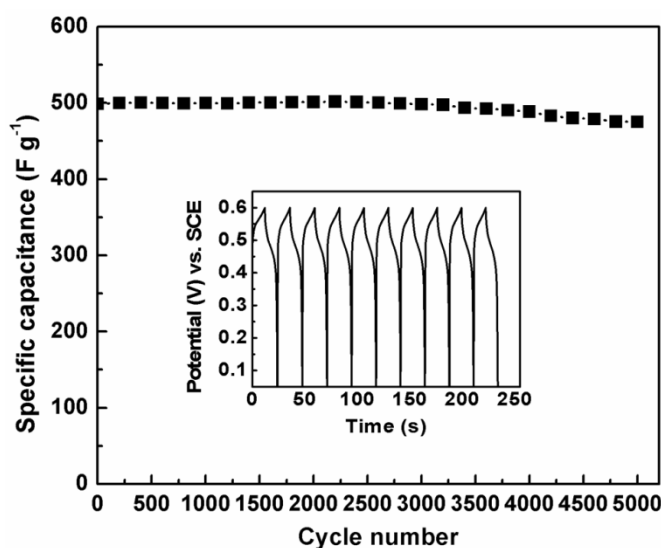
Figure 8.12 Cycle performance of porous $NiCo_2O_4$ nanosheet electrode at the current density of 10 A g^{-1}. The charge and discharge curves for the first ten cycles at the current density of 20 A g^{-1} (the inset in Fig. 8.12).

8.4 Conclusions

In summary, we have successfully synthesized mesoporous $NiCo_2O_4$ nanosheets by a microwave method combined with subsequent annealing. Structural and morphological features of the material confirmed the mesoporous structure with a large specific surface area. The $NiCo_2O_4$ nanosheets were applied as anode materials for lithium ion batteries. The material delivered a reversible capacity of 767 mA h g^{-1} (capacity retention 86 %) after 50 cycles, due to its advantageous structure. When used as electrode materials for supercapacitors, the as-prepared $NiCo_2O_4$ nanosheets showed superior pseudocapacitive performance and excellent cycling stability (4.8 % loss after 5000 cycles). These results clearly illustrate that the porous $NiCo_2O_4$ nanosheets are highly desirable as advanced electrode materials for lithium-ion batteries and supercapacitors. Moreover, this synthesis technique can be extended to prepare other mixed metal oxides with unique morphology and structure.

Chapter 9 Mesoporous MnCo$_2$O$_4$ with a flake-like structure as advanced electrode materials for lithium-ion batteries and supercapacitors

9.1 Introduction

Energy storage has appeared as one of the most essential topics in upcoming societies [27, 20, 208]. Owing to the intermittent availabilities of energy from other alternative energy sources and the increasing demand for energy, for mobile electronic devices to electric vehicles, it is now essential to develop advanced high-performance energy storage devices. As electrochemical energy storage devices, lithium ion batteries (LIB) and supercapacitors have received enormous interest due to their high energy and power densities. As a consistent energy storage device, rechargeable LIBs are currently unparalleled because of their high energy density, environmental benignity and long cycle life [1, 4]. They have been widely applied to many applications such as portable electronics, pure electric or hybrid electric vehicles, smart power grids and so on. Supercapacitors are exceptionally desirable energy storage devices, which can deliver high power and reasonable energy densities concurrently. Long calendar life and short charging time are also essential features for supercapacitors in supplementing the batteries. They are used for various power source applications including instant power sources for portable electronic devices, and as supporting power sources for hybrid electric car [324, 454, 207]. Electrode materials play a vital role in the development of high performance energy storage devices. Significant research efforts have been devoted towards discovering environmentally benign and inexpensive electrode materials for LIBs and supercapacitors.

Over the last decade, nanostructured transition metal oxides have been widely studied as alternative anode materials for LIBs owing to their high theoretical specific capacity (500 to 1000 mA h g^{-1}), compared to the commercially used graphite (372 mA h g^{-1}) [374, 476-482]. Transition metal oxides have also been investigated as electrode materials for supercapacitors [483-486, 497, 498]. However, most of the transition metal oxides show reduced cycling performance due to their low conductivity and typical agglomeration during long-term charge-discharge cycling. Recently, complex oxides of transition metal have attracted enormous attention as possible electrode materials for LIBs and supercapacitors, which can synergistically increase the electrochemical performances in terms of reversible capacity, structural stability and electrical conductivity [487-490]. It has been reported that $NiCo_2O_4$ possessed superior electronic conductivity and higher electrochemical performance than nickel oxides and cobalt oxides [337]. Owing to their synergistic effect many complex oxides such as $ZnMn_2O_4$ [462], $ZnCo_2O_4$ [491], $NiMn_2O_4$ [492], $CuCo_2O_4$ [170], $MnCo_2O_4$ [418, 493] and $NiCo_2O_4$ [408] have been studied as high capacity anode for LIBs and electrode materials for supercapacitors. Among different nanostructures, mesoporous materials have been established as a potential candidate for energy storage, because of their ability to alleviate volume changes during the charge-discharge process, high surface area and enlarged electroactive sites [408, 406]. Thus, complex oxides with porous features are expected to enhance electrochemical properties.

In this report, mesoporous flake-like $MnCo_2O_4$ was successfully synthesized by using a hydrothermal method. When investigated as anode materials for LIBs and as electrode materials for supercapacitors, the as-prepared flake-like $MnCo_2O_4$ demonstrated high specific capacity/capacitance and excellent cycling stability over prolonged charge-discharge cycling.

9.2 Experimental

9.2.1 Preparation of flake-like $MnCo_2O_4$

In a typical procedure, 0.2 g of $Mn(NO_3)_2 \cdot 4H_2O$ and 0.464 g of $Co(NO_3)_2 \cdot 6H_2O$ were added to 25 ml of deionized (DI) water and stirred at room temperature under magnetic stirring. Then, 0.518 g of glycine and 0.586 g of Na_2SO_4 salt was added to the above mixture. 1.5 ml of NaOH solution (5 M) was added drop wise to the mixture and stirred for 2 h. The mixture was then transferred into a 30 ml Teflon-lined stainless steel autoclave and maintained at 180 ^{o}C for 20 h in an oven. Afterward, the autoclave was cooled to room temperature naturally. The obtained product was filtered and washed with DI water and ethanol several times and dried under vacuum at 80 ^{o}C overnight. Finally, the precursor was calcined with a heating rate of 2 ^{o}C min^{-1} at 600 ^{o}C for 10 h to obtain the mesoporous flake-like $MnCo_2O_4$.

9.2.2 Physical Characterization

The crystal structures of the flake-like $MnCo_2O_4$ were investigated by using GBC MMA X-ray diffractometer (λ = 0.15405 nm). The morphology and detailed of the crystal structure of the sample were examined by field emission scanning electron microscopy (FESEM, Zeiss Supra 55VP) and transmission electron microscopy (TEM, JEOL 2011 TEM facility). Measurements of the specific surface area and porosity analysis were performed using the Brunauer-Emmett-Teller (BET) method and Barrett-Joyner-Halenda (BJH) equation, respectively, using a Micromeritics 3 Flex^{TM} surface characterization analyser at 77 K. Thermogravimetric analysis (TGA) was carried out under air flow with a heating rate of 10 ^{o}C min^{-1} from room temperature to 600 ^{o}C by using the 2960 SDT thermal analyser.

9.2.3 Electrochemical measurements

Electrochemical tests were carried out using CR2032 coin cells assembled in a high-

purity argon-filled glove box (water and oxygen contents: <1 ppm) (UniLab, MBRAUN, Germany). Flake-like $MnCo_2O_4$ was used as the working electrode while the battery grade lithium foil as the counter and reference electrodes for lithium ion batteries. The electrolyte was 1 M $LiPF_6$ in a mixer of ethylene carbonate and dimethyl carbonate at 1:1 (v/v). For supercapacitors, a beaker-type three-electrode cell was assembled with a working electrode, a platinum foil as a counter electrode and saturated calomel electrode (SCE) as a reference electrode in 2 M KOH solution. The working electrodes were fabricated by mixing flake-like $MnCo_2O_4$ as active materials, acetylene carbon black as the conducting material and poly(vinylidene fluoride) (PVDF) as the binder in a weight ratio of 60:20:20 (for lithium ion cells) and 70:20:10 (for supercapacitors) in N-methyl-2-pyrrolidone. The slurry mixture was applied (area of loading: 1 cm^2, and active material is around 0.8 mg) uniformly onto a copper foil substrate for lithium-ion cell test and nickel foam substrate for supercapacitors, respectively. For LIBs, the galvanostatic charge-discharge was conducted by the NEWARE-BTS battery tester with a potential window of 0.01–3.0 V. A cyclic voltammetry (CV) experiment was carried out using a CHI 660C electrochemistry workstation in the voltage range of 0.01 to 3.0 V (vs Li^+/Li) and at the scan rate of 0.1 mV s^{-1}. For supercapacitors, the electrochemical properties were evaluated by the CV technique and galvanostatic charge-discharge measurements.

9.3 Results and discussion

9.3.1 Structural and morphological analysis

A representative X-ray diffraction (XRD) pattern of the as-prepared flake-like $MnCo_2O_4$ is shown in Fig. 9.1. All of the diffraction peaks can be easily identified for the (111), (220), (311), (222), (400), (422), (511) and (440) crystal planes of the pure face-centred

cubic spinel $MnCo_2O_4$ phase in agreement with the standard value (JCPDS card no. 23-1237). No impurities were detected, indicating the pure phase of flake-like $MnCo_2O_4$.
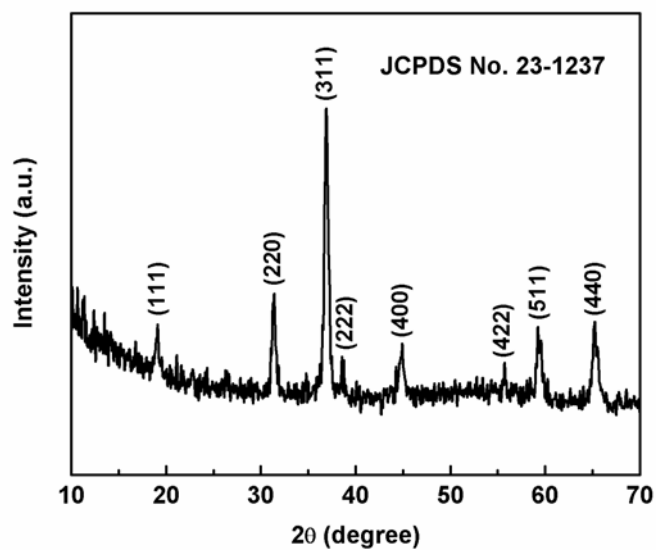
Figure 9.1 XRD pattern of flake-like $MnCo_2O_4$.
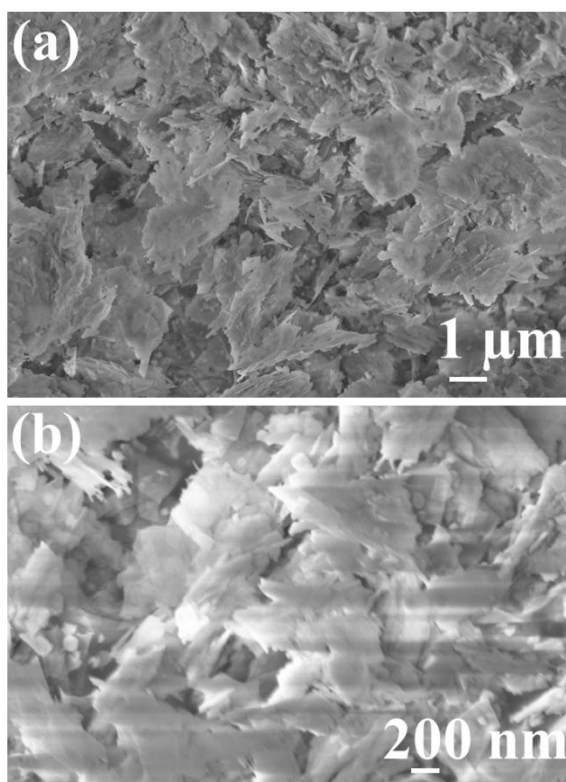
Figure 9.2 FESEM images of the flake-like Mn-Co based intermediate (a) low magnification and (b) high magnification.

The morphologies of the Mn-Co based intermediate and flake-like $MnCo_2O_4$ were examined by the field emission scanning electron microscopy (FESEM). From the low and high magnification SEM images in Fig. 9.2(a) and 9.2(b), the flake-like structure of Mn-Co based intermediate is observed. Interestingly, the flake-like structure was preserved even after high-temperature calcination of the intermediate, indicating excellent structural integrity. Figure 9.3 presents the FESEM images of the as-prepared flake-like $MnCo_2O_4$. From the low magnification SEM images (Fig. 9.3(a) and 9.3(b)), it can be seen that the materials are flake-like structures. The high magnification SEM images (Fig. 9.3(c) and 9.3(d)) show that the surface of the material is quite rough, and numerous mesopores are clearly observed on the surface of the flake-like $MnCo_2O_4$.
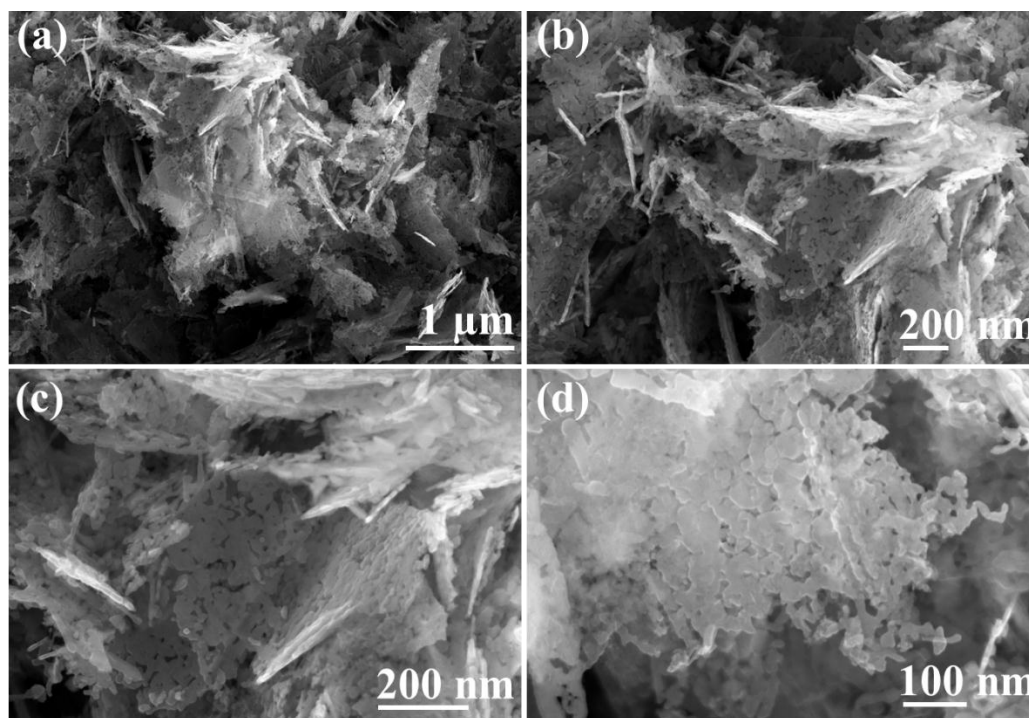
Figure 9.3 FESEM images of mesoporous flake-like $MnCo_2O_4$ ((a) and (b)) low magnification, ((c) and (d)) high magnification.

We also investigated the growth mechanism of Mn-Co based precursors and flake-like $MnCo_2O_4$. Strong alkaline conditions and the presence of glycine were indispensable for the growth of flake-like structures.
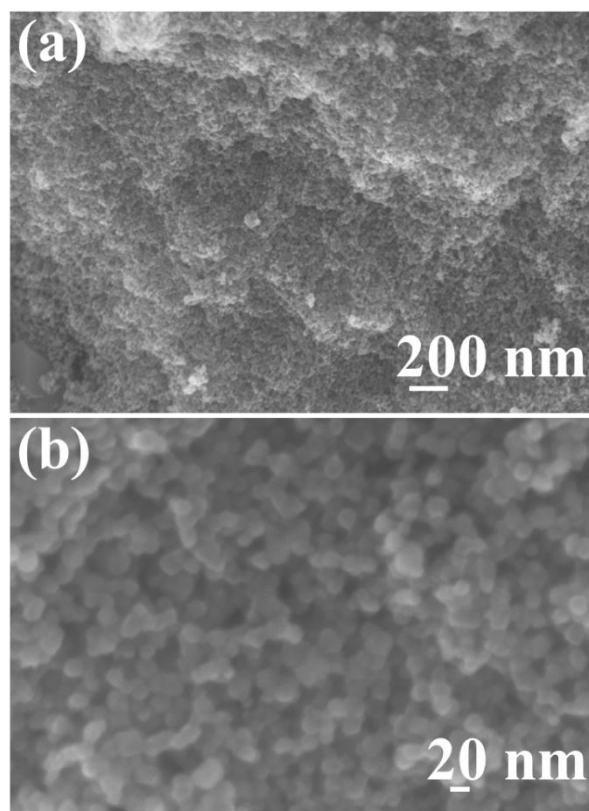
Figure 9.4 FESEM images (without glycine) (a) low magnification and (b) high magnification.

In the absence of glycine and without alkaline conditions, nanoparticles were formed (Fig. 9.4). Glycine was applied as the complexing and surface functionalizing agent. It predominantly plays a critical role in the control of shape and size. Assisted by amphiphilic glycine, the Mn-Co based precursors tend to form a layered structure, which was uniformly wrapped around by the hydrophobic part of glycine. Meanwhile, the hydrophilic part of glycine was dissolved in the aqueous solution. In the solution, the small particles of Mn-Co based precursor were firstly formed and later were re-organised into the flake-like structure under the assistance and surface functionalization of the glycine [502, 503]. During the hydrothermal process, more OH⁻ ions generate in the solution through the hydrolysis of glycine and it also helps to maintain the high pH value of the solution. In aqueous solution, metal composite hydroxides have strong

tendencies to aggregate nanocrystals. The final particle shape depends on whether orientated aggregation takes place.
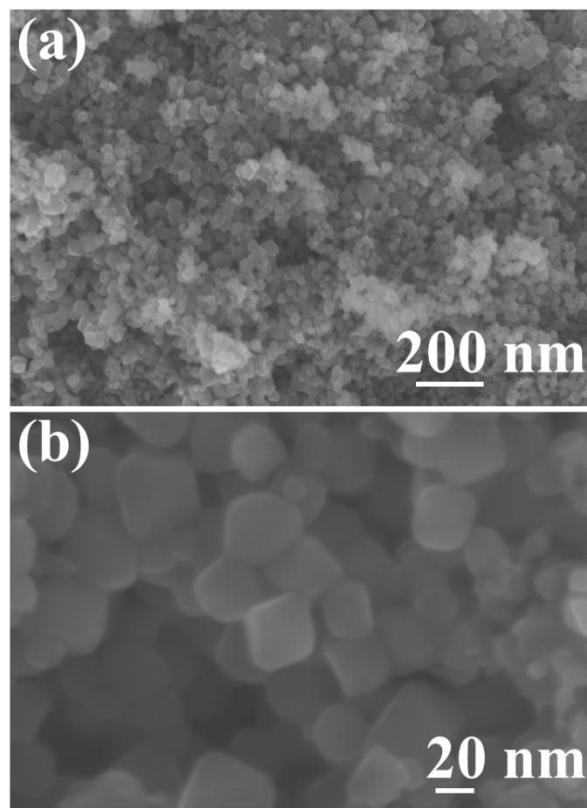
Figure 9.5 FESEM images (without Na_2SO_4) (a) low magnification and (b) high magnification.

Sodium sulfate (Na_2SO_4) plays an important role in hampering particle aggregation into forming more complex morphologies and also acts as the morphology directing agent. The sulfate ions (SO_4^{-2}) can co-ordinate with existing reactant cations (Mn^{2+}, Co^{3+}) via different co-ordination modes and strengths, which may change the dynamics of the nuclei and growth rate of crystals, resulting in oriented attachment. During the synthesis process, sulfate ions were strongly adsorbed to Mn-Co based precursor surfaces perpendicular to the c-axis of the cubic crystal system through bridging-bidentate absorption, leading to the retarded growth in the direction along the c-axis, which results in the formation of flake-like structure [505, 506]. In the absence of Na_2SO_4,

aggregated nanoparticles are formed (Fig. 9.5). The temperature also has a significant effect on morphology development. If the temperature is less than 180 ^{o}C, the products consist of mixed morphologies including particles and flakes (Fig. 9.6).
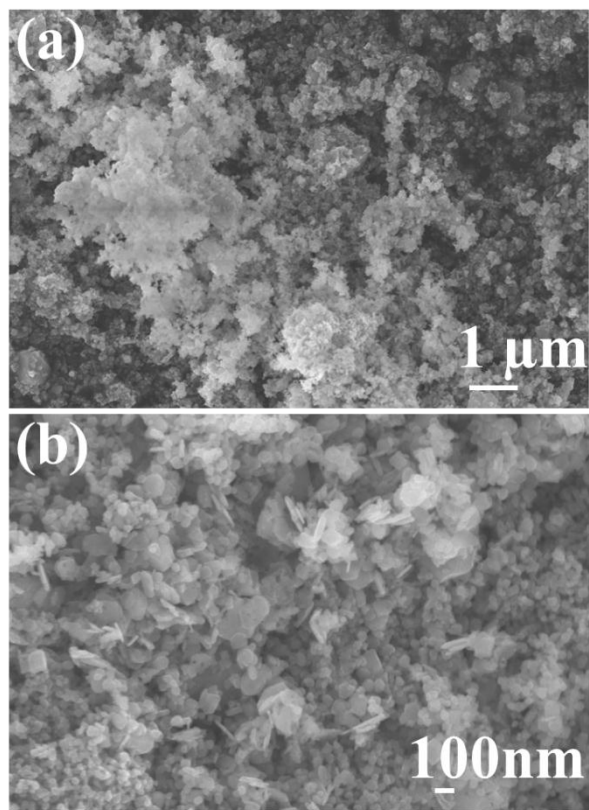
Figure 9.6 FESEM images (temperature less than 180 ^{o}C) (a) low magnification and (b) high magnification.

When the temperature is increased to 200 ^{o}C, the flake-like structure of Mn-Co based precursors can be obtained. The Mn-Co based precursors are calcined at 600 ^{o}C for 3 h in air to obtain mesoporous flake-like $MnCo_2O_4$.

The detailed crystal structure of the as-prepared flake-like $MnCo_2O_4$ were further analysed by transmission electron microscopy (TEM), selected-area electron diffraction (SAED) and high-resolution TEM (HRTEM). In the low magnification TEM image (Fig. 9.7(a)), the flake-like structure of $MnCo_2O_4$ is observed. All the selected area electron diffraction (SAED) pattern rings (Fig. 9.7(b)) taken from the corresponding

single flake-like $MnCo_2O_4$ can be fully indexed to the $MnCo_2O_4$ crystal structure. The high magnification TEM image (Fig. 9.7(c)) illustrates the porous nature of flake-like $MnCo_2O_4$. Figure 9.7(d) shows the lattice resolved HRTEM image of $MnCo_2O_4$ nanocrystal, in which the (220) crystal plane with a d spacing of 0.31 nm can be observed directly, further confirming the crystal structure of the as-prepared $MnCo_2O_4$.
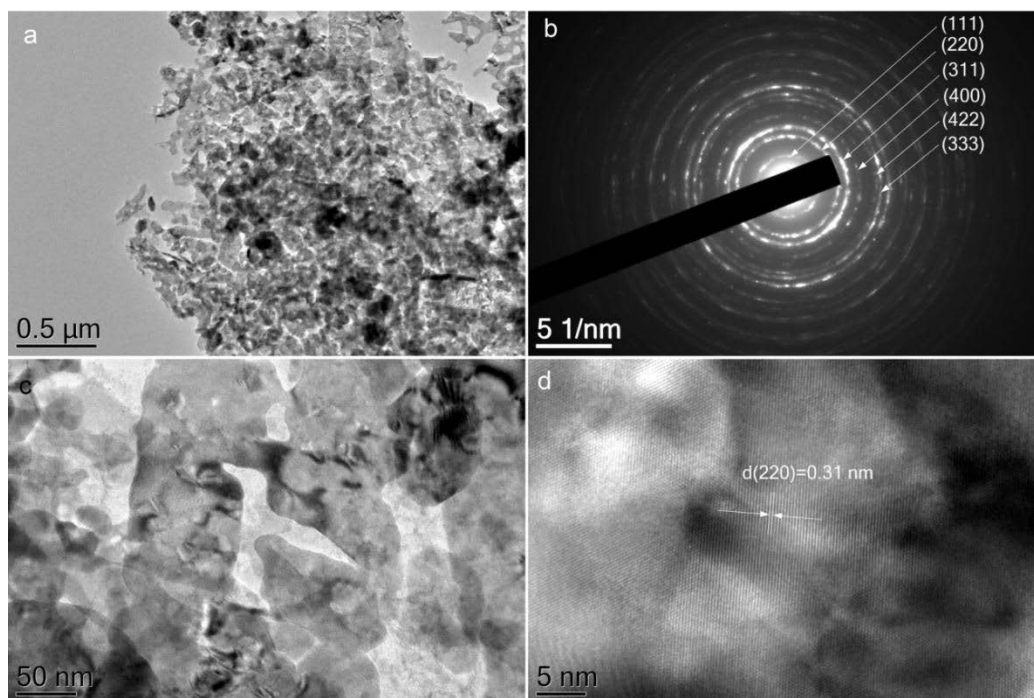
Figure 9.7 (a) Low magnification TEM image of flake-like $MnCo_2O_4$, (b) its corresponding selected area electron diffraction patterns (SAED), (c) high magnification TEM image, and (d) lattice resolved HRTEM image.

The material was further characterized by nitrogen adsorption and desorption isotherm to investigate the BET surface area and porous structure (Fig. 9.8). The isotherm of flake-like $MnCo_2O_4$ can be categorized as type IV according to the IUPAC classification with a distinct hysteresis loop, determining the presence of a mesoporous structure [360]. The material shows the BET surface area of 18.06 m^2 g^{-1}. According to the Barrett-Joyner-Halenda (BJH) pore size distribution data (inset, Fig. 9.8), the average pore size is about 13 nm, further confirming the mesoporous structure.
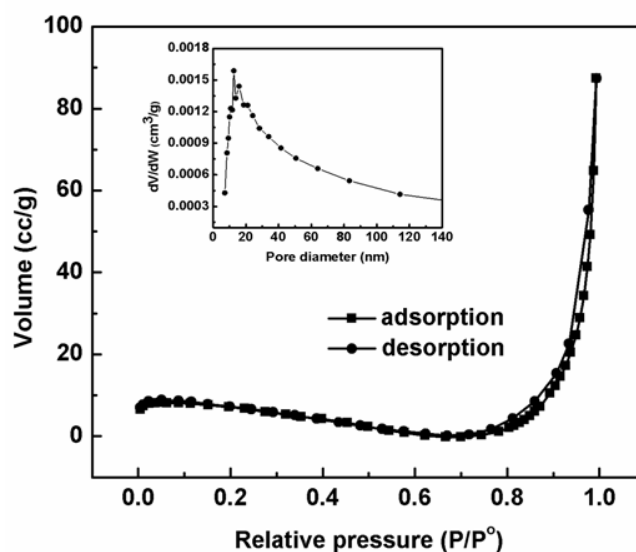
Figure 9.8 Nitrogen adsorption/desorption isotherms of flake-like $MnCo_2O_4$ and corresponding BJH pore size distributions (inset).
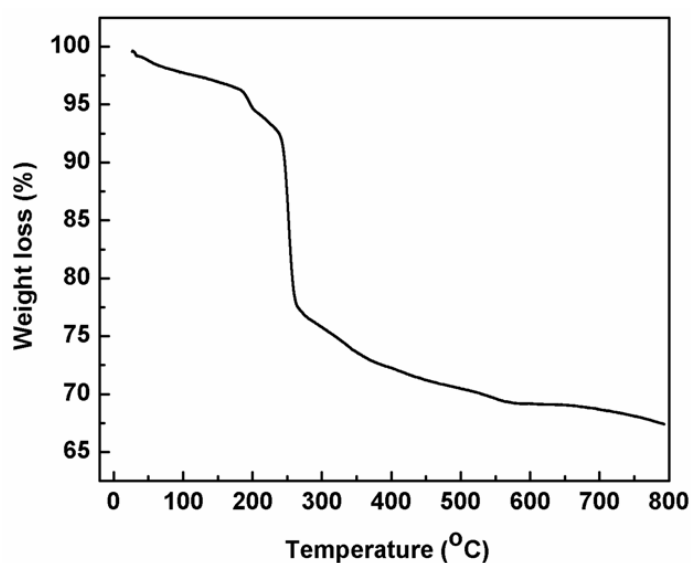
Figure 9.9 TGA curve for the Mn-Co based precursor.

The thermal behaviour of the Mn-Co based precursor was investigated by the thermogravimetric analysis (TGA). As shown in Fig. 9.9, the weight loss can be categorized into two major steps: first, the weight loss before 200 ^{o}C can be ascribed to the loss of physically adsorbed moisture. Due to the thermal decomposition, the second noticeable weight loss is associated with the conversion process of Mn-Co based

precursor to flake-like $MnCo_2O_4$. There is no apparent weight loss observed in the temperature range between 600 ^{o}C to 800 ^{o}C, indicating the complete decomposition of the precursor.

9.3.2 Electrochemical properties of flake-like $MnCo_2O_4$ for lithium ion batteries and supercapacitotrs

Cyclic voltammetry (CV) is an important tool to study electrochemical reactions (oxidation and reduction) and the electrochemical reversibility. The electrochemical properties of the as-synthesized flake-like $MnCo_2O_4$ were initially evaluated by CV measurement. Figure 9.10 shows the CV curves of the flake-like $MnCo_2O_4$ electrode in the first, second and third scanning cycles. During the first cathodic scan in the first cycle, an intense reduction peak is observed at 0.84 V versus Li^+/Li, which can be assigned to the reduction of Mn^{2+} and Co^{3+} to metallic Mn and Co, respectively. In the lithium ion extraction process, the oxidation peak at about 2.16 V in the first cycle, could be ascribed to the oxidation of Mn and Co metal to manganese and cobalt oxides [494]. The cathodic peaks shifted to higher potential (1.2 V) in the following cycles, which is related to some activation process initiated by the Li^+ intercalation in the first cycle [178]. From the second cycle, both reduction and oxidation peaks overlap very well, demonstrating that the electrode exhibits excellent electrochemical reversibility and stability during electrochemical reactions. Based on the above analysis and previous reports, the entire electrochemical process can be described as follows [494, 495]:

$$MnCo_2O_4 + 8Li^+ + 8e^- \rightarrow Mn + 2Co + 4Li_2O \qquad (9.1)$$

$$Mn + 2Co + 3Li_2O \leftrightarrow MnO + 2CoO + 6Li^+ + 6e^- \qquad (9.2)$$
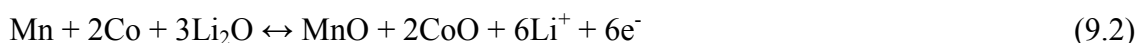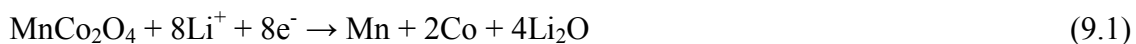
Figure 9.11(a) shows the first, second and fiftieth discharge and charge curves of the porous flake-like $MnCo_2O_4$ anode for LIBs in the potential range of 0.01 to 3.0 V (*vs* Li/Li^+) at the current density of 100 mA g^{-1}.
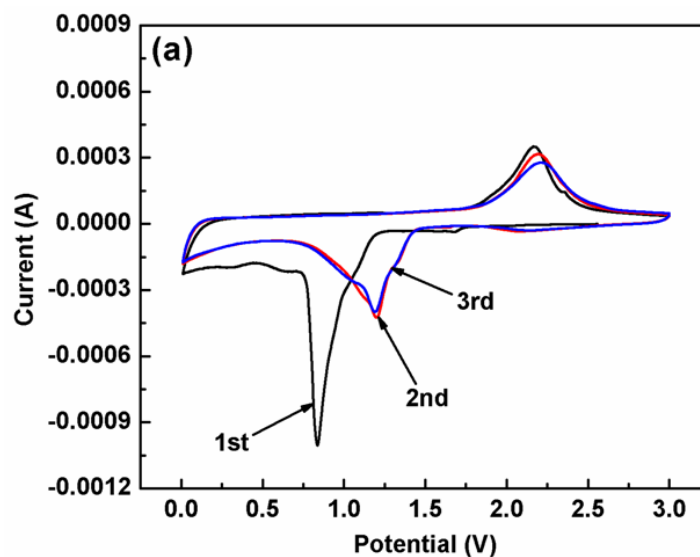
Figure 9.10 The first three consecutive CV curves of the electrode made from flake-like MnCo$_2$O$_4$ in the potential range of 0.01–3.0 V at a scan rate of 0.1 mV s^{-1}.

The increased deviation of voltage between charge-discharge curves could be ascribed to the polarization related to the ion transfer during charge-discharge cycling, which is generally observed in many metal oxides [415, 406]. The flake-like MnCo$_2$O$_4$ electrode delivered specific capacities of 1460, 1066 and 952 mA h g^{-1} in the 1st, 2nd and 100th cycles, respectively, which are higher than the theoretical value (906 mA h g^{-1}). The formation of a solid electrolyte interface (SEI) layer and an organic polymeric/gel-like layer by electrolyte decomposition, may contribute to the initial extra capacity at the first discharge [496]. The capacity is higher than the theoretical capacity because of the mesoporous architecture of flake-like MnCo$_2$O$_4$. The mesoporous structure can generate high reactivity for lithium storage. In lithium ion cells, liquid electrolytes can flood into mesopores, which induced high surface area contact with active flake-like MnCo$_2$O$_4$. The mesopores provide a short path for lithium transport and large surface area for interfacial lithium storage. This unique surface/interface characteristics for lithium ion diffusion reduce the polarization of the electrode and thus, increases the capacity. The

large reversible capacity may also be ascribed to the reversible formation/dissolution of polymeric gel-like layer from electrolyte [494, 34, 463].

Figure 9.11(b) presents the discharge capacity versus cycle number for the flake-like $MnCo_2O_4$ electrode at the current density of 100 mA g^{-1}. It is interesting to note that the capacities increased gradually before 30 cycles, which is generally observed for other transition metal oxides and can be ascribed to the reversible formation of polymeric gel-like layer originating from the kinetic activation of the electrode [418, 406, 417]. After 45 cycles, the capacity began to decrease as shown in Fig. 9.11(b). This phenomenon is likely due to the volume variation of the electrode during cycling. However, the capacity decays at a slow rate because of the mesoporous structure accompanied by the decomposition and reformation of the electrolyte [494]. The unique porous flake-like $MnCo_2O_4$ structure can buffer the volume expansion/contraction of the electrode during the repeated Li^+ intercalation/de-intercalation and effectively alleviate the pulverization problem, leading to enhanced cycling performance. The reversible capacity of 952 mA h g^{-1} was sustained at the end of the 100 cycles, which is 89 % of its initial reversible capacity. The Coulombic efficiencies of the flake-like $MnCo_2O_4$ electrode are shown in Fig. 9.11(b). The electrode shows an average Coulombic efficiency of 97 % from the second cycle.

The rate performance of the flake-like $MnCo_2O_4$ electrode was performed at different current densities from 100 mA g^{-1} to 2000 mA g^{-1}. As shown in Fig. 9.12, six cycles for each current density were carried out in the voltage range of 0.01-3.0 V. The flake-like $MnCo_2O_4$ electrode showed good rate capability with discharge capacities of 1141, 1039, 913, 809 mA h g^{-1} at the current densities of 100, 200, 500 and 1000 mA g^{-1}. The electrode still delivered the capacity of 629 mA h g^{-1} even at the high current density of 2000 mA g^{-1}, indicating the excellent rate performance of the electrode for high power

lithium ion batteries. Upon decreasing of the low current densities (500 mA g^{-1} and 100 mA g^{-1}), the discharge capacities can recover to the previous values, demonstrating the integrity of the electrode.
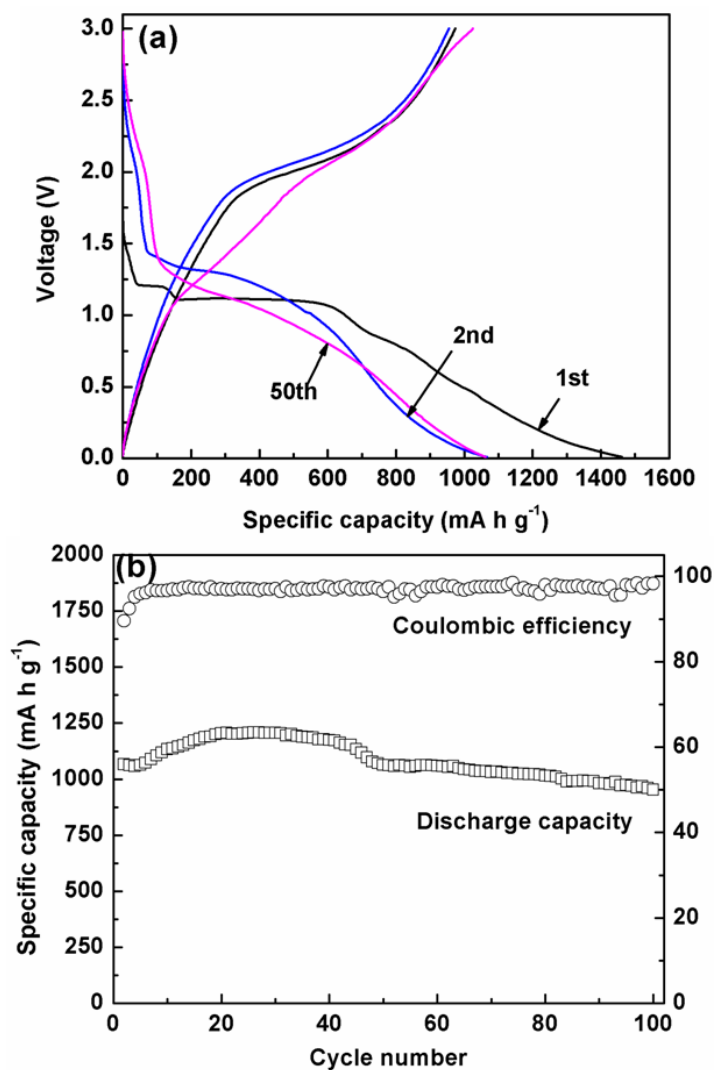
Figure 9.11 (a) Galvanostatic charge and discharge profiles for the first, second and fiftieth cycles, and (b) Cycling performance and Coulombic efficiency of the flake-like MnCo$_2$O$_4$ electrode at the current density of 100 mA g^{-1}.

The electrochemical impedance spectroscopy (EIS) was conducted further to determine the Li$^+$ transfer behaviour of mesoporous flake-like MnCo$_2$O$_4$. The Nyquist impedance plots were obtained in the frequency range from 100 kHz to 0.01 Hz at different charge-discharge cycles (as shown in Fig. 9.13). The impedance spectra display a depressed

semicircle in the high and medium frequency region and inclined lines in the low-frequency region. The high-frequency semicircle could be attributed to the existence of contact resistance because of the SEI layer. The medium-frequency semicircle indicates the charge transfer resistance (R_{ct}), which relates to charge transfer through the electrode-electrolyte interface. The inclined line represents a typical Warburg behaviour, which corresponded to the lithium diffusion process within the electrode materials [463, 500, 501].
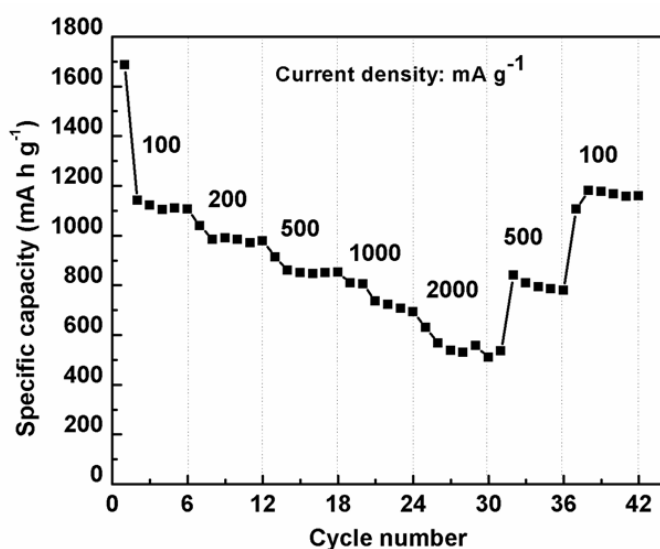
Figure 9.12 Rate capability test for the flake-like $MnCo_2O_4$ electrode at different current densities.

The numerical value of the diameter of the semicircle gives an approximate indication of the R_{ct}. It is apparent that from 5 to 40 cycles (Fig. 9.13), there are obvious decreases of R_{ct} estimated from the depressed semicircles. However, the charge transfer resistances slowly increase after 40 cycles, which indicates the lithium insertion and extraction process turned into difficult. After 75 cycles, the R_{ct} increases slightly compared with the 100 cycles. These results are consistent with discharge-charge cycling performance, which demonstrates that a reversible capacity is first increasing up to 40 cycles then slowly reducing to 100 cycles.

Owing to the unique porous structure, the flake-like $MnCo_2O_4$ is also suitable for supercapacitors. The electrochemical capacitive properties of flake-like $MnCo_2O_4$ as the electrode material for supercapacitors were investigated using cyclic voltammetry and galvanostatic charge-discharge in 2 M KOH aqueous electrolyte. Figure 9.14(a) shows the CV curves of the as-synthesized porous flake-like $MnCo_2O_4$ in a potential range of 0–0.5 V (*vs.* SCE) at different scan rates. All CV curves exhibit a similar shape and a pair of distinct redox peaks within 0-0.5 V (vs. SCE) is observed, which reveals the pseudocapacitive properties resulting from Faradic redox reactions.
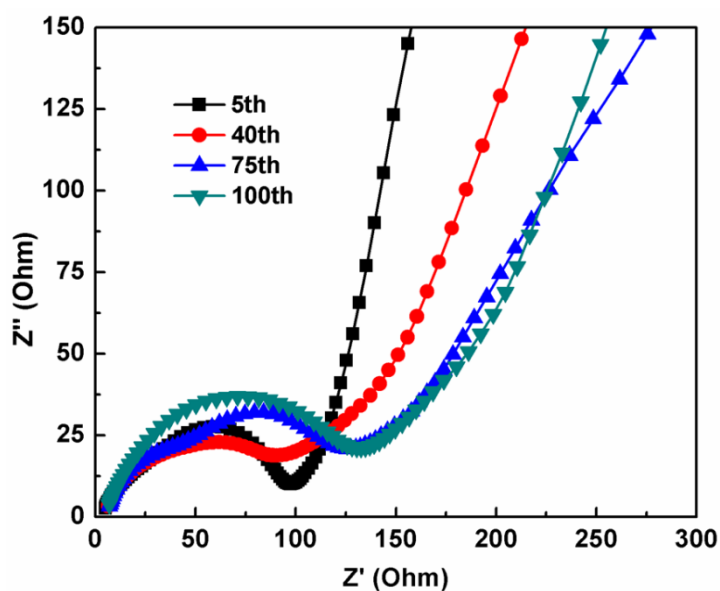
Figure 9.13 Electrochemical impedance spectra of the as-prepared flake-like $MnCo_2O_4$ electrode after 5, 40, 75 and 100 cycles.

The galvanostatic charge-discharge measurements were conducted in a potential window between 0 and 0.4 V (vs. SCE) at different current densities ranging from 1 to 10 A g^{-1}, which is shown in Fig. 9.14(b). It is exciting that the nonlinear charge-discharge curves further confirmed the pseudocapacitive behaviour of flake-like $MnCo_2O_4$. The specific capacitance can be calculated according to the formula:

$$C = I\Delta t/\Delta Vm \tag{9.3}$$

Where I is the discharge current (A g^{-1}), Δt is the discharge time (sec), ΔV is the potential window (V), m is the mass of active material (mg). The corresponding specific capacitances are 1487, 1410, 1162 and 950 F g^{-1} at the current density of 1, 2, 5 and 10 A g^{-1}, respectively.
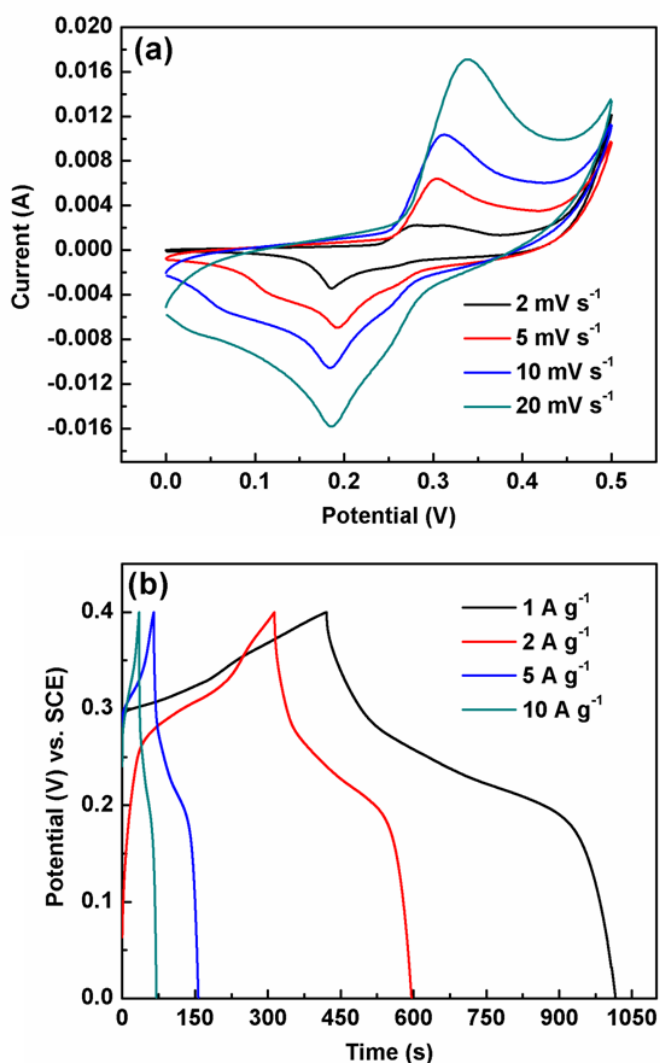
Figure 9.14 (a) CV curves at various scan rates ranging from 2 to 20 mV s^{-1}, and (b) Galvanostatic charge and discharge curves at different current densities (1 to 10 A g^{-1}) for the flake-like MnCo$_2$O$_4$ electrode in 2 M KOH electrolyte.

This reveals the stable reversible features of the porous flake-like MnCo$_2$O$_4$. It is well-known that the morphologies of the material play a significant role in determining electrochemical performances. The improved specific capacitance could be ascribed to the efficient utilization of mesoporous flake-like MnCo$_2$O$_4$. The mesoporous structure

of the flake-like $MnCo_2O_4$ significantly increases the electrode-electrolyte contact area. The mesoporous interconnected flake-like $MnCo_2O_4$ can also facilitate the transport of the electrolyte and shorten the proton diffusion distance. Furthermore, the flake-like structure on the conductive substrate could ensure good electrical contact [498, 499]. Therefore, the mesoporous flake-like $MnCo_2O_4$ demonstrated higher specific capacitance than that of the reported results [504].

The long-term cycling stability of any electroactive material is an essential requirement for supercapacitors. The cycling stability of flake-like $MnCo_2O_4$ was evaluated by the repeated discharging and charging measurement at a constant scan rate of 50 mV s^{-1}, in the potential range of 0 to 0.5 V. As shown in Fig. 9.15, the flake-like $MnCo_2O_4$ electrode exhibited stable cycling performance, and, 93.3 % of the initial specific capacitance was retained even after 2000 cycles.
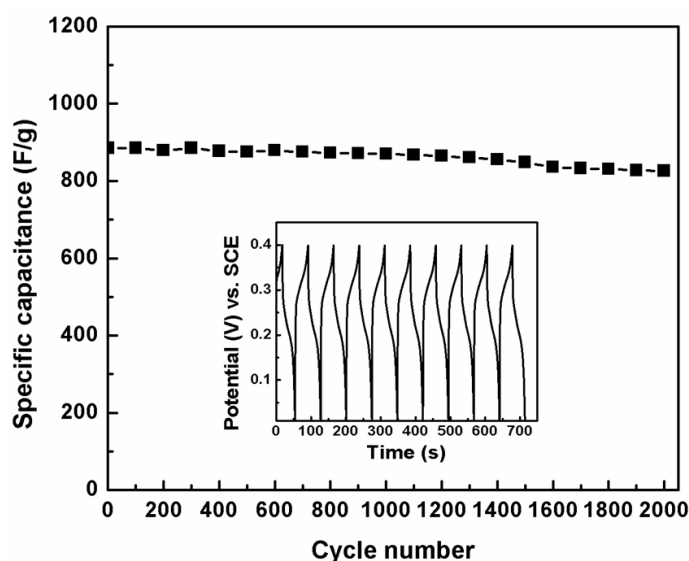
Figure 9.15 Cycling performance of flake-like $MnCo_2O_4$ at a scan rate of 50 mV s^{-1}. The charge and discharge curves for the first ten cycles (the inset in Fig. 10).

This demonstrates the excellent long-term electrochemical stability. The charge-discharge curves of flake-like $MnCo_2O_4$ at a current density of 10 A g^{-1} is shown in the inset of Fig. 9.15. The charge-discharge curves are almost the same for the first 10

cycles, further ratifying the electrochemical reversibility of mesoporous flake-like $MnCo_2O_4$.

The excellent electrochemical performance might be attributed to the favourable structure of the material. In particular, the mesoporous structure and relatively high surface area provides numerous electroactive sites for electrochemical reaction. The existence of pores in the flake-like $MnCo_2O_4$ could not only serve as a reservoir for electrolyte, but also enhance the diffusion kinetics in the interior of the electrode [408]. The porous structure can effectively mitigate the volume change during the high rate of insertion and extraction of OH^- ions, which can stabilize the integrity of the electrodes, therefore improving the cyclability.

9.4 Conclusions

In conclusion, flake-like $MnCo_2O_4$ was successfully synthesized by a simple hydrothermal approach, followed by thermal treatment in air. The materials possess a mesoporous structure and relatively high specific surface area, which is favourable for electrochemical reaction. When applied as an anode material for lithium ion batteries, a reversible capacity of 952 mA h g^{-1} at the current density of 100 mA g^{-1} could be retained after 100 cycles, which is equated 89 % of the initial reversible capacity. In supercapacitor applications, the flake-like $MnCo_2O_4$ exhibited a high specific capacitance and excellent cycling stability (6.7 % loss after 2000 cycles). In view of its simple preparation process and excellent electrochemical performance, the mesoporous flake-like $MnCo_2O_4$ might serve as an attractive candidate for lithium-ion batteries and supercapacitors.

Chapter 10 Conclusions and Future Perspective

10.1 Conclusions

Energy storage materials have attracted tremendous attention and research interest due to the increasing concern about the sustainable development of energy. The advancement of nanoscience and nanotechnology has offered the opportunity to design new energy storage materials for the next-generation high-performance lithium-ion batteries and supercapacitors with higher specific capacity/capacitance and longer cycle life. Owing to their high specific surface area, nanostructured materials can provide abundant active sites for electrochemical reactions, short diffusion pathways and high freedom for volume change during charge/discharge process to improve the structural integrity of the electrode.

In this thesis, three categories of nanostructured materials have been prepared and evaluated their electrochemical properties for lithium-ion batteries and supercapacitors. The first category is metal oxides and hydroxides. In this category, NiO nanosheets, Fe_2O_3 nanoparticles and $Ni(OH)_2$ nanospheres were synthesized by using hydrothermal and microwave methods and applied as anode materials for lithium ion batteries and electrode materials for supercapacitors. The improved electrochemical properties of these materials are closely related to their morphologies, specific surface area, and crystallinity.

In the second group, hybrid materials such as graphene/MnO_2 hybrid nanosheets were fabricated and investigated their applications as electrode materials for supercapacitors. In these hybrid materials, graphene nanosheets provide a highly conducting network for electron transfer. Meanwhile, MnO_2 nanosheets can efficiently inhibit the stack of graphene nanosheets, and, therefore, increases the accessible surface area and facilitate

the transport of ions in the electrode material, which improves the electrochemical performance.

The final category is mixed metal oxides such as highly porous $NiCo_2O_4$ nanoflakes and nanobelts, mesoporous flake-like $MnCo_2O_4$ and $NiCo_2O_4$ nanosheets. The mixtures of the metal oxides have also been demonstrated to be promising electrode materials for lithium-ion batteries and supercapacitors. Several factors could be responsible for the superior electrochemical performances of the above-mentioned mesoporous materials. Firstly, their higher specific surface area can significantly improve the interface contact between the electrode and electrolyte for ion diffusion, thus improved the high specific capacity/capacitance and also benefiting the charge transfer rate, and enhancing the rate capability. Secondly, the existence of pores could buffer the volume change during long-term cycling process, and effectively alleviate the aggregation and pulverization problem of the electrode material, thereby improving cycling stability. However, the commercial use of these materials as anodes for lithium ion batteries and electrodes for supercapacitors are still far from reality owing to their low capacity, high cost, safety and reduced rate capability.

10.2 Future Perspective

Based on understanding the principles of energy storage, the future perspective of nanostructured materials for lithium-ion batteries and supercapacitors should focus on; exploring new types of advanced energy storage materials with smart material-design strategies and improved synthesis technologies. It is imperative to develop more and more novel nanostructured materials with different shapes and sizes in order to further increase energy/power densities, improved charge-discharge rate capability and long

cycle life. It is also necessary to understand the mechanisms of charge storage in nanomaterials and kinetic transport at the electrode/electrolyte interface.

Except performances, safety issues, cost and fabrication should also be taken into account when developing an industrially applicable energy storage material. Further work is required to achieve controlled and large scale synthesis of nanostructures for commercial applications. The preparation of nanostructured materials via more sustainable and greener approaches should also be addressed to limit environmental pollution so that we can secure a bright future for human beings throughout the world.

APPENDIX: NOMENCLATURE

Abbreviations/Symbols	Full name
a.u.	Arbitrary unit
AFM	Atomic Force Microscopy
Ar	Argon
BET	Brunauer-Emmett-Teller
BJH	Barrett-Joyner-Halenda
CB	Carbon black
Cm	Centimeter
CV	Cyclic Voltammetry
C-rate	Current rate
DI	de-ionized
DMC	Dimethyl carbonate
DMF	Dimethyl formamide
EC	Ethylene carbonate
EIS	Electrochemical Impedance Spectroscopy
EG	Ethylene glycol
EDLCs	Electrochemical double layer capacitors
EVs	Electric vehicles
FESEM	Field-Emission Scanning Electron Microscopy
FTIR	Fourier transform infrared spectroscopy
g	Gram
GO	Graphene oxide
GNS	Graphene nanosheets
h	Hour

Hz	Hertz
I	Intensity
HEVs	Hybrid electric vehicles
HRTEM	High-resolution transmission electronic spectroscopy
JCPDS	Joint Committee on Powder Diffraction Standards
Li	Lithium
M	Molar concentration
mA h g^{-1}	Milli ampere hour per gram
min	Minute
mm	Millimeter
MWCNT	Multiwalled carbon nanotube
nm	Nanometer
NMP	1-methyl-2-pyrrolidinone
PC	Propylene carbonate
PPy	Polypyrrole
PVDF	Poly(vinylidene difluoride)
R_{ct}	Charge transfer resistance
$R\Omega$	Ohmic resistance
SAED	Selected area electron diffraction
SCE	Saturated calomel electrode
SEI	Solid Electrolyte Interface
SEM	Scanning electron Microscopy
TEM	Transmission electron microscopy
TGA	Thermogravimetric analysis
XRD	X-ray diffraction

º	Degree
Ω	Ohm
ºC	Degree celcius
Zw	Warburg impedance

References

[1] J. B. Goodenough, Y. Kim, Challenges for rechargeable Li batteries, *Chem. Mater.*, 22 (2010) 587-603.

[2] M. Armand, J. M. Tarascon, Building better batteries, *Nature*, 451 (2008) 652-657.

[3] J. Tollefson, Charging up the future, *Nature*, 456 (2008) 436-440.

[4] V. Etacheri, R. Marom, R. Elazari, G. Salitra, D. Aurbach, Challenges in the development of advanced Li-ion batteries: a review, *Energy Environ. Sci.*, 4 (2011) 3243-3262.

[5] J. M. Tarascon, M. Armand, Issues and challenges facing rechargeable lithium batteries, *Nature*, 414 (2001) 359-367.

[6] F. R. Gamble, J. H. Osiecki, M. Cais, R. Pishardy, F. J. Disalvo, T. H. Geballe, Intercalation complexes of lewis bases and layered sulfides-large class of new superconductors, *Science*, 174 (1971) 493-497.

[7] M. S. Whittingham, Hydrated intercalation complexes of layered disulfides, *Mater. Res. Bull.*, 9 (1974) 1681-1690.

[8] M. S. Whittingham, Electrical energy-storage and intercalation chemistry, *Science*, 192 (1976) 1126-1127.

[9] A. H. Thompson, Electron-electron scattering in TiS_2, *Phys. Rev. Lett.*, 35 (1975) 1786-1789.

[10] M. S. Whittingham, Role of ternary phases in cathode reactions, *J. Electrochem. Soc.*, 123 (1976) 315-320.

[11] M. S. Whittingham, Lithium batteries and cathode materials, *Chem. Rev.*, 104 (2004) 4271-4301.

[12] G.-A. Nazri, G. Pistoia, Lithium batteries: science and technology, 2009: Springer.

[13] P. G. Dickens, S. J. French, A. T. Hight, M. F. Pye, Phase-relationships in the ambient-temperature $Li_xV_2O_5$ system (0.1<x<1.0), *Mater. Res. Bull.*, 14 (1979) 1295-1299.

[14] C. R. Walk, J. S. Gore, $Li-V_2O_5$ secondary cell, *J. Electrochem. Soc.*, 122 (1975) C68-C68.

[15] K. Mizushima, P. C. Jones, P. J. Wiseman, J. B. Goodenough, Li_xCoO_2 (0<x<-1): a new cathode material for batteries of high-energy density, *Mater. Res. Bull.*, 15 (1980) 783-789.

[16] R. Yazami, P. Touzain, International meeting on lithium ion batteries, 1982, Rome, Abstract #23.

[17] R. Yazami, P. Touzain, A reversible graphite-lithium negative electrode for electrochemical generators, *J. Power Sources*, 9 (1983) 365-371.

[18] K. Ozawa, Lithium-ion rechargeable batteries with $LiCoO_2$ and carbon electrodes: the $LiCoO_2$/C system, *Solid State Ionics*, 69 (1994) 212-221.

[19] M. R. Palacin, Recent advances in rechargeable battery materials: a chemist's perspective, *Chem. Soc. Rev.*, 38 (2009) 2565-2575.

[20] P. G. Bruce, B. Scrosati, J. M. Tarascon, Nanomaterials for rechargeable lithium batteries, *Angew. Chem. Int. Ed.*, 47 (2008) 2930-2946.

[21] M. Winter, R. J. Brodd, What are batteries, fuel cells, and supercapacitors? *Chem. Rev.*, 104 (2004) 4245-4269.

[22] K. Xu, Nonaqueous liquid electrolytes for lithium-based rechargeable batteries, *Chem. Rev.*, 104 (2004) 4303-4417.

[23] D. Guyomard, J. M. Tarascon, Li metal-free rechargeable $LiMn_2O_4$/carbon cells-their understanding and optimization, *J. Electrochem. Soc.*, 139 (1992) 937-948.

[24] J. M. Tarascon, W. R. McKinnon, F. Coowar, T. N. Bowner, G. Amatucci, D. Guyomard, Synthesis conditions and oxygen stoichiometry effects on Li insertion into the spinel $LiMn_2O_4$, *J. Electrochem. Soc.*, 141 (1994) 1421-1431.

[25] P. Arora, Z. M. Zhang, Battery separators, *Chem. Rev.*, 104 (2004) 4419-4462.

[26] J. M. Tarascon, N. Recham, M. Armand, J. N. Chotard, P. Barpanda, W. Walker, L. Dupont, Hunting for better Li-based electrode materials via low temperature inorganic synthesis, *Chem. Mater.*, 22 (2010) 724-739.

[27] S. Arico, P. Bruce, B. Scrosati, J. M. Tarascon, S. W. Van, Nanostructured materials for advanced energy conversion and storage devices, *Nat. Mater.*, 4 (2005) 366-377.

[28] Y. G. Guo, J. S. Hu, L. J. Wan, Nanostructured materials for electrochemical energy conversion and storage devices, *Adv. Mater.*, 20 (2008) 2878-2887.

[29] Y. Wang, H. Li, P. He, E. Hosono, H. Zhou, Nano active materials for lithium ion batteries, *Nanoscale*, 2 (2010) 1294-1305.

[30] N. Meethong, H. Y. S. Huang, S. A. Speakman, W. C. Carter, Y. M. Chiang, Strain accommodation during phase transformations in olivine-based cathodes as a materials selection criterion for high-power rechargeable batteries, *Adv. Funct. Mater.*, 17 (2007) 1115-1123.

[31] A. D. Robertson, A. R. Armstrong, P. G. Bruce, Layered $Li_xMn_{1-y}Co_yO_2$ intercalation electrodes-influence of ion exchange on capacity and structure upon cycling, *Chem. Mater.*, 13 (2001) 2380-2386.

[32] P. Balaya, Size effects and nanostructured materials for energy applications, *Energy Environ. Sci.*, 1 (2008) 645-654.

[33] J. Jamnik, J. Maier, Nanocrystallinity effects in lithium battery materials-aspects of nano-ionics,` Part IV, *Phys. Chem. Chem. Phys.*, 5 (2003) 5215-5220.

[34] J. Maier, Nanoionics: ion transport and electrochemical storage in confined systems, *Nat. Mater.*, 4 (2005) 805-815.

[35] N. A. Kaskhedikar, J. Maier, Lithium storage in carbon nanostructures, *Adv. Mater.*, 21 (2009) 2664-2680.

[36] Q. Wang, H. Li, L. Q. Chen, X. J. Huang, Monodispersed hard carbon spherules with uniform nanopores, *Carbon*, 39 (2001) 2211-2214.

[37] O. Delmer, P. Balaya, L. Kienle, J. Maier, Enhanced potential of amorphous electrode materials: Case study of RuO_2, *Adv. Mater.*, 20 (2008) 501-+.

[38] P. Balaya, A. J. Bhattacharyya, J. Jamnik, Y. F. Zhukovskii, E. A. Kotomin, J. Maier, Nano-ionics in the context of lithium batteries, *J. Power Sources*, 159 (2006) 171-178.

[39] F. Jiao, P. G. Bruce, Mesoporous crystalline beta-MnO_2-a reversible positive electrode for rechargeable lithium batteries, *Adv. Mater.*, 19 (2007) 657-+.

[40] G.-A. Nazri, G. Pistoia (Ed.), Lithium batteries science and technology, Kluwer Academic/Plenum, Boston, 2004.

[41] B. W. van Schalkwijk, B. Scrosati (Ed.), Advances in lithium-ion batteries, Kluwer Academic/Plenum, New York, 2002.

[42] K. Sato, M. Noguchi, A. Demachi, N. Oki, M. Endo, A mechanism of lithium storage in disordered carbons, *Science*, 264 (1994) 556-558.

[43] J. R. Dahn, T. Zheng, Y. H. Liu, J. S. Xue, Mechanisms for lithium insertion in carbonaceous materials, *Science*, 270 (1995) 590-593.

[44] K. Persson, V. A. Sethuraman, L. J. Hardwick, Y. Hinuma, Y. S. Meng, A. van der ven, V. Srinivasan, R. Kostecki, G. Ceder, Lithium diffusion in graphitic Carbon, *J. Phys. Chem. Lett.*, 1 (2010) 1176-1180.

[45] R. Fong, U. von Sacken, J. R. Dahn, Studies of lithium intercalation into carbons using nonaqueous electrochemical cells, *J. Electrochem. Soc.*, 137 (1990) 2009-2013.

[46] R. Kanno, Y. Kawamoto, Y., S. Ohashi, N. Imanishi, O. Yamamoto, Carbon fiber as a negative electrode in lithium secondary cells, *J. Electrochem. Soc.*, 139 (1992) 3397-3404.

[47] E. Peled, The electrochemical behavior of alkali and alkaline earth metals in nonaqueous battery systems-the solid electrolyte interphase model, *J. Electrochem. Soc.*, 126 (1979) 2047-2051.

[48] S. Iijima, Helical microtubules of graphitic carbon, *Nature*, 354 (1991) 56-58.

[49] A. C. Dillon, Carbon nanotubes for photoconversion and electrical energy storage, *Chem. Rev.*, 110 (2010) 6856-6872.

[50] R. Lv., L. Zou, X. Gui, F. Kang, Y. Zhu, H. Zhu, J. Wei, J. Gu, K. Wang, D. Wu, High-yield bamboo-shaped carbon nanotubes from cresol for electrochemical application, *Chem. Commun.*, (2008) 2046-2048.

[51] J. S. Zhou, H. H. Song, B. C. Fu, B. Wu, X. H. Chen, Synthesis and high-rate capability of quadrangular carbon nanotubes with one open end as anode materials for lithium-ion batteries, *J. Mater. Chem.*, 20 (2010) 2794-2800.

[52] J. Eom, D. Kim, H. S. Kwon, Effects of ball-milling on lithium insertion into multi-walled carbon nanotubes synthesized by thermal chemical vapour deposition, *J. Power Sources*, 157 (2006) 507-514.

[53] C. H. Mi, , G. S. Cao, X. B. Zhao, A non-GIC mechanism of lithium storage in chemical etched MWNTs, *J. Electroanal. Chem.*, 562 (2004) 217-221.

[54] C. C. Li, X. M. Yin, L. B. Chen, Q. H. Li, T. H. Wang, Porous carbon nanofibers derived from conducting polymer: synthesis and application in lithium-ion batteries with high-rate capability, *J. Phys. Chem. C*, 113 (2009) 13438-13442.

[55] L. Ji, Z. Lin, A. J. Medford, X. Zhang, In-situ encapsulation of nickel particles in electrospun carbon nanofibers and the resultant electrochemical performance, *Chem. Eur. J.*, 15 (2009) 10718-10722.

[56] V. Subramanian, H. W. Zhu, B. Q. Wei, High rate reversibility anode materials of lithium batteries from vapor-grown carbon nanofibers, *J. Phys. Chem. B*, 110 (2006) 7178-7183.

[57] D. Deng, J. Y. Lee, One-step synthesis of polycrystalline carbon nanofibers with periodic dome-shaped interiors and their reversible lithium-ion storage properties, *Chem. Mater.*, 19 (2007) 4198-4204.

[58] C. Kim, K. S. Yang, M. Kojima, K. Yoshida, Y. J. Kim, , Y. A. Kim, M. Endo, Fabrication of electrospinning-derived carbon nanofiber webs for the anode material of lithium-ion secondary batteries, *Adv. Funct. Mater.*, 16 (2006) 2393-2397.

[59] L. Ji, X. Zhang, Fabrication of porous carbon nanofibers and their application as anode materials for rechargeable lithium-ion batteries, *Nanotechnology*, 20 (2009) 155705.

[60] S. W. Woo, K. Dokko, H. Nakano, K. Kanamura, Bimodal porous carbon as a negative electrode material for lithium-ion capacitors, *Electrochemistry*, 75 (2007) 635-640.

[61] Y. S. Hu, P. Adelhelm, B. M. Smarsly, S. Hore, M. Antonietti, J. Maier, Synthesis of hierarchically porous carbon monoliths with highly ordered microstructure and

their application in rechargeable lithium batteries with high-rate capability, *Adv. Funct. Mater.*, 17 (2007) 1873-1878.

[62] T. Wang, X. Y. Liu, D. Y. Zhao, Z. Y. Jiang, The unusual electrochemical characteristics of a novel three-dimensional ordered bicontinuous mesoporous carbon *Chem. Phys. Lett.*, 389 (2004) 327-331.

[63] H. S. Zhou S. M. Zhu, M. Hibino, I. Honma, M. Ichihara, Lithium storage in ordered mesoporous carbon (CMK-3) with high reversible specific energy capacity and good cycling performance, *Adv. Mater.* 15 *(*2003) 2107-+.

[64] K. S. Novoselov, A. K. Geim, S. V. Morozov, D. Jiang, Y. Zhang, S. V. Dubonos, I. V. Grigorieva, A. A. Firsov, Electric field effect in atomically thin carbon films, *Science*, 306 (2004) 666-669.

[65] A. K. Geim, K. S. Novoselov, The rise of graphene, *Nat. Mater.*, 6 (2007) 183-191.

[66] F. Bonaccorso, Z. Sun, T. Hasan, A. C. Ferrari, Graphene photonics and optoelectronics, *Nat. Photonics*, 4 (2010) 611-622.

[67] G. Eda, M. Chhowalla, Chemically derived graphene oxide: towards large-area thin-film electronics and optoelectronics, *Adv. Mater.*, 22 (2010) 2392-2415.

[68] S. Stankovich, D. A. Dikin, G. H. B. Dommett, K. M. Kohlhaas, E. J. Zimney, E. A. Stach, R. D. Piner, S. T. Nguyen, R. S. Ruoff, Graphene-based composite materials, *Nature*, 442 (2006) 282-286.

[69] D. Chen, L. H. Tang, J. H. Li, Graphene-based materials in electrochemistry, *Chem. Soc. Rev.*, 39 (2010) 3157-3180.

[70] H. Bai, Y. X. Xu, L. Zhao, C. Li, G. Q. Shi, Non-covalent functionalization of graphene sheets by sulfonated polyaniline, *Chem. Commun.*, (2009) 1667-1669.

[71] M. D. Stoller, S. J. Park, Y. W. Zhu, J. H. An, R. S. Ruoff, Graphene-based ultracapacitors, *Nano Lett.*, 8 (2008) 3498-3502.

[72] G. X. Wang, X. P. Shen, J. Yao, J. Park, Graphene nanosheets for enhanced lithium storage in lithium ion batteries, *Carbon*, 47 (2009) 2049-2053.

[73] E. Yoo, J. Kim, E. Hosono, H. Zhou, T. Kudo, I, Homma, Large reversible Li storage of graphene nanosheet families for use in rechargeable lithium ion batteries, *Nano Lett.*, 8 (2008) 2277-2282.

[74] M. H. Liang, L. J. Zhi, Graphene-based electrode materials for rechargeable lithium batteries, *J. Mater. Chem.*, 19 (2009) 5871-5878.

[75] G. X. Wang, J. Yang, J. Park, X. L. Gou, B. Wang, H. Liu, J. Yao, Facile synthesis and characterization of graphene nanosheets. *J. Phys. Chem. C*, 112 (2008) 8192-8195.

[76] P. Guo, H. Song, X. Chen, Electrochemical performance of graphene nanosheets as anode material for lithium-ion batteries, *Electrochem. Commun.*, 11 (2009) 1320-1324.

[77] P. C. Lian, X. F. Zhu, S. Z. Liang, Z. Li, W. S. Yang, H. H. Wang, Large reversible capacity of high quality graphene sheets as an anode material for lithium-ion batteries, *Electrochim. Acta*, 55 (2010) 3909-3914.

[78] S. Q. Chen, P. Chen, M. H. Wu, D. Y. Pan, Y. Yang, Graphene supported Sn-Sb@carbon core-shell particles as a superior anode for lithium ion batteries, *Electrochem. Commun.*, 12 (2010) 1302-1306.

[79] B. Wang, X. L. Wu, C. Y. Shu, Y. G. Guo, C. R. Wang, Synthesis of CuO/graphene nanocomposite as a high-performance anode material for lithium-ion batteries, *J. Mater. Chem.*, 20 (2010) 10661-10664.

[80] G. M. Zhou, D. W. Wang, F. Li, L. L. Zhang, N. Li, Z. S. Wu, L. Wen, G. Q. Lu, H. M. Cheng, Graphene-wrapped Fe_3O_4 anode material with improved reversible capacity and cyclic stability for lithium ion batteries, *Chem. Mater.*, 22 (2010) 5306-5313.

[81] G. X. Wang, B. Wang, X. L. Wang, J. Park, S. X. Dou, H. Ahn, K. Kim, Sn/graphene nanocomposite with 3D architecture for enhanced reversible lithium storage in lithium ion batteries, *J. Mater. Chem.*, 19 (2009) 8378-8384.

[82] S. L. Chou, J. Z. Wang, M. Choucair, H. K. Liu, J. A. Stride, S. X. Dou, Enhanced reversible lithium storage in a nanosize silicon/graphene composite, *Electrochem. Commun.*, 12 (2010) 303-306.

[83] S. M. Paek, E. Yoo, I. Honma, Enhanced cyclic performance and lithium storage capacity of SnO_2/graphene nanoporous electrodes with three-dimensionally delaminated flexible structure, *Nano Lett.*, 9 (2009) 72-75.

[84] J. Yao, X. P. Shen, B. Wang, H. K. Liu, G. X. Wang, In situ chemical synthesis of SnO_2-graphene nanocomposite as anode materials for lithium-ion batteries, *Electrochem. Commun.*, 11(2009) 1849-1852.

[85] Z. S. Wu, W. C. Ren, L. Wen, L. B. Gao, J. P. Zhao, Z. P. Chen, G. M. Zhou, F. Li, H. M. Cheng, Graphene anchored with Co_3O_4 nanoparticles as anode of lithium ion batteries with enhanced reversible capacity and cyclic performance, *ACS Nano*, 4 (2010) 3187-3194.

[86] H. L. Wang, L. F. Cui, Y. A. Yang, H. S. Casalongue, J. T. Robinson, Y. Y. Liang, Y. Cui, H. J. Dai, Mn_3O_4-Graphene hybrid as a high-capacity anode material for lithium ion batteries, *J. Am. Chem. Soc.*, 132 (2010) 13978-13980.

[87] D. H. Wang, D. W. Choi, J. Li, Z. G. Yang, Z. M. Nie, R. Kou, D. H. Hu, C. M. Wang, L. V. Saraf, J. G. Zhang, I. A. Aksay, J. Liu, Self-assembled TiO_2-graphene hybrid nanostructures for enhanced li-ion insertion, *ACS Nano*, 3 (2009) 907-914.

[88] Y. S. He, D. W. Bai, X. Yang, J. Chen, X. Z. Liao, Z. F. Ma, A $Co(OH)_2$-graphene nanosheets composite as a high performance anode material for rechargeable lithium batteries, *Electrochem. Commun.*, 12 (2010) 570-573.

[89] A. N. Dey, Electrochemical alloying of lithium in organic electrolytes, *J. Electrochem. Soc.*, 118 (1971) 1547-&.

[90] C. M. Park, J. H. Kim, H. Kim, H. J. Sohn, Li-alloy based anode materials for Li secondary batteries, *Chem. Soc. Rev.*, 39 (2010) 3115-3141.

[91] M. Winter, J. O. Besenhard, Electrochemical lithiation of tin and tin-based intermetallics and composites, *Electrochim. Acta*, 45 (1999) 31-50.

[92] M. G. Kim, J. Cho, Reversible and High-capacity nanostructured electrode materials for Li-ion batteries, *Adv. Funct. Mater.*, 19 (2009) 1497-1514.

[93] R. Teki, M. K. Datta, R. Krishnan, T. C. Parker, T. M. Lu, P. N. Kumta, N. Koratkar, Nanostructured silicon anodes for lithium ion rechargeable batteries, *Small*, 5 (2009) 2236-2242.

[94] W. Wang, M. K. Datta, P. N. Kumta, Silicon-based composite anodes for Li-ion rechargeable batteries, *J. Mater. Chem.*, 17 (2007) 3229-3237.

[95] G. X. Wang, J. H. Ahn, J. Yao, S. Bewlay, H. K. Liu, Nanostructured Si-C composite anodes for lithium-ion batteries, *Electrochem. Commun.*, 6 (2004) 689-692.

[96] C. J. Wen, R. A. Huggins, Chemical diffusion in intermediate phases in the lithium-silicon system, *J. Solid State Chem*, 37 (1981) 271-278.

[97] M. N. Obrovac, L. Christensen, Structural changes in silicon anodes during lithium insertion/extraction, *Electrochem. Solid State Lett.*, 7 (2004) A93-A96.

[98] T. D. Hatchard, J. R. Dahn, In situ XRD and electrochemical study of the reaction of lithium with amorphous silicon, *J. Electrochem. Soc.*, 151 (2004) A838-A842.

[99] P. Limthongkul, Y. I. Jang, N. J. Dudney, Y. M. Chiang, Electrochemically-driven solid-state amorphization in lithium-silicon alloys and implications for lithium storage, *Acta mater.*, 51 (2003) 1103-1113.

[100] C. K. Chan, H. L. Peng, G. Liu, K. Mcllwrath, X. F. Zhang, R. A. Huggins, Y. Cui, High-performance lithium battery anodes using silicon nanowires, *Nat. Nanotechnol.*, 3 (2008) 31-35.

[101] M. S. Park, Y. J. Lee, S. Rajendran, M. S. Song, H. S. Kim, J. Y. Lee, Electrochemical properties of Si/Ni alloy-graphite composite as an anode material for Li-ion batteries, *Electrochim. Acta*, 50 (2005) 5561-5567.

[102] L. F. Cui, Y. Yang, C. M. Hsu, Y. Cui, Carbon-silicon core-shell nanowires as high capacity electrode for lithium ion batteries, *Nano Lett.*, 9 (2009) 3370-3374.

[103] B. Hertzberg, A. Alexeev, G. Yushin, Deformations in Si-Li anodes upon electrochemical alloying in nano-confined space, *J. Am. Chem. Soc.*, 132 (2010) 8548-+.

[104] H. Li, X. Huang, L. Chen, Z. Wu, Y. Liang, A high capacity nano-Si composite anode material for lithium rechargeable batteries, Electrochem. *Solid-State Lett.*, 2 (1999) 547-549.

[105] S. M. Hwang, H. Y. Lee, S. W. Jang, S. M. Lee, S. J. Lee, H. K. Baik, J. Y. Lee, Lithium insertion in SiAg powders produced by mechanical alloying, *Electrochem. Solid-State Lett.*, 4 (2001) A97-A100.

[106] M. Yoshio, H. Wang, K. Fukuda, T. Umeno, N. Dimov, Z. Ogumi, Carbon-coated Si as a lithium-ion battery anode material, *J. Electrochem. Soc.*, 149 (2002) A1598-A1603.

[107] H. C. Shin, J. A. Corno, J. L. Gole, M. Liu, Porous silicon negative electrodes for rechargeable lithium batteries, *J. Power Sources*, 139 (2005) 314-320.

[108] H. Ma, F. Cheng, J. Chen, J. Zhao, C. Li, Z. Tao, J. Liang, Nest-like silicon nanospheres for high-capacity lithium storage, *Adv. Mater.*, (19 (2007) 4067-+.

[109] N. Tamura, R. Oshita, M. Fujimoto, M. Kamino, S. Fujitani, Advanced structures in electrodeposited tin base negative electrodes for lithium secondary batteries, *J. Electrochem. Soc.*, 150 (2003) A679-A683.

[110] G. R. Goward, N. J. Taylor, D. C. S. Souza, L. F. Nazar, The true crystal structure of $Li_{17}M_4$ (M=Ge, Sn, Pb)-revised from $Li_{22}M_5$, *J. Alloys Compd.*, 329 (2001) 82-91.

[111] I. Kim, G. E. Blomgren, P. N. Kumta, Sn/C composite anodes for Li-ion batteries, *Electrochem. Solid-State Lett.*, 7 (2004) A44-A48.

[112] G. Derrien, J. Hassoun, S. Panero, B. Scrosati, Nanostructured Sn-C composite as an advanced anode material in high-performance lithium-ion batteries, *Adv. Mater.*, 19 (2007), 2336-+.

[113] Y. Idota, T. Kubota, A. Matsufuji, Y. Maekawa, T. Miyasaka, Tin-based amorphous oxide: A high-capacity lithium-ion-storage material, *Science*, 276 (1997) 1395-1397.

[114] D. Deng, M. G. Kim, Y. J. Lee, J. Cho, Green energy storage materials: Nanostructured TiO_2 and Sn-based anodes for lithium-ion batteries, *Energy Environ. Sci.*, 2 (2009) 818-837.

[115] I. A. Courtney, J. R. Dhan, Electrochemical and in situ x-ray diffraction studies of the reaction of lithium with tin oxide composites, *J. Electrochem. Soc.*, 144 (1997) 2045-2052.

[116] I. A. Courtney, J. R. Dhan, Key factors controlling the reversibility of the reaction of lithium with SnO_2 and Sn_2BPO_6 glass, *J. Electrochem. Soc.*, 144 (1997) 2943-2948.

[117] T. Brousse, R. Retoux, U. Herterich, D. M. Schleich, Thin-film crystalline SnO_2-lithium electrodes, *J. Electrochem. Soc.*, 145 (1998) 1-4.

[118] D. Larcher, S. Beattie, M. Morcrette, K. Edstrom, J. C. Jumas, J. M. Tarascon, Recent findings and prospects in the field of pure metals as negative electrodes for Li-ion batteries, *J. Mater. Chem.*, 17 (2007) 3759-3772.

[119] H. B. Wu, J. S. Chen, H. H. Hng, X. W. Lou, Nanostructured metal oxide-based materials as advanced anodes for litium-ion batteries, *Nanoscale*, 4 (2012) 2526-2542.

[120] R. D. Cakan, Y. S. Hu, M. Antonietti, J. Maier, M. M. Titirici, Facile one-pot synthesis of mesoporous SnO_2 microspheres via nanoparticles assembly and lithium storage properties, *Chem. Mater.*, 20 (2008) 1227-1229.

[121] D. Deng, Y. J. Lee, Hollow core-shell mesospheres of crystalline SnO_2 nanoparticle aggregates for high capacity Li^+ ion storage, *Chem. Mater.*, 20 (2008) 1841-1846.

[122] C. Wang, Y. Zhou, M. Y. Ge, X. B. Xu, Z. L. Zhang, J. Z. Jiang, Large-scale synthesis of SnO_2 nanosheets with high lithium storage capacity, *J. Am. Chem. Soc.*, 132 (2010) 46-47.

[123] X. W. Lou, D. Deng, J. Y. Lee, L. A. Archer, Preparation of SnO_2/carbon composite hollow spheres and their lithium storage properties, *Chem. Mater.*, 20 (2008) 6562-6566.

[124] D. H. Wang, R. Kou, D. Choi, Z. G. Yang, Z. M. Nie, J. Li, L. V. Saraf, D. H. Hu, J. G. Zhang, G. L. Graff, J. Liu, M. A. Pope, I. A. Aksay, Ternary self-assembly of ordered metal oxide-graphene nanocomposites for electrochemical energy storage, *ACS Nano*, 4 (2010) 1587-1595.

[125] P. Poizot, S. Laruelle, S. Grugeon, L. Dupont, J. M. Tarascon, Nano-sized transition-metal oxides as negative-electrode materials for lithium-ion batteries, *Nature*, 407 (2000) 496-499.

[126] J. Cabana, L. Monconduit, D. Larcher, M. R. Palacin, Beyond intercalation-based Li-ion batteries: the state of the art and challenges of electrode materials reacting through conversion reactions, *Adv. Mater.*, 22 (2010) E170-E192.

[127] P. Poizot, S. Laruelle, S. Grugeon, L. Dupont, J. M. Tarascon, From the vanadates to 3d-metal oxides negative electrodes, *Ionics*, 6 (2000) 321-330.

[128] G. G. Amatucci, N. Pereira, Fluoride based electrode materials for advanced energy storage devices, *J. Fluorine Chem.*, 128 (2007) 243-262.

[129] S. B. Ni, T. Li, X. L. Yang, Fabrication of NiO nanoflakes and its application in lithium ion battery, *Mater. Chem. Phys.*, 132 (2012) 1108-1111.

[130] X. H. Wang, Z. B. Yang, X. L. Sun, X. W. Li, D. S. Wang, P. Wang, D. Y. He, NiO nanocone array electrode with high capacity and rate capability for Li-ion batteries, *J. Mater. Chem.*, 21 (2011) 9988-9990.

[131] J. Zhong, X. L. Wang, X. H. Xia, C. D. Gu, J. Y. Xiang, J. Zhang, J. P. Tu, Self-assembled sandwich-like NiO film and its application for Li-ion batteries, *J. Alloys Compd.*, 509 (2011) 3889-3893.

[132] E. Hosono, S. Fujihara, I. Honma, H. S. Zhou, The high power and high energy densities Li ion storage device by nanocrystalline and mesoporous Ni/NiO covered structure, *Electrochem. Commun.*, 8 (2006) 284-288.

[133] C. H. Xu, J. Sun, L. A. Gao, Large scale synthesis of nickel oxide/multiwalled carbon nanotube composites by direct thermal decomposition and their lithium storage properties, *J. Power Sources*, 196 (2011) 5138-5142.

[134] Y. Q. Zou, Y. Wang, NiO nanosheets grown on graphene nanosheets as superior anode materials for Li-ion batteries, *Nanoscale*, 3 (2011) 2615-2620.

[135] Z. Y. Wang, D. Y. Luan, S. Madhavi, C. M. Li, X. W. Lou, Alpha-Fe_2O_3 nanotubes with superior lithium storage capability, *Chem. Commun.*, 47 (2011) 8061-8063.

[136] B. Wang, J. S. Chen, H. B. Wu, Z. Wang, X. W. Lou, Quasiemulsion-templated formation of alpha-Fe_2O_3 hollow spheres with enhanced lithium storage properties, *J. Am. Chem. Soc.*, 133 (2011) 17146-17148.

[137] H. Liu, G. X. Wang, J. Park, J. Wang, C. Zhang, Electrochemical performance of alpha-Fe_2O_3 nanorods as anode material for lithium-ion cells, *Electrochim. Acta*, 54 (2009) 1733-1736.

[138] S. L. Liu, L. N. Zhang, J. P. Zhou, J. F. Xiang, J. T. Sun, J. G. Guan, Fiber-like $Fe(2)O(3)$ macroporous nanomaterials fabricated by calcinating regenerate cellulose composite fibers, *Chem. Mater.*, 20 (2008) 3623-3628.

[139] X. W. Li, L. Qiao, D. Li, X. H. Wang, W. H. Xie, D. Y. He, Three-dimensional network structured alpha-Fe_2O_3 made from a stainless steel plate as a high-performance electrode for lithium ion batteries, *J. Mater. Chem. A*, 1 (2013) 6400-6406.

[140] A. Banerjee, V. Aravindan, S. Bhatnagar, D. Mhamane, S. Madhavi, S. Ogale, Superior lithium storage properties of α- Fe_2O_3 nano-assembled spindles, *Nano Energy*, 2 (2013) 890-896.

[141] L. Taberna, S. Mitra, P. Poizot, , P. Simon, J. M. Tarascon, High rate capabilities Fe_3O_4-based Cu nano-architectured electrodes for lithium-ion battery applications, *Nat. mater.*, 5 (2006) 567-573.

[142] S. Wang, J. Zhang, C. Chen, Fe_3O_4 submicron spheroids as anode materials for lithium-ion batteries with stable and high electrochemical performance, *J. Power Sources*, 195 (2010) 5379-5381.

[143] Y. G. Li, B. Tan, Y. Y. Wu, Mesoporous CO_3O_4 nanowire arrays for lithium ion batteries with high capacity and rate capability, *Nano Lett.*, 8 (2008) 265-270.

[144] X. W. Lou, D. Deng, J. Y. Lee, J. Feng, L. A. Archer, Self-supported formatnion of needlelike Co_3O_4 nanotubes and their application as lithium-ion battery electrodes, *Adv. Mater.*, 20 (2008) 258-262.

[145] F. M. Zhan, B. Y. Geng, Y. J. Guo, Porous Co_3O_4 Nanosheets with extraordinarily high discharge capacity for lithium batteries, *Chem. Eur. J.*, 15 (2009) 6169-6174.

[146] J. M. Ma, A. Manthiram, Precursor-directed formation of hollow Co_3O_4 nanospheres exhibiting superior lithium storage properties, *RSC Adv.*, 2 (2012) 3187-3189.

[147] Y. Wang, H. Xia, L. Lu, J. Y. Lin, Excellent performance in lithium-ion battery anodes: rational synthesis of Co(CO$_3$)(0.5)(OH)0.11H(2)O nanobelt array and its conversion into mesoporous and single-crystal Co_3O_4, *ACS Nano*, 4 (2010) 1425-1432.

[148] Y. Shan, L. Gao, Multiwalled carbon nanotubes/Co_3O_4 nanocomposites and its electrochemical performance in lithium storage, *Chem. Lett.*, 33 (2004) 1560-1561.

[149] B. Wang, Y. Wang, J. Park, H. Ahn, G. X. Wang, In situ synthesis of Co_3O_4/graphene nanocomposite material for lithium-ion batteries and supercapacitors with high capacity and supercapacitance, *J. Alloys Compd.*, 509 (2011) 7778-7783.

[150] S. H. Lee, Y. H. Kim, R. Deshpande, P. A. Parilla, E. Whitney, D. T. Gillaspie, K. M. Jones, A. H. Mahan, S. B. Zhang, Reversible lithium-ion insertion in molybdenum oxide nanoparticles, *Adv. Mater.*, 20 (2008) 3627-3632.

[151] S. H. Lee, R. Deshpande, D. Benhammou, P. A. Parilla, A. H. Mahan, A. C. Dillon, Metal oxide nanoparticles for advanced energy applications, *Thin Solid Films*, 517 (2009) 3591-3595.

[152] Y. F. Shi, B. K. Guo, S. A. Corr, Q. H. Shi, Y. S. Hu, K. R. Heier, L. Q. Chen, R. Seshadri, G. D. Stucky, Ordered Mesoporous Metallic MoO_2 Materials with Highly Reversible Lithium Storage Capacity, *Nano Lett.*, 9 (2009) 4215-4220.

[153] A. Bhaskar, M. Deepa, T. N. Rao, U. V. Varadaraju, Enhanced nanoscale conduction capability of a MoO_2/Graphene composite for high performance anodes in lithium ion batteries, *J. Power Sources*, 216 (2012) 169-178.

[154] J. S. Chen, Y. L. Cheah, S. Madhavi, X. W. Lou, Fast synthesis of alpha-MoO_3 nanorods with controlled aspect ratios and their enhanced lithium storage capabilities, *J. Phys. Chem. C*, 114 (2010) 8675-8678.

[155] F. Leroux, G. R. Goward, W. P. Power, L. F. Nazar, Understanding the nature of low-potential Li uptake into high volumetric capacity molybdenum oxides, *Electrochem. Solid-State Lett.*, 1 (1998) 255-258.

[156] M. F. Hassan, Z. P. Guo, Z. Chen, H. K. Liu, Carbon-coated MoO_3 nanobelts as anode materials for lithium-ion batteries, *J. Power Sources*, 195 (2010) 2372-2376.

[157] X. J. Liu, H. Yasuda, M. Yamachi, Solid solution of nickel oxide and manganese oxide as negative active material for lithium secondary cells, *J. Power Sources*, 146 (2005) 510-515.

[158] Q. Fan, M. S. Whittingham, Electrospun manganese oxide nanofibers as anodes for lithium-ion batteries, *Electrochem. Solid-State Lett.*, 10 (2007) A48-A51.

[159] J. C. Park, J. Kim, H. Kwon, H. Song, Gram-scale synthesis of Cu_2O nanocubes and subsequent oxidation to CuO hollow nanostructures for lithium-ion battery anode materials, *Adv. Mater.*, 21 (2009) 803-807.

[160] L. Fu, J. Gao, T. Zhang, Q. Cao, L. C. Wang, Y. P. Wu, R. Holze, H. Q. Wu, Preparation of Cu_2O particles with different morphologies and their application in lithium ion batteries, *J. Power Sources*, 174 (2007) 1197-1200.

[161] W. Xiao, J. S. Chen, Q. Lu, X. W. Lou, Porous spheres assembled from polythiophene (PTh)-coated ultrathin MnO_2 nanosheets with enhanced lithium storage capabilities, *J. Phys. Chem. C*, 114 (2010) 12048-12051.

[162] L. B. Chen, N. Lu, C. M. Xu, H. C. Yu, T. H. Wang, Electrochemical performance of polycrystalline CuO nanowires as anode material for Li ion batteries, *Electrochim. Acta*, 54 (2009) 4198-4201.

[163] S. Ko, J. I. Lee, H. S. Yang, S. Park, U. Jeong, Mesoporous CuO particles threaded with CNTs for high-performance lithium-ion battery anodes, *Adv. Mater.*, 24 (2012) 4451-4456.

[164] L. Q. Lu, Y. Wang, Facile synthesis of graphene-supported shuttle-and urchin-like CuO for high and fast Li-ion storage, *Electrochem. Commun.*, 14 (2012) 82-85.

[165] P. Pavela, J. L. Tirado, C. Vidal-Abarca, Sol-gel preparation of cobalt manganese mixed oxides for their use as electrode materials in lithium cells, *Electrochim. Acta*, 52 (2007) 7986-7995.

[166] G. Q. Zhang, L. Yu, H. B. Wu, H. E. Hoster, X. W. Lou, Formation of $ZnMn_2O_4$ ball-in ball hollow microspheres as high-performance anode for lithium-ion batteries, *Adv. Mater.*, 24 (2012) 4609-4613.

[167] Y. Q. Chu, Z. W. Fu, Q. Z. Qin, Cobalt ferrite thin films as anode material for lithium ion batteries, *Electrochim. Acta*, 49 (2004) 4915-4921.

[168] R. Alcantara, M. Jaraba, P. Lavela, J. L. Tirado, J. C. Jumas, J. Olivier-Fourcade, Changes in oxidation state and magnetic order of iron atoms during the electrochemical reaction of lithium with $NiFe_2O_4$, *Electrochem. Commun.*, 5 (2003) 16-21.

[169] Y. Sharma, N. Sharma, G. V. S. Rao, B. V. R. Chowdari, Studies on spinel cobaltites, $FeCo_2O_4$ and $MgCo_2O_4$ as anodes for Li-ion batteries, *Solid State ionics*, 179 (2008) 587-597.

[170] Y. Sharma, N. Sharma, G. V. S. Rao, B. V. R. Chowdari, Lithium recycling behaviour of nano-phase-$CuCo_2O_4$ as anode for lithium-ion batteries, *J. Power Sources*, 173 (2008) 495-501.

[171] X. Yao, C. Zhao, J. Kong, D. Zhou, X. Lu, Polydopamine-assisted synthesis of hollow $NiCo_2O_4$ nanospheres as high performance lithium ion battery anodes, *RSC Adv.*, 4 (2014) 37928-37933.

[172] S. W. Kim, H. W. Lee, P. Muralidharan, D. H. Seo, W. S. Yoon, D. K. Kim, K. Kang, Electrochemical performance and ex situ analysis of $ZnMn_2O_4$ nanowires as anode materials for lithium rechargeable batteries, *Nano, Res.*, 4 (2011) 505-510.

[173] B. Qu, L. Hu, Q. Li, Y. Wang, L. Chen, T. Wang, High-performance lithium-ion battery anode by direct growth of hierarchical $ZnCo_2O_4$ nanostructures on current collectors, *ACS Appl. Mater. Interfaces*, 6 (2014) 731-736.

[174] L. Hu, B. Qu, C. Li, Y. Chen, L. Mei, D. Lei, L. Chen, Q. Li, T. Wang, Facile synthesis of uniform mesoporous $ZnCo_2O_4$ microspheres as a high-performance anode material for Li-ion batteries, *J. Mater. Chem. A*, 1 (2013) 5596-5602.

[175] H. S. Jadhav, R. S. Kalubarme, C. N. Park, J. Kim, C. J. Park, Facile and cost effective synthesis of mesoporous spinel $NiCo_2O_4$ as anode for high lithium storage capacity, *Nanoscale*, 6 (2014) 10071-10076.

[176] H. Guo, L. Liu, T. Li, W. Chen, J. Liu, Y. Guo, Y. Guo, Accurate hierarchical control of hollow crossed $NiCo_2O_4$ nanocubes for superior lithium storage, *Nanoscale*, 6 (2014) 5491-5497.

[177] L. Zhou, D. Zhao, X. W. Lou, Double-shelled $CoMn_2O_4$ hollow microcubes as high-capacity anodes for lithium ion batteries, *Adv. Mater.*, 24 (2012) 745-748.

[178] L. Yu, L. Zhang, H. B. Wu, G. Zhang, X. W. Lou, Controlled synthesis of hierarchical $Co_xMn_{3-x}O_4$ array micro/nanostructures with tunable morphology and composition as integrated electrodes for lithium-ion batteries, *Energy Environ. Sci.*, 6 (2013) 2664-2671.

[179] Y. Chen, M. Zhuo, J. Deng, Z. Xu, Q. Li, T. Wang, Reduced graphene oxide networks as an effective buffer matrix to improve the electrode performance of porous $NiCo_2O_4$ nanoplates for lithium-ion batteries, *J. Mater. Chem. A*, 2 (2014) 4449-4456.

[180] Y. Wang, J. Park, B. Sun, H. J. Ahn, G. X. Wang, Winter-flower-like $CoFe_2O_4$/MWCNTs hybrid material for high-capacity reversible lithium storage, *Chem. Asian J.*, 7 (2012) 1940-1946.

[181] J. Sui, C. Zhang, D. Hong, J. Li, Q. Cheng, Z. Li, W. Cai, Facile synthesis of MWCNT-$ZnFe_2O_4$ nanocomposites as anode materials for lithium ion batteries, *J. Mater. Chem.*, 22 (2012) 13674-13681.

[182] X. Hou, X. Wang, B. Liu, Q. Wang, T. Luo, D. Chen, G. Shen, Hierarchical MnCo$_2$O$_4$ nanosheet arrays/carbon cloths as integrated anodes for lithium-ion batteries with improved performance, *Nanoscale*, 6 (2014) 8858-8864.

[183] J. N. Reimers, J. R. Dhan, Electrochemical and in situ X-ray-diffraction studies of lithium intercalation in Li$_x$CoO$_2$, *J. Electrochem. Soc.*, 139 (1992) 2091-2097.

[184] T. Ohzuku, A. Ueda, Why transition-metal (di) oxides are the most attractive materials for batteries, *Solid State ionics*, 69 (1994) 201-211.

[185] T. Ohzuku, A. Ueda, N. Nagayama, Electrochemistry and structural chemistry of LiNiO$_2$ (R(3) over-bar-M) for 4 volt secondary lithium cells, *J. Electrochem. Soc.*, 140 (1993) 1862-1870.

[186] M. M. Thackeray, Structural considerations of layered and spinel lithiated oxides for lithium ion batteries, *J. Electrochem. Soc.*, 142 (1995) 2558-2563.

[187] X. X. Li, F. Y. Cheng, B. Guo, J. Chen, Template-synthesized LiCoO$_2$, LiMn$_2$O$_4$, and LiNi$_{0.8}$Co$_{0.2}$O$_2$ nanotubes as the cathode materials of lithium ion batteries. *J. Phys. Chem. B*, 109 (2005) 14017-14024.

[188] Q. Cao, H. P. Zhang, G. J. Wang, Q. Xia, Y. P. Wu, H. Q. Wu, A novel carbon-coated LiCoO$_2$ as cathode material for lithium ion battery, *Electrochem. Commun.*, 9 (2007) 1228-1232.

[189] J. M. Tarascon, E. Wang, F. K. Shokoohi, W. R. McKinnon, S. Colson, The spinel phase of LiMn$_2$O$_4$ as a cathode in secondary lithium cells. *J. Electrochem. Soc.*, 138 (1991) 2859-2864.

[190] C. J. Curtis, J. Wang, D. L. Schulz, Preparation and characterization of LiMn$_2$O$_4$ spinel nanoparticles as cathode materials in secondary Li batteries, *J. Electrochem. Soc.*, 151 (2004) A590-A598.

[191] J. Luo, Y. Wang, H. Xiong, Y. Xia, Ordered mesoporous spinel LiMn(2)O(4)by a soft-chemical process as a cathode material for lithium-ion batteries, *Chem. Mater.*, 19 (2007) 4791-4795.

[192] J. Cho, M. M. Thackeray, Structural changes of $LiMn_2O_4$ spinel electrodes during electrochemical cycling, *J. Electrochem. Soc.*, 146 (1999) 3577-3581.

[193] W. J. Zhang, Structure and performance of $LiFePO_4$ cathode materials: A review, *J. Power Sources*, 196 (2011) 2962-2970.

[194] V. Srinivasan, J. Newman, Existence of path-dependence in the $LiFePO_4$ electrode, *Electrochem. Solid-State Lett.*, 9 (2006) A110-A114.

[195] C. Delacourt, P. Poizot, S. Levasseur, C. Masquelier, Size effects on carbon-free $LiFePO_4$ powders, *Electrochem. Solid State Lett.*, 9 (2006) A352-A355.

[196] H. Huang, S. C. Yin, L. F. Nazar, Approaching theoretical capacity of $LiFePO_4$ at room temperature at high rates, *Electrochem. Solid State Lett.*, 4 (2001) A170-A172.

[197] X. L. Li, F. Y. Kang, X. D. Bai, W. Shen, A novel network composite cathode of $LiFePO_4$/multiwalled carbon nanotubes with high rate capability for lithium ion batteries, *Electrochem. Commun.*, 9 (2007) 663-666.

[198] Y. Ding, Y. Jiang, F. Xu, J. Yin, H. Ren, Q. Zhuo, Z. Long, P. Zhang, Preparation of nano-structured $LiFePO_4$/graphene composites by co-precipitation method, *Electrochem. Commun.*, 12 (2010) 10-13.

[199] L. Wang, H. Wang, Z. Liu, C, Xiao, S. Dong, P. Han, Z. Zhang, C. Bi, G. Cui, A facile method of preparing mixed conducting $LiFePO_4$/graphene composites for lithium-ion batteries, *Solid State Ionics*, 181 (2010) 1685-1689.

[200] A. Burke, Ultracapacitors: why, how and where is the technology, *J. Power Sources*, 91 (2007) 37-50.

[201] B. E. Conway, Electrochemical Supercapacitors, Scientific Fundamentals and Technological Applications, New York, Kluwer Academic Publishers/Plenum Press 1999.

[202] R. Kotz, M. Carlen, Principles and applications of electrochemical capacitors, *Electrochim. Acta*, 45 (2000) 2483-2498.

[203] H. I. Becker, Low voltage electrolytic capacitor, US Patent 2800616, United States, 1957.

[204] R.A. Rightmire, Electrical energy storage apparatus, US Patent 3288641, United States, 1966.

[205] P. Simon, Y. Gogotsi, Materials for electrochemical capacitors, *Nat. Mater.*, 7 (2008) 845-854.

[206] US Department of Energy, Basic Research Needs for Electrical Energy Storage, (www.sc.doe.gov/bes/reports/abstracts.html#EES2007), Washington DC, 2007.

[207] M. Jayalakshmi, K. Balasubramanian, Simple capacitors to supercapacitors-An overview, *Int. J. Electrochem. Sci.*, 3 (2008) 1196-1217.

[208] C. Liu, F. Li, L. P. Ma, H. M. Cheng, Advanced Materials for energy storage, *Adv. Mater.*, 22 (2010) E28-E62.

[209] W. Sugimoto, H. Iwata, Y. Murakami, Y. Takasu, Electrochemical capacitor behaviour of layered ruthenic acid hydrate, *J. Electrochem. Soc.*, 151 (2004) A1181-A1187.

[210] M. S. Wu, P. C. Chiang, Fabrication of nanostructured manganese oxide electrodes for electrochemical capacitors, *Electrochem. Solid-State Lett.*, 7 (2004) A123-A126.

[211] S. G. Kandalkar, J. L. Gunjakar, C, D. Lokhande, Preparation of cobalt oxide thin films and its use in supercapacitor application, *Appl. Surf. Sci.*, 254 (2008) 5540-5544.

[212] Y. Zhang, H. Feng, X. Wu, L. Wang, A. Zhang, T. Xia, H. Dong, X. Li, L. Zhang, Progress of electrochemical capacitor electrode materials: A review, *Int. J. Hydrogen Energy*, 34 (2009) 4889-4899.

[213] B. E. Conway, V. Birss, J. Wojtowicz, The role and utilization of pseudocapacitance for energy storage by supercapacitors, *J. Power Sources*, 66 (1997) 1-14.

[214] G. P. Wang, L. Zhang, J. Zhang, A review of electrode materials for electrochemical supercapacitors, *Chem. Soc. Rev.*, 41 (2012) 797-828.

[215] D. Qu, H. Shi, Studies of activated carbons used in double-layer capacitors, *J. Power Sources*, 74 (1998) 99-107.

[216] B. Xu, F. Wu, R. Chen, G. Cao, S. Chen, Z. Zhou, Y. Yang, Highly mesoporous and high surface area carbon: A high capacitance electrode material for EDLCs with various electrolytes, *Electrochem. Commun.*, 10 (2008) 795-797.

[217] E. R. Pinero, K. Kierzek, J. Machnikowski, F. Beguin, Relationship between the nanoporous texture of activated carbons and their capacitance properties in different electrolytes, *Carbon*, 44 (2006) 2498.

[218] C. Niu, E. K. Sichel, R. Hoch, D. Moy, H. Tennent, High power electrochemical capacitors based on carbon nanotube electrodes, *Appl. Phys. Lett.*, 70 (1997) 1480-1482.

[219] D. N. Futaba, K. Hata, T. Yamada, T. Hiraoka, Y. Hayamizu, Y. Kakudate, O. Tanaike, H. Hatori, M. Yumura, S. Iijima. Shape-engineerable and highly densely

packed single-walled carbon nanotubes and their application as super-capacitor electrodes, *Nat. Mater.*, 5 (2006) 987-994.

[220] T. Bordjiba, L. H. D. M. Mohamedi, New class of carbon-nanotube aerogel electrodes for electrochemical power sources, *Adv. Mater.*, 20 (2008) 815-819.

[221] H. Zhang, G. P. Cao, Z. Y. Wang, Y. S. Yang, Z. J. Shi, Z. N. Gu, Growth of manganese oxide nanoflowers on vertically-aligned carbon nanotube arrays for high-rate electrochemical capacitive energy storage, *Nano Lett.*, 8 (2008) 2664-2668.

[222] Y. W. Zhu, S. Murali, M. D. Stoller, A. Velamakanni, R. D. Piner, R. S. Ruoff, Microwave assisted exfoliation and reduction of graphite oxide for ultracapacitors, *Carbon*, 48 (2010) 2118-2122.

[223] Y. Wang, Z. Shi, Y. Huang, Y. Ma, C. Wang, M. Chen, Supercapacitor devices based on graphene materials, *J. Phys. Chem. C*, 113 (2009) 13103-13107.

[224] X. Zhao, B. M. Sanchez, P. J. Dobson, P. S. Grant, The role of nanomaterials in redox-based supercapacitors for next generation energy storage devices, *Nanoscale*, 3 (2011) 839-855.

[225] I. H. Kim, K. B. Kim, Electrochemical characterization of hydrous ruthenium oxide thin-film electrodes for electrochemical capacitor applications, *J. Electrochem. Soc.*, 153 (2006) A383-A389.

[226] T. P. Gujar, V. R. Shinde, C. D. Lokhande, W. Y. Kim, K. D. Jung, O. S. Joo, Spray deposited amorphous RuO_2 for an effective use in electrochemical supercapacitor, *Electrochem. Commun.*, 9 (2007) 504-210.

[227] Y. Wang, C. Y. Foo, T. K. Hoo, M. Ng, J. Lin, Designed smart system of the sandwiched and concentric architecture of $RuO_2/C/RuO_2$ for high performance in electrochemical energy storage, *Chem. Eur. J.*, 16 (2010) 3598-3603.

[228] J. K. Chang, M. T. Lee, W. T. Tsai, In situ MnK-edge X-ray absorption spectroscopic studies of anodically deposited manganese oxide with relevance to supercapacitor applications, *J. Power Sources*, 166 (2007) 590-594.

[229] H. Lee, J. Goodenough, Supercapacitor behavior with KCl electrolyte, *J. Solid State Chem.*, 144 (1999) 220-223.

[230] M. Nakayama, T. Kanaya, R. Inoue, Anodic deposition of layered manganese oxide into a colloidal crystal template for electrochemical supercapacitor, *Electrochem. Commun.*, 9 (2007) 1154-1158.

[231] M. Toupin, T. Brousse, D. Belanger, Charge storage mechanism of MnO_2 electrode used in aqueous electrochemical capacitor, *Chem. Mater.*, 16 (2004) 3184-3190.

[232] V. Subramanian, H. Zhu, B. Wei, Alcohol-assisted room temperature synthesis of different nanostructured manganese oxides and their pseudocapacitance properties in neutral electrolyte, *Chem. Phys. Lett.*, 453 (2008) 242-249.

[233] K. W. Nam, K. H. Kim, E. S. Lee, W. S. Yoon, X. Q. Yang, K. B. Kim, Pseudocapacitive properties of electrochemically prepared nickel oxides on 3-dimensional carbon nanotube film substrates, *J. Power Sources*, 182 (2008) 642-652.

[234] Y. G. Wang, Y. Y. Xia, Electrochemical capacitance characterization of NiO with ordered mesoporous structure synthesized by template SBA-15, *Electrochim. Acta*, 51 (2006) 3223-3227.

[235] J. W. Lang, L. B. Kong, W. J. Wu, Y. C. Luo, L. Kang, Facile approach to prepare loose-packed NiO nano-flakes materials for supercapacitors, *Chem. Commun.*, (2008), 4213-4215.

[236] Y. Ren, L. Gao, From three-dimensional flower-like alpha-Ni(OH)(2) nanostructures to hierarchical porous NiO nanoflowers: microwave-assisted fabrication and supercapacitor properties, *J. Am. Ceram. Soc.*, 93 (2010) 3560.

[237] C. Yuan, X. Zhang, L. Su, B. Gao, L. Shen, Facile synthesis and self-assembly of hierarchical porous NiO nano/micro spherical superstructures for high performance supercapacitors, *J. Mater. Chem.*, 19 (2009) 5772-5777.

[238] X. Zhang, W. Shi, J. Zhu, W. Zhao, J. Ma, S. Mhaisalkar, T. L. Maria, Y. Yang, H. Zhang, H. H. Hng, Q. Yan, Synthesis of porous NiO nanocrystals with controllable surface area and their application as supercapacitor electrodes, *Nano Res.*, 3 (2010) 643-652.

[239] L. B. Kong, W. J. Wu, M. Liu, Y. C. Luo, L. Kang, A facile approach to the preparation of loose-packed Ni(OH)(2) nanoflake materials for electrochemical capacitors, *J. Solid State Electrochem.*, 13 (2009) 333-340.

[240] S. Xing, Q. Wang, Z. Ma, Y. Wu, Y. Gao, Synthesis of mesoporous $Ni(OH)_2$ for high-performance supercapacitors, *Mater. Lett.*, 78 (2012) 99-101.

[241] L. Gong, X. Liu, L. Su, Facile solvothermal synthesis of $Ni(OH)_2$ nanostructure for electrochemical capacitors, *J. Inorg. Organomet. Polym.*, 21 (2011) 866-870.

[242] Z. Lu, Z. Chang, W. Zhu, X. Sun, Beta-phased $Ni(OH)_2$ nanowall film with reversible capacitance higher than theoretical Faradic capacitance, *Chem. Commun.*, 47 (2011) 9651-9653.

[243] F. Zhang, L. Hao, Q. B. Fu, X. G. Zhang, Preparation and electrochemical capacitance performance of Co_3O_4 nanosheets, *Chin. J. Inorg. Chem.*, 26 (2010) 827-831.

[244] J. Xu, L. Gao, J. Cao, W. Wang, Z. Chen, Preparation and electrochemical capacitance of cobalt oxide (Co_3O_4) nanotubes as supercapacitor material, *Electrochim. Acta*, 56 (2010) 732-736.

[245] T. Y. Wei, C. H. Chen, K. H. Chang, S. Y. Lu, C. C. Hu, Cobalt oxide aerogels of ideal supercapacitive properties prepared with an epoxide synthetic route, *Chem. Mater.*, 21 (2009) 3228-3233.

[246] V. Gupta, S. Gupta, N. Miura, Al-substituted alpha-cobalt hydroxide synthesized by potentiostatic deposition method as an electrode material for redox-supercapacitors, *J. Power Sources*, 177 (2008) 685-689.

[247] V. Gupta, T. Kusahara, H. Toyama, S. Gupta, N. Miura, Potentiostatically deposited nanostructured alpha-Co(OH)(2): A high performance electrode material for redox-capacitors, *Electrochem. Commun.*, 9 (2007) 2315-2319.

[248] W. J. Zhou, M. W. Xu, D. D. Zhao, C. L. Xu, H. L. Li, Electrodeposition and characterization of ordered mesoporous cobalt hydroxide films on different substrates for supercapacitors, *Microporous mesoporous Mater.*, 117 (2009) 55-60.

[249] H. Y. Lee, J. B. Goodenough, Ideal supercapacitor behavior of amorphous V_2O_5 center dot nH(2)O in potassium chloride (KCl) aqueous solution, *J. Solid State Chem.*, 148 (1999) 81-84.

[250] G. Wee, H. Z. Soh, Y. L. Cheah, S. G. Mhaisalkar, M. Srinivasan, Synthesis and electrochemical properties of electrospun V_2O_5 nanofibers as supercapacitor electrodes, *J. Mater. Chem.*, 20 (2010) 6720-6725.

[251] N. L. Wu, S. Y. Wang, C. Y. Han, D. S. Wu, L. R. Shiue, Electrochemical capacitor of magnetite in aqueous electrolytes, *J. Power Sources*, 113 (2003) 173-178.

[252] K. W. Chung, K. B. Kim, S. H. Han, H. Lee, Novel synthesis and electrochemical characterization of nano-sized cellular Fe_3O_4 thin film, *Electrochem. Solid State Lett.*, 8 (2005) A259-A262.

[253] J. Chen, K. Huang, S. Liu, Hydrothermal preparation of octadecahedron Fe_3O_4 thin film for use in an electrochemical supercapacitor, *Electrochim. Acta*, 55 (2009) 1-5.

[254] C. Yuan, J. Li, L. Hou, X. Zhang, L. Shen, X. W. Lou, Ultrathin mesoporous $NiCo_2O_4$ nanosheets supported on Ni foam as advanced electrodes for supercapacitors, *Adv. Funct. Mater.*, 22 (2012) 4592-4597.

[255] S. L. Kuo, J. F. Lee, N. L. Wu, Study on pseudocapacitance mechanism of aqueous MnFe(2)O(4) supercapacitor, *J. Electrochem. Soc.*, 154 (2007) A34-A38.

[256] N. Padmanathan, S. Selladurai, Mesoporous $MnCo_2O_4$ spinel oxide nanostructure synthesized by solvothermal technique for supercapacitor, *Ionics*, 20 (2014) 479-487.

[257] V. S. Kumbhar, A. D. Jagadale, N. M. Sinde, C. D. Lokhande, Chemical synthesis of spinel cobalt ferrite ($CoFe_2O_4$) nano-flakes for supercapacitor application, *Appl. Surf. Sci.*, 259 (2012) 39-43.

[258] Z. Y. Yu, L. F. Chen, S. H. Yu, Growth of $NiFe_2O_4$ nanoparticles on carbon cloth for high performance flexible supercapacitor, *J. Mater. Chem. A*, 2 (2014) 10889-10894.

[259] J. Xiao, S. Yang, Sequential crystallization of sea urchin-like bimetallic (Ni, Co) carbonate hydroxide and its morphology conserved conversion to porous $NiCo_2O_4$ spinel for pseudocapacitors, *RSC Adv.*, 1 (2011) 588-595.

[260] Q. Lu, Y. Chen, W. Li, J. G. Chen, J. Q. Xiao, F. Jiao, Ordered mesoporous nickel cobaltite spinel with ultra-high supercapacitance, *J. Mater. Chem. A*, 1 (2013) 2331-2336.

[261] H. Jiang, J. Ma, C. Li, Hierarchical porous $NiCo_2O_4$ nanowires for high-rate supercapacitors, *Chem. Commun.*, 48 (2012) 4465-4467.

[262] C. Wang, X. Zhang, D. Zhang, C. Yao, Y. Ma, Facile and low-cost fabrication of nanostructured $NiCo_2O_4$ spinel with high specific capacitance and excellent cycle stability, *Electrochim. Acta*, 63 (2012) 220-227.

[263] Q. Wang, B. Liu, X. Wang, S. Ran, L. Wang, D. Chen, G. Shen, Morphology evolution of urchin-like $NiCo_2O_4$ nanostructures and their applications as psuedocapacitors and photoelectrochemical cells, *J. Mater. Chem.*, 22 (2012) 21647-21653.

[264] C. Yuan, J. Li, L. Hou, L. Yang, L. Shen, X. Zhang, Facile template-free synthesis of ultralayered mesoporous nickel cobaltite nanowires towards high-performance electrochemical capacitors, *J. Mater. Chem.*, 22 (2012) 16084-16090.

[265] W. Y. Li, K. B. Xu, G. S. Song, X. Y. Zhou, R. J. Zou, J. M. Yang, Z. G. Chen, J. Q. Hu, Facile synthesis of porous $MnCo_2O_{4.5}$ hierarchical architectures for high-rate supercapacitors, *CrystEngComm*, 16 (2014) 2335-2339.

[266] Y. Xu, X. Wang, C. An, Y. Wang, L. Jiao, H. Yuan, Facile synthesis route of porous $MnCo_2O_4$ and $CoMn_2O_4$ nanowires and their excellent electrochemical properties in supercapacitors, *J. Mater. Chem. A*, 2 (2014) 16480-16488.

[267] S. Jiang, T. Shi, H. Long, Y. Sun, W. Zhou, Z. Tang, High-performance binder-free supercapacitor electrode by direct growth of cobalt-manganese composite oxide nansostructures on nickel foam, *Nanoscale Res. Lett.*, 9 (2014) 492-499.

[268] F. Bao, X. Wang, X. Zhao, Y. Wang, Y. Ji, H. Zhang, X. Liu, Controlled growth of mesoporous $ZnCo_2O_4$ nanosheet arrays on Ni foam as high-rate electrodes for supercapacitors, *RSC Adv.*, 4 (2014) 2521-2525.

[269] M. Zhu, D. Meng, C. Wang, G. Diao, Facile fabrication of hierarchically porous $CuFe_2O_4$ nanospheres with enhanced capacitance property, *ACS Appl. Mater. Interfaces*, 5 (2013) 6030-6037.

[270] J. Li, Q. M. Yang, I. Zhitomirsky, Nickel foam-based manganese dioxide-carbon nanotube composite electrodes for electrochemical supercapacitors, *J. Power Sources*, 185 (2008) 1569-1574.

[271] I. H. Kim, J. H. Kim, B. W. Cho, Y. H. Lee, K. B. Kim, Synthesis and electrochemical characterization of vanadium oxide on carbon nanotube film substrate for pseudocapacitor applications, *J. Electrochem. Soc.*, 153 (2006) A989-A996.

[272] V. Subramanian, H. W. Zhu, B. Q. Wei, Synthesis and electrochemical characterizations of amorphous manganese oxide and single walled carbon nanotube composites as supercapacitor electrode materials, *Electrochem. Commun.*, 8 (2006) 827-832.

[273] Z. S. Wu, W. C. Ren, D. W. Wang, F. Li, B. L. Liu, H. M. Cheng, High-energy MnO_2 nanowire/graphene and graphene asymmetric electrochemical capacitors, *ACS Nano*, 4 (2010) 5835-5842.

[274] J. Yan, Z. J. Fan, T. Wei, W. Z. Qian, M. L. Zhang, F. Wei, Fast and reversible surface redox reaction of graphene-MnO_2 composites as supercapacitor electrodes, *Carbon*, 48 (2010) 3825-3833.

[275] S. Chen, J. W. Zhu, X. Wang, From graphene to metal oxide nanolamellas: a phenomenon of morphology transmission, *ACS Nano*, 4 (2010) 6212-6218.

[276] H. Lee, J. Kang, M. S. Cho, J. B. Choi, Y. Lee, MnO_2/graphene composite electrodes for supercapacitors: the effect of graphene intercalation, *J. Mater. Chem.*, 21 (2011) 18215-18219.

[277] X. Xia, J. Tu, Y. Mai, R. Chen, X. Wang, C. Gu, X. Zhao, Graphene sheet/porous NiO hybrid film for supercapacitor applications, *Chem. Eur. J*, 17 (2011) 10898-10905.

[278] X. Cao, Y. Shi, W. Shi, G. Lu, X. Huang, Q. Yan, Q. Zhang, H. Zhang, Preparation of novel 3D graphene networks for supercapacitor applications, *Small*, 7 (2011) 3163-3168.

[279] X. Wang, S. Liu, H. Wang, F. Tu, D. Fang, Y. Li, Facile and green synthesis of Co_3O_4 nanoplates/graphene nanosheets composite for supercapacitor, *J. Solid State Electrochem.*, 16 (2012) 3593-3602.

[280] J. Yuan, J. Zhu, H. Bi, X. Meng, S. Liang, L. Zhang, X. Wang, Graphene-based 3D composite hydrogel by anchoring Co_3O_4 nanoparticles with enhanced electrochemical properties, *Phys. Chem. Chem. Phys.*, 15 (2013) 12940-12945.

[281] K. S. Ryu, K. M. Kim, N. G. Park, Y. J. Park, S. H. Chang, Symmetric redox supercapacitor with conducting polyaniline electrodes, *J. Power Sources*, 103 (2002) 305-309.

[282] A. Clemente, S. Panero, E. Spila, B. Scrosati, Solid-state, polymer-based, redox capacitors, *Solid State Ionics*, 85 (1996) 273-277.

[283] C. Arbizzani, M. M. Mastragostino, F. Soavi, Polymer-based supercapacitors, *J. Power Sources*, 97 (2001) 812-815.

[284] F. Fusalba, P. Gouerec, D. Villers, D. Belanger, Electrochemical characterization of polyaniline in nonaqueous electrolyte and its evaluation as electrode material for electrochemical supercapacitors, *J. Electrochem. Soc.*, 148 (2001) A1-A6.

[285] C. Arbizzani, M. M. Mastragostino, L. Meneghello, Polymer-based redox supercapacitors: A comparative study, *Electrochim. Acta*, 41 (1996) 21-26.

[286] H. Mi, X. Zhang, S. An, X. Ye, S. Yang, Microwave-assisted synthesis and electrochemical capacitance of polyaniline/multi-wall carbon nanotubes composite, *Electrochem. Commun.*, 9 (2007) 2859-2862.

[287] J. Wang, Y. Xu, X. Chen, X. Sun, Capacitance properties of single wall carbon nanotube/polypyrrole composite films, *Compos. Sci. Technol.*, 67 (2007) 2981-2985.

[288] J. Yan, T. Wei, B. shao, Z. J. Fan, W. Z. Qian, M. L. Zhang, F. Wei, Preparation of a graphene nanosheet/polyaniline composite with high specific capacitance, *Carbon*, 48 (2010) 487-493.

[289] K. Zhang, L. L. Zhang, X. S. Zhao, J. S. Wu, Graphene/polyaniline nanofibre composites as supercapacitor electrodes, *Chem. Mater.*, 22 (2010) 1392-1401.

[290] Q. Wu, Y. Xu, Z. Yao, A. Liu, G. Shi, Supercapacitors based on flexible graphene/polyaniline nanofiber composite films, *ACS Nano*, 4 (2010) 1963-1970.

[291] A. Burke, R & D considerations for the performance and application of electrochemical capacitors, *Electrochim. Acta*, 53 (2007) 1083-1091.

[292] H. Ohno, K. Fukumoto, Progress in ionic liquids for electrochemical reaction matrices, *Electrochemistry*, 76 (2008) 16-23.

[293] A. Lewandowski, M. Galinski, Practical and theoretical limits for electrochemical double-layer capacitors, *J. Power Sources*, 173 (2007) 822-828.

[294] M. Galinski, A. Lewandowski, I. Stepniak, Ionic liquids as electrolytes, *Electrochim. Acta*, 51 (2006) 5567-5580.

[295] A. Lewandowski, M. Galinski, Carbon-ionic liquid double-layer capacitors, *J. Phys. Chem. Solids*, 64 (2004) 281-286.

[296] H. Liu, P. He, Z. Li, Y. Liu, J. Li, A novel nickel-based mixed rare-earth oxide/activated carbon supercapacitor using room temperature ionic liquid electrolyte, *Electrochim. Acta*, 51 (2006) 1925-1931.

[297] J. Chen, F. Y. Cheng, Combination of lightweight elements and nanostructured materials for batteries, *Acc. Chem. Res.*, 42 (2009) 713-723.

[298] A. Manthiram, V. Murugan, A. Sarkar, T. Muraliganth, Nanostructured electrode materials for electrochemical energy storage and conversion, *Energy Environ. Sci.*, 2008, 1, 621-638.

[299] P. Poizot, S. Laruelle, S. Grugeon, L. Dupont, J. M. Tarascon, Nano-sized transition-metal oxides as negative-electrode materials for lithium-ion batteries, *Nature*, 407 (2000) 496-499.

[300] S. Mitra, P. Poizot, A. Finke, J. M. Tarascon, Growth and electrochemical characterization versus lithium of Fe_3O_4 electrodes made by electrodeposition, *Adv. Funct. Mater.*, 16 (2006) 2281-2287.

[301] P. Poizot, S. Laruelle, S. Grugeon, J. M. Tarascon, Rationalization of the low-potential reactivity of 3d-metal-based inorganic compounds toward Li, *J. Electrochem. Soc.*, 149 (2002) A1212-A1217.

[302] W. W. Zeng, K. L. Huang, K. L. Yang, S. Q. Liu, R. S. Liu, Solvothermal synthesis and capacitance performance of Co_3O_4 with different morphologies, *Acta Phys. Chim. Sin.*, 24 (2008) 263-268.

[303] E. H. Liu, W. Li, J. Li, X. Y. Meng, R. Ding S. T. Tan, Preparation and characterization of nanostructured NiO/MnO_2 composite electrode for electrochemical supercapacitors, *Mater. Res. Bull.*, 44 (2009) 1122-1126.

[304] C. Y. Cao, W. Guo, Z. M. Cui, W. G. Song, W. Cai, Microwave-assisted gas/liquid interfacial synthesis of flowerlike NiO hollow nanosphere precursors

and their application as supercapacitor electrodes, *J. Mater. Chem.*, 21 (2011) 3204-3209.

[305] C. Belhomme, M. Cassir, C. Tessier, E. Berthoumieux, Lithium depth profile in NiO molten carbonate fuel Cell cathode by nuclear microprobe, *Electrochem. Solid-State Lett.*, 3 (2000) 216-219.

[306] J. R. A. Sietsma, J. D. Meeldijk, J. P. D. Breejen, M. V. Helder, A. J. V. Dillen, P. E. D. Jongh, K. P. D. Jong, The Preparation of supported NiO and Co_3O_4 nanoparticles by the nitric oxide controlled thermal decomposition of nitrates, *Angew. Chem. Int. Ed.*, 46 (2007) 4547-4549.

[307] W. Wang, Y. Liu, C. Xu, C. Zheng, G. Wang, Synthesis of NiO nanorods by a novel simple precursor thermal decomposition approach, *Chem. Phys. Lett.*, 362 (2002) 119-122.

[308] X. Liu, G. Qiu, Z. Wang, X. Li, Rationally synthetic strategy: from nickel hydroxide nanosheets to nickel oxide nanorolls, *Nanotechnology*, 16 (2005) 1400-1405.

[309] Y. Wang, Q. Zhu, H. Zhang, Fabrication of β-Ni(OH)$_2$ and NiO hollow spheres by a facile template-free process, *Chem. Commun.*, (2005) 5231-5233.

[310] X. Wang, L. J. Yu, P. Hu, F. L. Yuan, Synthesis of single-crystalline hollow octahedral NiO, *Cryst. Growth Des.*, 7 (2007) 2415-2418.

[311] T. Kavitha, H. Yuvaraj, A facile approach to the synthesis of high-quality NiO nanorods: electrochemical and antibacterial properties, *J. Mater. Chem.*, 21 (2011) 15686-15691.

[312] H. Liu, G. X. Wang, J. Liu, S. Z. Qiao, H. Ahn, Highly ordered mesoporous NiO anode material for lithium ion batteries with an excellent electrochemical performance, *J. Mater. Chem.*, 21 (2011) 3046-3052.

[313] X. H. Huang, J. P. Tu, C. Q. Zhang, F. Zhou, Hollow microspheres of NiO as anode materials for lithium-ion batteries, *Electrochim. Acta*, 55 (2010) 8981-8985.

[314] Y. Yao, J. Zhang, Z. Wei, A. Yu, Hydrothemal synthesis of porous NiO nanosheets and application as anode material for lithium ion batteries, *Int. J. Electrochem. Sci.*, 2012, 7, 1433-1442.

[315] S. A. Needham, G. X. Wang, H. K. Liu, Synthesis of NiO nanotubes for use as negative electrodes in lithium ion batteries, *J. Power Sources*, 159 (2006) 254-257.

[316] R. Dedryv`ere, S. Laruelle, S. Grugeon, P. Poizot, D. Gonbeau, J. M. Tarascon, Contribution of X-ray photoelectron spectroscopy to the study of the electrochemical reactivity of CoO toward lithium, *Chem. Mater.*, 16 (2004) 1056-1061.

[317] X. Sun, G. Wang, J-Y. Hwang, J. Lian, Porous nickel oxide nano-sheets for high performance pseudocapacitance materials, *J. Mater. Chem.*, 21 (2011) 16581-16588.

[318] H. M. Shiri, M. Aghazadeh, Synthesis, characterization and electrochemical properties of capsule-like NiO nanoparticles, *J. Electrochem. Soc.*, 159 (2012) E132-E138.

[319] X. Wang, L. Qiao, X. Sun, X. Li, D. Hu, Q. Zhang, D. He, Mesoporous NiO nanosheet networks as high performance anodes for Li ion batteries, *J. Mater. Chem. A*, 1 (2013) 4173-4176.

[320] M. Rose, W. Bohlmann, M. Sabo, S. Kaskel, Element-organic frameworks with high permanent porosity, *Chem. Commun.*, (2008) 2462-2464.

[321] S. K. Meher, P. Justin, G. R. Rao, Microwave-mediated synthesis for improved morphology and pseudocapacitance performance of nickel oxide, *ACS Appl. Mater. Interfaces*, 3 (2011) 2063-2073.

[322] J. R. Miller, P. Simon, Materials science-electrochemical capacitors for energy management, *Science*, 321 (2008) 651-652.

[323] E. Frackowiak, F. Beguin, Carbon materials for the electrochemical storage of energy in capacitors, *Carbon*, 39 (2001) 937-950.

[324] B. E. Conway, Transition from "supercapacitor" to "battery" behavior in electrochemical energy storage, *J. Electrochem. Soc.*, 138 (1991) 1539-1548.

[325] M. Kaempgen, C. K. Chan, J. Ma, Y. Cui, G. Gruner, Printable thin film supercapacitors using single-walled carbon nanotubes, *Nano Lett.*, 9 (2009) 1872-1876.

[326] B. Wang, J. S. Chen, Z. Y. Wang, S. Madhavi, X. W. Lou, Green synthesis of NiO nanobelts with exceptional pseudo-capacitive properties, *Adv. Energy Mater.*, 2 (2012) 1188-1192.

[327] T. Brezesinski, J. Wang, S. H. Tolbert, B. Dunn, Ordered mesoporous alpha-MoO$_3$ with iso-oriented nanocrystalline walls for thin-film pseudocapacitors, *Nat. Mater.*, 9 (2010) 146-151.

[328] Q. Lu, J. G. Chen, J. Q. Xiao, Nanostructured electrodes for high-performance pseudocapacitors, *Angew. Chem. Int. Ed.*, 52 (2013) 1882-1889.

[329] N. Kang, T. Yu, G. H. Lim, T. Koh, B. Lim, facile synthesis of carbon-suported, ultrasmall ruthenium oxide nanocrystals for supercapacitor electrode materials, *Chem. Phys. Lett.*, 592 (2014) 192-195.

[330] X. Xia, J. Tu, X. Wang, C. Gu, X. Zhao, Hierarchically porous NiO film grown by chemical bath deposition via a colloidal crystal template as an electrochemical pseudocapacitor material, *J. Mater. Chem.*, 21 (2011) 671-679.

[331] A. L. M. Barmi, M. Aghazadeh, B. Arhami, H. M. Shiri, A. A. Fazl, E. Jangju, Porous cobalt hydroxide nanosheets with excellent supercapacitive behaviour, *Chem. Phys. Lett.*, 541 (2012) 65-69.

[332] S. Devaraj, N. Munichandraiah, Effect of crystallographic structure of MnO_2 on its electrochemical capacitance properties, *J. Phys Chem C*, 112 (2008) 4406-4417.

[333] M. Xu, L. Kong, W. Zhou, H. Li, Hydrothermal synthesis and pseudocapacitance properties of α-MnO_2 hollow spheres and hollow urchins, *J. Phys Chem C*, 111 (2007) 19141-19147.

[334] M. S. Wu, K. C. Huang, Fabrication of nickel hydroxide electrodes with open-ended hexagonal nanotube arrays for high capacitance supercapacitors, *Chem. Commun.*, 47 (2011) 12122-12124.

[335] H. Jiang, T. Zhao, C. Li, J. Ma, Hierarchical self-assembly of ultrathin nickel hydroxide nanoflakes for high-performance supercapacitors, *J. Mater. Chem.*, 21 (2011) 3818-3823.

[336] J. Yan, E. Khoo, A. Sumboja, P. S. Lee, Facile coating of manganese oxide on tin oxide nanowires with high-performance capacitive behaviour, *ACS Nano*, 4 (2010) 4247-4255.

[337] T. Y. Wei, C. H. Chen, H. C. Chien, S. Y. Lu, C. C. Hu, A Cost-effective supercapacitor material of ultrahigh specific capacitances: spinel nickel cobaltite aerogels from an epoxide-driven sol-gel process, *Adv. Mater.*, 22 (2010) 347-351.

[338] J. Liu, J. Jiang, C. Cheng, H. Li, J. Zhang, H. Gong, H. J. Fan, Co_3O_4 nanowire@MnO_2 ultrathin nanosheet core/shell arrays: a new class of high-performance pseudocapacitive materials, *Adv. Mater.*, 23 (2011) 2076-2081.

[339] G. Hu, C. Li, H. Gong, Capacitance decay of nano porous nickel hydroxide, *J. Power Sources*, 195 (2010) 6977-6981.

[340] M. Aghazadeh, A. N. Golikand, M. Ghaemi, Synthesis, Characterization and electrochemical properties of ultrafine β-Ni(OH)$_2$ nanoparticles, *Int. J. Hydrogen Energy*, 36 (2011) 8674-8679.

[341] G. Fu, Z. Hu, L. Xie, X. Jin, Y. Xie, Y. Wang, Z. Zhang, Y. Yang, H. Wu, Electrodeposition of nickel hydroxide films on nickel foil and its electrochemical performances for supercapacitor, *Int. J. Electrochem. Sci.*, 4 (2009) 1052-1062.

[342] F. S. Cai, G. Y. Zhang, J. Chen, X. L. Gou, H. K. Liu, S. X. Dou, Ni(OH)$_2$ tubes with mesoscale dimensions as positive-electrode materials of alkaline rechargeable batteries, *Angew. Chem. Int. Ed.*, 43 (2004) 4212-4216.

[343] J. Chen, D. H. Bradhurst, S. X. Dou, H. K Liu, Nickel hydroxide as an active material for the positive electrode in rechargeable alkaline batteries, *J. Electrochem. Soc.*, 146 (1999) 3606-3612.

[344] T. K. Ying, X. P. Gao, W. K. Hu, F. Wu, D. Noreus, Studies on rechargeable NiMH batteries, *Int. J. Hydrogen Energy*, 31 (2006) 525-530.

[345] E. Shangguan, Z. Chang, H. Tang, X. Z. Yuan, H. Wang, Synthesis and characterization of high-density non-spherical Ni(OH)$_2$ cathode material for Ni-MH batteries, *Int. J. Hydrogen Energy*, 35 (2010) 9716-9724.

[346] L. X. Yang, Y. J. Zhu, H. Tong, Z. H. Liang, L. Li, L. Zhang, Hydrothermal synthesis of nickel hydroxide nanostructures in mixed solvents of water and alcohol, *J. Solid State Chem.*, 180 (2007) 2095-2101.

[347] L. Kumari, W. Z. Li, Self-assembly of β-Ni(OH)$_2$ nanoflakes to form hollow submicrospheres by hydrothermal route, *Physica E.*, 41 (2009) 1289-1292.

[348] B. N. Wang, X. Y. Chen, D. W. Zhang, Controllable synthesis and characterization of Cuo, β-Ni(OH)$_2$ and Co$_3$O$_4$ nanocrystals in the MCln- NH$_4$VO$_3$-NaOH system, *J. Phys. Chem. Solids*, 71 (2010) 285-289.

[349] D. Yang, R. Wang, M. He, J. Zhang, Z. Liu, Ribbon and boardlike nanostructures of nickel hydroxide: synthesis, characterization and electrochemical properties, *J. Phys. Chem. B*, 109 (2005) 7654-7658.

[350] S. Zhang, H. C. Zheng, Self-assembled hollow spheres of β-Ni(OH)$_2$ and their derived nanomaterials, *Chem. Mater.*, 21 (2009) 871-883.

[351] M. Cao, X. He, J. Chen, C. Hu, Self-assembled nickel hydroxide three-dimensional nanostructures: a nanomaterial for alkaline rechargeable batteries, *Cryst. Growth Des.*, 7 (2007) 170-174.

[352] M. Vidotti, C. Greco, E. A. Ponzio, S. C. Torresi, Sonochemically synthesized Ni(OH)$_2$ and Co(OH)$_2$ nanoparticles and their application in electrochromic electrodes, *Electrochem. Commun.*, 8 (2006) 554-560.

[353] G. A. Tompsett, W. C. Conner, K. S. Yngvesson, Microwave synthesis of nanoporous materials, *ChemPhysChem.*, 7 (2006) 296-319.

[354] I. Bilecka, M. Niederberger, Microwave Chemistry for inorganic nanomaterials synthesis, *Nanoscale*, 2 (2010) 1358-1374.

[355] L. R. Hou, C. Z. Yuan, L. Yang, L. F. Shen, F. Zhang, X. G. Zhang, Urchin-like Co$_3$O$_4$ microspherical hierarchical superstructures constructed by one-dimension nanowires toward electrochemical capacitors, *RSC Adv.*, 1 (2011) 1521-1526.

[356] W. Wei, Z. Z. Yang, Template synthesis of hierarchically structured composites, *Adv. Mater.*, 20 (2008) 2965-2969.

[357] F. Wang, S. Xiao, Y. Hou, C. Hu, L. Liu, Y. Wu, Electrode materials for aqueous asymmetric supercapacitors, *RSC Adv.*, 3 (2013) 13059-13084.

[358] W. Deng, X. Ji, Q. Chen, C. E. Banks, Electrochemical capacitors utilising transition metal oxides: an update of recent developments, *RSC Adv.*, 1 (2011) 1171-1178.

[359] P. Oliva, J. Leonardi, J. F. Laurent, C. Delmas, J. J. Braconnier, M. Figlarz, F. Fievet, A. de Guibert, Review of the structure and the electrochemistry of nickel hydroxides and oxy-hydroxides, *J. Power Sources*, 8 (1982) 229-255.

[360] A. Vinu, D. P. Sawant, K. Ariga, M. Hartmann, S. B. Halligudi, Benzylation of benzene and other aromatics by benzyl chloride over mesoporous AlSBA-15 catalysts, *Microporous Mesoporous Mater.*, 80 (2005) 195-203.

[361] J. Yan, W. Sun, T. Wei, Q. Zhang, Z. Fan, F. Wei, Fabrication and electrochemical performances of hierarchical porous $Ni(OH)_2$ nanoflakes anchored on graphene sheets, *J. Mater. Chem.*, 22 (2012) 11494-11502.

[362] U. M. Patil, K. V. Gourav, V. J. Fulari, C. D. Lokhande, O. S. Joo, Characterization of honeycomb-like "$Ni(OH)_2$" thin films synthesized by chemical bath deposition method and their supercapacitor application, *J. Power Sources*, 188 (2009) 338-342.

[363] M. Zhu, G. Diao, Review on the progress in synthesis and application of magnetic carbon nanocomposites, *Nanoscale*, 3 (2011) 2748-2767.

[364] Y. Cui, C. M. Lieber, Functional nanoscale electronic devices assembled using silicon nanowire building blocks, *Science*, 291 (2001) 851-853.

[365] H. Hiramatsu, F. E. Osterloh, A simple large-scale synthesis of nearly monodisperse gold and silver nanoparticles with adjustable sizes and with exchangeable surfactants, *Chem. Mater.*, 16 (2004) 2509-2511.

[366] B. M. Klahr, A. B. F. Martinson, T. W. Hamann, Photoelectrochemical investigation of ultrathin film iron oxide solar cells prepared by atomic layer deposition, *Langmuir*, 27 (2011) 461-468.

[367] K. Sivula, R. Zboril, F. L. Formal, R. Robert, A. Weidenkaff, J. Tucek, J. Frydrych, M. Gratzel, Photoelectrochemical water splitting with mesoporous

hematite prepared by a solution-based colloidal approach, *J. Am. Chem. Soc.*,132 (2010) 7436-7444.

[368] C. Wu, P. Yin, X. Zhu, C. OuYang, Y. Xie, Synthesis of hematite (alpha-Fe_2O_3) nanorods: Diameter-size and shape effects on their applications in magnetism, lithium ion battery, and gas sensors, *J. Phys. Chem. B*, 110 (2006) 17806-17812.

[369] G. Zhang, Y. Gao, Y. Zhang, Y. Guo, Fe_2O_3-pillared rectorite as an efficient and stable fenton-like heterogeneous catalyst for photodegradation of organic contaminants, *Environ. Sci. Technol.*, 44 (2010) 6384-6389.

[370] B. Sun, J. Horvat, H. S. Kim, W. S. Kim, J. Ahn, G. Wang, Synthesis of mesoporous alpha-Fe_2O_3 nanostructures for highly sensitive gas sensors and high capacity anode materials in lithium ion batteries, *J. Phys. Chem. C*, 114 (2010) 18753-18761.

[371] J. S. Chen, T. Zhu, X. H. Yang, H. G. Yang, X. W. Lou, Top-down fabrication of alpha-Fe_2O_3 single-crystal nanodiscs and microparticles with tunable porosity for largely improved lithium storage properties, *J. Am. Chem. Soc.*, 132 (2010) 13162-13164.

[372] L. Chen, H. Xu, L. Li, F. Wu, J. Yang, Y. Qian, A comparative study of lithium-storage, performances of hematite: Nanotubes vs. Nanorods, *J. Power Sources*, 245 (2014) 429-435.

[373] C. Wang, L. Wang, K. Tang, Synthesis of mesoporous Fe_2O_3 nanorods and their electrochemical performance, *Int. J. Electrochem. Sci.*, 8 (2013) 4543-4550.

[374] J. Zhang, T. Huang, Z. Liu, A. Yu, Mesoporous Fe_2O_3 nanoparticles as high performance anode materials for lithium-ion batteries, *Electrochem. Commun.*, 29 (2013) 17-20.

[375] X. H. Ma, X. Y. Feng, C. Song, B. K. Zou, C. X. Ding, Y. Yu, C. H. Chen, Facile synthesis of flower-like and yarn-like α-Fe_2O_3 spherical cluster as anode materials for lithium-ion batteries, *Electrochim. Acta*, 93 (2013) 131-136.

[376] M. S. Wu, Y. H. Ou, Y. P. Lin, Iron oxide nanosheets and nanoparticles synthesized by a facile single-step coprecipitation method for lithium-ion batteries, *J. Electrochem. Soc.*, 158 (2011) A231-A236.

[377] X. C. Duan, L. Mei, J. M. Ma, Q. H. Li, T. H. Wang, W. J. Zheng, Facet-induced formation of hematite mesocrystals with improved lithium storage properties, *Chem. Commun.*, 48 (2012) 12204-12206.

[378] Y. M. Lin, P. R. Abel, A. Heller, C. B. Mullins, Alpha-Fe_2O_3 nanorods as anode material for lithium ion batteries, *J. Phys. Chem. Lett.*, 2 (2011) 2885-2891.

[379] J. Chen, L. Xu, W. Li, X. Gou, Alpha-Fe_2O_3 nanotubes in gas sensor and lithium-ion battery applications, *Adv. Mater.*, 17 (2005) 582-586.

[380] Z. Wang, D. Luan, S. Madhavi, C. M. Li, X. W. Lou, Alpha-Fe_2O_3 nanotubes with superior lithium storage capability, *Chem. Commun.*, 47 (2011) 8061-8063.

[381] J. Lu, Q. Peng, Z. Y. Wang, C. Y. Nan, L. H. Li, Y. D. Li, Hematite nanodiscs exposing (001) facets: synthesis, formation mechanism and application for Li-ion batteries, *J. Mater. Chem. A*, 1 (2013) 5232-5237.

[382] M. V. Reddy, T. Wu, C. H. Sow, Z. X. Shen, C. T. Lim, G. V. Subba Rao, B. V. R. Chowdari, alpha-Fe_2O_3 nanoflakes as an anode material for Li-ion batteries, *Adv. Funct. Mater.*, 17 (2007) 2792-2799.

[383] L. Chun, X. Wu, , X. Lou, Y. Zhang, Hematite nanoflakes as anode electrode materials for rechargeable lithium-ion batteries, *Electrochim. Acta*, 55 (2010) 3089-3092.

[384] Y. Han, Y. Wang, L. Li, Y. Wang, L. Jiao, H. Yuan, S. Liu, Preparation and electrochemical performance of flower-like hematite for lithium-ion batteries, *Electrochim. Acta*, 56 (2011) 3175-3181.

[385] S. Zeng, K. Tang, T. Li, Z. Liang, D. Wang, Y. Wang, Y. Qi, W. Zhou, Facile route for the fabrication of porous hematite nanoflowers: Its synthesis, growth mechanism, application in the lithium ion battery, and magnetic and photocatalytic properties, *J. Phys. Chem. C*, 112 (2008) 4836-4843.

[386] M. Zhu, Y. Wang, D. Meng, X. Qin, G. Diao, Hydrothermal synthesis of hematite nanoparticles and their electrochemical properties, *J. Phys. Chem. C*, 116 (2012) 16276-16285.

[387] M. Kruk, M. Jaroniec, Gas adsorption characterization of ordered organic-inorganic nanocomposite materials, *Chem. Mater.*, 13 (2001) 3169-3183.

[388] J. Zhang, Y. Sun, Y. Yao, T. Huang, A. Yu, Lysin-assisted hydrothermal synthesis of hierarchically porous Fe_2O_3 microspheres as anode materials for lithium-ion batteries, *J. Power Sources*, 222 (2013) 59-65.

[389] P. Tartaj, J. M. Amarilla, Iron oxide porous nanorods with different textural properties and surface composition Preparation, characterization and electrochemical lithium storage capabilities, *J. Power Sources*, 196 (2011) 2164-2170.

[390] S. Laruelle, S. Grugeon, P. Poizot, M. Dolle, L. Dupont, J. M. Tarascon, On the origin of the extra electrochemical capacity displayed by MO/Li cells at low potential, *J. Electrochem. Soc.*, 149 (2002) A627-A634.

[391] K. M. Shaju, F. Jiao, A. Debart, P. G. Bruce, Mesoporous and nanowire Co_3O_4 as negative electrodes for rechargeable lithium batteries, *Phys. Chem. Chem. Phys.*, 9 (2007) 1837-1842.

[392] A. K. Mondal, D. Su, Y. Wang, S. Chen, G. Wang, Hydrothermal synthesis of nickel oxide nanosheets for lithium-ion batteries and supercapacitors with excellent performance, *Chem. Asian J.*, 8 (2013) 2828-2832.

[393] X. D. Wang, J. H. Song, J. Liu, Z. L. Wang, Direct-current nanogenerator driven by ultrasonic waves, *Science*, 316 (2007) 102-105.

[394] C. R. Xia, M. L. Liu, Novel cathodes for low-temperature solid oxide fuel cells, *Adv. Mater.*, 14 (2002) 521-523.

[395] B. Tian, X. Zheng, T. J. Kempa, Y. Fang, N. Yu, G. Yu, J. Huang, C. M. Lieber, Coaxial silicon nanowires as solar cells and nanoelectronic power sources *Nature*, 449 (2007) 885-889.

[396] F. Y. Cheng, H. B. Wang, Z. Q. Zhu, Y. Wang, T. R. Zhang, Z. L. Tao, J. Chen, Porous $LiMn_2O_4$ nanorods with durable high-rate capability for rechargeable Li-ion batteries, *Energy Environ. Sci.*, 4 (2011) 3668-3675.

[397] W. Y. Li, L. N. Xu, J. Chen, Co_3O_4 Nanomaterials in lithium-ion batteries and gas sensors, *Adv. Funct. Mater.*, 15 (2005) 851-857.

[398] J. Liu, H. Xia, D. Xue, L. Lu, Double-shelled nanocapsules of V_2O_5-based composites as high-performance anode and cathode materials for li ion batteries, *J. Am. Chem. Soc.*, 131 (2009) 12086-12087.

[399] S. Ci, J. Zou, G. Zeng, Q. Peng, S. Luo, Z. Wen, Improved electrochemical properties of single crystalline NiO nanoflakes for lithium storage and oxygen electroreduction, *RSC Adv.*, 2 (2012) 5185-5192.

[400] J. F. Li, S. L. Xiong, X. W. Li, Y. T. Qian, A facile route to synthesize multiporous $MnCo_2O_4$ and $CoMn_2O_4$ spinel quasi-hollow spheres with improved lithium storage properties, *Nanoscale*, 5 (2013) 2045-2054.

[401] Y. Qiu, S. Yang, H. Deng, L. Jin, W. Li, A novel nanostructured spinel $ZnCo_2O_4$ electrode material: morphology conserved transformation from a hexagonal shaped nanodisk precursor and application in lithium ion batteries, *J. Mater. Chem.*, 20 (2010) 4439-4444.

[402] J. F. Li, S. L. Xiong, Y. Liu, Z. Ju, Y. T. Qian, High electrochemical performance of monodisperse $NiCo_2O_4$ mesoporous microspheres as an anode material for Li-ion batteries. *ACS Appl. Mater. Interfaces*, 5 (2013) 981-988.

[403] L. Zhou, H. B. Wu, T. Zhu, X. W. Lou, Facile preparation of $ZnMn_2O_4$ hollow microspheres as high-capacity anodes for lithium-ion batteries, *J. Mater. Chem.*, 22 (2012) 827-829.

[404] L. F. Hu, L. M. Wu, M. Y. Liao, X. S. Fang, High-performance $NiCo_2O_4$ nanofilm photodetectors fabricated by an interfacial self-assembly strategy, *Adv. Mater.*, 23 (2011) 1988-1992.

[405] Y. G. Li, P. Hasin, Y. Y. Wu, $Ni_xCo_{3-x}O_4$ nanowire arrays for electrocatalytic oxygen evolution, *Adv. Mater.*, 22 (2010) 1926-1929.

[406] L. Li, Y. Cheah, Y. Ko, P. Teh, G. Wee, C. Wong, S. Peng, M. Srinivasan, The facile synthesis of hierarchical porous flower-like $NiCo_2O_4$ with superior lithium storage properties, *J. Mater. Chem. A*, 1 (2013) 10935-10941.

[407] X. Fang, X. Yu, S. Liao, Y. Shi, Y. S. Hu, Z. Wang, G. D. Stucky, Lithium storage performance in ordered mesoporous MoS_2 electrode material, *Microporous Mesoporous Mater.*, 151 (2012) 418-423.

[408] L. Li, S. Peng, Y. Cheah, P. Teh, J. Wang, G. Wee, Y. Ko, C. Wong, M. Srinivasan, Electrospun porous $NiCo_2O_4$ nanotubes as advanced electrodes for electrochemical capacitors, *Chem. Eur. J.*, 19 (2013) 5892-5898.

[409] Q. Wang, X. Wang, B. Liu, G. Yu, X. Hou, D. Chen, G. Shen, NiCo$_2$O$_4$ nanowire arrays supported on Ni foam for high performance flexible all-solid-state supercapacitors, *J. Mater. Chem. A*, 1 (2013) 2468-2473.

[410] R. Ding, L. Qi, H Wang, A facile and cost-effective synthesis of mesoporous NiCo$_2$O$_4$ nanoparticles and their capacitive behaviour in electrochemical capacitors, *J. Solid State Electrochem.*, 16 (2012) 3621-3633.

[411] J. Liu, C. Liu, Y. Wan, W. Liu, Z. Ma, S. Ji, J. Wang, Y. Zhou, P. Hodgson, Y. Li, Facile synthesis of NiCo$_2$O$_4$ nanorod arrays on Cu conductive substrates as superior anode materials for high-rate Li-ion batteries, *CrystEngComm.*, 15 (2013) 1578-1585.

[412] H. Guan, C. Shao, Y. Liu, N. Yu, X. Yang, Fabrication of NiCo$_2$O$_4$ nanofibers by electrospinning, *Solid State Commun.*, 131 (2004) 107-109.

[413] L. Liu, Y. Li, S. M. Yuan, M. Ge, M. M. Ren, C. S. Sun, Z. Zhou, Nanosheet-based NiO microspheres: controlled solvothermal synthesis and lithium storage performances, *J. Phys. Chem. C*, 114 (2010) 251-255.

[414] S. L. Xiong, J. S. Chen, X. W. Lou, H. C. Zeng, Mesoporous Co$_3$O$_4$ and CoO@C topotactically transformed from chrysanthemum-like Co(CO$_3$)0.5(OH) center dot 0.11H$_2$O and their lithium-storage properties, *Adv. Funct. Mater.*, 22 (2012) 861-871.

[415] L. Hu, H. Zhong, X. R. Zheng, Y. M. Huang, P. Zhang, Q. W. Chen, CoMn$_2$O$_4$ spinel hierarchical microspheres assembled with porous nanosheets as stable anodes for lithium-ion batteries, Sci. Rep., 2 (2012) 986.

[416] J. S. Do, C. H. Weng, Preparation and characterization of CoO used as anodic material of lithium battery, *J. Power Sources*, 146 (2005) 482-486.

[417] S. Grugeon, S. Laruelle, L. Dupont, J. M. Tarascon, An update on the reactivity of nanoparticles Co-based compounds towards Li, *Solid State Sci.*, 5 (2003) 895-904.

[418] J. Li, S. Xiong, X. Li, Y. Qian, Spinel $Mn_{1.5}Co_{1.5}O_4$ core-shell microspheres as Li-ion battery anode material with a long cycle life and high capacity, *J. Mater. Chem.*, 22 (2012) 23254-23259.

[419] L. Tian, H. L. Zou, J. X. Fu, X. F. Yang, Y. Yang, H. L. Guo, X. H. Fu, C. L. Liang, M. M. Wu, P. K. Shen, M. Q. Gao, Topotactic conversion route to mesoporous quasi-single-crystalline Co_3O_4 nanobelts with optimizable electrochemical performance, *Adv. Funct. Mater.*, 20 (2010) 617-623.

[420] D. Liu, G. Cao, Engineering nanostructured electrodes and fabrication of film electrodes for efficient lithium ion intercalation, *Energy Environ. Sci.*, 3 (2010) 1218-1237.

[421] Y. Chen, J. Zhu, B. Qu, B. Lu, Z. Xu, Graphene improving lithium-ion battery performance by construction of $NiCo_2O_4$/graphene hybrid nanosheet arrays, *Nano Energy*, 3 (2014) 88-94.

[422] M. V. Reddy, G. V. S. Rao, B. V. R. Chowdari, Metal Oxides and oxysalts as anode materials for Li ion batteries, *Chem. Rev.*, 113 (2013) 5364-5457.

[423] R. Dedryvere, D. Foix, S. Franger, S. Patoux, L. Daniel, D. Gonbeau, Electrode/electrolyte interface reactivity in high-voltage spinel $LiMn_{1.6}Ni_{0.4}O_4/Li_4Ti_5O_{12}$ lithium-ion battery, *J. Phys. Chem. C*, 114 (2010) 10999-11008.

[424] S. Chen, J. W. Zhu, X. D. Wu, Q. F. Han, X. Wang, Graphene Oxide-MnO_2 nanocomposites for supercapacitors, *ACS Nano*, 4 (2010) 2822-2830.

[425] V. Subramanian, H. W. Zhu, R. Vajtai, P. M. Ajayan, B. Q. Wei, Hydrothermal synthesis and pseudocapacitance properties of MnO_2 anostructures, *J. Phys. Chem. B*, 109 (2005) 20207-20214.

[426] Y. Wang, Z. Q. Shi, Y. Huang, Y. F. Ma, C. Y. Wang, M. M. Chen, Y. S. Chen, Supercapacitor devices based on graphene materials, *J. Phys. Chem. C*, 113 (2009) 13103-13107.

[427] A. E. Fischer, K. A. Pettigrew, D. R. Rolison, R. M. Stroud , J. W. Long, Incorporation of homogeneous, nanoscale MnO_2 within ultraporous carbon structures via self-limiting electroless deposition: Implications for electrochemical capacitors, *Nano Lett.*, 7 (2007) 281-286.

[428] J. K. Chang, M. T. Lee, W. T. Tsai, M. J. Deng, H. F. Cheng, I. W. Sun, Pseudocapacitive mechanism of manganese oxide in 1-ethyl-3-methylimidazolium thiocyanate ionic liquid electrolyte studied using X-ray photoelectron spectroscopy, *Langmuir*, 25 (2009) 11955-11960.

[429] J. W. Long, K. E. Swider, C. I. Merzbache, D. R. Rolison, Voltammetric characterization of ruthenium oxide-based aerogels and other RuO_2 solids: The nature of capacitance in nanostructured materials, *Langmuir*, 15 (1999) 780-785.

[430] J. H. Jang, K. Machida, Y. Kim, K. Naoi, Electrophoretic deposition (EPD) of hydrous ruthenium oxides with PTFE and their supercapacitor performances, *Electrochim. Acta*, 52 (2006) 1733-1741.

[431] K. R. Prasad, N. Miura, Electrochemically deposited nanowhiskers of nickel oxide as a high-power pseudocapacitive electrode, *Appl. Phys. Lett.*, 85 (2004) 4199-4201.

[432] C. Lin, J. A. Ritter, B. N. Popov, Characterization of sol-gel-derived cobalt oxide

xerogels as electrochemical capacitors, *J. Electrochem. Soc.*, 145 (1998) 4097-4101.

[433] V. Srinivasan, J. W. Weidner, Studies on the capacitance of nickel oxide films: effect of heating temperature and electrolyte concentration, *J. Electrochem. Soc.*, 147 (2000) 880-885.

[434] R. Ma, Y. Bando, L. Zhang, T. Sasaki, Hydrothermal synthesis and electrochemical measurements, *Adv. Mater.*, 16 (2004) 918-922.

[435] S. C. Pang, M. A. Anderson, T. W. Chapman, Novel electrode materials for thin-film ultracapacitors: Comparison of electrochemical properties of sol-gel-derived and electrodeposited manganese dioxide, *J. Electrochem. Soc.*, 147 (2000) 444-450.

[436] F. Y. Cheng, J. Chen, X. L. Gou, P. W. Shen, High-power alkaline Zn-MnO$_2$ batteries using ɣ-MnO$_2$ nanowires/nanotubes and electrolytic zinc powder, *Adv. Mater.*, 17 (2005) 2753-2756.

[437] J. Jiang, A. Kucernak, Electrochemical supercapacitor material based on manganese oxide: preparation and characterization, *Electrochim. Acta*, 47 (2002) 2381-2386.

[438] H. J. Zheng, F. Q. Tang, Y. Jia, L. Z. Wang, Y. C. Chen, M. Lim, L. Zhang, G. Q. Lu, Layer-by-layer assembly and electrochemical properties of sandwiched film of manganese oxide nanosheet and carbon nanotube, *Carbon*, 47 (2009) 1534-1542.

[439] R. Liu, S. B. Lee, MnO$_2$/poly(3,4-ethylenedioxythiophene) coaxial nanowires by one-step coelectrodeposition for electrochemical energy storage, *J. Am. Chem. Soc.*, 130 (2008) 2942-2943.

[440] Y. Hou, Y. W. Cheng, T. Hobson, J. Liu, Design and synthesis of hierarchical MnO$_2$ nanospheres/carbon nanotubes/conducting polymer ternary composite for high performance electrochemical electrodes, *Nano Lett.*, 10 (2010) 2727-2733.

[441] Y. Qian, S. Lu, F. Gao, Preparation of MnO$_2$/graphene composite as electrode material for supercapacitors, *J. Mater. Sci.*, 46 (2011) 3517-3522.

[442] H. Huang, X. Wang, Graphene nanoplate-MnO$_2$ composites for supercapacitors: a controllable oxidation approach, *Nanoscale*, 3 (2011) 3185-3191.

[443] W. S. Hummers, R. E. Offeman, Preparation of graphitic oxide, *J. Am. Chem. Soc.*, 80 (1958) 1339.

[444] S. B. Ma, K. Y. Ahn, E. S. Lee, K. H. Oh, K. B. Kim, Synthesis and characterization of manganese dioxide spontaneously coated on carbon nanotubes, *Carbon*, 45 (2007) 375-382.

[445] E. Post, Manganese oxide minerals: crystal structures and economic and environmental significance, *Proc. Natl. Acad. Sci.* USA, 96 (1999) 3447-3454.

[446] L. Athouel, F. Moser, R. Dugas, O. Crosnier, D. Belanger, T. Brousse, Variation of the MnO$_2$ birnessite structure upon charge/discharge in an electrochemical supercapacitor electrode in aqueous Na$_2$SO$_4$ electrolyte, *J. Phys. Chem. C*, 112 (2008) 7270-7277.

[447] K. K. Lee, S. Deng, H. M. Fan, S. Mhaisalkar, H. R. Tan, E. S. Tok, K. P. Loh, W. S. Chin, C. H. Sow, Alpha-Fe$_2$O$_3$ nanotubes-reduced graphene oxide composites as synergistic electrochemical capacitor materials, *Nanoscale*, 4 (2012) 2958-2961.

[448] Z. Li, Y. Mi, X. Liu, S. Liu, S. Yang, J. Wang, Flexible graphene/MnO$_2$ composite papers for supercapacitor electrodes, *J. Mater. Chem.*, 21 (2011) 14706-14711.

[449] R. Devanathan, Recent developments in proton exchange membranes for fuel cells, *Energy Environ. Sci.*, 1 (2008) 101-119.

[450] L. Lu, H. Yang, J. Burnett, Investigation on wind power potential on Hong Kong islands-an analysis of wind power and wind turbine characteristics, *Renewable Energy*, 27 (2002) 1-12.

[451] P. V. Kamat, Meeting the clean energy demand: Nanostructure architectures for solar energy conversion, *J. Phys. Chem. C*, 111 (2007) 2834-2860.

[452] B. Scrosati, J. Hassoun, Y. K. Sun, Lithium-ion batteries. A look into the future, *Energy Environ. Sci.*, 4 (2011) 3287-3295.

[453] J. R. Miller, A. F. Burke, Electrochemical capacitors: challenges and opportunities for real-world applications, *Electrochem. Soc. Interface*, 17 (2008) 53-57.

[454] C. Arbizzani, M. Mastragostino, S. Soavi, New trends in electrochemical supercapacitors, *J. Power Sources*, 100 (2001) 164-170.

[455] C Jiang, E. Hosono, H. Zhou, Nanomaterials for lithium ion batteries, *Nano Today*, 1 (2006) 28-33.

[456] N. Yan, L. Hu, Y. Li, Y. Wang, H. Zhong, X. Hu, X. Cong, Q. Chen, Co_3O_4 Nanocages for high-performance anode material in lithium-ion batteries, *J. Phys. Chem. C.*, 116 (2012) 7227-7235.

[457] X. Wang, X. Li, X. Sun, F. Li, Q. Liu, Q. Wang, D. He, Nanostructured NiO electrode for high rate Li-ion batteries, *J. Mater. Chem.*, 21 (2011) 3571-3573.

[458] J. Zhu, W. Shi, N. Xiao, X. Rui, H. Tan, X. Lu, H. H. Hng, J. Ma, Q. Yan, Oxidation-etching preparation of MnO_2 tubular nanostructures for high-performance supercapacitors, *ACS Appl. Mater. Interfaces*, 4 (2012) 2769-2774.

[459] X. Xia, J. Tu, Y. Zhang, Y. Mai, X. Wang, C. Gu X. Zhao, Free-standing Co_3O_4 nanowire array for high performance supercapacitors, *RSC Adv.*, 2 (2012) 1835-1841.

[460] M. Bomio & P. Lavela, J. L. Tirado, Electrochemical evaluation of CuFe$_2$O$_4$ samples obtained by sol-gel methods used as anodes in lithium batteries, *J Solid State Electrochem.*, 12 (2008) 729-737.

[461] Y. Wang, D. Su, A. Ung, J Ahn, G. Wang, Hollow CoFe$_2$O$_4$ nanospheres as a high capacity anode material for lithium ion batteries, *Nanotechnology*, 23 (2012) 055402.

[462] Z. Bai, N. Fan, C. Sun, Z. Ju, C. Guo, J. Yang, Y. Qian, Facile synthesis of loaf-like ZnMn$_2$O$_4$ nanorods and their excellent performance in Li-ion batteries, *Nanoscale*, 5 (2013) 2442-2447.

[463] C. Fu, G. Li, D. Luo, X. Huang, J. Zheng, L. Li, One-step calcination-free synthesis of multicomponent spinel assembled microspheres for high-performance anodes of Li-ion batteries: A case study of MnCo$_2$O$_4$, *ACS Appl. Mater. Interfaces*, 6 (2014) 2439-2449.

[464] B. Cui, H. Lin, J. B. Li, X. Li, J. Yang, J. Tao, Core-ring structured NiCo$_2$O$_4$ nanoplatelets: Synthesis, characterization, and electrocatalytic applications, *Adv. Funct. Mater.*, 18 (2008) 1440-1447.

[465] G. Gao, H. B. Wu, X. W. Lou, Citrate-assisted growth of NiCo$_2$O$_4$ nanosheets on reduced graphene oxide for highly reversible lithium storage, *Adv. Energy Mater.*, 4 (2014) 1400422.

[466] L. Yu, G. Zhang, C. Yuan, X. W. Lou, Hierarchical NiCo$_2$O$_4$@MnO$_2$ core-shell heterostructured nanowire arrays on Ni foam as high-performance supercapacitor electrodes, *Chem. Commun.*, 49 (2013) 137-139.

[467] H. L. Wang, Q. M. Gao, L. Jiang, Facile approach to prepare nickel cobaltite nanowire materials for supercapacitors, *Small*, 7 (2011) 2454-2459.

[468] X. Y. Yu, X. Z. Yao, T. Luo, Y. Jia, J. H. Liu, X. J. Huang, Facile synthesis of urchin-like $NiCo_2O_4$, Hollow microspheres with enhanced electrochemical properties in energy and environmentally related applications, *ACS Appl. Mater. Interfaces*, 6 (2014) 3689-3695.

[469] Y. Chen, B. Qu, L. Hu, Z. Xu, Q. Li, T. Wang, High performance supercapacitor and lithium-ion battery based on 3D hierarchical NH_4F-induced nickel cobaltate nanosheet-nanowire cluster arrays as self-supported electrodes, *Nanoscale*, 5 (2013) 9812-9820.

[470] G. Q. Zhang, H. B. Wu, H. E. Hoster, M. B. C. Park, X. W. Lou, Single-crystalline $NiCo_2O_4$ nanoneedle arrays grown on conductive substrates as binder-free electrodes for high-performance supercapacitors, *Energy Environ. Sci.*, 5 (2012) 9453-9456.

[471] L. Shen, Q. Che, Hongsen Li, X. Zhang, Mesoporous $NiCo_2O_4$ nanowire arrays grown on carbon textiles as binder-free flexible electrodes for energy storage, *Adv. Funct. Mater.*, 24 (2014) 2630-2637.

[472] G. Zhang, X. W. Lou, General solution growth of mesoporous $NiCo_2O_4$ nanosheets on various conductive substrates as high-performance electrodes for supercapacitors, *Adv. Mater.*, 25 (2013) 976-979.

[473] J. F. Li, S. L. Xiong, X. W. Li, Y. Qian, Spinel $Mn_{1.5}Co_{1.5}O_4$ core-shell microspheres as Li-ion battery anode materials with a long cycle life and high capacity, *J. Mater. Chem.*, 22 (2012) 23254-23259.

[474] S. L. Xiong J. S. Chen X. W. Loo H. C. Zeng, Mesoporous Co_3O_4 and CoO@C topotactically transformed from chrysanthemum-like Co(CO_3)0.5(OH) centre dot $0.11H_2O$ and their lithium-storage properties, *Adv. Funct. Mater.*, 22 (2012) 861-871.

[475] A. K. Mondal, D. Su, S. Chen, X. Xie, G. Wang, Highly porous $NiCo_2O_4$ nanoflakes and nanobelts as anode materials for lithium ion batteries with excellent rate capability, *ACS Appl. Mater. Interfaces*, 6 (2014) 14827-14835.

[476] Y. Yu, C. H. Chen, Y. Shi, A tin-based amorphous oxide composite with a porous, spherical, multideck-cage morphology as a highly reversible anode material for lithium-ion batteries, *Adv. Mater.*, 19 (2007) 993-997.

[477] Y-S. Hu, L. Kienle, Y-G. Guo, J. Maier, High lithium electroactivity of nanometer-sized rutile TiO_2, *Adv. Mater.*, 18 (2006) 1421-1426.

[478] G. Zhao, N. Zhang, K. Sun, Electrochemical preparation of porous MoO_3 film with a high rate performance as anode for lithium ion batteries, *J. Mater. Chem. A*, 1 (2013) 221-224.

[479] Y. Liu, H. Zhang, P. Ouyang, Z. Li, One-pot hydrothermal synthesized MoO_2 with high reversible capacity for anode application in lithium ion battery, *Electrochim. Acta*, 102 (2013) 429-435.

[480] B. Zhang, Y. Zhang, Z. Miao, T. Wu, Z. Zhang, X. Yang, Micro/nano-structure Co_3O_4 as high capacity anode materials for lithium-ion batteries and the effect of the void volume on electrochemical performance, *J. Power Sources*, 248 (2014) 289-295.

[481] N. Spinner, W. E. Mustain, Nanostructural effects on the cycle life and Li^+ diffusion coefficient of nickel oxide anodes *J. Electroanal. Chem.*, 711 (2013) 8-16.

[482] C. Hu, J. Guo, Jin Wen, Hierarchical nanostructure CuO with peach kernel-like morphology as anode material for lithium-ion batteries, *Ionics*, 19 (2013) 253-258.

[483] K. K. Purushothaman, I. M. Babu, B. Sethuraman, G. Muralidharan, Nanosheet-assembled NiO microstructures for high-performance supercapacitors, *ACS Appl. Mater. Interfaces*, 5 (2013) 10767-10773.

[484] L. Yu, Y. X. Yan, Q. Liu, J. Wang, B. Yang, B. Wang, X. Y. Jing, L. H. Liu, Exfoliation at room temperature for improving electrochemical performance for supercapacitors of layered MnO_2, *J. Electrochem. Soc.*, 161 (2014) E1-E5.

[485] K. Deori, S. K. Ujjain, R. K. Sharma, S. Deka, Morphology controlled synthesis of nanoporous Co_3O_4 nanostructures and their charge storage characteristics in supercapacitors, *ACS Appl. Mater. Interfaces*, 5 (2013) 10665-10672.

[486] D. Li, F. Meng, X. Yan, L. Yang, H. Heng, Y. Zhu, One-pot hydrothermal synthesis of Mn_3O_4 nanorods grown on Ni foam for high performance supercapacitor applications, *Nanoscale Res. Lett.*, 8 (2013) 535.

[487] L. J. Wang, B. Liu, S. H. Ran, L. M. Wang, L. N. Gao, F. Y. Qu, D. Chen, G. Z. Shen, Facile synthesis and electrochemical properties of $CoMn_2O_4$ anodes for high capacity lithium-ion batteries, *J. Mater. Chem. A*, 1 (2013) 2139-2143.

[488] E. Vila, R. M. Rojas, J. L. M. Vidales, Q. G. Martinez, Structural and thermal properties of the tetragonal cobalt manganese spinels $Mn_xCo_{3-x}O_4$ (1.4<x<2.0), *Chem. mater.*, 8 (1996) 1078-1083.

[489] L. F. Hu, L. M. Wu, M. Y. Liao, X. H. Hu, X. S. Fang, Electrical transport properties of large, individual $NiCo_2O_4$ nanoplates, *Adv. Funct. Mater.*, 22 (2012) 998-1004.

[490] H. Jiang, K. Ma, C. Li, Hierarchical porous $NiCo_2O_4$ nanowires for high-rate supercapacitors, *Chem. Commun.*, 48 (2012) 4465-4467.

[491] S. H. Choi, Y. C. Kang, Yolk-shell, hollow and single-crystalline $ZnCo_2O_4$ powders: preparation using a simple one-pot process and application in lithium-ion batteries, *ChemSusChem*, 6 (2013) 2111-2116.

[492] X. L. Zhang, F. Y. Cheng, K. Zhang, Y. L. Liang, S. Q. Yang, J. Liang, J. Chen, Facile polymer-assisted synthesis of $LiNi_{0.5}Mn_{1.5}O_4$ with a hierarchical micro-nano structure and high rate capability, *RSC Adv.*, 2 (2012) 5669-5675.

[493] J. Gomez, E. E. Kalu, High-performance binder-free Co-Mn composite oxide supercapacitor electrode, *J. Power Sources*, 230 (2013) 218-224.

[494] J. Li, S. Xiong, X. Li, Y. Qian, A facile route to synthesize multiporous $MnCo_2O_4$ and $CoMn_2O_4$ spinel quasi-hollow spheres with improved lithium storage properties, *Nanoscale*, 5 (2013) 2045-2054.

[495] J. Li, J. Wang, X. Liang, Z. Zhang, H. Liu, Y. Qian, S. Xiong, Hollow $MnCo_2O_4$ submicrospheres with multilevel interiors: From mesoporous spheres to yolk-in-double-shell structures, *ACS Appl. Mater. Interfaces*, 6 (2014) 24-30.

[496] N. Munichandraiah, L. G. Scanlon, R. A. Marsh, Surface films of lithium: an overview of electrochemical studies, *J. Power Sources*, 72 (1998) 203-210.

[497] Q. Qu, P. Zhang, B. Wang, Y. Chen, S. Tian, Y. Wu, R. Holze, Electrochemical performance of MnO_2 nanorods in neutral aqueous electrolytes as a cathode for asymmetric supercapacitors, *J. Phys. Chem. C*, 113 (2009) 14020-14027.

[498] T. Xue, C. L. Xu, D. D. Zhao, X. H. Li, H. L. Li, Electrodeposition of mesoporous manganese dioxide supercapacitor electrodes through self-assembled triblock copolymer templates, *J. Power Sources*, 164 (2007) 953-958.

[499] J. W. Long, B. Dunn, D. R. Rolison, H. S. White, Three-dimensional battery architectures, *Chem. Rev.*, 104 (2004) 4463-4492.

[500] D. Aurbach, A. Nimberger, B. Markovsky, E. Levi, E. Sominski, A. Gedanken, Nanoparticles of SnO produced by sonochemistry as anode materials for rechargeable lithium batteries, *Chem. Mater.*, 14 (2002) 4155-4163.

[501] J. Li, S. Xiong, Y. Liu, Z. Ju, Y. Qian, High electrochemical performance of monodisperse $NiCo_2O_4$ mesoporous microspheres as an anode material for Li-ion batteries, *ACS Appl. Mater. Interfaces*, 5 (2013) 981-988.

[502] X. Yang, X. Dong, J. Wang, G. Liu, Glycine-assisted hydrothermal synthesis of $YPO_4:Eu3^+$ nanobundles, *Mater. Lett.*, 63 (2009) 629-631.

[503] Z. C. Zhang, J. F. Hui, Z. C. Liu, X. Zhang, J. Zhuang, X. Wang, Glycine-mediated synthesis of pt concavenanocubes with high index {hk0} facets and their enhanced electrocatalytic activities, *Langmuir*, 28 (2012) 14845-14848.

[504] W. Li, K. Xu, G. Song, X. Zhou, R. Zhou, J. Yang, Z. Chen, J. Hu, Facile synthesis of porous $MnCo_2O_{4.5}$ hierarchical architectures for high rate supercapacitors, *CrystEngComm.*, 16 (2014) 2335-2339.

[505] X. L. Wu, Y. G. Guo, L. J. Wan, C. W. Hu, α-Fe_2O_3 nanostructures: Inorganic salt-controlled synthesis and their electrochemical performance toward lithium storage, *J. Phys. Chem. C.*, 112 (2008) 16824-16829.

[506] D. Su, M. Ford, G. X. Wang, Mesoporous NiO crystals with dominantly exposed {110} reactive facets for ultrafast lithium storage, *Sci. Rep.*, 2 (2012) 924.